Using High-resolution imaging satellite constellations to understand glacier mass balance and dynamics in High Mountain Asia

Shashank Bhushan

A dissertation submitted in partial fulfillment of the
requirements for the degree of

Doctor of Philosophy

University of Washington

2023

Reading Committee:

David Shean, Chair

Jessica Lundquist

Scott Henderson

David Rounce

Program Authorized to Offer Degree:
Civil & Environmental Engineering

University of Washington

Abstract

Using High-resolution imaging satellite constellations to understand glacier mass balance and dynamics in High Mountain Asia

Shashank Bhushan

Chair of the Supervisory Committee:
Assistant Professor David Shean
Civil & Environmental Engineering

Meltwater from glaciers in High Mountain Asia (HMA) is an essential source of discharge for major Asian rivers, which sustain one of the most densely populated regions on Earth. HMA glaciers are in a state of overall decline, with models projecting that this decline will continue in the coming decades as the Earth warms. An improved understanding of past, present, and future glacier change in HMA is crucial for informing ongoing and future policy decisions. While recent efforts have documented the long-term to interannual evolution of HMA glacier mass balance and ice flow, these records do not capture local, fine-scale processes operating on shorter timescales (e.g., surface debris-cover evolution, basal sliding), and their effect on glacier mass balance and dynamics.

Precise geodetic measurements of 3D surface displacement from high-resolution satellite imagery can be used to study glacier motion and associated volume changes over time. The dissertation outlines several new methods to derive geodetic products from commercial satellite imaging constellations (Planet Labs, Maxar). We use these methods to generate new data products that document HMA glacier change with unprecedented spatial and temporal resolution.

In the second chapter, I developed automated workflows for multi-view stereo camera model refinement and image geolocation corrections for the Planet Labs SkySat-C constellation. The refined camera models are used to generate accurate and self-consistent DEM products at 2 m resolution and orthoimages at the native 0.7-0.9 m resolution. I analyzed sample DEM products for a triplet stereo collection over Mt. Rainier, USA, and two video collections over Mt. St. Helens, USA. The output DEM products display ≤ 1 m relative and ≤ 2 to 3 m absolute vertical accuracy, which easily captures the 5 to 15 m of elevation change signals over Mt. St. Helens due to the melting of seasonal snow and glacier flow.

In the third chapter, I used very-high-resolution images acquired by the Maxar constellation to prepare a time series of contemporaneous DEM and surface velocity products for six debris-covered glaciers in Nepal. I combined these measurements with publicly available ice thickness estimates to produce flow-corrected Lagrangian surface mass balance (SMB) maps and used these maps to study local surface melt signals. Our results show melt reduction under thick debris cover and enhanced ablation over ice cliffs. These ice cliffs were responsible for 17 to 43% of the total ablation over debris-covered areas, even though they occupied $\leq 11\%$ of the entire area. Our seasonal SMB products reveal the timing and patterns of summer accumulation and ablation, underscoring the importance of snow avalanches for low elevation debris-covered glaciers in the region.

Finally, the fourth chapter outlines new techniques to derive monthly to seasonal surface velocity time series for HMA glaciers using near-daily, high-resolution (~ 3 m) optical imagery from the PlanetScope constellation. To address the geolocation issues associated with Planet data, I combined 1000s of noisy velocity maps derived from individual image pairs using robust spatiotemporal statistics to obtain systematic, analysis-ready monthly velocity measurements. Our results offer detailed documentation of the surge front propagation and seasonal variability for the Gando Glacier during the 2018-2021 surge event. We also observe previously undetected seasonal velocity variations over the slow-moving, heavily debris-covered Ngozumpa and Khumbu Glaciers, including the Khumbu Icefall. Our observations indicate that peak glacier velocities occur during the summer and monsoon months, with a summer speedup of ∼67% observed over the main, fast-flowing western tributary of Ngozumpa Glacier. These methods and datasets offer new insights on the seasonal evolution of subglacial hydrology, basal sliding, meltwater storage, and glacier sensitivity to future change.

TABLE OF CONTENTS

LIST OF FIGURES

Figure Number Page

LIST OF TABLES

Table Number Page

ACKNOWLEDGMENTS

During the week of Feb 13th, I was on a writing retreat in Portland. I got bogged down with a processing issue and started trying to solve it obsessively. Even though the issue was something out of my control, a feeling of negativity soon crept in, and I started losing confidence in myself and all my work. This period was one of the most stressful and punishing periods of grad school; when the entire world was celebrating Valentine's week, I was right up there questioning each and every decision of my life and wondering if I could exit the program even at this moment, less than 2 months away from my defense. Fortunately, I had a few special people in my life who helped me in this crucial period, and I could not have completed the degree without them. This dissertation is theirs as much as it is mine! My parents and sister were there to talk to and calm me down when I woke up shivering and fearing everything in front of me. My high school buddies Sanket and Rishu were always available to chat and offer perspectives from a non-academic lens. My friend Eric kept checking on me frequently, and when I came back to Seattle, gave me all his attention and offered his perspective on both the mental state and technical front. David and Scott talked with me at length, discussing the technical issues, and did all they could to rebuild my confidence and get me back on track. Slowly I started to work again, but I realized as soon as I spent some time alone, the feeling of negativity started creeping in again. My friend Michelle offered a lot of support and welcomed me to co-work with her and her friends either virtually or in coffee shops :) And with all their support, we are here! Thank you all! I now progress with the rest of the conventional acknowledgment.

"No Dream is ever chased alone."

– Rahul Dravid

I have been a Dravid fan for most of my life, always trying to model myself and my behavior with features Dravid was associated with, such as team person, selfless, stoic, humble, calm, and helpful. Grad school taught me where I was falling short with some of these virtues and kept reminding me to strive for these virtues, even in times of distress and pressure. I am very sure I failed on these fronts multiple times during the past five years, but through these experiences and several acts of kindness by folks around me, we are here, reading my favorite section of this Ph.D. dissertation. The quote also rings true with this effort, and this section describes the heroic support provided by many people who made this possible! It's going to be a long one, so if you want to cut through to the methods and science, please feel free to skip it! However, if you're willing to get a glimpse of some personal stories and motivations which enabled this dissertation, I hope you will enjoy this section!

I would begin by acknowledging the support provided by my advisor, David Shean. I first met David during the summer of 2017, and I became a fan in the first instance. I was in awe of his technical prowess and command-line wizardry and was like, "man, I want to learn and be as cool as David." I accepted his offer to join his new lab as one of the inaugural members and returned as a grad student. David has supported me in multiple ways, some of which include guiding my research, tricks to write better, providing feedback on presentations so that they are tuned for the audience present, helping to rationalize my feelings, supporting me mentally when I have been burdened by my own expectations, taking the blame for my shortcomings with higher-ups, and whatnot! I recall several meetings with David where I was bogged down with frustration, and confused on what do next, and I remember walking out of those meetings felling content and happy for next steps :) I am grateful to David for sharing his research enthusiasm and his set of tools, both of which I used and built upon to conduct the research outlined in this thesis. I am grateful to David for inviting me to collaborate on his research and proposals, and introducing me to his colleagues. I am also grateful to David to allow me to collaborate with other students on independent research projects in addition to the main research I conducted for the thesis. It has been a learning experience for both of us, and I am fortunate to have shared this journey with David. Thank you for your time working with me, thank you for providing your thoughts on future career pathways, thank you for sharing your experiences, thank you for your patience with me as I started up or on instances when I was dealing with personal issues. One such instance was right after we concluded the preliminary analysis for the Chamoli disaster, and I was pretty much depleted. Around the same time, the second wave of COVID-19 broke out in South Asia. This wave was dreadful; so many of my family and friends were affected. People were on the road, rushing and hustling for non-existent medical supplies and dying due to a lack of oxygen and hospital beds. I was rife with emotions of fear, shame, and guilt. It remains one of the worst and most excruciating moments in my life. I had a heartfelt chat with David, who mostly listened; he comforted me by saying that nothing is expected from me at this point, and I can take all the time to process the grief. We also discussed the utility of science and engineering in making our world better and the realization that every science project, big or small, is important. We discussed how the Covid vaccine was built upon research originating from multiple Ph.D. and MS dissertations, and we should always take pride in our work. I used this “paid time off” to volunteer as remote support to groups working on the ground to help patients needing medical support, calling and enquiring hospitals and medical stores in India to update their inventory in real-time and assisting in facilitating food distribution to the needy. This experience was necessary, as I am not sure I could continue working on this dissertation in such a precarious situation. I felt connected, which reduced my fearful feelings, I could channel the guilt by being helpful in the present moment, and I could channelize the sense of shame from destroying me internally to help me take future steps to make myself aware of all the societal privileges I have enjoyed in my life, and how I can give back. During one of these meetings, David also encouraged going for therapy, which I eventually did a few weeks after talking to some other friends :) Thank you for being the professor when introducing geospatial data analysis and surveying, thank you for being the research mentor when editing papers/proposals and suggesting ideas, thank you for sharing your technical wizardry as a colleague, and thank you for being a friend when talking about everything else, David! I look forward to some more interesting future collaborations!

I want to acknowledge my committee members, Scott Henderson, Jessica Lundquist, Michelle Koutnik, and David Rounce. All of them provided essential support in various ways; here, I try to narrate some of those.

Scott Henderson is a special person; he always amazes me with his kind gestures, willingness to help the community, and passion for promoting communal growth more than individualistic scientific pursuits. Scott noticed when other members of our group or I were going through rough times, and as always, he was there to offer a helping hand. He always kept checking in and offered to meet for coffee or lunch to chat about projects, impending career decisions, and life. I can never forget a gloomy December day in 2021 when we were stressed with annual AGU prep, and Scott came to the office with a box of donuts to bring some joy in our (students) otherwise stressed up lives :) During the final two months leading up to the defense, Scott agreed to spend 30 minutes with me every week where I discussed progress, and Scott provided feedback to keep me going and not get bogged down with perfection. Thanks for everything, Scott :)

Jessica Lundquist has always been an inspirational leader for members of our group, myself included. I am always impressed by her scientific temper, time management, and big-picture, forward-looking research agenda. I am grateful for the support and essential guidance she provided during our meetings, email chats, or thesis edits. But one of her most important contributions to my life as a grad student was the seminar series she organized, where faculty members were asked to share their personal stories, how they ended up here, and incidents that have kept them going. This was very different from talks where a senior academician just talks about their breakthrough work or articles. I am a sucker of good motivating stories, and this seminar series was very special and essential for me at a point of grad school when I really needed to believe that there is light at the end of the tunnel. Her own talk during that seminar series was so real; where she talked about her vulnerabilities as a grad student, her day-to-day struggles, and how she managed to keep going taking on these challenges with a smile. Many people talk about how academia should be made more welcoming and humane, but this leadership act of hers was an actual step in this direction. Thank you, Jessica!

David Rounce provided critical guidance from his experience on debris-covered glaciers and was always happy to discuss how he navigates his personal life while pursuing excellence in academia. He was always there to discuss ideas and offer feedback when I needed it, and helped me realize the value of our observational products in large-scale glacier modeling. I still remember meeting David in person at the AGU Fall Meeting in New Orleans in 2017. I asked David how he managed to work on so many interesting and diverse topics simultaneously and how he even got those unique ideas. He laughed and told me not to worry and to take it easy. It will come automatically as I keep working when I encounter the shortcomings of a particular approach or when I find a new process that is poorly understood but is important to understand the future evolution of the system in question fully. That remains one of the most valuable pieces of advice I have ever got in academia! Thank you, David R.!

I first met Michelle Koutnik during my first talk at GLunch, where I presented some of my preliminary work on debris-covered glaciers in Jammu and Kashmir. After the talk, Anthony facilitated our introduction, and I still remember the enthusiasm she had for my work. She was one of the instructors at the scientific writing course during which I was also working on the NASA proposal, and she was always happy to bounce off ideas and offer support. She is an exemplary scientist, managing and leading several big research projects, but she always finds the time to reach out with kind and encouraging emails when I was stressed with the General Exams or when I was working on the dissertation. Thank you, Michelle, for your time to see this through!

Thank you Faisal Hossain for serving on my Qualifying Exam committee! Thank you for making all of us realize the value and power of using our scientific results for providing engineering solutions for social upliftment. Also, thank you for inviting me to all of your groups' celebrations and parties, making me feel like to be at a South Asian family dinner every time, even though I was in reality 7000 miles away from home!

This work would not have been possible without the support of Anthony Arendt, who I comically refer to as the "honoree member of my committee". Anthony was the one who brought me to the US as an undergrad intern and served as my first mentor here. Anthony provided valuable guidance on pursuing science with objectivity, maintaining work-life balance, and being helpful and humble while doing all of this! In many ways, he was the academic equivalent of Dravid for me. He has continued to support me through my Ph.D. and is always available to talk through my thoughts and emotions. I regard Anthony as one of the best leaders I have worked with, and I am always inspired by his effort to support early-career people, making them feel welcome and comfortable. He and Kristen are someone who I also consider good friends. I love our conversations; we share our passion for cooking and food, and I never hesitate to open up to them! I can never forget the lavish dinner Anthony and Kristen prepared a week before my General Exam when I was super stressed! Thank you for always being there!

I have been very fortunate to work with some wonderful collaborators during my Ph.D, who have inspired me in so many ways! Early on, I was really inspired by an incident when we were working towards a deadline on the HMA glacier mass balance paper, and we were all stressed. Paul Montesano, who was in a NASA meeting, took the time to sneak out whenever the opportunity presented itself and provided really great edits on the discussion sections :) Paul was not obliged to this, but he did this to get the team through!! While working on the SkySat project, I got the first opportunity to interact with Oleg, the magician, and the rest is history. Oleg has been instrumental in so much I have done in grad school, I really appreciate his careful and concise explanations for difficult topics. Working with Friedrich on photogrammetry and all things historical has been so much fun! During the early days of the pandemic, I was delighted to receive an email from Whyjay, Will, and Max about the potential to collaborate on a feature-tracking intercomparison exercise. It has been a delight to work with this awesome group; I have got a chance to learn a ton of stuff from them! I hope we continue working together in the future, friends :) Near the end of 2020, I got the opportunity to start a formal collaboration with Michelle and work on photogrammetry experiments. Working with her during one of the toughest days was really helpful, helping me to make progress and make research fun again. The time spent while working on the Chamoli disaster was hectic and stressful but was arguably one of the most productive times of grad school, where I learned about so many new things. This research was also helpful for me to realize the importance of our work as Earth Scientists and also the value of connecting our research findings with societal implications. I hope someday I will get to connect more of our science with society. Thank you, Dan Shugar, for bringing us together, for leading us so well, and for providing us with the opportunity to collaborate. Thank you to Jessica for providing me with the opportunity to contribute to icepyx! Thank you, everyone, for working together with me; you all were crucial in making this possible!

So much of academia is just a set of unwritten rules, and it would have been impossible for me to navigate this pathway without the support I received from several senior colleagues. Pranjal Dwivedi was always there to discuss confusing aspects of grad school and life, when I needed input from him. Ravi Appana was always present to offer support whenever I needed it, providing sources of motivation and advice, passing on cool opportunities, checking in always how things are going :) Conversing with Umesh always provided a new perspective on life and research, and I am very grateful to him for openly sharing his experiences with me. I am greateful to Vibhor da for sharing his experiences and providing important perspectives. One of them was to try out the Art of Living, which has been a game changer in many ways. Saurabh Vijay was always happy to chat whenever I was confused about a life step and always ready to humbly listen to what I was going through! Sai was very welcoming when I joined UW CEE, and has always been helpful, providing me great advice on anything related to academia, life. I am so greatful to have you as a friend, Sai! Chatting with Billy and Shad at conferences has always been fun; thanks for providing us all (students) with a positive atmosphere! I met Tri Datta for the first time during the SnowEx Hackweek and was totally inspired by the energy she brings to science! I have not been able to be in touch with her more often, but I become hopeful about science again whenever she speaks on topics and issues on twitter, which others prefer to remain quiet on. I hope the world gets more leaders like her! Taryn Black went the extra mile to make the ESS community more welcoming and was always happy to help and chat about things! Thank you to Jigyasu Agarwal and Hrishabh Gupta for introducing me to the world of GIS! Beyond the UW community and senior scientists, I have also taken a lot of inspiration from many young colleagues around me. Discussions with Emma Marshall, Lucas Zeller, Mira Khadka, Albin Wells, Johnny Burton, Matt Olson, Rainey Aberle, and many others have been very insightful and provided me with a lot of perspectives about science and life. I always look forward to grabbing lunch/dinner/coffee/beer with you all at meetings and am very thankful to call you all my friends. Thank you, everyone!

The internship at Planet has been crucial to my growth as an independent scientist and team player. I will always be grateful to Kelsey, Antonio, and the entire data pipeline team for providing such a friendly environment in the all-remote team! Duy Nguyen went out of his way to help me run custom jobs on the Planet computer system, without which I would not have been able to complete my internship. Thank you, Duy, for the support and the friendly conversations we had. Joe Kington has provided mentorship even after the internship, I still remember how energized I felt after talking to Joe in New Orleans, AGU 2020 when otherwise I was going through a rough patch! Seth Price has been crucial in helping me complete this dissertation by kindly taking out the time to reprocess the imagery used in Chapter 4. On top of being a great scientist and engineer, Seth is a lovely and caring human being, always happy to provide support and motivation and chat about computer things :) The ever-smiling Sam Roy is a joy to be around, I am really happy to have a friend and mentor like him :) Tanya Harrison continues to be an inspiration on multiple fronts. Thank you for supporting our work, and thank you for inspiring me to be fearless and keep going!

Michelle Hu, Eric Gagliano, Friedrich Knuth, and Joachim Meyer (Joe) remain the closest friends I made during my Ph.D. program. Michelle has been kind and helpful in so many ways. I consider her one of my most fun collaborators; I loved all our sessions going through snaphus on the Pleiades, stereo DEMs and weird results. She was always available to listen and help me rationalize my thoughts and feelings. She took the lead on many days when I was going through rough patches and was always happy to act as my advisor/instructor to keep me on track. But most importantly, I admire the openness with which Michelle spoke her mind out, and took the lead on DEI activities in the department. I give her a lot of credit in providing me with opportunities to understand my privileges and view our community around us with a much more considerate lens. Michelle not only introduced me to the intricacies in mapping snow, but she organized my first snowshoeing experience. I am 200% sure that trip could not have been any better. I would not have done any snow expedition if not you! Thank you Michelle and Ash for joining in on so many fun activities, and thank you Michelle, for your support in the final phase of this PhD! Also, sorry if I bothered you by asking to organize maybe too many (:) ?) work sessions and meetings to keep me on track :D I hope in some other world/life I would be able to repay these act of kindness to others around me.

Eric was the most vibrant desk mate I could ask for!! Full of energy, the kind Eric was always there to help everyone around with a smile! Eric and I shared some lovely memories in the lab, often staying weirdly late hours to get things done just before deadlines, doing runs in Costco to grab wholesale goods at discounted rates, and touring to so many Seattle areas restaurants and ice cream shops :D Eric has always been available for emotional support and mental support, and he listens to folks around without judgement! Thanks for the special support during the final stages of the thesis! Eric is the group glue, he brings our lab together for all fun activities, which all of us would have skipped using too much work as a reason. Eric has always set an example of being kind and humble but one of the best thing I like about him is his ability to take a stand when the situation requires! The fact that Eric and I will cease to be desk mates sometime in the future is something I do not want to imagine, but hopefully, we will continue being friends for the rest of our lives :) Thank you buddy!

Friedrich was the one who introduced me to everything which is the US, always providing tidbits on how to survive here. In many ways, he acted as an elder brother, providing his support whenever I needed. One such occasion was when I was going through a very rough personal patch in 2022, and a deadline was looming on our heads to complete a work. Friedrich dropped everything aside, brought me some awesome lunch, and offered to walk along the shores of Golden Gardens. Friedrich was also the first person to checkout#hurricaneiscooking, when I made a kebab for the first time! Thanks for teaching me so much about historical film imagery, photogrammetry, and leading life in a cheerful and kind way :) Also, thanks for your snow boarding, and driving lessons, :wink: I promise you someday I will drive and show you around a new city :) More importantly, thank you so much for always being there :)

I met Joe in the 2018 GeoHackWeek, and have been fortunate to know him since as a friend! Joe, like my other friends, shares a love for biryani! It has been awesome to go on many such biryani hunts with Joe! Joe is also a connector, working out friends dinner nights during conferences, making the hackweeks more fun, and making academia more fun in general. I have had many honest and meaningful conversations with Joe, and one which I will not forget will be the AGU 2020 chat at a museum restaurant! Joe listened so patiently and passed on some very encouraging words, which I really needed :) Joe always keeps checking in on us and cheering us up from Salt Lake City, we always look forward to hang out together, and if that is delayed by logistical constraints, we keep in touch via zoom/facetime! Thank you Joe, for everything :)

The TACO lab is the TACO lab because of all its members, with their unique personalities and qualities! Seth has been an awesome desk buddy, and has always inspired me to live a balanced and happy life. On many occasions when I was stressing through for work, he was there to remind me it's okay, the problem is probably not that important to not to take a break and do something else:) Thanks Seth for all the joint bike rides and walk the talks! Quinn, and his enthusiasm for conducting research is unparalleled, something which always keeps inspiring me. Thank you for keeping me motivated with your discipline and passion! Greg and Romain joined us late in my Ph.D., but made our lab's atmosphere so much more fun :) Thank you Greg for all your help in ice physics, and to you, Molly and Nuna for hosting us several times in Snowqualmie! Thank you Romain for always being available to discuss anything related to errors and glaciers and DEMs:) Thank you Greg for introducing me to Fondue, and thank you Romain for introducing me to Matte :) I am looking forward to work more with you all in the future. Chris and Alan provide our lab with the non icy, non snowy touches, and it was great to learn more about their research! More importantly, hanging out with all of the TACO lab members has been very refreshing and memorable, even though I get properly beaten and promptly finish last in all the sports/recreation events :)

The hydro community at UW is awesome, and I feel privileged to have worked and played with you all in these years. Steven, Cassie, Victoria, Sam, and Indira started at approximately the same time we did, and have been super fun to learn and hang out with. The new blood consisiting of Eli, Bareera, Carina, Danny, Hannah, Hordur, Adi, Shahzaib, Sarath, and George, joined us later, and made this journey even more fun! Thank you all for filling the otherwise yellow-painted Wilcox Hall with energy and life :) Thank you Pritam and Sanchit for providing moments of desi fun, and for always providing emotional support for things related to home! A shout out to all the senior students of Hydro: Amanda, Claire, Yifan, Justin, Ryan, Christine, Nishan, and Shahryar! A special shout out to Claire and Amanda for organising fun events, always making time to bring us all together before COVID hit! Thanks for creating the tradition of this friendly student atmosphere in the department, and thanks for the support you provided to your new colleagues :)

The awesome friends from school who still continue to be great friends, thank you all so much! You all provide me with a landing base and bring me back to my roots! Thank you, Sanket, Rishu, Rishav, Mayank, Aman, Apporva, Prasun, Kunal, Pallavi, and Abdul, for your support all throughout these years! The friends and seniors who later went on to become friends at ISM, thank you for making Dhanbad so much fun! Varun da, thanks for mentoring me through this unknown path of science and grad school, my only dream after entering ISM was to work for Schlumberger, never did I know we would be at this! Thank you, Manish, Fawz, Gagan, Sumit, and Shah Rhythm, Vivek, DP, Amit, Vishal Babu, for always being available to chat and meet whenever the opportunity presented itself, even after I moved to the US. Debanjan da for providing me with crucial support as I learned the ropes of applied research! Remya and Pradep for making IISc. Bangalore fun, I am fortunate to have met you 2 and call you 2 my friends :) Thank you, Don, for being my first friend in Seattle and for teaching me everything related to programming, which I practice these days! Thank you all for being what you are, someone who I can blindly trust and talk about anything!

Thank you to my wonderful roommates Ananya and Ninan, you will go down as one of the most integral people who made this possible! The combined knowledge we share about cinemas from all over the world could easily make our trio millionaires, if who wants to become a millionaire was only about movies! Thank you for standing with me through thick and thin, for providing support during moments of distress, and for celebrating every small milestone together! If not for you guys and Daler Mehndi, I would have never danced :D You are the best, and you all made the pandemic bearable! Thank you to my first year roommate Argha da, who took care of me in so many ways, and who more importantly taught me to cook! The Hurriance, and the hurricaneiscooking would not have been possible without you! Thank you to Mihir, Rahul, Shiva, Gayatri, Amandeep, Debosmita, Ayushi, Shabab, Sami and the entire Microsoft/Amazon gang for all fun activities we did together! Thank you Sachidanand Baba for accompanying in all the fun park explorations in the Seattle area, and for serving as the elderly like family member away from home! Thank you to Dianne for welcoming me into your family in the US when I arrived, and to all of your family members who joyously welcomed me in all the celebrations :) What would I be without you all, in this all new world :)

Alright, now I will take you all with me to travel back in time and look into some inspirations going up, and how I got here! My parents have been an integral part of my journey throughout; their love for each other, and their love for our family never fails to amaze me. Raising the two of us was never an easy task, but they embraced the challenge with pride and continuously grew stronger. The biggest life lesson I got from them was you can never be happy until everyone you care for is also happy, so watching out for our loved ones through rough periods is equally important as is watching out for yourself. My granddad is my first teacher, introducing me to the wonderful world of numbers and alphabets from two different languages. He was always there to help me stay disciplined and continued telling me to keep taking notes of every small experiment I do daily. I wish I had always followed his advice; that would have reduced so much of my anxiety in graduate school :) One of the things I keep missing in the US is his towering presence around me, reminding me things will be fine when I go through a rough patch and always to stick to basics and be disciplined :) My grandma was the perfect foil to my granddad, providing us with the opportunity to use some instances where we could sneak out and live our lives to the fullest. I miss the stacked fridge with food and cold beverages, but more importantly, I miss her everyday calls, checking on how I was doing, how things were… I did not understand why she used to be so concerned about me back in the day. I realize I could never properly reciprocate her love, and I realized this only after she went away to the heavens, days before I joined grad school. I never realized the love by which someone calls you in the middle of the day in the US, half asleep, checking if you are okay because they saw something in their dream! Miss you, Ma! Rubi Fua and Bablu Fufa have filled our lives and our house with joy from day one! Bablu Fufa was the one who introduced me to DIY electronics assembly and got our first computer. I used to admire him for how he could do so much stuff on his own, the only initial year experience which is close to grad school :) Rubi Fua was always there to hear me out, give me input, and prepare some lovely food for which I had craving for but eating out was not possible. Having Pankaj Fufa and Guddi Fua visiting us was a breath of fresh air, they were the most modern and open-minded couple in our family growing up, and with them around, we could suddenly imagine doing activities which we would never even dare to think of normally. I still remember when I was leaving for Dhanbad to get admission to undergrad, all of them came along to say me goodbye, with my luggage being distributed among 2 motorbikes and a rickshaw on the way to the train station! Visiting Muzaffarpur every summer vacation, and meeting my Nana, Nani, Mama, Mami and so many of our family members was the favorite time of my childhood, I am indebted to all of the them for supporting me throughout my life. Raju mama and Sweety mami introduced us to our first pizza ever, and to fancy hotel experiences: one of my childhood motivations to study hard and improve our lives. I used that motivation for a long time; thanks for sharing your part of the world with us :) Thank you to Deepak Baba for being the inspiration to do a Ph.D., and thank you to everyone from the Sharan family for all the love and care you all have showered on us throughout the years! Thank you, all!

I have been blessed with a wonderful sibling and some of the best cousins you could ever ask for! I know I have made their lives a bit difficult by being the behaved guy and them being pressured to be like me, but trust me, I love you all the way you are! Till the time we were together before I joined undergrad, I can only recollect the fights I had with my sister, Shivi, for all sort of things. We did not talk much during our respective undergrads, but became one of the best friends after moving to Seattle :) Thanks for being so fun, and I apologize for being so annoying all my life! Thank you specially for taking care of everyone back home while I was 7000 miles away! Sankalp was most fun to hang out with growing up, and I cherish all our adventures in Muzaffarpur and Patna till day. Spending time with Choti, Shipra and Bhanu during summer and winter breaks taught me so much about living in a pack, and I miss all the stupid things we all did together as kids. Mishti, Lipi, Anuj and Raj, the new blood, nowadays remind me how important it is to live life with no expectations, every time I meet them, I feel energized! I am proud of what all you have done, and I will always be thankful for all the support and love you all keep showering at each other :) Thank you!

Teachers form an integral part of everyone's life, and I have been blessed to be trained by so many kind teachers all my life! All teachers who I crossed paths with in Don Bosco Academy have contributed immensely to how I see the world today! Pinky Ma'am continues to be my strong confidant till this day, and I am grateful to her for always being there when I need some advice and support from her. Thank you, Sanjay sir, for taking care of my math and making it so easy, so that I could focus more on the humanities, the subjects which I still love more. Thank you so much! Professors at ISM Dhanbad provided new perspectives, and I will always be grateful to Dr. Syed and Dr. Kulkarni for introducing me to the world of research and glaciers! Where would I have been without you!

Thank you to all the colleagues at eScience who make spending time at eScience so much fun! Thank you, Jenny for maintaining an incredibly friendly atmosphere at eScience! Thank you Valentina for all the tidbits and being my late hour co-working partner when I stayed late at the eScience studio :) Thank you to Yu-Chan and Barb for taking care of all the admin support through APL! Thank you Cindy and Lily for taking care of all student employees requests and issues so well! Thank you for all your efforts in providing us with the necessary support so that we could conduct our research and studies in a timely manner. Thank you to Jill for providing assistance and guidance when I was preparing my first proposal! Thank you to Jon, Karen, Janice, Bryan, Charlotte, Kimboo, Ted, Janice, Eric, and everyone at CEE office for providing admin support and assistance! Thank you to the UAW student union for constantly working towards improving our work contracts. Specifically, thank you for putting in the effort towards making mental health care more accessible and affordable! Thank you so much to the UW Mental Health group for providing top notch services! Thank you to the therapists who organised the Doctoral student support group and all the student members who supported each other with open and affectionate hearts :)

And finally, thank you to NASA and UW Graduate School for providing the financial support for conducting this research. Thank you to the FINESST program managers and reviewers for showing faith in the research idea and providing funding. This research also contributed to awards provided by the NASA Cryosphere (HiMAT-1), NASA Terrestrial Hydrology program (HiMAT-2, Stereo2SWE), and the NASA Commercial SmallSat Data program. Thank you for providing our group the opportunity to conduct this research!

DEDICATION

To my grandmother, granddad, parents, and all my lovely family members

To the native people of Nepal, Uttrakhand, Washington, Colorado, Yukon and High Mountain Asia over where I worked during my Ph.D.

Chapter 1

INTRODUCTION

Mountain glaciers and seasonal snowpacks are integral to the earth system and serve important functions at various spatiotemporal scales (Figure 1.1). Locally, glaciers are important in sustaining unique mountain species' habitats (e.g., Hotaling et al., 2017; Losapio et al., 2021). On a regional scale, glacier meltwater is an essential contributor to river discharge (e.g., Wulf et al., 2016), especially during dry seasons (e.g., Frans et al., 2018), providing freshwater supplies for drinking (e.g., Somers et al., 2018), livelihood (e.g., Mark et al., 2010) and hydropower (e.g., Farinotti et al., 2019b). On a more global scale, glaciers serve essential functions in the total surface energy balance of the earth, and their meltwater is a major contributor to global sea level rise (e.g., Gardner et al., 2013; Hugonnet et al., 2021). Recent large-scale observational studies have established with high confidence that most glaciers worldwide are undergoing mass loss and retreat, with the decline rates increasing with time (e.g., Dussaillant et al., 2019; Hugonnet et al., 2021; Menounos et al., 2019). Melting of glaciers also alters their interaction with the local terrain, resulting in formation of new glacier lakes (e.g., Shugar, 2020), changes in mountain slope stability (e.g., Fischer et al., 2006; Holm et al., 2004), thereby modifying the chances, frequency, magnitude, and location of high altitude natural hazards such as glacier lake outburst floods, landslides and avalanches (e.g., Ballesteros-Cánovas et al., 2018,?; Coe et al., 2018; Harrison et al., 2018; Kääb et al., 2021).

High Mountain Asia (HMA) is home to the largest mass of glacier ice outside the polar regions (Pfeffer et al., 2014), earning it the informal title of "the Third Pole". HMA glacier and snow melt water replenish the discharge of prominent South Asian rivers (e.g., Armstrong et al., 2019), which support one of the most densely populated (Figure 1.2) and water-stressed regions on the planet (e.g., Rasul, 2014). As with glaciers around the world, HMA glaciers are experiencing an ongoing decline in glacier mass balance (e.g., Benn et al., 2017; Bolch et al., 2012; Kääb et al., 2012; Maurer et al., 2019; Miles et al., 2021; Shean et al., 2020), although with considerable region-wide variations. Prognostic models project that HMA glacier mass loss is going to continue (e.g., Kraaijenbrink et al., 2017; Rounce et al., 2020), with direct implications for river discharge patterns (e.g., Huss and Hock, 2018; Khanal et al., 2021; Rounce et al., 2020) and mountain hazard incidents (e.g., Harrison et al., 2018; Kirschbaum et al., 2019). Better understanding current and predicting future glacier changes

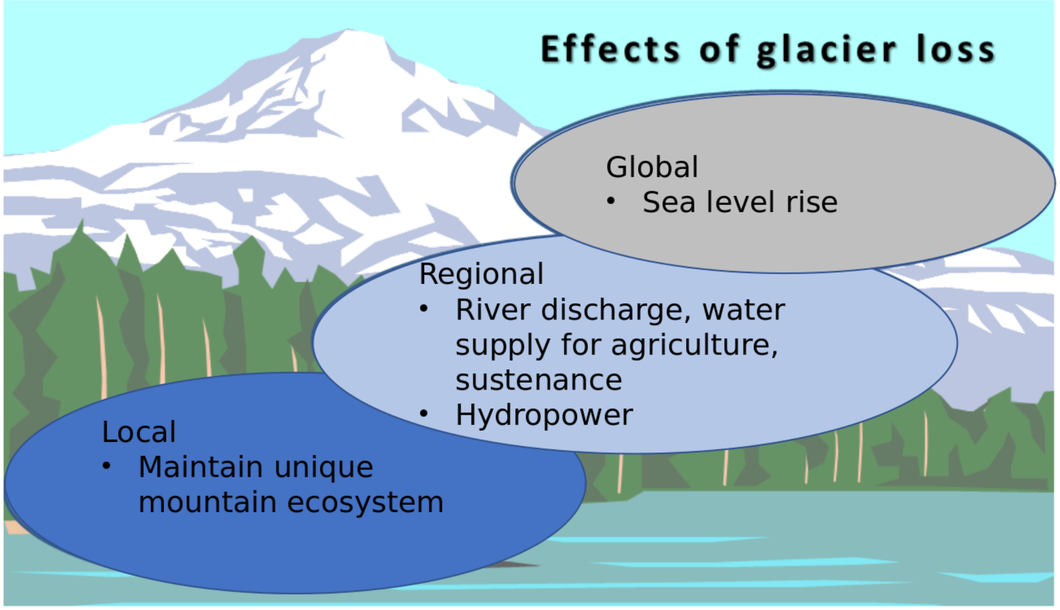

Figure 1.1: Schematic diagram modified from USGS enlisting the influence of glacier mass loss at global, regional and local scales.

in HMA is crucial for informing ongoing and future policy decisions (e.g., Immerzeel et al., 2020).

1.1 Science Research Gap

Recent remote sensing studies using medium-resolution satellite imagery have significantly enhanced our knowledge of long-term glacier changes (e.g., Dehecq et al., 2019; Hugonnet et al., 2021). However, these observations do not fully capture the intricate local processes that operate on annual to seasonal timescales. Several key aspects remain only partially understood, such as: ***a) The impact of debris cover and associated geomorphic features (e.g., ice cliffs, melt ponds) on glacier mass balance, b) the evolution of seasonal glacier surface mass balance, and c) dynamics in response to local climatic variations.*** Debris cover is widespread in High Mountain Asia (HMA), with approximately 30% of the glacier ablation area covered by debris. It alters the feedback between surface mass balance and climate by modifying local melt rates. The extent of this melt feedback modification depends on factors such as debris thickness, debris composition, and the presence of isolated ice cliffs and melt ponds (Figure 1.3). With the anticipated increase in debris cover as glaciers decelerate further (e.g., Herreid and Pellicciotti, 2020),

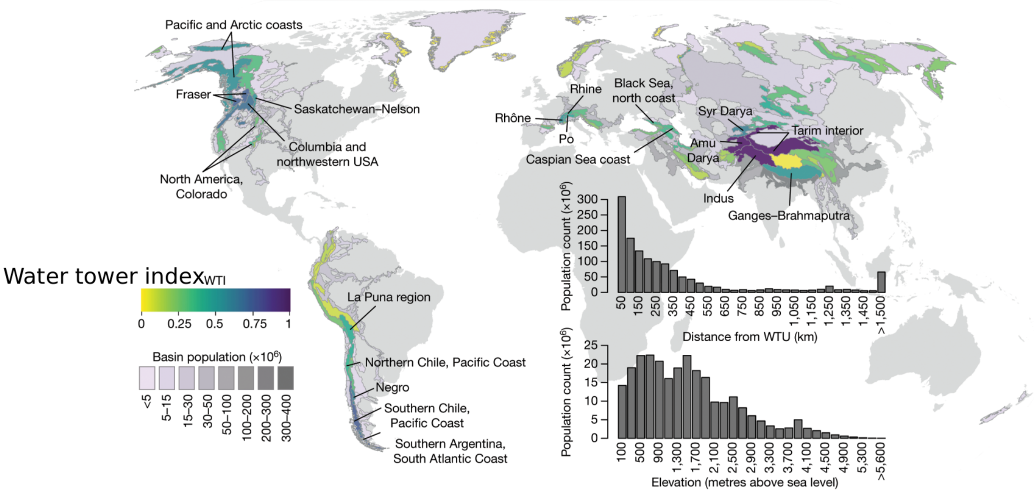

Figure 1.2: From Immerzeel et al. (2020), this figure ranks the relative importance of mountain glacier systems around the world for sustaining environmental and downstream water demands using the Water Tower Index (WTI). Note the higher WTI for mountain ranges in HMA, and the relatively higher population density of downstream communities which are affected by the rivers originating from these mountains.

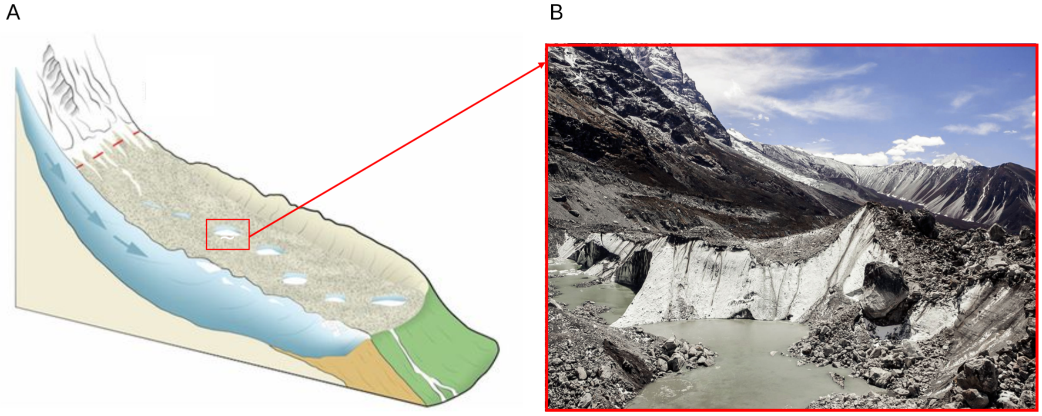

Figure 1.3: A) Schematic diagram of debris-covered glacier adapted from Benn et al. (2012); Racoviteanu et al. (2022) and B) field photograph by Eduardo Soteras (accessed from Qiu (2015)), showing an exposed ice cliff with an associated melt pond at the debris-covered Lirung Glacier, Nepal. Note the highly heterogeneous debris surface in (B).

understanding the relative impacts of debris, ice cliffs, and melt ponds on glacier melting becomes crucial (e.g., Racoviteanu et al., 2022).

Similarly, it is vital to acquire distributed, seasonal surface mass balance and surface velocity data to effectively constrain glacier evolution models on seasonal timescales to improve projections of seasonal surface mass balance and better estimate when and to what extent glacier meltwater contributes to river discharge (e.g., Khanal et al., 2021; Rounce et al., 2020). The magnitudes of these processes are often smaller than the signal-to-noise ratio of current state-of-the-art geodetic products derived from medium-resolution satellite imagery (e.g., ASTER, Landsat).

1.2 High-resolution satellite imagery

Fortunately, this body of research was conducted during a period which is kind of like "the golden age of satellite remote sensing". In addition to optical satellites operated by publicly-funded national space organizations, a range of very-high resolution imaging satellites is operated by commercial companies, such as Maxar DigitalGlobe and CNES/Airbus. Imagery delivered by these commercial satellites has enabled the derivation of geodetic products with high vertical and horizontal accuracy, previously facilitating the study of local geophysical processes at small scales and shorter timescales (e.g., Benn et al., 2017; Brun et al., 2018; Ruiz et al., 2015). While federally funded researchers can obtain imagery from these satellites at limited to no costs for scientific research, the timely acquisition of tasked imagery over lower latitude targets, such as glaciers in the HMA region, is becoming increasingly challenging. This is primarily due to the escalating competition and demand for limited high-resolution satellite resources from various sectors, including private entities and government defense agencies. An exciting alternative may lie in very-high to high-resolution imagery provided by commercial SmallSat and CubeSat constellations, such as the ones operated by Planet Labs and BlackSky. These constellations offer improved operational capabilities, including higher revisit rates, through the deployment of multiple smaller and more cost-effective satellites in orbit (e.g., Millan et al., 2019b; Roy et al., 2021a; Saunier et al., 2022). The emergence of this new opportunity also brings forth two challenges: data quality and quantity. The use of off-the-shelf, smaller-sized electronics and control systems in these constellations can lead to reduced geometric and radiometric image quality (e.g., Cooley et al., 2017; d'Angelo et al., 2016), rendering the default image products unsuitable for precise geodetic applications (e.g., Ghuffar, 2018; Millan et al., 2019a). On the other hand, the near-daily, high-resolution data provided by the Planet Cubesat constellation necessitates an upgraded, big-data approach for processing and analysis to fully leverage the delivered image archive.

1.3 Organisation of the Dissertation

In this dissertation, I used high-resolution, commercial satellite imagery and developed novel methods to obtain new cryospheric change observations. Broadly, this research aims to answer three main questions:

- Can high-resolution optical imagery acquired by commercial smallsat and cubesat constellations be used for geodetic studies, particularly involving the cryosphere?
- What are the dominant controls on the surface mass balance (SMB) of debris-covered glaciers? How does surface mass balance vary with seasons? Can we study these processes using satellite observations?
- Do debris-covered glaciers in HMA exhibit flow seasonality? Can we study the flow seasonality using near-daily, repeat imagery acquired by the PlanetScope cubesat constellation?

The dissertation is subsequently divided into four further chapters. Satellite photogrammetry is the common link between all these chapters, which were used to study cryospheric processes such as glacier surface mass balance, glacier dynamics, glacial-induced landslides, and seasonal snow depth.

As part of the 2018 NASA CSDA Pilot Program Study, our team conducted an evaluation of the quality of Planet's SkySat and PlanetScope Dove constellations. During this assessment, we identified various geometric issues in the original product offerings and proposed effective solutions to address them. In the second chapter of the dissertation, we detail automated procedures developed for refining camera models and correcting image geolocation of very high-resolution (0.7 to 0.9 m) SkySat Triplet stereo and video data products. The chapter further describes our experiments to perform detailed accuracy assessments, evaluation of different stereo processing options (e.g., two-view stereo vs joint multiview triangulation) and presents case studies to measure elevation changes due to seasonal snow melt and glacier flow. We have released our workflow under an open-source MIT License, allowing others to benefit from it, and we continue to enhance the software capabilities through successive NASA grants. This work has been published in the ISPRS Journal of Photogrammetry and Remote Sensing as ***"Automated digital elevation model (DEM) generation from very-high-resolution Planet SkySat triplet stereo and video imagery"***, and is reproduced as is in Chapter 2.

The third chapter, titled ***"Seasonal and annual surface mass balance for debris-covered glaciers in High-Mountain Asia from flow-corrected satellite stereo***

DEM time series", will be submitted for peer-review in spring/summer 2023. This chapter focuses on presenting high-resolution observations of surface mass balance over six debris-covered glaciers in Nepal. The chapter outlines the workflows employed to derive flow-corrected Lagrangian SMB (Surface Mass Balance) maps. The SMB maps are generated by integrating DEMs derived from very high-resolution Maxar stereo imagery with publicly available ice thickness estimates. The resulting SMB maps offer very high level of detail, enabling the identification of melt signals over individual ice cliffs and capturing the overall heterogeneity in ablation across the debris-covered areas. The findings derived from the SMB maps are utilized to assess the relative impact of debris thickness and ice cliffs on ablation within the debris-covered areas. Furthermore, the chapter presents seasonal SMB results over two glaciers, shedding light on Nepal's distinctive summer snow accumulation climatic regime. Additionally, it highlights the importance of accumulation by snow avalanches for debris-covered glaciers at lower elevations.

The fourth chapter, titled ***"Seasonal to monthly glacier velocity estimation using near-daily, PlanetScope Dove Classic imagery"***, is currently being prepared for submission to a peer-reviewed journal in summer 2023. The chapter presents the outcomes of our accuracy assessment experiments focusing on the geometric and radiometric quality of Planet imagery and details our innovative workflow that integrates thousands of noisy glacier surface velocity maps to derive analysis-ready, monthly median velocities with precision of 0.02 to 0.03 m/day. We applied our workflow to investigate the seasonal velocity variability during the 2018-2021 surge event of the Gando Glacier and documented previously undetected spatially-varying seasonal velocity evolution across the slow-moving, heavily debris-covered Ngozumpa and Khumbu glaciers in the Nepal Himalayas. This included examining the flow evolution over the topographically complex and fast-flowing Khumbu Icefall.

The fifth chapter, titled ***"Photogrammetry applications beyond high-resolution glacier surface mass balance and dynamics: Contributions to collaborative efforts"***, summarises my contributions to collaborative research projects during the Ph.D. program. I discuss my contributions to the HMA-wide glacier mass balance study (Shean et al., 2020), the response effort to the Chamoli disaster (Shugar et al., 2021), the study of the pre-collapse motion of Chamoli rock ice avalanche (Van Wyk de Vries et al., 2022a), the feature tracking methods intercomparison study (Zheng et al., 2023), and the experiments for evaluating the impact of satellite stereo geometry and software processing on output DEM quality for snow depth mapping (Hu et al., in prep). I establish a two-way connection in how the three core chapters benefited from the co-author projects and vice versa.

Appendix A, B, and C contains the supplementary materials accompanying Chapter 2, Chapter 3, and Chapter 4, respectively.

Chapter 2

AUTOMATED DIGITAL ELEVATION MODEL (DEM) GENERATION FROM VERY-HIGH-RESOLUTION PLANET SKYSAT TRIPLET STEREO AND VIDEO IMAGERY

The chapter has been published as: **S. Bhushan**, D. Shean, O Alexandrov, S. Henderson (2021). ***"Automated digital elevation model (DEM) generation from very-high-resolution Planet SkySat triplet stereo and video imagery"*** in ISPRS Journal of Photogrammetry and Remote Sensing. `https://doi.org/10.1016/j.isprsjprs.2020.12.012`

2.1 Abstract

The Planet SkySat-C SmallSat constellation can acquire very high resolution (0.7 m to 0.9 m) triplet stereo and video imagery with short revisit times, providing an exciting opportunity for global, on-demand 3D mapping of dynamic surface features. However, a lack of suitable processing software, limited geolocation accuracy, and scene-to-scene offsets currently limit the potential for accurate SkySat digital elevation model (DEM) production. We developed an open-source workflow to refine the SkySat-C camera models and improve absolute image geolocation using external reference DEMs, without manual ground control point (GCP) selection. The refined camera models are used to generate accurate and self-consistent DEMs with 2-m posting and orthoimages at native resolution. We present sample DEM products for a triplet stereo collection over Mt. Rainier, USA and two video collections over Mt. St. Helen's, USA. The output DEMs display <1 to 2 m relative and <2 to 3 m absolute vertical accuracy when compared to DEMs generated with stereo image pairs acquired by the DigitalGlobe/Maxar WorldView satellites and airborne LiDAR. Differencing the two SkySat-C video DEMs over Mt. St. Helen's shows elevation change of ∼5 to 15 m due to melting of seasonal snow and glacier flow. Our workflow can be scaled for batch processing of SkySat stereo imagery, and extended to other frame camera systems with limited initial geolocation accuracy.

2.2 Introduction

Digital Elevation Models (DEM)s offer continuous measurements of surface elevation on a regular grid (Deilami and Hashim, 2011). They are widely used in Geographic Information System (GIS) analyses, with applications across multiple disciplines, including Earth science, architecture, reconnaissance and natural hazard monitoring/modeling (e.g., Albino et al., 2015; Brun et al., 2017; Kim et al., 2015; Morrison et al., 2005). In recent decades, the availability of high-quality data from spaceborne optical stereoscopic (e.g., SPOT, ASTER, Cartosat-1, ALOS PRISM) and Synthetic Aperture Radar (SAR; e.g., ERS-1/2, TanDEM-X) instruments has enabled DEM generation and analysis on a global scale. Commercial satellites in sun-synchronous polar orbits (e.g., Maxar/DigitalGlobe WorldView-1/2/3 and GeoEye-1, CNES/Airbus Pleiades) can be tasked to collect very-high-resolution (sub-meter) stereo imagery with resulting DEM vertical accuracy of $<$ 0.2-0.5 m after correction (e.g., d'Angelo and Kuschk, 2012; de Franchis et al., 2014; Leotta et al., 2019; Noh and Howat, 2015; Shean et al., 2016; Zhang et al., 2019). Large archives of accurate, high-resolution DEMs and orthoimages derived from sub-meter commercial imagery have changed the way many geodetic problems are approached, with applications in both regional scale mapping, geodetic change detection studies (e.g., Howat et al., 2019; Porter et al., 2018; Shean et al., 2020; Tian et al., 2012) and detailed temporal analyses of local surface processes (e.g., Brun et al., 2018; Dai et al., 2018; Kehrl et al., 2017; Rounce et al., 2018; Willis et al., 2015).

Growing demand for sub-meter commercial satellite imagery, however, has led to increased competition for limited satellite resources, which can result in missed tasking acquisitions, especially for low-latitude targets with limited time windows (e.g., field campaigns, end of summer melt season on glaciers). Also, most end users have limited or no control of the commercial stereo acquisition geometry, which could be optimized for user-specific applications and target properties. For example, a user might want larger convergence angles for relatively flat terrain (e.g., Büyüksalih and Jacobsen, 2006), and smaller convergence angles for dense forest canopy and high-relief terrain (e.g., Montesano et al., 2019; Piermattei et al., 2018).

The recent proliferation of low-cost, small imaging satellites (”SmallSats” or “CubeSats”) has revolutionized Earth observation, with constellations of inexpensive satellites now offering greater operational capacity and reduced revisit interval (hours-days). Planet (formerly Planet Labs, Inc.) operates multiple constellations of optical imaging satellites, which offer both high resolution (~140 Dove satellites with 3-5 m ground sample distance [GSD]) and very-high-resolution (~19 SkySat-C satellites with 0.7 to 0.9 m GSD) products (Marta, 2018). The Dove constellation provides Planet's flagship PlanetScope archive with “always-on”, ~daily global coverage. The SkySat-C constellation operates in tasking mode for mono, triplet stereo or video collection with short repeat interval for small areas.

While these SmallSat constellations can offer improved operational capacity, the instruments and control systems are typically inferior to the larger, more traditional optical imaging satellites. For example, products from Maxar/DigitalGlobe WorldView satellites have absolute geolocation accuracy of $<$ 3-5 m CE90 (DigitalGlobe, 2016), while typical SkySat-C products have geolocation accuracy of $<$ 50 m Root Mean Square Error (RMSE) (Marta, 2018).

2.2.1 Previous Work

Many previous studies document stereo DEM quality for existing commercial sub-meter imaging satellites, but few evaluations are available for SmallSat platforms. d'Angelo et al. (2016) evaluated sample products from the first-generation SkySat-A/B sensors over urban landscapes, offering details on sensor geometry, image acquisition modes, and camera models. They also explored preliminary SkySat sensor geometry/geolocation correction strategies and stereo reconstruction using the SkySat video products. The d'Angelo et al. (2016) geolocation correction study used a National Agriculture Imagery Program (NAIP) reference image basemap to improve geolocation of a SkySat-B mono collect over Chicago, USA. They concluded that the individual SkySat scenes suffered from non-rigid geolocation offsets, which varied across the full SkySat mono collect, requiring multiple ground control points (GCPs) per scene for rectification. After correction, their final orthoimage geolocation accuracy was 5 m RMSE. The d'Angelo et al. (2016) stereo reconstruction study used a subset of scenes from a SkySat-A video collection (60 out of 3600 images) over Las Vegas, USA. To improve input camera models, d'Angelo et al. (2016) automatically tied the video scenes to a reference image basemap using identifiable road networks and ran a bundle adjustment optimization. They then produced 14 individual DEMs via dense correlation of 14 "anchor" images with their respective 20 neighboring images, and created per-pixel mean and median DEM composites. When the median DEM composite was compared to an airborne LiDAR point cloud, the normalized median absolute deviation (NMAD) (e.g., Höhle and Höhle, 2009) of elevation difference values was 1.2 m.

Wan et al. (2016) performed super-resolution experiments on disparity maps obtained by correlating multiple image pairs from a SkySat-A video sequence over an open-pit mine in Usak, Turkey. A sub-pixel registration step was required prior to merging the disparity maps to improve the accuracy of the resolution-enhanced composite disparity maps. Ghuffar (2018) performed experiments for a set of overlapping near-nadir (view angles between 2 to 5°), multi-date, multi-orbit, images from Planet Dove instruments (PlanetScope) over several natural landscapes. They performed a bundle adjustment to reduce the rational polynomial coefficient (RPC) model bias of all input images, generated DEMs from all possible image pairs, and generated a final per-pixel mean DEM composite with elevation difference NMAD values of 4-9 m over ”static” surfaces for their test sites (compared to reference DEMs derived from airborne LiDAR and ALOS PRISM stereo images). These previous studies demonstrate that SmallSat/CubeSat imagery can be used for stereo reconstruction and geodetic analysis, but only after the user performs several correction and processing steps, often requiring manual intervention.

2.2.2 Study Objectives

NASA established the Commercial Smallsat Data Acquisition Program in 2017, with a 2019 pilot study to evaluate Planet data for NASA Earth Science research applications. During the course of this pilot study, the program coordinated multiple tasking campaigns with the Planet SkySat-C platforms for a range of priority science targets. The imagery acquired during this pilot is now available to all NASA researchers for further evaluation and analysis (see `https://earthdata.nasa.gov/esds/csdap/csdap-pilot-evaluation` for further details, (NASA Earth Science Division, 2020)).

To our knowledge, stereo reconstruction using products from the newer SkySat-C instruments has not been documented in the remote sensing literature. Here, we 1) review the SkySat-C instrument specifications, operational modes, and standard products, 2) present a new workflow for SkySat-C sensor geometry correction and image geolocation refinement, 3) describe a workflow for SkySat-C stereo reconstruction and DEM/orthoimage composite generation, 4) evaluate the quality and accuracy of these DEM products, and 5) present two case studies using SkySat-C data to study dynamic glaciers and snow on active stratovolcanoes (Mt. St. Helen’s and Mt. Rainier in Washington state, USA). We also present a brief evaluation of popular commercial and open-source Structure from Motion (SfM) software packages for SkySat-C processing.

2.3 SkySat-C background

2.3.1 Satellite and instrument description

The SkySat-C constellation consists of 19 small (60 x 60 X 95 cm), lightweight (100 kg) optical imaging satellites, with 13 of the satellites in sun-synchronous orbits (inclinations of ∼98.3° and ∼95.3° and altitude of ∼500 km (Christopherson et al., 2019)). The high inclination angle translates to a equatorial revisit time of 4 to 5 days for any individual satellite (Marta, 2018), but the full constellation includes multiple orbit planes, and can provide sub-daily revisit time nearly anywhere on Earth. Six additional SkySat-C satellites

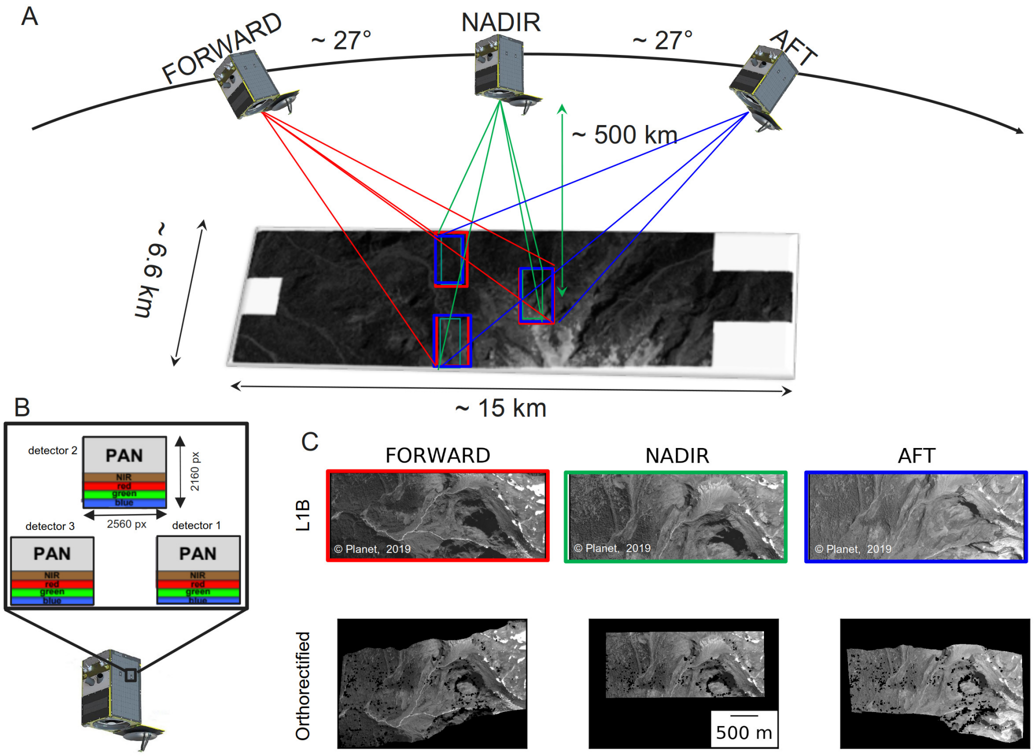

Figure 2.1: A) SkySat-C triplet stereo image acquisition geometry (not to scale). B) SkySat-C focal plane schematic. C) Sample Level-1B (L1B) scenes and orthoimages for the same surface features, as viewed by detector 2 with forward, nadir, and aft orientation. Satellite illustration and image data ©Planet, 2019.

(14 to 19) were launched in August and September 2020 in a mid-inclination orbit (∼53°) at lower altitude (∼400 km), further improving image ground sample distance (GSD) and revisit times for lower latitudes. All SkySat-C satellites include an active propulsion system which offers improved agility and pointing accuracy over the earlier SkySat-A/B satellites.

The SkySat-C instrument consists of a Ritchey-Chretien Cassegrain f/10.3 optical telescope with 3.6 m focal length and 35 cm primary mirror diameter (d'Angelo et al., 2016; Zhai et al., 2018). The sensor focal plane includes three 5.5 megapixel complementary metal–oxide–semiconductor (CMOS) detectors (2560 by 2160 pixels each) (Marta, 2018) (Figure 2.1B). The upper portion of each detector captures panchromatic images, while the lower portion of the detector captures 4-band multispectral images with filters for blue, green, red and near-infrared (NIR) bands. The three detectors are arranged in a "tuning fork" orientation, with detector 2 forward of detectors 1 and 3 (Figure 2.1B). Each individual detector has a relatively small ground footprint, with panchromatic image dimensions of ∼2.5 km by 1 km (covering ∼2.5 km^2) and native Level-1A (L1A) image ground sample distance (GSD) of ∼0.9 m at nadir. In June 2020, Planet lowered the orbits of SkySat-C constellation to ∼450 km, which should provide a native ∼0.7 m GSD at nadir, but these products were not available at the time of our evaluation.

2.3.2 Acquisition modes

The SkySat-C satellite can be operated in multiple acquisition modes, including mono, triplet stereo, and video collection. Products from each acquisition mode are comprised of many overlapping ”scenes” acquired by some or all of the three detectors.

Mono collection

The conventional monoscopic products are collected in a ”pushframe” mode with all three detectors continuously acquiring image data at a rate of up to 40 frames per second (fps) with exposure cycling to enable high-dynamic range (HDR)-like integration during post-processing. This results in ∼900 L1A scenes with ∼85-90% along-track overlap between scenes acquired by each detector. The cross-track overlap between scenes from adjacent detectors is ∼10%. During post-processing, the scenes undergo a virtual “pushframe” time-delay integration (TDI) and super-resolution enhancement procedure. The resulting Level-1B (L1B) product GSD is ∼0.7 m at nadir, with reduced along-track overlap of ∼15% between adjacent scenes from the same detector. The typical combined mono collect ground footprint dimensions are ∼6.6 x 15 km, covering ∼90 km^2 (Figure 2.1A).

Triplet stereo collection

The triplet stereo acquisition mode includes three overlapping mono collections on the same pass, with forward-facing (27° off-nadir), nadir, and aft-facing (-27° off-nadir) geometry (Figure 2.1). The collections are separated by ∼35 seconds.

Video collection

The SkySat-C satellites can also collect 30 fps high-definition (HD) video for a fixed ground target over a period of 30, 60, 90 or 120 seconds. Only the panchromatic portion of detector 2 (Figure 2.1B) is used during video collection, with no exposure cycling, providing ∼0.9 m GSD at nadir (Figure 2.2). The resulting video includes ∼900-3600 overlapping scenes acquired for a range of off-nadir angles spanning approximately -45° to +45° for a symmetrical

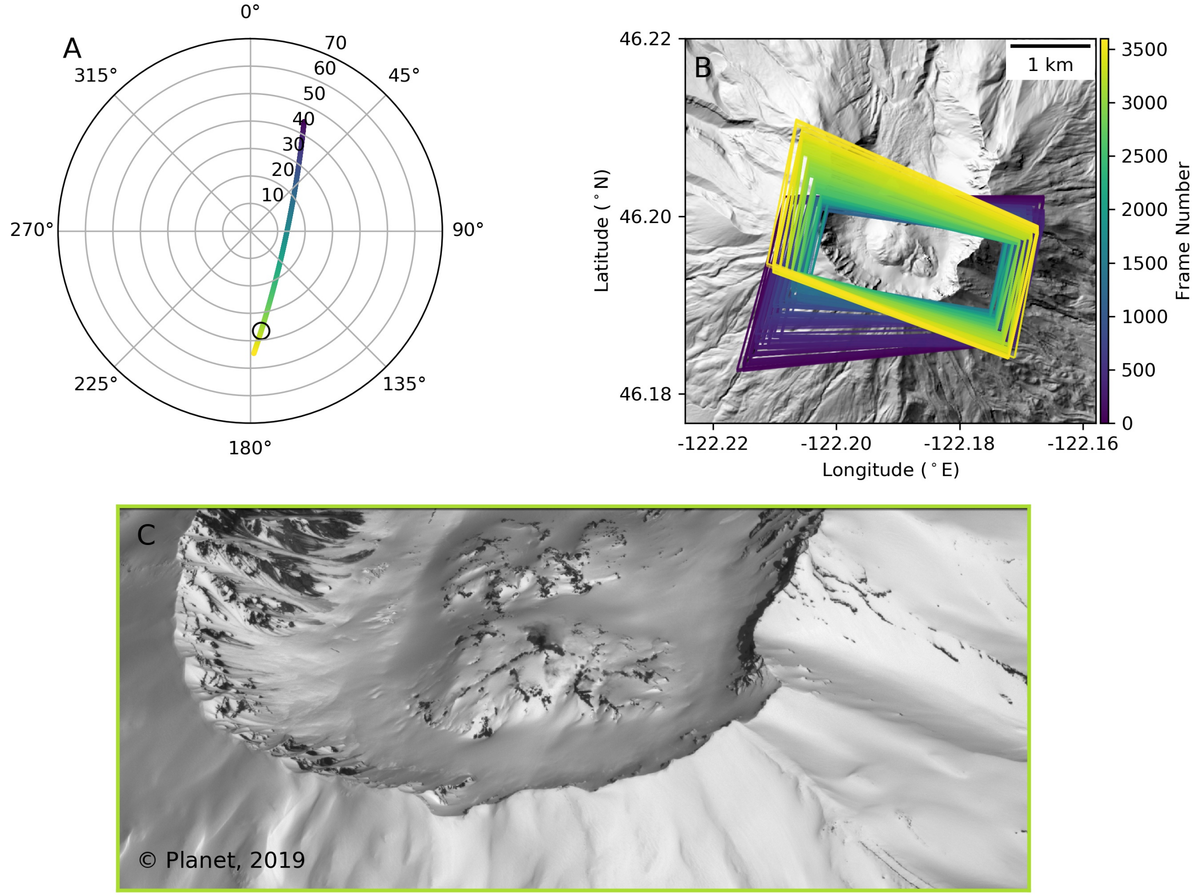

Figure 2.2: SkySat-C 120-second video test case for Mt. St. Helen's, WA, acquired April 20, 2019. A) Skyplot showing SkySat-C video acquisition geometry (satellite azimuth and elevation angles) relative to ground target center (-122.192°E, 46.195°N). B) Footprints for all video scenes plotted over shaded relief map from reference WorldView DEM composite. C) Sample off-nadir video scene (frame 3143), corresponding to black circle in (A). L1A Image data in (C) is ©Planet, 2019.

~120-second video (Figure 2.2A), resulting in an average angular separation of ~0.022° between consecutive scenes.

2.3.3 Camera models

Planet provides rational polynomial coefficient (RPC) camera models for all L1A and L1B SkySat scenes. These RPC models are generated using keypoint matches between the individual L1A images and a proprietary reference orthoimage basemap (derived from National Agriculture Imagery Program [NAIP], Advanced Land Observation Satellite [ALOS], Landsat-8, and other image sources), with corresponding elevation data extracted from regional and global DEMs (e.g., National Elevation Dataset [NED], Shuttle Radar Topographic Mission [SRTM], InterMap World 30) (Marta, 2018). This RPC generation method works well for most cases, but can be problematic over dynamic surface features like glaciers and landslides, which display time-variable vertical and horizontal surface displacements. In addition, images acquired over non-planar terrain with variable relief can have additional geolocation issues due to geolocation errors in the original basemap and inconsistencies between the DEM used for SkySat RPC elevation control and that used for orthorectification of the basemap imagery. In such cases, the RPCs for overlapping SkySat scenes can suffer from offsets which are non-rigid in nature. In addition to the RPC camera models, the video products include a rigorous, custom pinhole camera model and relevant metadata (i.e., ephemeris, attitude) for each scene.

2.4 Methods

2.4.1 Overview

We developed automated processing workflows for SkySat products acquired using the triplet stereo and video acquisition modes (Figure 2.3), which can also be extended to process overlapping mono image collections with suitable geometry. The workflows exclusively use open-source tools, including the Ames Stereo Pipeline (ASP, version 2.7.0 (Beyer et al., 2020, 2018; Shean et al., 2016)) and custom Python tools to perform camera model refinement, stereo reconstruction and co-registration to reference elevation data without manually identified GCPs. The `skysat_stereo` (Bhushan et al., 2020) code repository accompanying this manuscript contains processing libraries, wrapper scripts and additional documentation of these workflows. The main steps in the common SkySat processing workflow include 1) overlapping stereo scene identification, 2) bundle adjustment, 3) pairwise stereo reconstruction, 4) DEM compositing, 5) DEM co-registration and 6) orthomosaic generation (Figure 2.3). The following sections offer details on each processing step, and we reference the corresponding software utility names in bold (e.g., `stereo_corr`).

2.4.2 Stereo pair identification

The first step in our workflow is the selection of overlapping scene pairs to be used for feature matching and camera refinement during bundle adjustment and the successive pairwise stereo reconstruction procedure. The strategy for this step depends on the input product type, as described in the following sections.

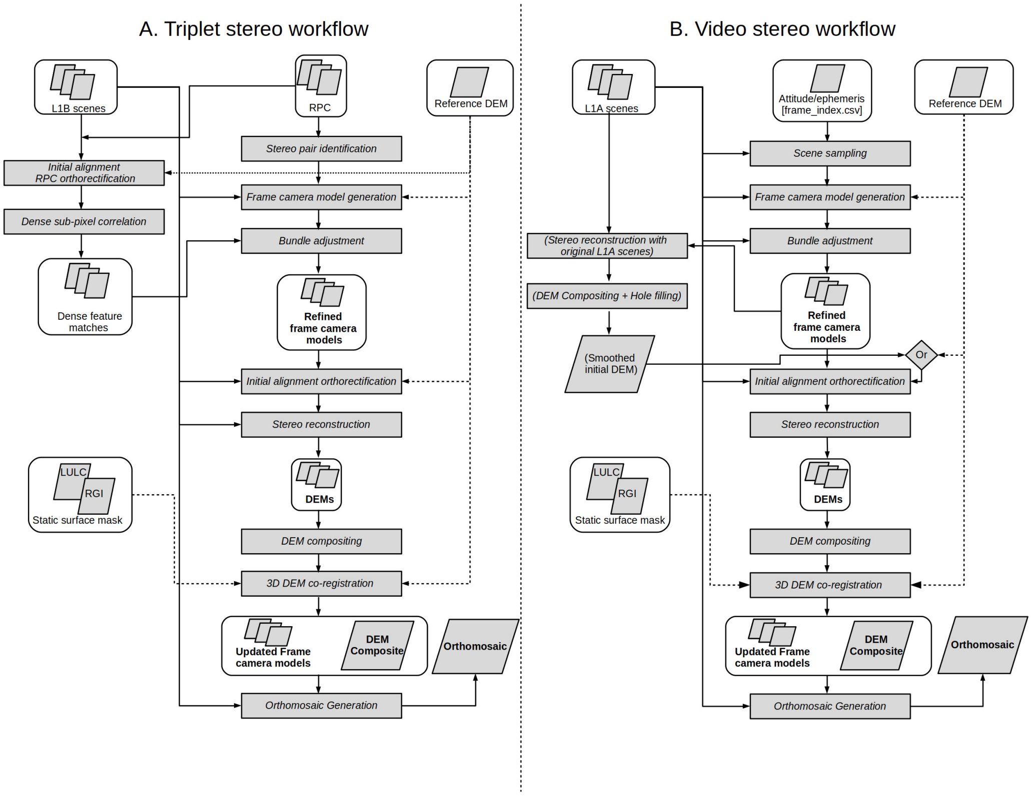

Figure 2.3: Flowchart outlining workflow for A) SkySat-C triplet stereo and B) video stereo products. Processing steps are denoted by gray rectangles, with products denoted by gray parallelograms. External inputs (e.g., reference DEMs) are connected by dashed lines while optional processing steps and products are enclosed in parentheses. Final output products are identified with bold text.

Triplet stereo

For the L1B triplet stereo products, we compute a list of all overlapping sf cene pairs using the original RPC models (`skysat_overlap.py`). A typical SkySat triplet stereo collection will produce ~800 unique scene pairs.

Pairwise video stereo

Pair identification for the SkySat video scenes is more flexible, as all scenes inherently overlap, with negligible perspective difference between any two consecutive video scenes (average convergence angle of ~0.022°). Pairs must be selected to appropriately balance performance (eliminating redundant processing), vertical accuracy of triangulated points, and feature matching success for the target terrain characteristics. In general, a larger pair convergence angle will improve triangulated position accuracy (e.g., Delon and Rougé, 2007), but the increased perspective difference can lead to difficulties during feature matching.

Our video pair selection workflow first selects a subset of ”reference” scenes from the full 30 fps video sequence using either a user-specified total number (n) of scenes spaced equally across the full video sequence, or a fixed sampling interval (e.g., every m^{th} scene) (Figure A.1A) (`skysat_preprocess.py`). We prefer the strategy of sampling user-specified total number of scenes, as the first and last scenes are always included. After a subset of scenes is identified, stereo pairs are identified by pairing each reference scene with several neighbouring (”source”) scenes from the same subset using a user-defined interval p (Figure A.1B). By design, a larger interval (p) between the reference and source scenes translates to a higher convergence angle for the resulting stereo pairs. This strategy offers a good compromise between performance and optimum stereo geometry, but can exclude scenes near the beginning and end of the video sequence, resulting in a smaller ground footprint of the final DEM composite. To avoid this limitation, our workflow includes additional pairs with smaller convergence angles at the beginning and end of the video sequence (Figure A.1B).

For this study, we extracted a subset of n=60 equally spaced scenes from 120-second SkySat video samples (Figure A.1A), resulting in consecutive scenes with an average angular separation of ~1.36°. Feature matching during subsequent bundle adjustment (Section 2.4.4) was limited to 20 consecutive scenes from this 60-scene subset, with maximum average convergence angle of ~27°. For stereo reconstruction, pairs were created from the 60-image subset using an interval of p=10 between the reference and source scenes. Corresponding convergence angles were between 11° to 18°, with additional pairs formed near the beginning and end of the video sequence (Figure A.1B), resulting in a total of 62 stereo pairs.

Multi-view video stereo

We implemented and tested an experimental multi-view stereo (MVS) workflow which simultaneously processes many scenes, rather than multiple independent pairs. We follow the approach described by d'Angelo et al. (2016), processing k user-selected reference scenes with their respective o neighboring scenes from the subset of n video scenes (Figure A.1C). For this study, we used k=14 and o=20, which produced 14 multi-view DEMs from the subset of n=60 scenes, in contrast to the 62 DEMs produced by the pairwise video stereo workflow (Section 2.4.2).

2.4.3 Frame camera model generation

After identifying a subset of overlapping scenes, we use the ASP `cam_gen` utility to produce frame camera models for each scene. We use a simple pinhole model, as the relatively long focal length and small detector size of the SkySat-C instrument does not require a more complex lens distortion model. We assume a focal length of 3.6 m and pixel pitch of 6.5 and 5.2 μm for the L1A and L1B scenes, respectively.

The `cam_gen` tool performs camera resection (e.g., Mikhail et al., 2001) using the above camera intrinsics (interior orientation) and a known ground footprint to solve for the corresponding camera extrinsics (exterior orientation: position and orientation) with least-squares minimization. The footprint can be estimated using the original L1B RPC camera model and an external reference DEM. When available, we directly use available footprint corner coordinates extracted from the frame_index.csv metadata distributed with L1A video products, with height values sampled from a reference DEM. The L1A metadata also includes Earth-centered, Earth-fixed (ECEF) camera positions that are used as an initial estimate for camera position during resection.

2.4.4 Bundle adjustment and camera model refinement

Inaccurate camera extrinsics can introduce systematic horizontal and vertical error in DEMs from individual stereo pairs (e.g., Mikhail et al., 2001) and overlapping DEMs from multiple pairs (Ozcanli et al., 2016; **?**). To mitigate these issues, our workflow (`ba_skysat.py`) uses known camera intrinsics and a bundle adjustment technique (e.g., Triggs et al., 2000) to iteratively refine camera extrinsics (position and orientation) by minimizing reprojection errors for triangulated points from all input scenes (e.g., Amer, 2006).

Prior to the optimization, keypoint matches are automatically computed between overlapping scenes to define the optimization constraints and establish connections between the individual frame camera models. During initial optimization, we prioritize self-consistency between the full set of camera models, which can introduce some arbitrary drift of the triangulated match points and the entire camera set in space. To mitigate this issue during the triplet stereo processing, our workflow fixes the absolute position and orientation of the first three scenes captured by detector 1 in both the forward and nadir views (i.e., the first three stereo pairs involving detector 1), allowing all other camera models to float during initial optimization. A second round of bundle adjustment is then performed with all camera models fixed except those comprising the first three stereo pairs. For the video products, we allow the entire camera set and triangulated match points to float during initial bundle adjustment optimization, and then shift the entire self-consistent camera set back to its original location (defined by initial ground footprints in original L1A metadata) using a single transformation with translation and rotation components.

The above strategy requires a relatively uniform distribution of keypoint matches between overlapping scenes. This criterion is easily fulfilled by the video collections due to significant overlap between scenes and the smaller convergence angles. However, keypoint matching between overlapping scenes in the triplet stereo collections can fail due to the large perspective differences (convergence angles of $\sim$27° and $\sim$55°), especially over challenging terrain like mountains and forests. As a result, several overlapping scene pairs can have a sparse and/or non-uniform spatial distribution of keypoint matches, which can adversely affect the joint refinement of all camera models for the triplet stereo collection.

To avoid this issue, we use a dense, uniform grid of keypoint matches for each overlapping stereo scene pair (e.g., Dehecq et al., 2020). In this method, the L1B images are orthorectified using the original camera models and a reference DEM. Disparity maps are produced between the orthorectified images using ASP's dense sub-pixel correlation routines, and keypoint matches on a regular grid are extracted from these dense disparity maps. These matches are then back-projected into the original sensor coordinate system with the same camera model and DEM used during orthorectification (Figure A.2), and the resulting keypoint matches from each pair are used during bundle adjustment of all L1B scenes. The dense keypoint matches on a systematic grid can offer improved results over the sparse keypoint matches obtained by SIFT/SURF operators (Figure A.2). This strategy also helps to prevent large shifts in the position and orientation of cameras with fewer overlapping scenes, such as those on the periphery of the triplet stereo collection camera set.

2.4.5 Stereo reconstruction

After refining extrinsics for all cameras, we use the ASP `stereo` utility for pairwise stereo correlation and triangulation. Our stereo processing routine (`skysat_stereo_cli.py`) is similar to the workflow described in Shean et al. (2016), except for the stereo correlation steps (disparity initialization and refinement), where we prefer ASP's implementation of the More Global Matching algorithm (MGM) (Facciolo et al., 2015) and Bayes Expectation-Maximization (EM) affine-adaptive sup-pixel refinement (Nefian et al., 2009). The combination of MGM matching algorithm and the Bayes EM affine-adaptive sup-pixel refinement offers more detail in the output DEMs, while also reducing blunders and artifacts for scenes with repetitive texture and sites with steep relief.

As described in Shean et al. (2016), the initial alignment orthorectification of input scenes prior to stereo reconstruction removes most terrain-induced disparity, which improves image alignment, correlator performance and dense disparity map quality. This orthorectification can be performed using either a pre-existing reference DEM (e.g., SRTM) or a gap-filled, "smoothed initial DEM" derived from an earlier `stereo` run using ASP's default block-matching correlator with the original or downsampled L1A/L1B scenes (e.g., Dehecq et al., 2020; Deschamps-Berger et al., 2020).

After initial alignment orthorectification, we use MGM and sub-pixel refinement to produce dense disparity maps for each stereo pair, followed by the default ASP disparity map filtering. Our workflow uses default MGM correlation and refinement kernel sizes of 7 x 7 pixels and 15 x 15 pixels, respectively. For input scenes with limited texture (e.g., fresh snow), we recommend using larger correlation and refinement kernels of 9 x 9 and 21 x 21 pixels, respectively.

For the pairwise stereo processing workflow, we generate a dense point cloud for each stereo pair using the filtered disparity map, refined camera models and the standard ASP stereo triangulation routine (`stereo_tri`). For the SkySat video multi-view stereo workflow (Section 2.4.2), we perform a joint triangulation that combines all disparity maps computed between a reference scene and each of the 20 neighbouring scenes (Slabaugh et al., 2001).

Regardless of pairwise or MVS triangulation strategy, our workflow generates gridded DEMs from the output dense point clouds using the ASP `point2dem` utility. We use a DEM posting (output grid cell size) of 2 m and universal transverse mercator (UTM) projection, with the appropriate UTM zone determined by the center latitude and longitude of the point cloud.

2.4.6 DEM compositing

Our workflow uses the ASP `dem_mosaic` tool to produce per-pixel weighted-average and median DEM composites from all DEMs generated during pairwise stereo reconstruction (`skysat_dem_mos.py`). We also compute additional per-pixel metrics, such as the count and NMAD of valid elevation values, which are used to evaluate the relative accuracy of the output DEM composites. These metrics are used to filter the video DEM composites, removing any values with per-pixel DEM count of less than 2 and per-pixel elevation NMAD of greater than 5 m.

2.4.7 DEM co-registration: absolute geolocation refinement

The bundle adjustment step (Section 2.4.4) improves the self-consistency of the full set of SkySat camera models. If successful, the resulting pairwise DEMs should also be self-consistent, with limited relative horizontal and vertical offsets. However, without incorporating accurate GCPs during bundle adjustment, the absolute geolocation accuracy of the DEMs will be limited by the absolute geolocation accuracy of the initial L1A/L1B camera models provided by Planet (< 50 m for SkySat products (Marta, 2018)).

To improve SkySat DEM geolocation accuracy, our workflow uses the ASP `pc_align` utility to align the per-pixel median DEM composite with an external reference DEM that has relatively high resolution and accuracy. This tool ingests the raster DEMs as a regularly spaced point clouds with a point at each grid cell center. Horizontal point coordinates are computed from the raster geotransform, and vertical point coordinates are obtained from the raster cell values. A sample containing 75% of the points over ”static” surfaces (e.g., exposed bedrock) is extracted from each point cloud, and the point-to-plane Iterative Closest Point (ICP) algorithm (Pomerleau et al., 2013) is used to determine the rigid-body transformation (3-D rotation and translation) needed to co-register these samples.

The full point cloud is then transformed and regridded to produce a new DEM with improved geolocation. The final absolute vertical accuracy of the DEM is estimated using the median and NMAD of the residual elevation difference values between the co-registered SkySat DEM and the reference DEM over static surfaces (e.g., Shean et al., 2016).

The same transformation is used to update the set of self-consistent frame camera models (e.g., d'Angelo and Reinartz, 2012; Dehecq et al., 2020) which are needed for subsequent orthorectification steps. Refined RPC camera models can also be generated from these transformed frame camera models.

2.4.8 Orthomosaic generation

We use the ASP `mapproject` utility to create final orthoimages at native GSD for all input L1A/L1B SkySat scenes using the refined frame camera models and co-registered DEM composite. We then generate several orthoimage composite and mosaic products using the ASP `dem_mosaic` utility. These include a per-pixel weighted-average composite, a per-pixel median composite, and a blended mosaic product that prioritizes input orthoimages with higher resolution.

2.5 Case studies

We now present two case studies to demonstrate the capabilities of our SkySat stereo processing workflows, evaluate the accuracy of final products, and demonstrate potential for quantitative Earth science research applications. The supplementary materials also include products and results from two additional SkySat triplet stereo datasets (Figure A.3) and five additional SkySat video datasets (Figure A.4) acquired, processed and evaluated during the NASA CSDAP Pilot study.

2.5.1 SkySat triplet stereo

Our first case study involves an August 27, 2019 triplet stereo collection over the western flank of Mt. Rainier in Washington state, USA (Figure 2.4). This site covers a diverse landscape including glaciers, exposed bedrock, river valleys, and dense conifer forests, with over 2 km of total relief.

Reference DEM

We produced Digital Surface Models (DSMs) at 1 m and 10 m posting from publicly available airborne LiDAR data (hereafter referred to as "LiDAR reference DEM") collected over Mt. Rainier during 2007 and 2008 (Robinson and Swinney, 2010). See `lidar_processing` in Bhushan et al. (2020) for additional details. The LiDAR point cloud has RMSE of 0.037 m with a 2-sigma spread of 0.072 m when compared to GPS check points over flat roads (Robinson and Swinney, 2010).

The 10-m LiDAR reference DEM was used to initialize the SkySat frame camera models and perform initial alignment orthorectification of input scenes before stereo reconstruction. We assume that both the SkySat DEMs and LiDAR DEM capture the same canopy surface. Exposed static surfaces needed for co-registration and accuracy assessment (Section 2.4.7) were identified in the 1 m LiDAR reference DEM by masking forested areas (as defined by the 2016 National Land Cover Database (Dewitz, 2019)) and glacier/snowfield polygons defined by the Randolph Glacier Inventory v6.0 (RGI Consortium, 2017a). See the `dem_mask.py` utility in the `dem_coreg` package (Shean et al., 2019a) for additional details.

In order to evaluate the influence of reference DEM quality on the final accuracy of the output SkySat DEM composite, we also prepared a reference DEM using the void-filled, 1-arcsecond (∼30 m posting) SRTM-GL1 ellipsoidal DEM (Farr et al., 2007; NASA Shuttle Radar Topography Mission (SRTM), 2013), which is hereafter referred to as the "SRTM reference DEM".

Data processing

We ran the full SkySat triplet stereo workflow described in Section 2.4 using each of the two reference DEMs. We also reran the workflow without the camera model refinement and bundle adjustment steps, using the original L1B RPC camera models provided by Planet.

We evaluated the relative accuracy of the output SkySat DEM products over different landcover (”forest”, ”non-forest”, see Section 2.5.1) and terrain (slope $<= 10°$, slope $> 10°$) classes. To avoid including true elevation change since the reference DEM acquisition date (2000 and 2007/2008), we estimated the absolute accuracy of the 2019 SkySat DEM products over ”non-glacierized” surfaces (including forest classes), and ”exposed static surfaces” (”non-glacierized, non-forest” classes).

Results

The SkySat triplet stereo workflow using refined camera models provided a considerable improvement in the relative accuracy of the DEM composite (Figure 2.5D) compared to the workflow using the original L1B RPC camera models (Figure 2.5B). We observe improvements in scene-to-scene alignment (reduced feature offsets at seam boundaries) in the corrected orthomosaic and DEM composite. The median of the per-pixel NMAD values for the full DEM composite (”Full area” in Figure 2.6A) was reduced from 3.59 m when using the original L1B RPC models (Figure 2.5B) to only 0.73 m when using the refined frame camera models (Figure 2.5D). Much of the residual per-pixel spread can be attributed to variable landcover type (e.g., vegetation) and terrain characteristics (e.g., steep relief), with reduced per-pixel NMAD values observed over ”non-forest” pixels and surface slopes $<= 10°$ (Figure 2.6A).

Our camera refinement workflow also improved the absolute accuracy of the SkySat triplet stereo DEM composite as compared to the 1-m LiDAR reference DEM (Figure 2.5E). The absolute vertical elevation difference over static surfaces is $\sim \pm 2$ m near the center of the triplet stereo collect footprint, with higher offsets (up to $\sim \pm 10$ m) near the margins, which primarily cover forested areas (Figure 2.4). We observe negligible residual bias (0.12 m) and limited spread (2.49 m NMAD) over ”exposed static surfaces” (Figure 2.6B). We also observe real elevation change signals over glaciers between the ~2007/08 LiDAR reference and the 2019 SkySat DEMs (Figure 2.5E), with thinning near glacier termini and thickening upstream, as has been documented by other recent studies (Menounos et al., 2019; Sisson et al., 2011).

We obtain comparable relative accuracy for the SkySat DEM composites produced using the LiDAR and SRTM reference DEMs (Figure A.5). The observed median (±NMAD) elevation difference between the two SkySat DEMs is 1.35 (±2.08) m (Figure A.5B), and

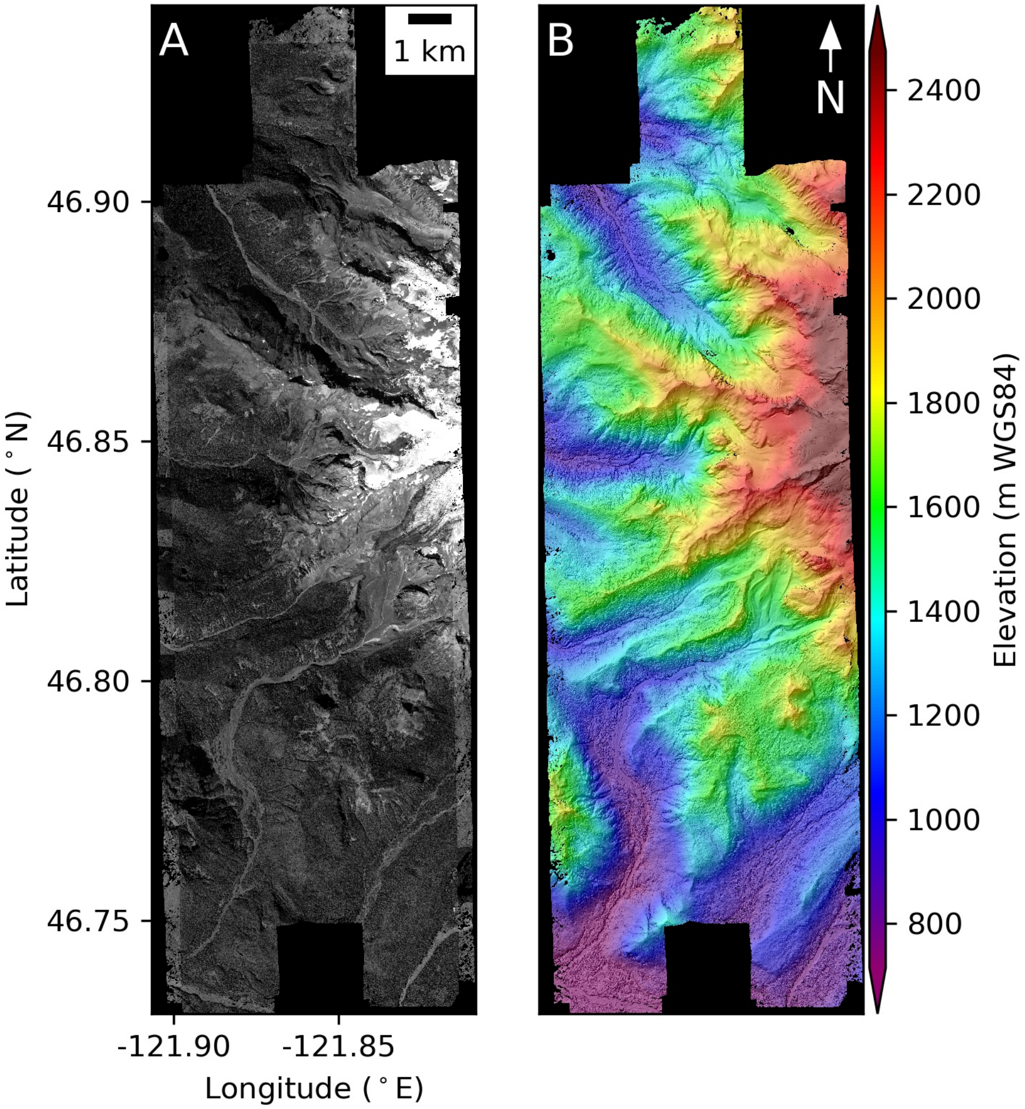

Figure 2.4: SkySat triplet stereo products, acquired August 27, 2019 (identifiers: 20190827_214711_ssc9, 20190827_214745_ssc9, 20190827_214821_ssc9) A) Orthomosaic with sort order based on orthoimage resolution, and B) median DEM composite. These final products were derived from L1B imagery that is ©Planet, 2019.

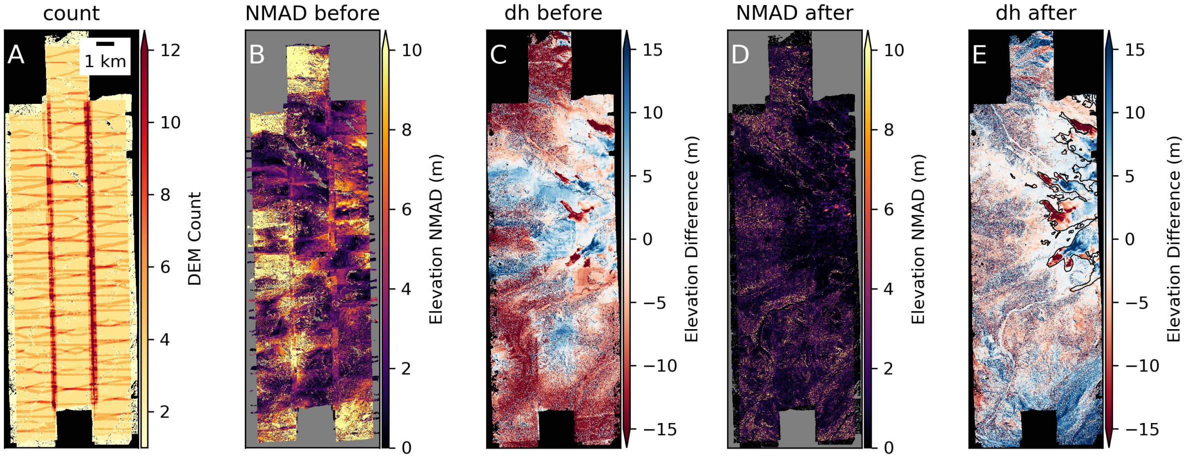

Figure 2.5: Mt. Rainier SkySat triplet stereo case study metrics. A) DEM Count Map. Per-pixel NMAD and elevation difference between SkySat DEM composite and 1 m LiDAR reference DEM B,C) with ("before") and D,E) without ("after") bundle adjustment and camera model refinement. Our workflow with refined camera models improved both relative (D) and absolute (E) accuracy. Black lines in (E) show glacier and perennial snowfield outlines from the Randolph Glacier Inventory (RGI) v6.0 (RGI Consortium, 2017a). Glacier thinning, especially at lower elevations, is apparent between the ~2007/08 timestamp of the LiDAR reference DEM and the 2019 SkySat DEM.

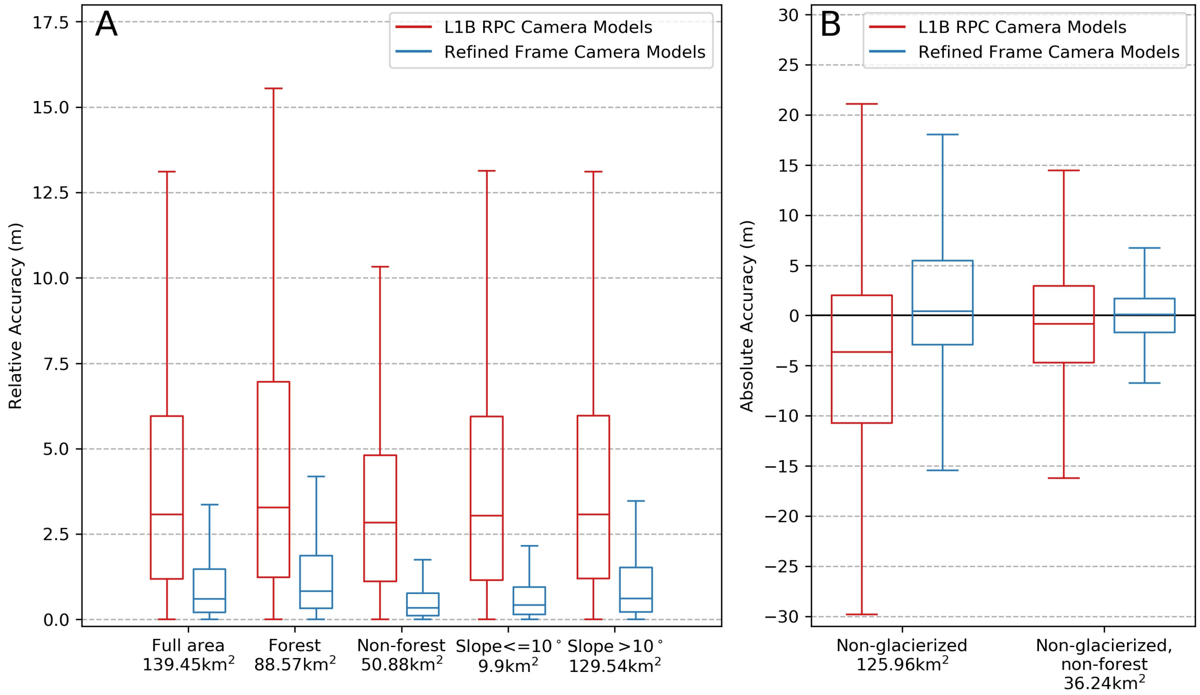

Figure 2.6: Accuracy metrics using original L1B RPC camera models (red) and refined frame camera models (blue) for the Mt. Rainier SkySat triplet stereo case study. A) Relative accuracy as represented by per-pixel NMAD values of the DEM composite (Figure 2.5B, D) for different landcover and terrain classes, with respective areas. B) Absolute accuracy as represented by elevation difference between the SkySat DEM composite and the reference LiDAR DEM (Figure 2.5C, E) over static surfaces. Boxes show median and interquartile range, with whiskers at 1.5 times the interquartile range.

this can be partly attributed to offsets between the two reference DEMs (Figure A.5A). After relative co-registration of the two SkySat DEMs, the elevation difference values are reduced to 0.12 (±1.63) m (Figure A.5C). The residual elevation differences in Figure A.5C are likely related to artifacts over vegetation and steep slopes introduced during the initial alignment orthorectification step using the SRTM reference DEM, potentially related to the reduced accuracy and variable penetration (Figure A.5A) of the C-band radar (e.g., Kellndorfer et al., 2004).

The reference DEM analysis confirms that high-quality SkySat DEMs can be produced using publicly available coarse-resolution reference DEMs like SRTM. This finding is relevant for most locations across the globe that do not yet have LiDAR or stereo-derived reference DEMs.

2.5.2 SkySat video stereo

Our second case study involves multiple SkySat video collections over Mt. St. Helen's in Washington state, USA (Figure 2.7). Geologically, Mt. St. Helen's is an extremely dynamic system with large elevation change signals on short timescales due to active volcanism (e.g., Kennedy and Russell, 2012), dynamic glaciers (e.g., Schilling et al., 2004), mass wasting, seasonal snow accumulation, and wind/avalanche snow redistribution. The steep walls of the summit crater and volcanic domes provide an opportunity to evaluate the SkySat video multi-view stereo products over terrain which is notoriously challenging for traditional two-view, and even triplet, stereo reconstruction due to occlusions.

Two 120-second SkySat videos were acquired for this study - one on April 20, 2019, near peak snow water equivalent (SWE) (hereafter, the ”snow-on” collection) and the other on October 1, 2019, near the end of the summer snow/ice melt season (”snow-off” collection) (Figure 2.7A, B). A light dusting of early-season snow was present on some surfaces during the October 1 video collection (Figure 2.7B).

Reference DEMs

We used two reference DEMs derived from WorldView stereo images to process the SkySat video collections over Mt. St. Helen's - a summer reference DEM composite and a single spring reference DEM. The summer DEM composite (hereafter referred to as the ”summer reference DEM”) was generated from eight 2-m WorldView-1/2/3 DEMs acquired between 2013-2015 and co-registered to an airborne LiDAR DEM prior to compositing (Menounos et al., 2019; Shean et al., 2016). This summer reference DEM was used to initialize the frame camera models for both the snow-on and snow-off collections (Section 2.4.2), and to co-register the snow-off SkySat DEM over static surfaces (Section 2.4.7). Due to the limited availability of snow-free static surfaces within the small footprint of the snow-on SkySat DEM, we created the second reference DEM (hereafter referred to as the "spring reference DEM") from a WorldView-2 stereo pair acquired on April 28, 2019 (8 days after the snow-on SkySat video collection). To create this spring reference DEM, we used ASP with default MGM settings and then co-registered this spring reference DEM to the summer reference DEM over static surfaces distributed across the much larger WorldView footprint (median difference of 0.06 m, NMAD of 1.01 m). The snow-on SkySat DEM composite was then co-registered to the spring reference DEM assuming that there was negligible elevation change during the eight day period.

Data processing

To evaluate the quality of the original, uncorrected SkySat video products, we ran our video processing workflow for both the snow-on and snow-off video collections using the original L1A RPC camera models without initial alignment orthorectification (Section 2.4.5). We then ran our full SkySat video processing workflow (Figure 2.3B) using refined camera models.

Our default video processing workflow using an external reference DEM for the initial alignment orthorectification step worked well for most SkySat video samples (Figure A.4). The extreme relief of the St. Helen's crater and scale relative to the SkySat footprint, however, required an alternative strategy to avoid introducing artifacts that could lead to failed correlation and data gaps over the steep crater walls. The underlying issue is related to geolocation inconsistency between the L1A scenes and the external reference DEM, so we first generated a "smoothed initial DEM" from the original L1A scenes (Section 2.4.5, Figure 2.3B) and then used this DEM for initial alignment orthorectification, rather than the external reference DEM.

Results

Our workflow produced spatially continuous SkySat video DEM products with few data gaps, even over steep slopes on the crater walls (> 40 to 50°). This is true for both the snow-on collect with limited surface texture over fresh snow (Figure 2.7A), and the snow-off collect with shadows on north-facing slopes (Figure 2.7E). The refined camera models from our workflow offer significantly improved relative DEM accuracy (Figure 2.7D,H and 2.8A,B) compared to DEMs derived with the original RPC camera models (Figure A.6).

The snow-off DEM composite displays better relative accuracy than the snow-on DEM composite, with median per-pixel NMAD values of 0.45 and 1.64 m, respectively (2.8B). The larger per-pixel NMAD values for the snow-on DEM composite are indicative of residual

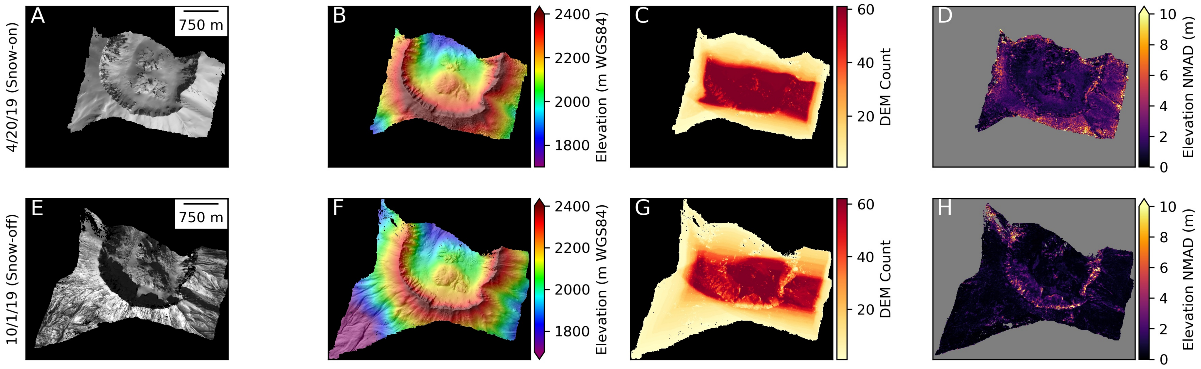

Figure 2.7: SkySat video products for Mt. St. Helen's, acquired April 20, 2019 (near peak SWE, top row) and October 1, 2019 (near end of melt season, bottom row): A,E) Orthoimage mosaic, B,F) DEM composite from 62 stereo pairs, C,G) per-pixel DEM count, and D,H) per-pixel NMAD, which captures relative accuracy of the DEM composite. Note quality over steep crater walls and <1 m relative accuracy over crater floor and flanks. The orthoimage mosaics were derived from L1A imagery that is ©Planet, 2019

.

camera inconsistencies after bundle adjustment, likely due to a reduced number of feature matches over snow. We also observe artifacts and larger per-pixel NMAD values of ~5 m in some areas of the snow-on DEM composite (Figure 2.7D), likely due to erroneous disparities obtained during correlation over fresh snow with limited texture. The snow-off DEM composite also displays larger per-pixel NMAD values on northwest flank due to moving clouds during video collection (Figure 2.7H).

The snow-on and snow-off DEM composites show limited absolute median bias (±NMAD) of 0.16 (±1.60) m and +0.30 (±1.83) m, respectively, compared to non-glacierized static surfaces in the corresponding spring and summer reference DEMs (Figure 2.8C). These metrics provide estimates for the absolute accuracy of the SkySat DEMs, though some component of the observed residual elevation differences can be attributed to errors in the reference DEMs.

Elevation change from multiple SkySat DEMs

We computed elevation change for the ~5.5 month time-period (April 20 to October 1) by subtracting the co-registered snow-on DEM composite from the snow-off DEM composite (Figure 2.9B). Relatively large negative elevation change signals are observed on the crater floor and within gullies/depressions on the flanks. Large negative signals are observed near the base of the western crater wall (green box in Figure 2.9B). Limited elevation change is

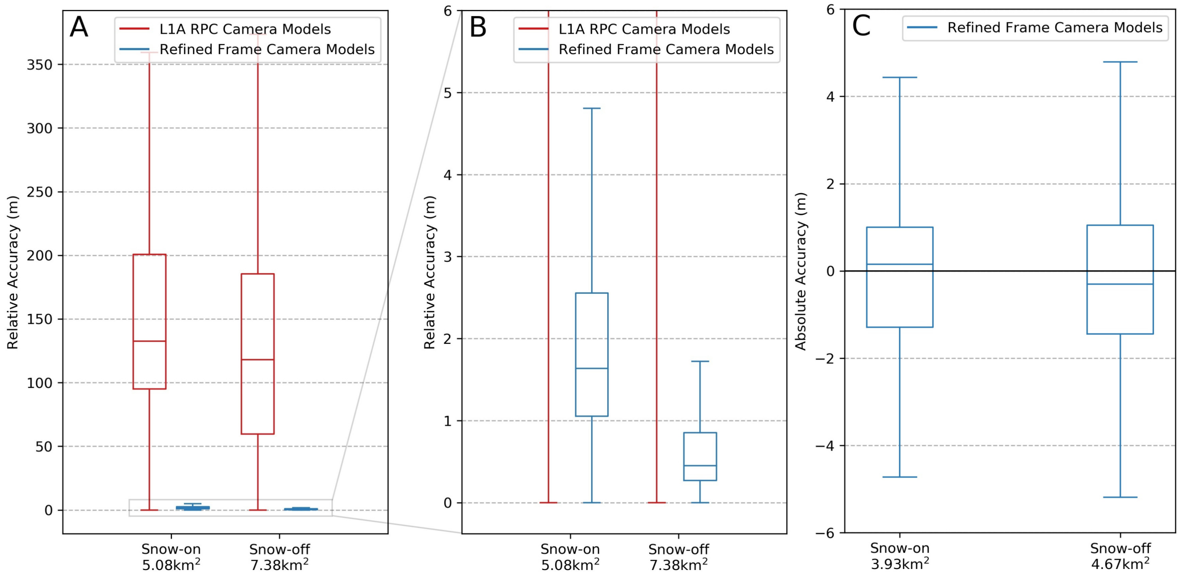

Figure 2.8: Accuracy metrics using original L1A RPC camera models (red) and refined frame camera models (blue) for the Mt. St. Helen's SkySat video stereo case study. A) Relative accuracy as represented by per-pixel NMAD values of the snow-on and snow-off DEM composites (Figure 2.7D,H), with respective areas listed. B) Same as in a (A), but zoomed to show detail of distribution for refined products. C) Absolute accuracy as represented by elevation difference between the SkySat DEM composite and corresponding reference DEM over non-glacierized surfaces. Boxes show median and interquartile range, with whiskers at 1.5 times the interquartile range.

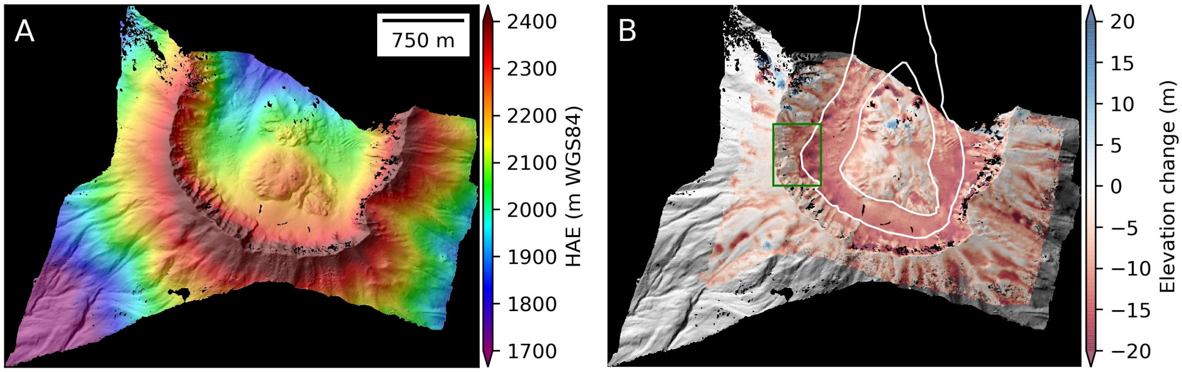

Figure 2.9: A) Mt. St. Helen's SkySat video DEM composite from October 1, 2019. B) Elevation difference between the April 20, 2019 and October 1, 2019 DEM composites, documenting seasonal snow melt and other processes. White lines shows approximate Crater Glacier outline. Green box on west crater wall highlights large elevation change signals of ~10-20 m.

observed over the volcanic domes within the crater and ridges on the flanks.

The observed elevation change can be attributed to several processes. The negative elevation change over the crater floor and flanks can primarily be attributed to melting of relatively thick (>5-15 m) seasonal snowpack. The large negative signals within gullies and depressions on the flanks are indicative of preferential spring snow accumulation due to wind redistribution. Some of the observed elevation change over the Crater Glacier is also related to ice melt during summer, snow/firn compaction (e.g., Belart et al., 2017), and ice flow processes (e.g., Sold et al., 2013) including vertical submergence, advection of thickness anomalies, and crevasse opening/closing. The large elevation change values at the base of the western crater wall (green box in Figure 2.9B) are likely related to melt of locally thick avalanche deposits present in the spring DEM and other local ice flow processes.

The near-zero elevation change over the volcanic domes can potentially be attributed to limited spring snow accumulation due to wind redistribution and/or increased geothermal heat flux causing continuous melting of snow during the accumulation season. The near-zero elevation change on the upper portion of the interior crater walls likely indicates limited or no snow accumulation in these areas, due to steep (>50°) surface slopes.

2.6 Discussion

We successfully generated high-quality DEM composites from the SkySat triplet stereo and video images. The bundled RPC models and L1A corner coordinates were not accurate enough to produce usable DEMs. This finding is consistent with those of previous geodetic studies involving products from Planet Dove (Ghuffar, 2018) and earlier SkySat sensors (d'Angelo et al., 2016). Our workflows correct these camera model issues to produce 2-m DEM composites with both high precision (<1 to 2 meter relative vertical accuracy, Figure 2.6A and 2.8A,B) and accuracy (<2 to 3 m absolute vertical accuracy, Figure 2.6B and 2.8C). Qualitatively, the 2-m DEM composites are able to resolve small-scale features such as narrow gullies and glacier crevasses at both of our study sites (Figure 2.4 and 2.9).

2.6.1 SkySat triplet stereo evaluation

The per-pixel NMAD values for the Mt. Rainier triplet stereo DEM composite are slightly higher than the corresponding values for the video DEM composites, with larger residual offsets observed for scenes along the margins of the collection. This result can be attributed to two main causes. First, these marginal scenes mostly cover dense forests (Figure 2.4), which are challenging for satellite stereo photogrammetry (e.g., Montesano et al., 2017, 2019; St-Onge and Grandin, 2019). Second, the scenes along the margins of a triplet collection have less overlap with neighboring scenes, and comparatively weaker connections during bundle adjustment.

The latter issue can potentially be corrected by individually co-registering each of the pairwise DEMs to a reference DEM after the bundle adjustment step, rather than creating a DEM composite and then co-registering. This alternative co-registration approach improved both the relative and absolute accuracy of the Mt. Rainier triplet stereo DEM products (Figure A.7). We attribute this success to the adequate distribution of both local topographic relief and static surfaces for all individual pairwise DEMs. However, this may not be the case for other sites with relatively flat or planar terrain, where some or all of the small pairwise SkySat DEMs may lack sufficient relief and/or static surface distribution. For this reason, our default workflow uses the DEM composite during the co-registration step, but the user can select the individual pairwise DEM co-registration strategy using the `multi_align` option in the `skysat_pc_cam.py` tool.

Some of these issues can also be addressed by exploiting the rigid relative orientation of the three detectors (Figure 2.1), which should be consistent during the triplet stereo collection sequence. We explored this option by approximating a larger "virtual detector" combining three scenes acquired by the three detectors at a given timestamp, and accounting for the relative geometry of the three detectors in the SkySat focal plane. The resulting products included systematic artifacts and high triangulation errors indicative of residual detector geometry error. Beyond rigorous on-orbit geometric calibration of each SkySat-C using L1A images, it could be possible to improve our generic SkySat workflow by independently modeling each of the three detectors, but imposing constraints for their relative orientation during bundle adjustment.

2.6.2 SkySat video stereo evaluation

The limited per-pixel NMAD values for the SkySat video products indicate that the bundle adjustment step produced self-consistent camera models. We attribute this success to the high scene count and consistent, overlapping footprints of the SkySat video. When interpreting the absolute vertical accuracy of the Mt. St. Helen's video DEM composites, it is important to acknowledge the negative impact of both the limited distribution of static surfaces available for co-registration and the generally steep slopes within the crater, as the accuracy of both the SkySat and reference WorldView DEMs should be lower over steep terrain (e.g., Müller et al., 2014; Shean et al., 2016). We observe sub-meter absolute accuracy for a SkySat DEM composite produced from a similar symmetrical video collection over the relatively flat terrain over the Grand Mesa in Colorado, USA (Figure A.4A-D), compared to a reference WorldView DEM.

2.6.3 Limitations and considerations

As with any remote sensing technique, there are some limitations to consider when working with SkySat products.

Field of view

The individual SkySat scenes have a relatively small footprint (~2.5 km^2), with limited overlap between adjacent scenes (~10-15%) in the L1B mono collects. These limitations can lead to complications during several processing steps in our workflow. For instance, accurate feature matching over small overlapping ground footprints is difficult between scenes acquired from very different perspectives (e.g., larger convergence angles of $\sim$ 27 to 55°), especially for steep terrain. Similarly, the small overlap between adjacent scenes results in a weaker scene to scene connections during bundle adjustment (Section 2.4.4 and 2.6.1). These two issues are less relevant for the SkySat video products, as they have small perspective difference between scenes and high scene overlap percentage (~95-100%). However, the small combined video footprint (~2.5 to 10 km^2), may have limited or no static surfaces available for co-registration (Section 2.4.7).

Surface texture

An essential component of any optical stereo photogrammetry workflow involves sparse and dense feature matching during bundle adjustment and image correlation, respectively. Given the relatively poor initial RPC geolocation accuracy for SkySat scenes, an initial bundle adjustment step is essential for subsequent stereo reconstruction. Feature matching success depends on adequate surface texture at spatial scales comparable to the native image GSD. For example, very high-resolution (VHR) imagery over urban areas should yield many unique features/keypoints, while VHR imagery over fresh snow on flat terrain may appear essentially featureless. A well-distributed set of sparse feature matches (i.e., not concentrated in one image corner) between overlapping images is essential to properly constrain the bundle adjustment optimization. For VHR satellite images with a large ground footprint (e.g., WorldView-2 swath width of 16.4 km), a well-distributed network of feature matches can usually be computed even if parts of the overlapping images have limited texture. However, the limited ground footprint of individual SkySat scenes can be problematic for feature matching, especially over surfaces with limited texture at ∼1 m spatial scales (e.g., fresh snow). In such cases, a complete network of feature matches may not be constructed during bundle adjustment, due to limited correspondences between overlapping scenes. Similar problems can arise due to the presence of opaque clouds (e.g., Figure 2.7E and A.4M) and open water (e.g, Figure A.4Q). If poorly distributed feature matches are present near the more central, "anchor" scenes of a SkySat triplet stereo collect (i.e., regions with high DEM count in Figure 2.5A), the bundle adjustment algorithm can introduce camera position and orientation error in adjacent scenes.

Even with perfectly calibrated camera models, erroneous disparities can pass stereo correlation filters, especially over surfaces with limited texture. Detector saturation over high-albedo surfaces can also result in failed correlation (e.g., Dai and Howat, 2018; Shean et al., 2016). Fortunately, our evaluation of SkySat products over multiple snow and ice targets (Figure 2.4, 2.7, A.3, A.4) suggests that the 11-bit radiometric resolution, exposure cycling, and 0.9 m GSD of the SkySat products is generally sufficient to resolve small-scale features on most high-albedo snow and ice surfaces.

Reference DEM Considerations

Our workflow requires a reference DEM during camera resection, initial alignment orthorectification, and 3D co-registration (Figure 2.3). The choice of reference DEM is thus an important consideration, which depends on several factors. A reference DEM with high horizontal and vertical accuracy, limited sensor-dependent relative errors (e.g., variable radar penetration, LiDAR flightline offsets), complete overlap with the SkySat collection, limited data gaps, and limited time offset relative to the SkySat collection will produce better results during all processing steps. Additionally, if possible, the GSD of the reference DEM should be less than or approximately equal to that of the SkySat DEM composite to improve absolute geolocation accuracy during ICP co-registration.

Where available, we recommend using a reference DEM derived from airborne laser scanning (LiDAR) or other very-high-resolution stereo satellite imagery (e.g., DigitalGlobe/Maxar WorldView-3) that has been corrected with accurate control data. Alternatively, as demonstrated in Section 2.5.1, high-quality SkySat DEMs can also be generated using publicly available reference DEMs with limited resolution and accuracy (e.g., SRTM, NED). Furthermore, if the intended use case is to measure relative elevation change between the SkySat DEM and a reference DEM, then the absolute geolocation accuracy of the reference DEM is less relevant, as relative offsets between the two will be minimized during co-registration.

It is interesting to note that the snow-on SkySat DEM composite has better apparent absolute accuracy than the snow-off SkySat DEM composite (Figure 2.8C). This might be attributed to the more limited time interval (8 days) between the snow-on SkySat DEM and spring reference DEM, with minimal expected surface elevation change over surfaces assumed to be static. In contrast, the snow-off SkySat DEM and the corresponding summer reference DEM composite are separated by several years, and some surfaces assumed to be static likely changed (e.g., mass wasting over steep crater walls), leading to an apparent decrease in SkySat DEM accuracy.

The better apparent absolute accuracy of snow-on DEM composite may also be a direct consequence of the relatively smooth, snow-covered surface. Thick snow will fill small gullies, cover small ridges, and accumulate at the base of steep slopes, all serving to reduce surface roughness. This reduced small-scale roughness may be slightly more forgiving of any reduction in DEM resolving power due to residual camera alignment issues and "blurring" during pairwise DEM compositing.

2.6.4 Multi-view triangulation

Our default workflow uses a pairwise (two-view) stereo triangulation strategy for multiple image pairs, instead of using true multi-view triangulation for all images. Based on previous tests, we hypothesized that the quality of the per-pixel median composite from all pairwise DEMs would match or potentially exceed the quality of DEM products produced using multi-view triangulation. We tested an experimental multi-view stereo implementation for the SkySat video collections (Sections 2.4.2, 2.4.5). The resulting multi-view DEM composites contain more noise than the pairwise DEM composites, with visible seam boundaries (Figure A.8). This result is consistent with those from previous studies suggesting that a DEM composite derived from many self-consistent pairwise DEMs (e.g., Ozcanli et al., 2016) is able to resolve more detail with better signal-to-noise ratio than a DEM obtained by conventional multi-view implementations (e.g., **?**). This limitation can potentially be improved by assigning increased weight to pairs with larger convergence angles (and reduced uncertainty) during multi-view triangulation (Delon and Rougé, 2007).

2.6.5 Structure from Motion

To further explore multi-view triangulation options, we attempted to process SkySat video and triplet stereo datasets using two commercial SfM packages, Pix4DMapper and Agisoft Metashape, and one open-source package, COLMAP (Schönberger and Frahm, 2016; Schönberger et al., 2016).

We found that the initial bundle adjustment step for these packages was relatively unstable for SkySat scenes. When solving for both extrinsics and intrinsics, multiple runs with identical input images and settings produced different solutions. When solving for extrinsics only, both COLMAP and Pix4DMapper provided reasonable solutions for the snow-on Mt. St. Helen's video dataset, but neither package successfully refined all cameras for the Mt. Rainier triplet stereo dataset.

One possible path forward might involve initial camera resection and bundle adjustment with our workflow, followed by dense reconstruction and multi-view triangulation with one of these SfM packages (e.g., Zhang et al., 2019). Future analysis will allow for more detailed evaluation of our pairwise stereo DEM composites vs. SfM multi-view stereo DEM products.

2.7 Conclusions and summary

The SkySat-C constellation offers new potential for on-demand, large-scale, 3D mapping of the Earth's surface, with relatively limited tasking competition, short repeat imaging interval, and low cost. The $\sim$100 km^2 ground footprint of the SkySat triplet stereo products and area tasking strategy has the potential for systematic 3D reconstruction of larger areas over a short time window. The SkySat video products cover a more limited $\sim$2.5 to 10 km^2 area, but they can be used for multi-view stereo reconstruction over sites which are challenging for two-image or triplet stereo (e.g., steep mountains and dense vegetation). However, the accuracy of the resulting DEM products is limited by the relatively poor geolocation accuracy of the original Level-1A/1B SkySat camera models and inconsistent orientation of individual scenes in both the collects and videos. As a result of these limitations, and the absence of robust processing software, SkySat imagery has not yet seen widespread use for stereo reconstruction.

We developed an automated, open-source workflow to refine the SkySat camera models and improve absolute geolocation accuracy using external reference DEMs, without manual GCP selection. These refined camera models are then used to produce accurate, self-consistent DEM and orthoimage composites from both the SkySat triplet stereo and video products.

We found that pairwise triangulation followed by compositing produced better output products with more detail and less noise than true multi-view triangulation. We also obtained comparable relative accuracy for SkySat DEM composites produced using both a 1-m LiDAR DSM and the 30-m SRTM-GL1 as reference DEMs, confirming that high-quality SkySat DEMs can be produced on a global scale using publicly available coarse-resolution reference DEMs like SRTM.

The small overlap (∼10%) between adjacent L1B scenes in each SkySat triplet stereo collect can cause issues during bundle adjustment. We were able to mitigate these issues by co-registering individual pairwise DEMs to a reference DEM, rather than the full DEM composite. This strategy may work for sites with adequate relief and static surface distribution, but may fail for planar surfaces. Future availability of L1A scenes with greater scene-to-scene overlap (∼90%) and additional camera position metadata should offer new opportunities to constrain the triplet stereo bundle adjustment optimization and improve stereo reconstruction results.

We presented case studies for SkySat stereo samples collected over Mt. Rainier and Mt. St. Helen's, which include terrain and landcover that is challenging for stereo reconstruction. The output DEM composites have <1 to 2 m relative and <2 to 3 m absolute vertical accuracy compared to reference airborne LiDAR and WorldView stereo DEMs, with highest accuracy over vegetation-free surfaces and limited surface slopes. Qualitatively, the output 2-m SkySat DEMs have few data gaps and are able to resolve small-scale surface features such as narrow gullies and glacier crevasses. We also computed elevation difference between two repeat SkySat video DEM composites over Mt. St. Helen's, collected during spring (peak snow extent/depth) and late summer (minimum snow extent/depth). These products document total snow depth of ∼5-15 m and other elevation change due to avalanches and glacier flow.

The methods presented here can be applied to other frame camera imaging systems, including those on planetary orbiters (e.g., Edwards and Broxton, 2006; Edwards et al., 2005), aerial/UAV platforms (e.g., Alexandrov, 2017; Knuth et al., 2020; Meyer and Skiles, 2019), and the Planet Doves. We hope to improve our current workflow with additional bundle adjustment constraints, better multi-view stereo triangulation approaches, and more sophisticated point cloud processing. We are also working to produce improved landcover classification products derived from contemporaneous SkySat multispectral imagery at native resolution for use during co-registration (e.g., Deschamps-Berger et al., 2020; Hu and Shean, 2020). Finally, we will continue to improve the open-source code accompanying this manuscript, and hope to scale processing efforts to study the Earth's evolving surface on a regional to global scale using the growing SkySat stereo archive.

Acknowledgements

We acknowledge Compton J. Tucker and others at NASA Goddard Space Flight Center and NASA Headquarters for coordinating the Commercial Smallsat Data Acquisition Program Pilot and assisting with preliminary SkySat tasking campaigns. Paris Good at Planet provided invaluable assistance with data acquisition and facilitated discussions with Planet engineering teams. Thanks are also due to Ross Losher, Antonio Martos, Kelsey Jordahl and others at Planet for initial guidance on SkySat-C sensor specifications and camera models. Resources supporting this work were provided by the NASA High-End Computing (HEC) Program through the NASA Advanced Supercomputing (NAS) Division at Ames Research Center. The Maxar WorldView L1B stereo imagery used to generate reference DEMs was available under the NGA NextView/EnhancedView license. Friedrich Knuth and Michelle Hu provided feedback on initial manuscript outline and code development. Eric Gagliano assisted in latex formatting. We thank two anonymous reviewers for providing valuable and constructive input that significantly improved the quality of this manuscript. We also acknowledge input from the larger ASP community during photogrammetry discussions.

Funding

This research was supported by the NASA Terrestrial Hydrology Program (THP) and the NASA Cryosphere Program. SB was supported by a NASA FINESST award (80NSSC19K1338) and the NASA HiMAT project (NNX16AQ88G). DS, OA and SH were supported by NASA THP award 80NSSC18K1405. Tasking, data access, and supplemental support was provided by the NASA Commercial Smallsat Data Acquisition Program 2018 Pilot Study.

Author contributions

Shashank Bhushan led the study, developed processing workflows with input from all co-authors, processed data, generated figures and wrote the first draft of the manuscript with David Shean. David Shean managed the project, acquired funding, provided guidance on methodology, and essential support in manuscript development, organisation and writing. Oleg Alexandrov led the modification of the ASP codebase to support SkySat sensors and provided valuable insight on photogrammetry theory and workflows. Scott Henderson documented initial issues with SkySat metadata and performed initial video processing experiments. All authors contributed to the final version of the manuscript.

Chapter 3

SEASONAL AND ANNUAL SURFACE MASS BALANCE FOR DEBRIS-COVERED GLACIERS IN HIGH-MOUNTAIN ASIA FROM FLOW-CORRECTED SATELLITE STEREO DEM TIME SERIES

The chapter is under preparation for submission to the Journal of Glaciology as: **S. Bhushan**, D. Shean, J. M. Hu, G. Guillet, and D. Rounce. ***"Seasonal and annual surface mass balance for debris-covered glaciers in High-Mountain Asia from flow-corrected satellite stereo DEM time series"***

3.1 Abstract

Glaciers in High Mountain Asia (HMA) are experiencing varying rates and patterns of mass loss due to a complex interplay between glacier surface processes, local conditions and climate forcing. Spatially distributed estimates of surface mass balance (SMB) can provide valuable insight into these drivers, but observations are currently limited in both space and time. We used very-high-resolution (VHR) optical stereo images acquired by commercial satellite constellations to prepare time series of contemporaneous DEM and surface velocity products for six debris-covered glaciers in Nepal. We then produced flow-corrected Lagrangian SMB maps to isolate local surface melt signals with enough detail to study individual melt ponds and ice cliffs. Our results show melt reduction under thick debris cover and enhanced ablation over ice cliffs. Ice cliffs were responsible for $17-43\%$ of the total ablation over debris-covered areas, even though they occupied $\leq 11\%$ of the total area. Our seasonal SMB time series reveals the timing and patterns of summer accumulation and ablation, underscoring the importance of snow avalanches for low elevation debris-covered glaciers in the region. Our approach can be applied to other glaciers with repeat, cloud-free, VHR stereo imagery, enabling regional SMB analyses.

3.2 Introduction

High Mountain Asia (HMA) glacier and snow melt provide essential water resources to one of the most densely populated regions in the world (e.g., Immerzeel et al., 2020). Current HMA glacier mass loss accounts for $\sim 10\%$ of the total sea level rise contribution by all glaciers, ice caps, and ice sheets (Gardner et al., 2013). The majority of HMA glaciers are losing mass (e.g., Hugonnet et al., 2021; Maurer et al., 2019; Shean et al., 2020) as global and regional temperatures continue to rise (e.g., Hansen et al., 2006; Lalande et al., 2021). This mass loss is projected to continue in the future (e.g., Huss and Hock, 2018; Kraaijenbrink et al., 2017; Rounce et al., 2020), with a recent study suggesting that even if global temperature is limited to 1.5° C above to pre-industrial levels, 46% of HMA glacier mass will be lost by 2100 (Rounce et al., 2023).

While calibration of prognostic glacier mass balance models has significantly improved from integrating HMA-wide geodetic glacier mass balance observations derived from medium resolution DEMs (e.g., 30 m or 100 m ASTER products) (e.g., Brun et al., 2017; Hugonnet et al., 2021; Shean et al., 2020), the effect of debris cover on surface mass balance (SMB) at fine spatial scales is still poorly understood. Glacier surface mass balance is controlled by accumulation and ablation, driven by regional climatology. Debris cover is a widespread feature in HMA, with approximately 30% of the ablation area of HMA glaciers covered by debris (e.g., Herreid and Pellicciotti, 2020; Scherler et al., 2018). The presence of supraglacial debris and associated geomorphic features (i.e., ice cliffs and melt ponds) modify the fundamental feedback between surface mass balance and climate by locally modifying ice melt. Debris-covered glaciers display a notable degree of surface heterogeneity, marked by small-scale variations in debris composition (such as sediments, loose rocks, and boulders), debris thickness, as well as the occurrence of exposed, steep ice cliffs and melt ponds in areas entirely devoid of debris (e.g., Benn et al., 2012; Racoviteanu et al., 2022). Thick debris cover reduces ice melt, potentially by 50% for debris thickness of $\sim$ 10 cm, while thin debris covers decrease surface albedo compared to clean ice and enhance melt(e.g., Kraaijenbrink et al., 2017; Mihalcea et al., 2006; Nicholson and Benn, 2006). The presence of ice cliffs (e.g., Sakai et al., 2002) and supraglacial ponds (e.g., Sakai et al., 2016) further complicates the melt feedback provided by debris thickness. Exposed ice cliffs generally display higher melt rates due to interception of outgoing longwave radiation by surrounding debris (e.g., Buri et al., 2016) while south-facing cliffs are subject to direct absorption of incoming shortwave radiation (e.g., Buri and Pellicciotti, 2018). Supraglacial ponds permit additional local heat absorption and melting due to their lower albedo (e.g., Miles et al., 2018a), while sustaining ice cliffs around their edges (e.g., Kneib et al., 2022a; Steiner et al., 2019; WATSON et al., 2017). Despite their importance, studying these features has proven difficult with coarse satellite observations due to their small size and transient nature (e.g., Brun et al., 2018), thus the majority of mass balance models applied over debris-covered glaciers do not account for them (e.g., Racoviteanu et al., 2022), with the notable exception of (Kraaijenbrink et al., 2017).

Another challenge in model calibration is the lack of distributed SMB measurements at short timescales. Changes in seasonal to annual SMB directly reflect short-term changes in meteorological conditions. Projecting correct seasonal SMB is crucial for determining seasonal timings and magnitudes of glacier meltwater runoff and associated contributions to river discharge. However, measuring annual or sub-annual SMB from a limited number of publicly available ASTER DEMs acquired within a yearly interval is challenging due to the lower vertical accuracy of individual DEMs ($\sim$ 10 to $15m$, see Figure 2 in Shean et al., 2020) compared to the seasonal signals. Additionally, distributed geodetic elevation change measures the combined change from vertical ice flow (flux divergence) and surface mass balance (e.g., Berthier and Vincent, 2012; Cuffey and Paterson, 2010; Miles et al., 2021). Hence, direct elevation change measurements can not be used to directly calibrate elevation-dependent surface mass balance gradients, a standard output produced by glacier evolution models (e.g., Huss and Hock, 2015; Rupper and Roe, 2008; Zekollari and Huybrechts, 2018). Large-scale glacier models are thus calibrated using decadal glacier-wide geodetic mass balance observations, which all suffer from overfitting and/or overparameterization, which is a primary source of uncertainty in projections at the individual glacier scale (Rounce et al., 2020).

3.2.1 Study Objectives

We build upon previous studies to develop methods for estimating glacier surface mass balance from satellite remote sensing observations. Specifically, we discuss the underlying theory, describe the input data (e.g., VHR stereo imagery, modeled estimates of ice thickness and debris thickness), and the ensuing methodology to obtain high-resolution SMB products. We use the developed methods and high-resolution SMB products to tackle two main research questions:

- **1)** can these measurements be used to uncover the controls of the surface features (e.g., debris thickness, ice cliffs) on debris-covered ice ablation?
- **2)** can these measurements be used to assess the patterns of seasonal accumulation and ablation over monsoon-dominated debris-covered glaciers in Nepal?

We finally discuss the limitations of our approach and summarize the potential of scaling these methods for regional analysis.

3.3 Study Sites

Our study sites lie in the Central Himalayan mountain range in Nepal. The region is highly tectonically active (e.g., Nakata, 1989), with high rates of uplift (e.g., Lavé and Avouac, 2001)

Table 3.1: Description of the six glaciers considered in this study.

Glacier Name	RGIId[a]	Area (km^2)	Debris cover%	Debris thickness range (m)[b]
Ngozumpa	15.03473	61.05	38.29	0.03, 0.13, 0.48, 1.78, 3.00
Khumbu	15.03733	19.08	38.54	0.02 , 0.06, 0.29, 1.73 , 3.00
Black Changri Nup	15.03734	1.26	53.36	0.09, 0.30, 0.92, 3.00, 3.00
Imja Lhotse Shar	15.03743	14.25	40.75	0.03, 0.09, 0.32, 0.53, 0.84
Langtang	15.04121	37.77	44.75	0.04, 0.20, 0.67, 1.49, 3.00
Lirung	15.04045	1.46	97.00	0.15, 0.21, 0.36, 0.53, 0.63

---

[a] Randolph Glacier Inventory v6.0, Id (Pfeffer et al., 2014; RGI Consortium, 2017a)

[b] 5th, 16th, 50th, 84th, 95th percentile

and erosion (e.g., Marc et al., 2019) that provide an abundant supply of loose rock material for sustaining debris-covered glaciers (e.g., Racoviteanu et al., 2022). The regional climate is heavily influenced by the Indian Summer Monsoon from June to September (e.g., Wang and LinHo, 2002; Webster et al., 1998), traditionally accounting for liquid precipitation at low elevations, and snow accumulation at high elevations (e.g., Ageta and Higuchi, 1984; Perry et al., 2020). The monsoon season coincides with the boreal summer extending from May to October, followed by a cold and dry winter from November to March (e.g., Pelto et al., 2021; Stumm et al., 2021). Glaciers in the region are generally classified as ”summer accumulation type”, and are more sensitive to increasing summer temperatures than conventional ”winter accumulation type” glaciers (e.g., Naito, 2011).

In this study, we focus on six well-studied debris-covered glaciers in Nepal: Ngozumpa, Khumbu, Changri Nup, and Imja glaciers in the Sagarmatha National Park and Langtang and Lirung glaciers in the Langtang National Park (Figure 3.1). These glaciers (Figure 1, Table 3.1) vary in size ($2km^2$ to $70km^2$), debris cover extent and thickness (from partial to fully debris-covered), and geometry (zero to multiple tributaries), allowing us to test our methods and analyze results for a representative sample of debris-covered glaciers in the region. We validate our results using previously determined ice cliff distribution, flux divergence, sub-debris melt rates, and ice cliff melt contribution determined from independent datasets and methods.

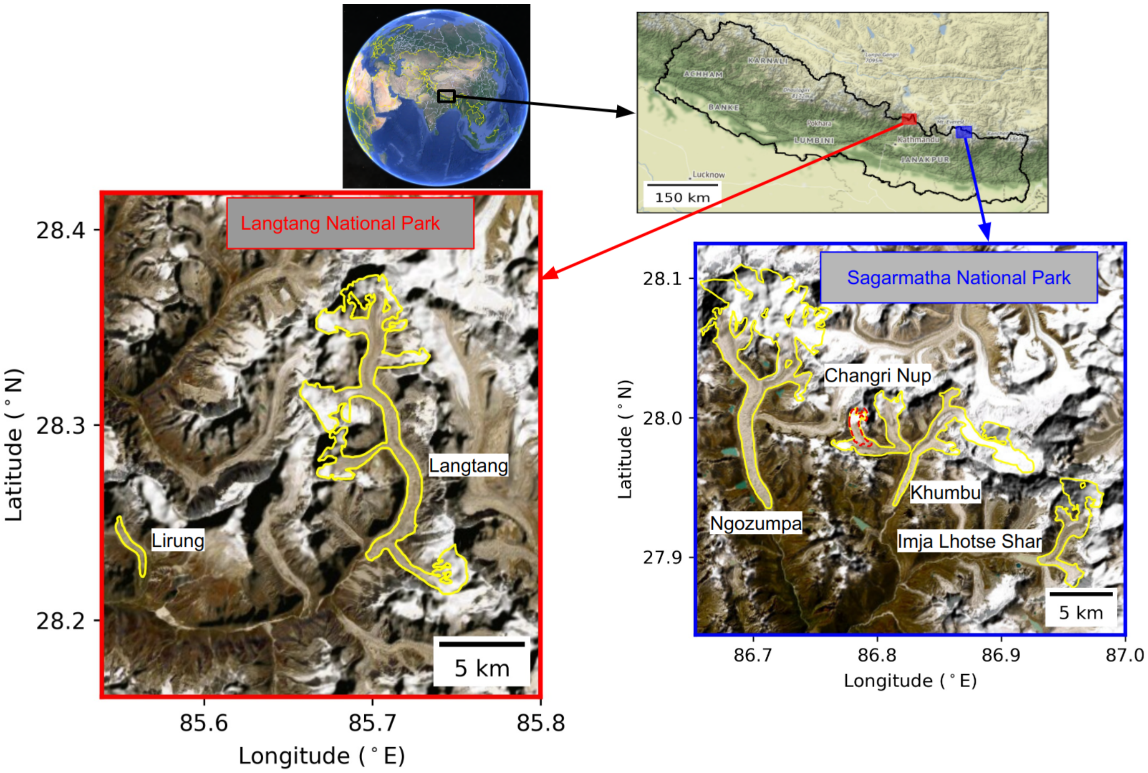

Figure 3.1: Study area location in Nepal. Globe imagery from Google Earth. Panels show the ESRI World Imagery satellite basemap for Langtang National Park and Sagarmatha National Park with the six study glaciers as represented in RGI v6.0 outlined in yellow. Note that from the Changri Nup Glacier complex, we only consider Black Changri Nup Glacier (outlined in dashed red line) in this study.

Table 3.2: List of Maxar stereo images used in this study

Date of acquisition	Sensor	Catalog ID1	Catalog ID2	Finest PAN resolution (m)	Glaciers
20121223	GE01	1050410000E8C900	1050410000E0AE00	0.42	Ngozumpa
20150115	WV03	1040010006A12900	104001000665F400	0.31	Ngozumpa
20150122	WV03	1040010006841E00	10400100060FE200	0.35	Lirung
20150222	WV03	1040010008B92D00	10400100087E2400	0.32	Langtang
20150508	WV03	104001000BA62E00	104001000B3B2300	0.37	Lirung
20151002	WV01	10200100457F0C00	1020010042C0CE00	0.51	Imja Lhotse Shar
20151102	WV03	10400100130D8500	10400100125E8E00	0.35	Black Changri Nup, Khumbu
20151229	WV01	1020010046506C00	10200100496BE700	0.54	Lirung
20160107	WV02	103001004F89CB00	103001004E783B00	0.55	Langtang
20160422	WV02	103001005401B300	103001005444C600	0.50	Black Changri Nup
20161025	WV03	1040010024438E00	104001002469AD00	0.34	Black Changri Nup, Khumbu
20161029	WV02	103001005E3EFF00	103001005E3A0D00	0.53	Imja Lhotse Shar
20161106	WV02	103001005F7EBB00	103001005FAB7A00	0.52	Lirung
20171222	WV01	102001006F214E00	10200100688AC000	0.53	Lirung

3.4 Data

3.4.1 Very-high-resolution optical Stereo Imagery

We obtained cloud-free archived Level-1B Maxar WorldView-1/2/3 and GeoEye-1 panchromatic stereo imagery through the NGA NextView/Enhanced View License (Table 3.2). The in-track stereo imagery were collected between December 2012 to December 2017 over the six glaciers of interest.

3.4.2 Ice thickness estimates

Accurate, distributed ice thickness estimates are needed to compute temporal flux divergence and Lagrangian elevation change measurements. Ideally, one should use distributed ice thickness measurements derived from in situ measurements [e.g., Ice Penetrating Radar (IPR)] for best results (e.g., Van Tricht et al., 2021b). However, such measurements are sparse and limited to only a few points on certain glaciers in High Mountain Asia (e.g., Pritchard et al., 2020). For these reasons, we used modeled global ice thickness estimates. Our primary source for ice thickness estimates was prepared by Farinotti et al. (2019a), which is an ensemble product derived by considering five different approaches based on Glen's flow law and the shallow ice approximation. These approaches derive ice thickness by either inverting the surface mass balance gradient to match the volumetric change in flux (e.g., Huss and Farinotti, 2012; Maussion et al., 2019), or by using the relationship between observed surface slope and characteristic basal shear stress (e.g., Frey et al., 2014; Fürst et al., 2017; Ramsankaran et al., 2018). While these estimates are known to have bias, several previous studies have shown that they can still provide reasonable estimates of flux divergence or flux divergence gradients (e.g., Miles et al., 2021; Mishra et al., 2022; Pelto et al., 2021; Steiner et al., 2021).

3.4.3 Debris-cover extent and thickness

We utilized global, distributed debris thickness products from (Rounce et al., 2021) to examine the effect of debris thickness on ice melt. The debris thickness products were derived using thermal remote sensing observations from Landsat-8 and a combination of sub-debris melt and surface temperature inversion models for glacier areas identified as debris-covered by Scherler et al. (2018). The debris thickness maps were also used to determine debris cover extent in the ablation area.

3.5 Theory

3.5.1 Glacier surface elevation change using continuity principles

Assuming a constant vertical density profile, constant bed elevation, and negligible englacial and basal melt, the Eulerian surface elevation change rate over a glacier can be expressed using the relation (Equation 8.77 in Cuffey and Paterson, 2010):

$$\frac{\partial h}{\partial t} = \frac{\dot{b_s}}{\rho} - \nabla \cdot (H\overline{\boldsymbol{u}}) \tag{3.1}$$

where h is the surface elevation, $\dot{b_s}$ is the specific surface mass balance rate, which is equal to the mass per unit area added by accumulation or removed by ablation (Cuffey and Paterson, 2010), ρ is the density of material (ice, snow or firn) added or subtracted due to surface mass balance, H is the ice thickness and $\overline{\boldsymbol{u}}$ is the column average velocity. The term $\nabla \cdot (H\overline{\boldsymbol{u}})$ represents the ice flux divergence, which accounts for elevation change due to ice flow. Flux divergence is negative for compressional flow, resulting in surface thickening or emergence. Negative flux divergence is expected to occur over majority of ablation area; or locally around downstream to regions of peak velocity in icefalls, or when bed bumps larger than local ice thickness are encountered. Flux divergence is positive for extensional flow, resulting in surface thinning or submergence. Positive flux divergence is expected to occur in the accumulation area; or locally around upper reaches of icefalls, or when ice stretches over bumps in bedrock which are larger than local ice thickness.

Surface elevation change rate ($\frac{\partial h}{\partial t}$) and surface velocity ($\boldsymbol{u_s}$) can be obtained from remote sensing data. The column-averaged velocity can be estimated from the surface velocity observations using the equation:

$$\overline{\boldsymbol{u}} = f\boldsymbol{u_s} \tag{3.2}$$

where the coefficient f is the ratio of column-averaged velocity to horizontal surface velocity. For glaciers with negligible basal sliding, f is often assumed to be 0.8 (e.g., Nuimura et al., 2011; Rounce et al., 2018; Vincent et al., 2016).

Substituting equations 3.2 into equation 3.1 and rearranging, we obtain an equation for surface mass balance as a function of observed surface elevation change rate, observed surface velocity and estimated ice thickness:

$$\frac{\dot{b_s}}{\rho} = \frac{\partial h}{\partial t} + f\nabla\cdot(H\boldsymbol{u_s}) \tag{3.3}$$

Eulerian surface elevation change rate ($\frac{\partial h}{\partial t}$) includes signals due to advection of small-scale surface roughness (e.g., rocks, ice cliffs, crevasses), superimposed over long-wavelength signals due to SMB or ice flux. These signals manifest as alternating positive and negative elevation change measurements depending on displacement distance and feature orientation and dimensions. To minimize these apparent elevation change signals, we calculate surface elevation change in a Lagrangian frame of reference ($\frac{Dh}{Dt}$) moving with individual surface features using displacements from surface velocity observations. The Lagrangian surface elevation change rate ($\frac{Dh}{Dt}$) is related to the Eulerian surface elevation change rate ($\frac{\partial h}{\partial t}$) by the material derivative equation:

$$\frac{Dh}{Dt} = \frac{\partial h}{\partial t} + \boldsymbol{u_s}\nabla h \tag{3.4}$$

The term $\boldsymbol{u_s}\nabla h$ in Equation 3.4 accounts for the expected slope-parallel elevation change – the elevation decrease of a surface particle relative to the vertical datum as it moves downslope, independent of surface thinning or thickening due to surface mass balance.

Rearranging Equation 3.4) and substituting into Equation 3.3, we obtain an equation for surface mass balance as a function of the Lagrangian elevation change rate:

$$\frac{\dot{b_s}}{\rho} = \frac{Dh}{Dt} - \boldsymbol{u_s}\nabla h + f\nabla\cdot(H\boldsymbol{u_s}) \tag{3.5}$$

which we use to determine the Lagrangian SMB rates ($\frac{\dot{b_s}}{\rho}$) in units of m/yr. The material density (ρ) can assumed to be constant and equal to ice density over the ablation areas. Therefore, our Lagrangian SMB rates when used to examine the control of surface features on debris-covered ice ablation can be interpreted in meters of ice equivalent (m i.e./yr). For our second objective, we use Lagrangian SMB measurements over the entire glacier to assess the patterns and timings of seasonal accumulation and ablation. In this case, the material density will be spatially variable over the accumulation area depending on snow and firn presence. We also do not account for firn compaction rates over the accumulation area in Equation 3.5 (e.g., Pelto et al., 2021; Zeller et al., 2022) due to paucity of field derived measurements. As a result, interpreting the Lagrangian SMB rates over the accumulation area in snow or water equivalent units is not straightforward. We discuss the potential impacts of unaccounted snow/firn densities and compaction rates in our estimates later in the limitations section **??**.

Through the rest of the manuscript, we refer the terms $\frac{\partial h}{\partial t}$, $\frac{Dh}{Dt} - \boldsymbol{u_s}\nabla h$ and $\frac{\dot{b_s}}{\rho}$ as Eulerian elevation change rate (dh/dt), slope-corrected Lagrangian elevation change rate (Dh/Dt) and Lagrangian SMB rate, respectively. All these values are reported in units of m/yr, unless otherwise noted.

3.6 Previous Work

Several recent studies used remote sensing observations to isolate mountain glacier elevation change due to surface mass balance over seasonal to decadal time periods (Table 3.3). In most cases, elevation and velocity observations from remote sensing measurements were combined with ice thickness estimates from models or field measurements using the continuity equation (e.g., Berthier and Vincent, 2012; Cuffey and Paterson, 2010) to isolate SMB (Table 3.3).

These studies show that the centimeter-scale accuracy and sub-meter-scale resolution of DEMs derived from Unoccupied Aerial Vehicle (UAV) Structure-from-Motion (SfM) and Airborne Laser Scanning (ALS) can be used to provide high-resolution seasonal and annual SMB measurements. Though DEMs derived from very-high resolution (VHR) satellite stereo imagery acquired by commercial satellite constellations cannot match this accuracy and resolution, the much greater spatial coverage and large archives offer the potential to scale these methods for remote and inaccessible regions. To our knowledge, with the exception of Brun et al. (2018), satellite DEMs have not been used to study seasonal mass balance of large debris-covered glaciers in HMA.

3.7 Methods

To assess the influence of surface debris features on ice ablation (Objective 1, Section 3.2.1), we estimated Lagrangian SMB rates using DEM pairs with temporal baselines of approximately one year or integer multiples of a year to ensure we covered at least one full summer and winter season completely, depending on stereo data availability (Table 3.2). Stereo data for Ngozumpa Glacier had the longest temporal baseline (2.08 years),

Table 3.3: Summary of recent work involving glacier surface mass balance estimates from remote sensing observations. Velocity is derived from feature tracking of orthoimages/hillshades for the source listed.

Study	Study Site(s)	Elev. source	Vel. source	Ice thickness source	Obs. period
Brun et al. (2018)	Black Changri Nup, Nepal	UAV, Pleiades-HR	UAV	IPR transects[a]	Annual
Mishra et al. (2022)	Annapurna III, Nepal	UAV	UAV	Consensus estimates[b]	Seasonal
Pelto et al. (2019)[c]	5 glaciers, B.C., Canada	ALS	–	–	Seasonal
Anderson et al. (2021)	Kennicott Glacier, AK, USA	USGS[d], Maxar	Landsat	Self[e]	Decadal
Bisset et al. (2020)	28 glaciers in HMA	ASTER	ITS_LIVE	Consensus estimates	Decadal
Miles et al. (2021)	5527 glaciers in HMA	ASTER	ITS_LIVE	Consensus estimates	Decadal
Pelto and Menounos (2021)	5 glaciers, B.C., Canada	ALS	ALS, Planet	Multiple[f]	Interannual
Van Tricht et al. (2021b)	2 glaciers, Swiss Alps	UAV	UAV	Multiple[g]	Interannaul

---

[a] Vincent et al. (2016)

[b] Farinotti et al. (2019a)

[c] Seasonal glacier-wide mass balance only

[d] DEM derived by digitization of 1957 topographical map by Das et al. (2014)

[e] Estimated from DEM slope and surface velocity using Shallow Ice Approximation

[f] Combination of Consensus estimates and OGGM(Maussion et al., 2019) model output, calibrated using ice-penetrating radar transects (Pelto et al., 2020)

[g] Interpolated from ice-penetrating radar transects(Langhammer et al., 2019; Zekollari et al., 2013)

while the data for Langtang Glacier had the shortest (0.83 years). For assessing patterns of seasonal accumulation and ablation (Objective 2, Section 3.2.1), we computed elevation change estimates from DEM pairs with smaller temporal baselines over Black Changri Nup Glacier (20151102, 20160422, 20161025) and Lirung Glacier (20150122, 20150508, 20151229) (Table 3.2). In this section, we outline our data processing and analysis workflow.

3.7.1 DEM Generation

We used stereo photogrammetry techniques implemented in the NASA Ames Stereo Pipeline v3.0.1-alpha (Build date: 2022-04-16) (Beyer et al., 2018; Shean et al., 2016) to obtain DEMs from Maxar WorldView-1/2/3, GeoEye-1 stereo imagery (Table 1). Before pairwise stereo reconstruction, input stereo images were orthorectified to a common resolution and extent using the 8-m HiMAT DEM composite (Shean et al., 2020). We used the dem-blur option of the ASP dem_mosaic utility to reduce data gaps and artifacts in this DEM composite. We used the high-quality stereo processing settings outlined in (Bhushan and Shean, 2021; Shugar et al., 2021). The DEMs were posted at 2 m resolution in the UTM45N projection, with heights relative to the WGS84 ellipsoid. We then performed relative alignment between DEMs for all pairwise combinations. The alignment was performed using the Iterative Closest Point (ICP) point-to-plane co-registration procedure (Pomerleau et al., 2013) implemented in ASP over non-glacierized (Pfeffer et al., 2014; RGI Consortium, 2017a), static surfaces.

3.7.2 Surface velocity generation

We computed surface velocity for each glacier during each study period by tracking moving features on corresponding pairs of 2m shaded relief maps. Unlike the input imagery, shaded relief maps are immune to variable surface snow cover and illumination conditions (e.g., Rounce et al., 2018; Van Tricht et al., 2021b). Our choice of using shaded relief maps also makes our workflow adaptable to other openly distributed DEM products (e.g., REMA, ArcticDEM, EarthDEM) where corresponding proprietary orthoimages are unavailable.

We first derived shaded relief maps from the co-registered DEM products using the gdaldem hillshade utility and the combined illumination algorithm. Pairs of shaded relief maps were then processed using the script disp_mgm_corr.py. The script employs ASP's parallel_stereo program in the 'correlator-mode'. Dense image correlation was performed using a 9 x 9 More Global Matching (MGM) correlation kernel (Facciolo et al., 2015), and subpixel refinement was performed using a 15 x 15 SGM_poly4 kernel. The obtained pixel-wide disparities were then filtered using ASP's texture smoothing option, which included a two-stage procedure: a 41 x 41 px kernel median filter followed by a moving average texture smoothing filter of maximum kernel size 25 px and scale 0.50. Our texture smoothing operation was crucial to suppress noise stemming from DEM errors (Kraaijenbrink et al., 2016a) and remove signals due to ice cliff backwasting (Rounce et al., 2018) and large changes in surface morphology (i.e., ice cliffs and surface ponds), which are unrelated to glacier flow. Disparity measurements were then converted to surface velocity by considering the temporal baseline and input shaded relief map's resolution. Data gaps in the velocity maps were filled with a 51 px Gaussian filling operation (filtlib.py/gaussfill), and patches of discontinuous velocities around regions with large gaps were manually discarded. For the very slow flowing Lirung Glacier, we found that our default texture smoothing option was too aggressive, and instead used a reduced size 15 x 15 px median filter kernel.

3.7.3 Accounting for glacier flow

For all temporal intervals involving two DEMs, we displaced elevation pixels in the second DEM to their expected initial position in the first DEM grid using corresponding contemporaneous surface displacement maps (Section 3.7.2) (e.g., Shean et al., 2019b; Van Tricht et al., 2021b). We subtracted the first DEM from the modified second DEM to measure Lagrangian elevation change rates ($\frac{Dh}{Dt}$), which are free from signals due to advection of rough surface features. We produced an additional modified DEM by displacing elevation pixels from the first DEM to their expected horizontal positions at the second timestamp as per the surface displacement maps. We subtracted this modified first DEM from the original first DEM to obtain expected slope-parallel elevation change ($\boldsymbol{u_s}(\nabla h)$), assuming the glacier surface to be in steady state during the period of investigation.

We computed ice flux as the product of two dimensional, column-averaged ice velocity and ice thickness. Flux divergence ($f\nabla\cdot(H\boldsymbol{u_s})$) was derived by computing pixel wise gradients of ice flux in a fixed grid.

3.7.4 Length scale consideration

Ice flow is primarily governed by surface slope and longitudinal driving stresses calculated over length scales that are proportional to several times (k) the local ice thickness (e.g., Alley et al., 2018; Cuffey and Paterson, 2010; Kamb and Echelmeyer, 1986). Therefore, when computing the flux divergence and expected slope-parallel elevation change, it is crucial to consider comparable large length scales rather than performing calculations at the input DEM/velocity map resolution, which also capture variations due to rough local surface and bed geometries. The value of the proportionality factor (k) depends on ice viscosity, ice thickness and local shape factor (Equation 8.99 in Cuffey and Paterson, 2010). For mountain glaciers, previous studies have used k = [2,8] (Armstrong et al., 2022; Dehecq et al., 2019; Van Tricht et al., 2021b; Van Wyk de Vries et al., 2022b) to average longitudinal

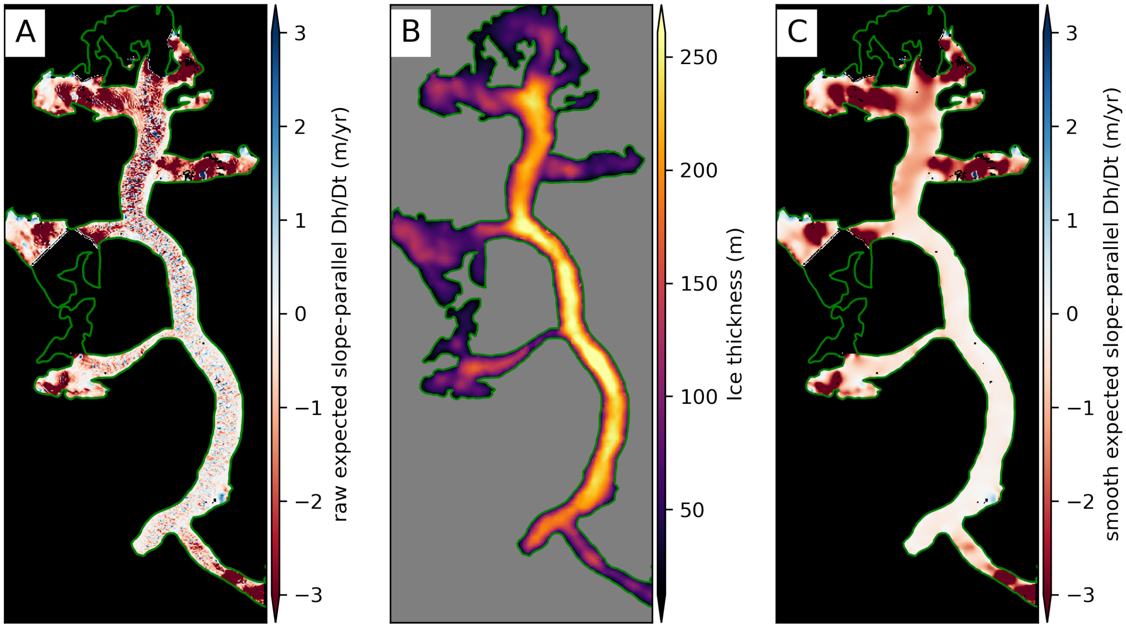

Figure 3.2: Example of locally adaptive Gaussian filter over Langtang Glacier. A) Initial expected slope-parallel change map, B) ice thickness map which is used to determine size of spatially varying Gaussian filter and C) smooth expected slope-parallel change map after application of adaptive Gaussian filtering. Green outline represents RGI v6.0 glacier extent. Note the removal of aliasing artifact caused due to rough local slope after the filtering is applied.

stress or flux divergence measurements. In this study, we used a Gaussian filter with kernel sizes equal to (k=5) times local ice thickness to smooth our flux divergence and expected slope-parallel elevation change estimates. This choice provided a good compromise between reducing anomalies in the measurements and preserving the underlying long wavelength signal.

We developed an adaptive filtering technique that incorporates spatially variable kernel sizes, which are determined based on a second raster with local ice thickness values. To improve the computational efficiency of our approach, we first divide the input glacier's ice thickness distribution into discrete classes (n=20) using the equal interval scheme. For each of these classes, we generated a spatial mask containing the indices of the raster pixels falling within that class and set the corresponding Gaussian filter kernel size (k) to five times the median ice thickness in that class. We then extracted pixels from gradient rasters (e.g., flux divergence and expected slope-parallel change) using these masks, as well as additional pixels sampled from either side around a buffer region determined by the filter's kernel size for that class. Next, we applied a moving window Gaussian filter to each of the 20 sets of sampled pixels with the appropriate kernel sizes. Finally, we stored the smoothed results from each of the 20 sets of masks in a single two-dimensional array, providing us with continuous estimates of the gradient measurements. This discretization simplification is based on the assumption that ice thickness values do not change very abruptly and filter sizes required for gradient pixels would not vary considerably on pixel to pixel basis. We refer the reader to the functions (**thickness_division** and **adaptive_gaussian_smooth_alt**) in the code **glac_dyn.py** for more details on the implementation. Figure 3.2 provides a working example of the proposed filter used to derive smooth expected slope-parallel elevation change.

3.7.5 Ice cliff delineation

Several methods have been proposed to map ice cliffs in recent years with varying degrees of success. These methods can be divided into two main categories, which either use optical image spectral characteristics (e.g., Anderson et al., 2021; Kneib et al., 2021; Kraaijenbrink et al., 2016b; Steiner et al., 2019) or surface slope and roughness values from a high-resolution DEM (e.g., Brook et al., 2013; Herreid and Pellicciotti, 2018; King et al., 2020). Methods using spectral characteristics of optical satellite imagery are limited by emission and illumination angles, as near nadir imagery presents challenges for steep cliffs. Optical image-based techniques can also fail to map ice cliffs covered by a very thin layer of debris. These features act as ice cliffs, melting at comparable or even higher rates, but would be considered debris-covered ice in image data. Techniques based on DEM slope and surface roughness struggle to differentiate ice cliffs from moraines or steep debris cones. Additionally, satellite stereo DEMs fail to reconstruct steep ice cliff faces which are oriented away from satellite view.

We used a semi-automated approach to map "ablating" ice cliffs involving a combination of local slope derived from DEM measurements at both time periods and slope-corrected Lagrangian Dh/Dt. This method takes advantage of the fact that ice cliffs are steep surfaces and melt at higher rates than their surroundings, and segments areas of active melt. Specifically, we identified features with slopes greater than 10° in both input DEMs. We then preserved features with elevation change rates less than $-2m$ and removed small features with less than 15 connected pixels. Finally, there were some misclassifications of features present on steep adjoining moraines, which we removed by manual inspection with orthoimagery for context in QGIS.

3.7.6 Lagrangian SMB rate

Lagrangian SMB rate was calculated using equation 3.5 by substituting values of slope-corrected Lagrangian elevation change rate ($\frac{Dh}{Dt} - \boldsymbol{u_s} \cdot (\nabla h)$, Section 3.7.3), and flux divergence ($f \cdot \nabla (H \cdot \boldsymbol{u_s})$, Section 3.7.3). The Lagrangian SMB rate map was partitioned over debris-covered and clean ice regions using the extents from debris thickness data. Ablation rates over ice cliffs were computed from the Lagrangian SMB rate map using the delineated ice cliff mask (Section 3.7.5). We aggregated the following values in 50 m elevation bins on each glacier: median Lagrangian SMB rate, median Lagrangian SMB rate over debris-covered regions (M_{debris}), median Lagrangian SMB rate over ablating ice cliffs ($M_{\text{ice cliff}}$), area occupied by ablating ice cliffs ($A_{\text{ice cliff}}$), area occupied by debris-covered ice (A_{debris}), and quantile measures of debris thickness. We also computed a ice cliff melt enhancement factor M_f for each bin as:

$$M_f = \frac{M_{\text{ice cliff}}}{M_{\text{debris}}} \tag{3.6}$$

For each bin with median negative Lagrangian SMB rate (abllation), we computed the combined debris area melt rate M_{total}:

$$M_{\text{total}} = \frac{A_{\text{ice cliff}} * M_{\text{ice cliff}} + A_{\text{debris}} * M_{\text{debris}}}{A_{\text{ice cliff}} + A_{\text{debris}}} \tag{3.7}$$

and the percent contribution of ice cliffs M_{total}

$$\text{Ice cliff melt\%} = \frac{M_{\text{total}} - M_{\text{debris}}}{M_{\text{total}}} * 100 \tag{3.8}$$

where $M_{\text{ice cliff}}$ and M_{debris} denote the median ablation rate over melting ice cliffs and debris-covered ice in each bin, respectively.

3.8 Results

3.8.1 Surface velocity and Flux Divergence

Our velocity measurements are able to resolve detailed spatial velocity variations over the study glaciers (Figure 3.3, 3.4). In general, the glaciers have maximum surface velocity over steep icefalls. Velocity is less than 5 m/yr over the lower debris-covered ablation areas for all glaciers except the Lhotse Shar Glacier, which terminates in Imja Lake. Residual data gaps occur over accumulation areas and some areas of fast flow due to loss of coherence in the shaded relief maps over longer timescale, or due to lack of texture in input shaded relief maps over snow-covered areas.

All glaciers have negative flux divergence (positive emergence velocity) over the majority

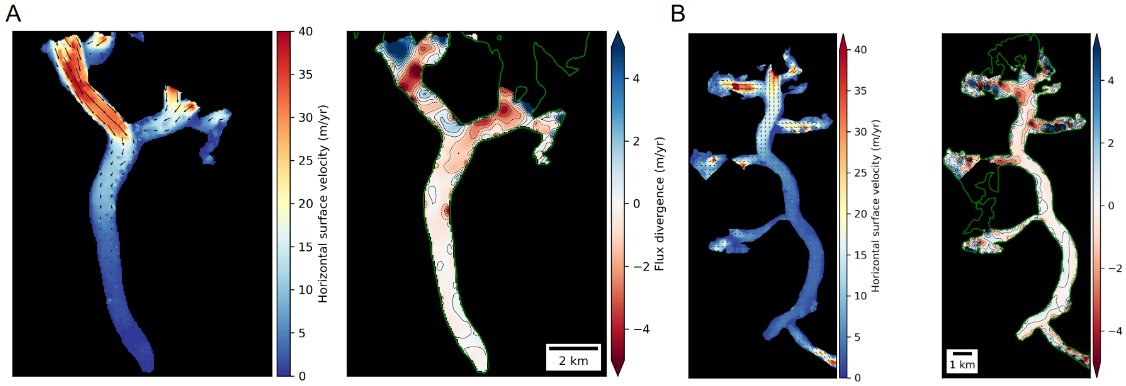

Figure 3.3: Annual surface velocity and flux divergence maps for A) Ngozumpa Glacier and B) Langtang Glacier. Green polygons in the flux divergence maps show RGI glacier extent. Negative flux divergence (red) denotes positive emergence, while positive flux divergence (blue) denotes submergence.

of their debris-covered ablation zones. Some local areas of positive flux divergence are observed near areas of complex glacier geometries, such as tributary confluence zones or along margins where flow direction changes abruptly (Figure 3.3, 3.4). Zones of maximum emergence velocities are not coincident with areas of fastest glacier flow; rather maximum emergence velocities are observed a few kilometers downstream from the areas of most rapid horizontal glacier flow. All glaciers except Lhotse Shar have near zero flux divergence over their lower debris-covered ablation areas, indicating that emergence is limited over near-stagnant areas.

3.8.2 Surface mass balance maps

Figure 3.5 show Eulerian and Lagrangian elevation change products after correction for flux divergence for Imja Lhotse Shar Glacier. Advection of rough surface features introduces aliasing artifacts in the Eulerian dh/dt map (Figure 3.5A,B,C), but not in the slope-corrected Lagrangian Dh/Dt map (Figure 3.5E). The slope-corrected Lagrangian Dh/Dt map resolve local melt signals over steep ice cliffs in the debris-covered ablation area. Additionally, the Lagrangian SMB rate map shows enhanced melt signals over the northwestern tributary and near the calving front (Figure 3.5F), which were compensated by negative flux divergence (3.4C) and thus not apparent in the Eulerian dh/dt map (Figure 3.5C). Near the base of the icefall in the eastern tributary, we observe positive Lagrangian SMB rates indicating surface accumulation (Figure 3.5F), which again, is not apparent in the Eulerian dh/dt map (Figure 3.5 C). Isolated positive Lagrangian SMB rates are observed over melt ponds and

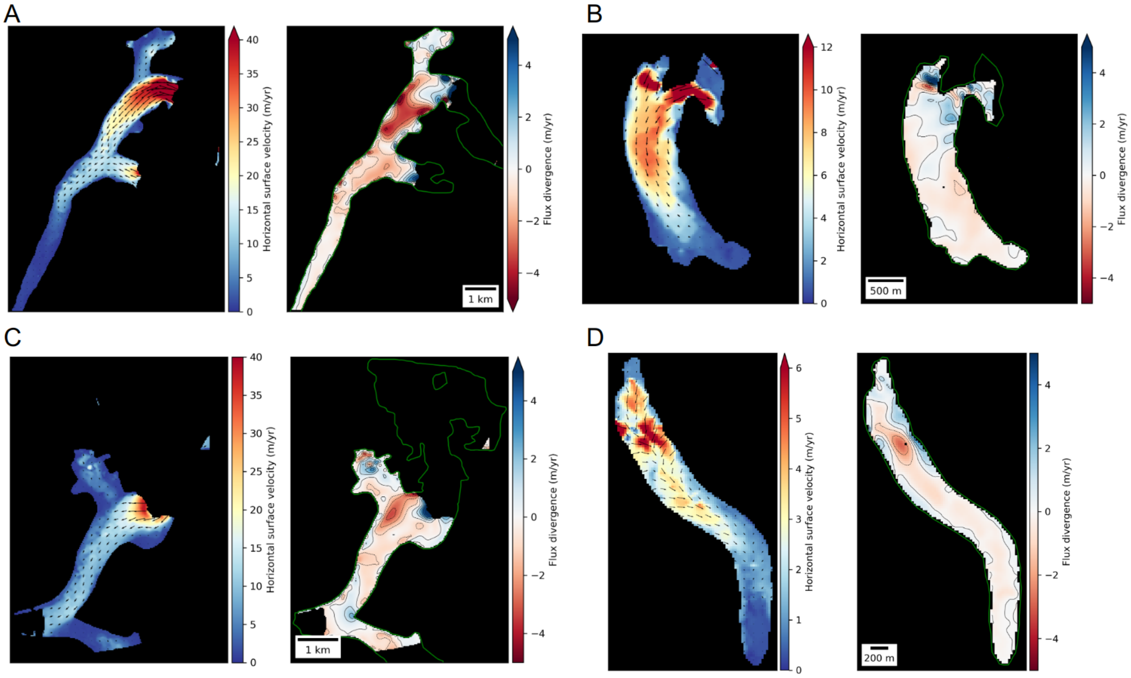

Figure 3.4: Annual surface velocity and flux divergence maps for A) Khumbu, B) Black Changri Nup, C) Imja and D) Lirung Glacier. Green polygons in the flux divergence maps show glacier extent. Negative flux divergence (red) denotes positive emergence, while positive flux divergence (blue) denotes submergence. Note the difference in the velocity color scale to bring out spatial variations in flow for slow moving glaciers.

the confluence of Lhotse Shar and Imja Glacier.

The Lagrangian observation framework produces less of a difference over Black Changri Nup (Figure B.2) and Lirung Glaciers (Figure B.4), where the surface velocities are lower (Figure 3.4 B,D). For Khumbu, Ngozumpa, Langtang and Lirung Glaciers, Lagrangian SMB rates are less negative over the stagnant debris covered tongues, resulting in the ice cliffs standing out with clearly more negative Lagrangian SMB rates (Figure B.3, B.1, B.4, B.5). More negative SMB rates are observed farther upstream, with local melt rates exceeding 4 m/yr over areas consisting of both clean and debris-covered ice (Figure B.3,B.1,B.5. However, for Black Changri Nup Glacier, the SMB rates are consistently more negative (-1 to -2 m/yr) over the majority of the debris-covered tongue (Figure B.2). At Lirung Glacier, very high ablation rates (3 to ¿20 m/yr) are observed over the large ice cliff 1 km from its snout, with limited melt further south (Figure B.4).

3.8.3 Surface mass balance profiles

To investigate how elevation and debris thickness affect surface mass balance (SMB), we examined the Lagrangian SMB profile in relation to glacier hypsometry and debris thickness across the glaciers of interest. We begin by presenting the results for Lirung Glacier, which lacks any branches and is entirely debris-covered (Figure 3.6A). Our observations show that Lagrangian SMB rates become more negative at higher elevations, with the most negative Lagrangian SMB rate occurring approximately 300 m above the terminus (Figure 3.6B). Concurrently, we also note a decrease in median debris thickness, dropping from around 60 cm at the terminus to roughly 20 cm at the area of maximum melt on a per-bin basis.

We observe a similar pattern of more negative Lagrangian SMB rates at higher elevations from the terminus for the rest of the studied glaciers, though with differences in profile slopes (Figure B.6). For Langtang and Ngozumpa Glacier (Figure B.6 B,C), there is limited variability in the SMB profiles till 400 m and 200 m above the terminus, respectively, but a clear increase towards more negative values after that. Over the ablation bins for Black Changri Nup and Imja Lhotse Shar Glaciers, the SMB profile amplitude is smaller (Figure B.6 D,F). Over Khumbu Glacier, we observe a clear trend towards more negative Lagrangian SMB values from the lowest survey bin (Figure B.6 E), but we note that our measurements did not cover the last 300 m length of the Khumbu Glacier. Similar to Lirung Glacier, debris is generally thicker at lower elevations and thinner at higher elevations (Figure:**??**), but with local variations (e.g., Langtang, Ngozumpa, Khumbu and Imja Lhotse Shar Glaciers).

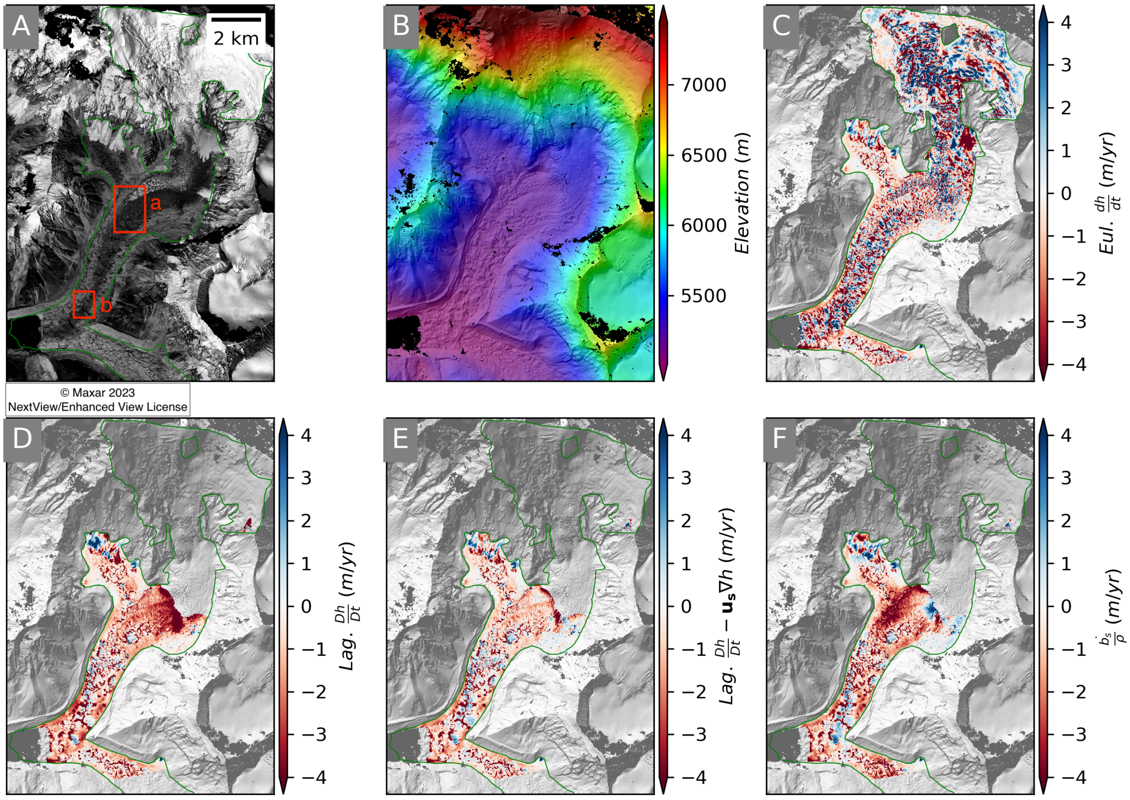

Figure 3.5: Surface elevation change products over Imja Lhotse Shar Glacier for the period October 02, 2015 to October 29, 2016: A) Panchromatic WV01 orthoimage from October 02, 2015, B) Color shaded relief map, C) Eulerian elevation change rate ($\frac{dh}{dt}$), D) Lagrangian elevation change rate ($\frac{Dh}{Dt}$), E) slope-corrected Lagrangian elevation change rate ($\frac{Dh}{Dt} - \mathbf{u_s}\nabla h$), and F) Lagrangian SMB rate ($\frac{\dot{b}_s}{\rho}$) obtained by adding flux divergence to (E). Surface changes and Lagrangian SMB rates over red panels (a) and (b) in the orthoimage (A) are shown in detail in Figure 3.10 A,B). Note the reduction in signal aliasing for products in Lagrangian frame of reference (D, E, F) and enhancement of SMB signal where flux divergence is high (F).

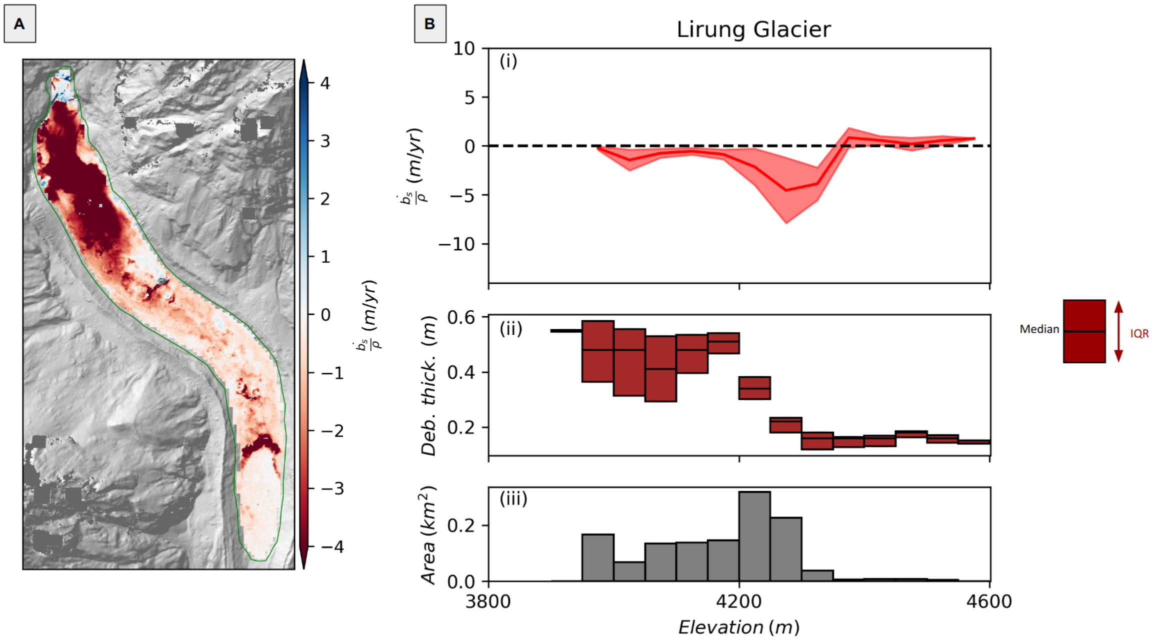

Figure 3.6: Annual Lagrangian SMB products over Lirung Glacier for the period November 06, 2016 to December 22, 2017: A) Lagrangian SMB rate, B) median SMB and debris thickness aggregated over 50 m elevation bins. Shaded area around the Lagrangian SMB rate curve represents NMAD range for that elevation bin, while limits of box plot for debris thickness represents bin's interquartile debris thickness range. Note less negative Lagrangian SMB rates observed at lower elevations, where debris is thicker.

Table 3.4: Consolidated contribution by ice cliffs to debris-covered area ablation.

Glacier	Ice cliff area%	Ice cliff contribution to debris-covered area ablation%
Langtang	6.9	24.1
Lirung	3.6	16.9
Ngozumpa	9.8	35.1
Black Changri Nup	6.0	28.6
Khumbu	11.5	39.6
Imja Lhotse Shar	9.5	42.5

3.8.4 Contribution of ice-cliff to surface melting of debris-covered glaciers

Ice cliff SMB rates are considerably more negative than surrounding debris-covered ice. Quantitatively, we observe melt enhancement factors (M_f) of 2 to 25x over ice cliffs (Figure 3.7C). One 50 m bin over Langtang Glacier and two bins over Khumbu Glacier show enhancement factors greater than 50, as the observed Lagrangian SMB rates over debris-covered ice is very close to -0 m/yr. Corresponding bin-wise melt contribution range from as low as $\leq 5\%$ to $\geq 50\%$ for the different glaciers (Figure 3.7D). Generally, both the ice cliff melt enhancement and percentage contribution to total debris ablation decreases with increase in elevation (Figure 3.7C,D). Our results indicate that the melt contribution of ice cliffs to the total bin wise debris melt is driven jointly by the bin debris thickness and ice cliff area percentage of the bin (Figure 3.7).

Aggregated over the entire debris-covered ablation area of each glacier, the melting ice cliffs account for 16.9 to 42.5% of the total debris-covered area ablation rates, even though they only occupy 3.6 to 11.5% of the total debris-covered area (Table 3.4).

3.8.5 Seasonality in surface mass balance

Lagrangian surface elevation change maps over Black Changri Nup Glacier show striking seasonal accumulation and ablation patterns (Figure 3.8). During the winter period (November 2015 to April 2016), with the exception of prominent negative signals over ice cliffs, we observe near-zero Lagrangian SMB over most of the debris-covered tongue (Figure 3.8B). In the summer period (April 2016 to October 2016), the majority of the debris-covered tongue registers negative Lagrangian SMB, with notably high melt over ice cliffs. This pattern of ablation is similar to what is observed or expected for typical mountain glaciers. At elevations higher than 5500 m, we observe limited positive Lagrangian SMB during the winters (Figure 3.8B), with a clearly negative Lagrangian SMB profile (Figure 3.8 C). This observation is supported and corroborated by the end of winter orthoimagery where we

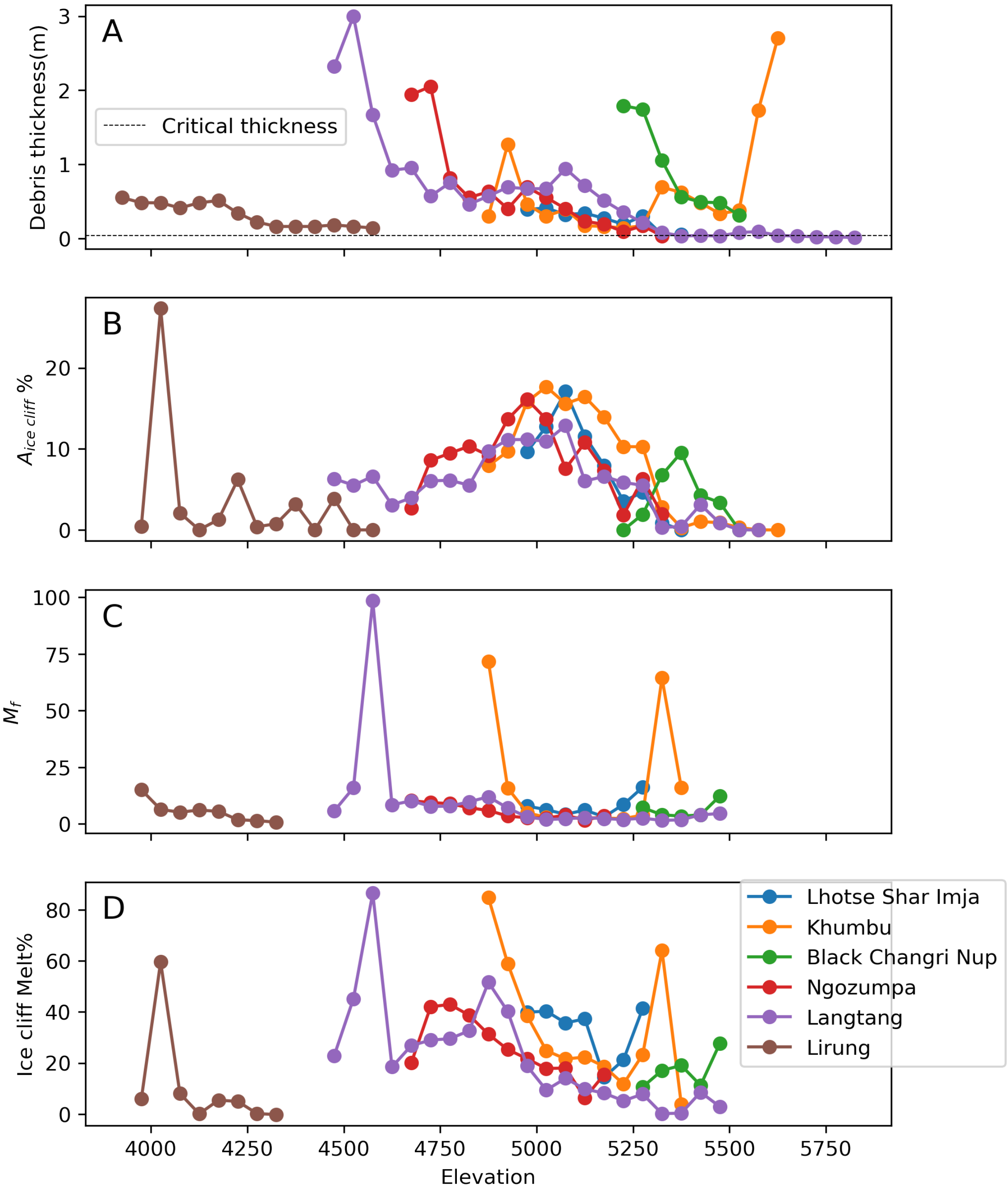

Figure 3.7: Summary of ice cliff melt contribution statistics aggregated over 50 m elevation bins for the six debris-covered glaciers in the study. A) Median debris thickness, B) Percent area occupied by ice cliffs ($A_{\text{ice cliff}}$%), C) ice cliff melt enhancement factor (M_f) and D) Ice cliff melt%. The dashed line in (A) denotes the theoretical, critical thickness above which ice melt is insulation by debris. While variability exists, note the increased M_f and increased M_f and ice cliff melt% for bins with thick debris and higher ice cliff area%.

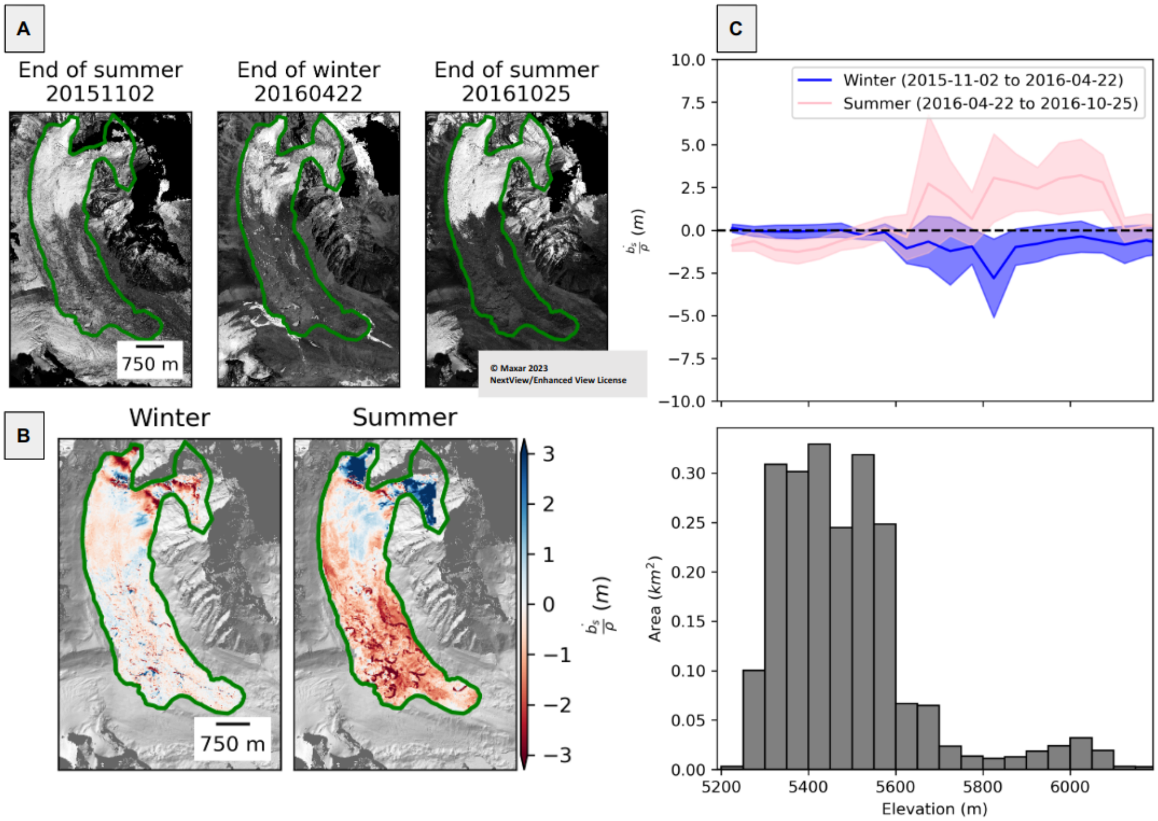

Figure 3.8: Seasonal orthoimage and Lagrangian surface elevation change products for Black Changri Nup Glacier. A) Panchromatic Maxar WV-02/03 orthoimagery acquired at end of summer (November 2, 2015), end of winter (April 22, 2016), and end of the following summer (October 25, 2016). B) Lagrangian SMB (m) for the winter period (20151102 to 20160422) and the summer period (20160422 to 20161025). C) Median Lagrangian SMB (m) in 50 m elevation bins during summer (pink) and winter (blue). The shaded area represents the NMAD spread in SMB values in each bin. Bar plot showing glacier hypsometry calculated from end of summer (November 2, 2015) DEM. Green outlines show glacier extent as used in (Brun et al., 2018; Vincent et al., 2016). Notice the reduction in snow cover extent at the end of the winter period and an increase in snow cover extent at the end of the summer 2016 in the accumulation zone (A). This summer snow accumulation signal is also reflected in the SMB maps (B) and profile (C).

observe reduction in snow cover from the preceding end of summer extent (Figure 3.8A). At the end of summer, we observe more positive Lagrangian SMB rates at higher elevations (Figure 3.8B), with a clear positive bin-wise SMB profile (Figure 3.8C). This observation is also supported by more homogeneously snow covered areas at high elevations in the end of summer orthoimagery(Figure 3.8A).

The high-resolution orthoimages and seasonal elevation change maps for Lirung Glacier capture deposition from avalanche event(s) over the upper glacier. We were unable to prepare contemporaneous velocities from the shaded relief maps for these periods, as the avalanche deposits covered surface features needed for coherent feature tracking. We therefore limited our analysis to Eulerian elevation change products, without correction for flux divergence. We observe a large positive elevation change over the upper glacier, with maximum local deposit thickness of 30 to ~ 55 m (Figure 3.9B). We observe a large decrease in surface elevation over this same area in the subsequent 7 months, likely due to melting and compaction of avalanche deposits (Figure 3.9B). Orthoimages show that the entire glacier surface was again covered in debris at the end of the melt season. However, the annual elevation change map for the full period shows a residual positive elevation change of over 10 m, indicative of net accumulation (Figure 3.9C). The maximum magnitude of flux divergence magnitude over avalanche deposition areas for the period between 2016 to 2017 is $\sim \pm 1$ m/yr (Figure 3.4D), an order of magnitude smaller than avalanche related signals.

3.9 Discussion

3.9.1 Importance of flow corrected SMB maps

Ablation rates over debris-covered glaciers are expected to be highly heterogeneous due to spatial variations in debris thickness, ice cliffs, and melt ponds, but properly resolving the ablation rates at large spatial scales remains challenging. Our results show that slope-corrected Lagrangian Dh/Dt derived using high-resolution DEMs and contemporaneous surface displacements better resolve the enhanced melt structure of steep ice cliffs (e.g., Figure 3.10 A,B), especially over areas with faster surface velocity (≥ 5 m/yr). Isolated positive signals next to some of the ice cliffs in the slope-corrected Lagrangian Dh/Dt maps are most likely due to infilling of the adjoining supraglacial ponds (Figure 3.10C). Some of these observed patches of positive Lagrangian Dh/Dt might also be due to apparent downstream debris mobilization and accumulation (e.g., Figure 3.10 B), as observed in recent studies (e.g., Mishra et al., 2022; Westoby et al., 2020). Flux divergence corrections reveal additional detail, showcasing the value of distributed vs tongue-averaged flux divergence estimates used in earlier studies (e.g., Brun et al., 2018; Mishra et al., 2022). By experimental design, flux divergence measurements vary smoothly. The isolated, small scale, areas of

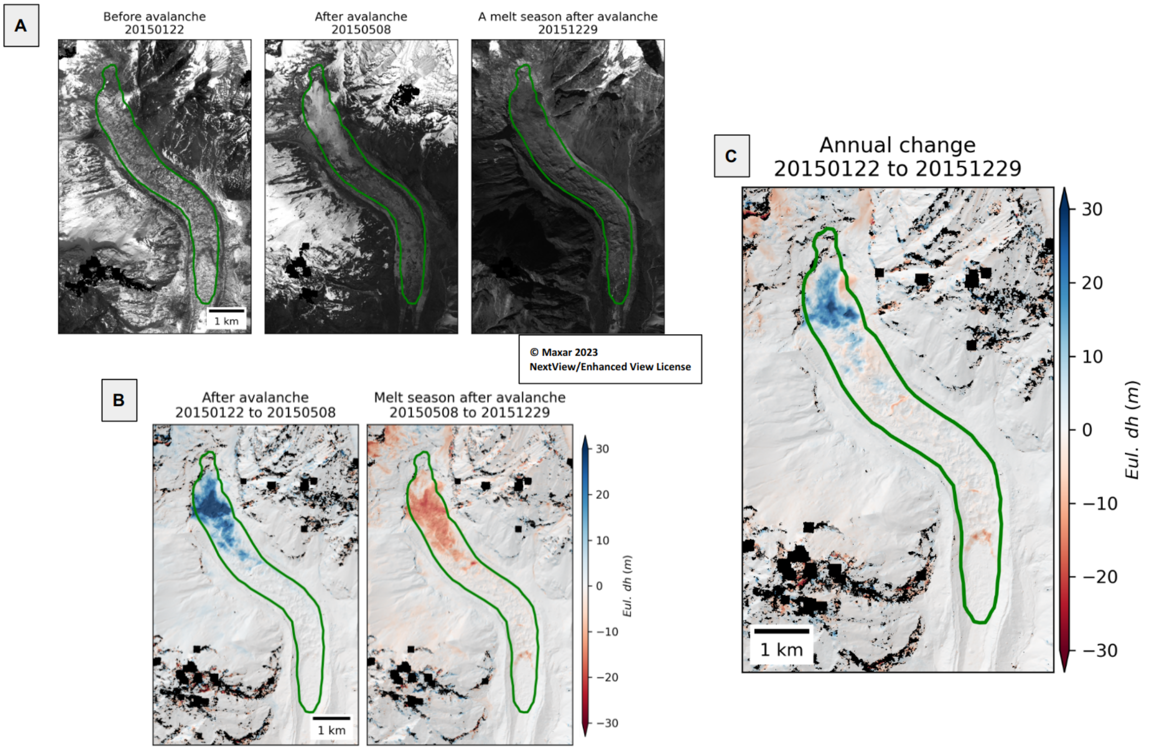

Figure 3.9: Seasonal orthoimage and surface elevation change products over Lirung Glacier capturing accumulation due to avalanche event(s). A) Panchromatic Maxar WW-01/03 orthoimage time series (Table 2) before the avalanche (January 22, 2015), after the avalanche (May 8, 2015) and a full melt season after the avalanche (December 29, 2015). B) Eulerian elevation change maps capturing the avalanche deposits (20150122 to 20150508) and melt and compaction of the avalanche deposits during the melt season (20150508 to 20151229). C) Annual elevation change map spanning the full time period (20150122 to 20151229). Green outlines show RGI v6 glacier extent. Note the 30 to $\sim$ 55 m thick snowpack deposition by the avalanche (B), and a net positive annual elevation change even after the end of melt season, when the glacier has been fully covered with debris again (A).

high flux divergence may be explained by large variations in the modeled bed and observed surface topography (e.g., around icefalls, glacier tributaries), or due to residual errors in ice thickness and surface velocity measurements.

To ensure that our Lagrangian framework conserves mass, we conducted a comparison between Eulerian dh/dt and slope-corrected Lagrangian Dh/Dt estimates over the entire survey area for each glacier in the study, hypothesizing that differences should be zero. We found differences to be minimal, with the largest difference of 0.09 m/yr. However, assessing whether the flux divergence correction conserved mass proved challenging because our measurements mainly covered the ablation area, where we expect non-zero flux divergence due to net emergence. For Lirung and Black Changri Nup glaciers, where the Lagrangian SMB measurements covered almost the entire glacier area, the difference in glacier-wide mean Eulerian dh/dt and Lagrangian SMB rates were 0.15 m/yr and 0.02 m/yr, respectively. The slightly higher non-zero difference over Lirung Glacier can be attributed to its unique state, where the current RGI polygon indicates that the glacier is disconnected from its upstream accumulation area. In this case, this difference essentially represents the mean emergence velocity for Lirung Glacier, which is close to the value of 0.16 ± 0.1 m/yr reported by Miles et al. (2018a). Overall, these comparisons provide confidence that our Lagrangian framework measurements conserve mass over the entire survey area.

3.9.2 Surface mass loss over debris-covered glaciers

The SMB rates observed near the terminus of all six studied glaciers were less negative compared to further upstream. This phenomenon can be explained by the thick debris cover that offsets the typical effect of high melt at lower elevations due to higher summer air temperatures, as noted in previous studies (e.g., Nicholson and Benn, 2006; Rounce and McKinney, 2014; östrem, 1959). SMB rates became more negative upstream as debris thickness decreased (Figure B.6). These findings support the notion that debris thickness is a major control over ice melt. It should be noted that our debris thickness estimates are not completely independent, as the parent model (Rounce et al., 2021) was calibrated using elevation change estimates (Shean et al., 2020) from a period (2000-2018) which overlapped with our investigation period.

Our analysis also reveals that while ice cliffs occupy a small percentage of debris-covered area, they account for a large fraction of total debris zone ablation. The observed relationship between bin-wise melt contribution by ice cliffs, debris thickness, and area occupied by ice cliffs has important implications for debris-covered regions in different stages of mobility. For more stagnant regions with very thick debris cover, fewer but long staying ice cliffs are expected to occur, mostly sustained by surrounding supraglacial ponds (e.g., Buri and

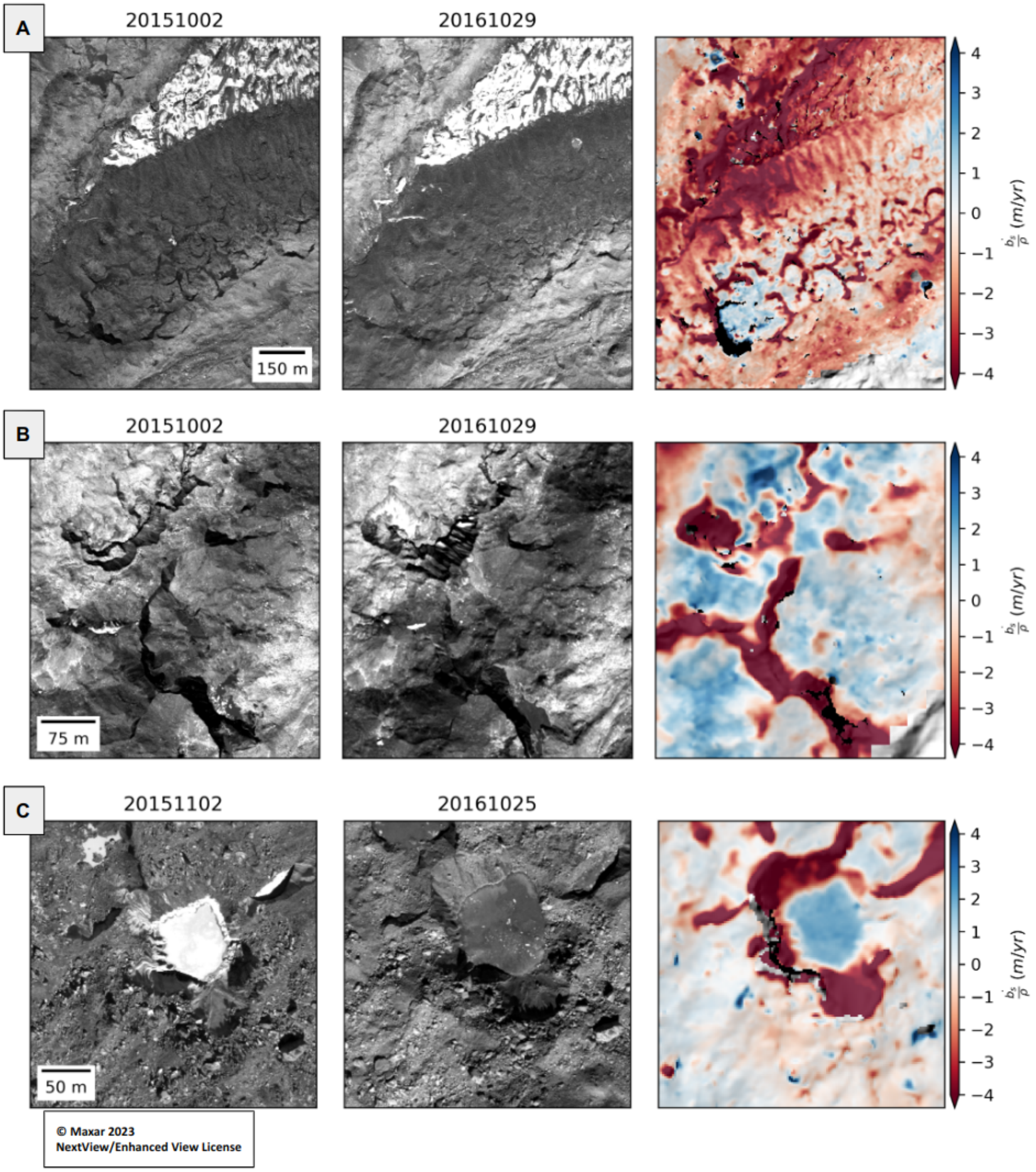

© Maxar 2023
NextView/Enhanced View License

Figure 3.10: High-resolution products showing detailed geomorphic changes and Lagrangian SMB rates over: A,B) locations marked in Figure 3.5, and C) in Figure B.3. Note the detail with which the start of path Lagrangian SMB products are able to resolve the melt rates over the changing ice cliffs.

Pellicciotti, 2018; Kneib et al., 2022a). Sub-debris melt over these regions will be low, driving up the relevant contribution of ice cliff ablation. This can be observed over the Lirung Glacier case study. Over actively flowing regions, compressional flow is expected to produce more temporally dynamic ice cliffs by exposing the upstream crevasse openings as ice cliffs (e.g., Anderson et al., 2021). In these regions, even though the ice cliffs size and location will evolve with time, the number of ice cliffs is expected to be high (e.g., Kneib et al., 2022a), again resulting in considerable contribution to total melt by the ice cliffs.

3.9.3 Comparison with existing estimates

Our debris-covered SMB and ice cliff ablation rate estimates compare very favorably with existing estimates derived from independent methods and/or data sources. Buri et al. (2021) estimated ice cliff contribution to debris-covered area ablation using energy balance models for four glaciers in Langtang National park. Their estimates of ice cliff contribution to total debris zone ablation for Lirung and Langtang Glacier were $11 \pm 5\%$ and $21 \pm 4\%$, respectively, which is in line with our estimates of 16.9% and 24.1% for the same glaciers. We do note that ice cliffs were identified manually in their study, and the area occupied by ice cliffs in their study was lower than what is reported in ours. For Ngozumpa Glacier, using the same in-track stereo image pair (Table 3.2), Thompson et al. (2016) derived DEMs using a different software and estimated ice cliff contribution to debris-covered area ablation as 39%, which is close to our estimate of 35.1%. We note that Thompson et al. (2016) did not perform a correction for flux divergence and attributed all thinning signal to surface melting, which can explain the slightly higher melt contribution obtained in their study (Brun et al., 2018).

Over the debris-covered tongue of Black Changri Nup Glacier, Brun et al. (2018) estimated mean SMB of 1.10 ± 0.27 for the period November 23, 2015 to November 16, 2016 and 1.20 ± 0.36 m/yr for the period November 22, 2015 to November 13, 2016 using UAV and Pleiades-HR derived DEMs, respectively. Their measurements corresponds very well with our mean Lagrangian SMB estimate of -1.18 m/yr over the debris-covered tongue of Black Changri Nup Glacier for the period of November 15, 2015 to October 25, 2016. Additionally, Brun et al. (2018) estimated that ice cliff contributed upto $24 \pm 5\%$ of the total debris zone ablation, similar to our estimate of 28.6%. Some of the differences on the melt contribution by ice cliffs could also be due to the different strategies used for ice cliff delineation. These comparisons are all very close, and provide confidence in our estimates, even though we used different datasets and methodology.

3.9.4 Seasonality of surface mass balance in Nepal

Our seasonal case studies on Black Changri Nup and Lirung Glaciers offer crucial insights into the distinctive accumulation and ablation patterns of debris-covered glaciers in Nepal. During the observation period, Black Changri Nup Glacier likely received very limited accumulation by snowfall during winters, and there was a net reduction in snow cover at high elevations at the end of winter. On the other hand, sustained snow accumulation was observed for the cumulative summer period. Black Changri Nup accumulation area is located at very high elevation with potentially temperatures near or below freezing even during the summers, which allows for snow accumulation during monsoon. The same might not be true for glaciers with accumulation areas located at lower elevations, where summer temperature will be above freezing in (Figure 4 in Wagnon et al., 2013). The cumulative elevation loss over at higher elevations during the winter period can potentially be explained by snow sublimation (e.g., Litt et al., 2019; Mandal et al., 2022) or by snow redistribution due to stronger wind flow at higher altitudes (e.g., Huintjes et al., 2015; Wagnon et al., 2013). Similar patterns of mass balance were also observed for nearby Mera Glacier using glaciological surveys Wagnon et al. (2013). Finally, we note that our current seasonal DEM observations covered only one full year of summer and winter, so it might be possible that 2015 was an anomalously low snow winter.

For debris-covered glaciers in the region which have their accumulation areas at lower elevations, or which are disconnected from their accumulation areas, snow accumulation by avalanches is expected to play a major role in long term mass inflow and sustenance. We were able to observe such an event over Lirung Glacier, where a snow avalanche resulted in deposition of huge volume of snowpack. However, monitoring such events remains a challenge, due to their erratic temporal nature and the current non systematic, tasking based collection system for commercial VHR stereo imagery.

3.9.5 Sources of uncertainty

Lagrangian SMB uncertainty stems from errors from the input datasets (e.g., DEMs, ice thickness measurements), uncertainties introduced during processing (e.g., feature tracking to derive surface velocity, during flow correction of elevation change rates, Gaussian filtering of gradient measurements) and uncertainties introduced by our simplifying assumptions (e.g., contribution of basal sliding to glacier flow, f). Uncertainty in elevation change rates from DEM errors can be assessed by analysing statistics over non-glacierized, static surfaces. Similarly, combined surface velocity uncertainty due to DEM errors and feature tracking errors can be assessed by examining Lagrangian Dh/Dt statistics over non-glacierized, static areas. In this study, the NMAD spread of Lagrangian elevation change rates over static, non-glacierized surfaces was in the order of 0.5 m/yr, with limited residual systematic biases. The NMAD spread was high for Langtang Glacier (1.3 m/yr) due to residual snow cover on the February 02, 2015 DEM limiting static surfaces available for co-registration.

The ice thickness estimates are the most uncertain inputs in our workflow (e.g., Brun et al., 2018; Van Tricht et al., 2021b). Modeled ice thickness estimates have shown to deviate from in situ IPR-derived ice thickness measurements by $\sim 30\%$ (e.g., Van Tricht et al., 2021a). The ice thickness and surface velocity uncertainty propagates to uncertainties in flux divergence estimates. The flux divergence uncertainties will potentially have a smaller effect on our final SMB estimates over areas of slow flow (e.g., Mishra et al., 2022; Rounce et al., 2021), but likely higher for areas with fast flow (as shown in flux divergence uncertainty grids provided in Miles et al., 2021). Our use of large length scales for computing flux divergence reduces the uncertainty in flux divergence, but determining this improvement numerically is difficult in the absence of spatially distributed reference measurements (Van Tricht et al., 2021b). Residual uncertainty in the smooth flux divergence maps after filtering would be more important for measurements averaged over longer length scales (e.g., for ablation area wide SMB estimates Van Tricht et al., 2021b), but would not affect the measurements of ablation contribution by ice cliffs to the surrounding melting debris-covered area considerably (e.g., Brun et al., 2018).

Finally, our assumption of no contribution of basal sliding to glacier flow is a simplification. The glaciers in Nepal likely have some regions where basal sliding is an important contributor (e.g., Kraaijenbrink et al., 2016a), which will require a spatially variable f parameter when computing flux divergence, but we expect the changes in our Lagrangian SMB estimates due to variations in f parameter to be smaller than the elevation change uncertainty (e.g., Armstrong et al., 2022; Van Tricht et al., 2021b).

3.9.6 Limitations and considerations for future work

While our study provides advancements on several aspects such as high resolution DEMs, contemporaneous surface velocity, standard Gaussian filtering approach on gradient rasters), there are several other aspects on which it can be improved further. Here we discuss the most important limitations due to these issues in detail, and explore how some of these issues can be addressed in future work.

Flux divergence over debris-covered glaciers

We derive our flux divergence measurements using modeled estimates of ice thickness and several simplifying assumptions which can affect our measurement numbers (Section 3.9.5). Regionally representative in situ measurements of ice thickness over debris-covered glaciers will allow for improved calibration of modeled ice thickness estimates, which would greatly reduce uncertainties in our flux divergence measurements. Future studies exploring seasonal glacier velocity patterns (e.g., Armstrong et al., 2017), linkages of debris surface hydrology to glacier basal conditions (e.g., Benn et al., 2017; Miles et al., 2018b), could help assess the relative contribution of basal sliding to glacier flow, and better parameterization of the same when computing flux divergence. Future work could also explore use of full stokes models to estimate flux divergence (e.g., Hubbard et al., 2000; Vincent et al., 2021) with different potential parameterizations and explore how these measurements compare with smooth flux divergence estimates obtained on finite grids, such as in this study and by Van Tricht et al. (2021b).

Ice cliff delineation

In this study, we identified ice cliffs based on thresholds on slope and melt rates. While our estimates are in line with existing estimates (Section 3.9.3), we acknowledge that our measurements are biased towards steeper cliffs with high ablation rates. As noted previously, each approach to delineate ice cliffs has drawbacks (Section 3.7.5), but future studies could employ a combination of approaches using complementary data (optical image, DEM, elevation change maps) to increase confidence in our ice cliff delineations. Approaches involving image segmentation based on convolutional neural networks could also be explored with the above suggested data layers as input. Additionally, we will explore M3C2 change detection techniques (e.g., Kneib et al., 2022b; Lague et al., 2013; Mishra et al., 2022) in future work.

Full glacier-wide SMB: Surface velocity and material density

Our preferred method of estimating surface displacement from hillshade breaks over very fast flowing areas (e.g., icefalls) due to feature decorrelation at annual timescales, and due to lack of texture in smooth snow-covered DEMs over the accumulation areas (Section 3.7.2, 3.8.1). Contemporaneous velocities are crucial for maintaining feature correspondence over debris-covered ablation areas while tracking ice cliffs, but observations over the described problematic fast flowing areas can potentially by substituted by composite ice velocity products generated from short baseline pairs using complementary optical (e.g., Altena and Kääb, 2020, Chapter 4) or Synthetic Aperture Radar satellite sources . We will explore these strategies in future work.

The second limitation to obtaining glacier-wide SMB in units of m w.e./yr is correctly accounting for firn compaction in the elevation change measurements, and account for varying material densities in the accumulation areas (Section 3.5). The need for correcting seasonal to annual geodetic surveys for firn compaction have been established in several previous studies (e.g., Belart et al., 2017; Florentine et al., 2019; Sold et al., 2013), but performing the same remains challenging due to difficulties in obtaining such measurements in remote areas (e.g., Kronenberg et al., 2022; Pelto et al., 2019; Zeller et al., 2022) and the high uncertainties involved with standard firn compaction models (e.g., Belart et al., 2017). Beyond the issue of accounting for firn compaction, the seasonally evolving density values of snow and firn poses additional challenges when inferring mass changes from short time-period geodetic surveys (e.g., Berthier et al., 2023; Florentine et al., 2019; Huss, 2013; Pelto et al., 2019). Future work could explore the use a single value of snow density with proper bounds (e.g., 450 to 600 kg/m^3 as in Pelto et al., 2019). Similarly, until more field estimates become available, firn compaction rates can be accounted for by using larger error bounds in firn densities (for example, 700 ± 100 kg/m^3 as used in Pelto et al., 2019).

Sub-seasonal SMB estimates: Residual artifacts in satellite stereo DEMs

Using DEMs derived from WorldView-1/2/3 and GeoEye-1 stereo imagery, we were able to estimate surface elevation change with a reasonable accuracy of ~ 0.5 to 1 m. But we discovered that several of the DEMs that were not used in this study suffered from large errors due to unmodelled jitter vibrations and CCD artifacts (e.g., Shean et al., 2016). Similar and some times even larger signals have observed in Pleiades-HR derived DEMs (e.g., Shean and Bhushan, 2021; Shugar et al., 2021). We tried empirical correction of elevation change maps (e.g., Deschamps-Berger et al., 2020; Nuth and Kääb, 2011; Shean et al., 2021; Shugar et al., 2021), but these corrections considerably altered the underlying small scale melt signals over ice cliffs. There have been recent developments in ASP (**jitter_solve** tool) which allow to refine camera pose measurements to account for jitter vibrations. We will explore this strategy in future work, which if successful, could greatly improve our ability to measure short term elevation change, potentially at sub-seasonal time scales (e.g., Kneib et al., 2022b).

3.10 Conclusion and summary

In the present study, we developed a workflow that combines surface elevation and surface velocity observations obtained from VHR satellite stereo imagery with published ice thickness estimates to generate flow-corrected Lagrangian SMB measurements. The high-resolution Lagrangian SMB maps capture the spatial heterogeneity in the SMB patterns over six well studied debris-covered glaciers in Nepal in great detail. Our measurements confirm that debris thickness exerts an important control on the melt rates of sub-debris ice. At the same time, high resolution SMB estimates reveal that ice cliff can explain a large portion of the total debris-covered area ablation ranging from 17 to 43%, even though they occupy only a small portion of the total area (< 11%). Our results indicate that local melt contribution by ice cliff is jointly driven by debris thickness and percentage of ice cliffs.

We found that Lagrangian frame of reference is essential to estimate correct melt structures around ice cliffs, and that large length scales are required when computing flux divergence and slope-corrected Lagrangian elevation change. The employed Lagrangian framework conserve mass over the survey area and our measurements compare well with previous estimates derived from independent data and methods.

We presented two case studies exploring seasonal surface elevation changes over Black Changri Nup and Lirung Glacier which depict the unique patterns of accumulation and ablation for glaciers in Nepal. Our analysis revealed that Black Changri Nup Glacier experienced minimal winter accumulation, with a significant reduction in snow pack at high elevation areas during this period instead. While ablation was prevalent over the debris-covered area during the summer, snow accumulation was observed at high elevation areas. This initial result highlights the importance of summer snow accumulation for glaciers in Everest region of Nepal. Our seasonal record captures a snow avalanche event over the otherwise, low-lying completely debris-covered Lirung Glacier. Based on our results, we hypothesise that accumulation by avalanches might be important over glaciers located at lower elevations, or which are disconnected from their accumulation areas. Systematic monitoring of these avalanche events remains a challenge however, due to current limitations on data acquisition interval by tasking based commercial satellite stereo imagery.

The presented methods can be applied to the currently under utilised high-resolution stereo image archive over HMA glaciers (Shean, 2017; Shean et al., 2020) for conducting regional scale SMB analysis. Future work will focus on improving velocity and SMB coverage over fast flowing glacier regions, improving handling of firn and snow densities, and robust uncertainty characterisation. We hope to continue improving our DEM production (e.g., jitter) and co-registration workflows (e.g., snow surface masking, Deschamps-Berger et al., 2020; Hu and Shean, 2022), and plan to integrate data from other VHR sources (e.g., Planet SkySat, Plieades Glacier Observatory, Berthier et al., 2014; Bhushan et al., 2021) to obtain SMB measurements at longer spatiotemporal scales. We also stress on the need of more in situ ice thickness measurements, which will be crucial to calibrate ice thickness models as ice thickness is an integral part of our workflow. Future regionally distributed seasonal SMB measurements will further improve our understanding of debris-covered glaciers in HMA and provide complementary context for glaciological measurements (e.g., Stumm et al., 2021; Vincent et al., 2016; Wagnon et al., 2013). Ultimately, these efforts will enable us to better calibrate glacio-hydrologic models (e.g., Khadka et al., 2020; Nicholson et al., 2021; Rounce et al., 2020; Srivastava and Azam, 2022) and enhance our overall understanding of HMA glaciers response to the changing climate.

Acknowledgements

Shashank Bhushan was supported by the NASA FINESST fellowship (80NSSC19K1338). David Shean, David Rounce and Grégoire Guillet were supported by the NASA HiMAT-2 award (80NSSC20K1595). J. Michelle Hu was supported by the NASA Terrestrial Hydrology Program Award (80NSSC18K1405). Resources supporting this work were provided by the NASA High-End Computing (HEC) Program through the NASA Advanced Supercomputing (NAS) Division at Ames Research Center. Maxar WorldView L1B stereo imagery was available under the NGA NextView/EnhancedView license. We thank Ph.D. Committee member Scott Henderson for providing feedback on the manuscript draft. We thank Fanny Brun for providing shapefile for Black Changri Nup Glacier. We acknowledge discussions with Lucas Zeller, Albin Wells, Ben Pelto and Evan Miles at meetings and conferences which were helpful in method development and result interpretations. We are thankful to Oleg Alexandrov and Scott McMichael for providing support with NASA ASP processing, and to the ever-growing ASP user community for stimulating insightful discussions on ASP processing. We thank all research teams who have performed and continue to perform field research in HMA, this research would not be possible without their efforts.

Author contribution statement

SB and DS conceived the project. SB, DS and DR participated in funding acquisition. SB performed literature survey, led method and code development, produced and analysed results, produced the figures and wrote the first draft of the manuscript. DS supervised the entire research and provided essential feedback during methods development, analysis and manuscript writing and editing. JMH provided assistance during method development, contributed to DEM production pipeline development, provided feedback in making figures and writing structre. GG provided feedback on writing of the introduction and theory section, and provided assistance in results interpretation. DR provided feedback on methods, results interpretation and analysis. All authors contributed to review and editing of the manuscript, especially DS.

Chapter 4

SEASONAL TO MONTHLY GLACIER VELOCITY ESTIMATION USING NEAR-DAILY, PLANETSCOPE DOVE CLASSIC IMAGERY

The chapter will be submitted for peer-review as: **S. Bhushan**, D. Shean, S. Henderson, and S. Price. ***"Seasonal to monthly glacier velocity estimation using near-daily, PlanetScope Dove Classic imagery"***

4.1 Abstract

Glacier flow seasonality is influenced by the availability of meltwater at the glacier bed and the seasonal evolution of the basal hydrologic system. Understanding short-term changes in glacier velocity is crucial for determining the impact of meteorological changes on glacier flow at seasonal time scales in general, but also for undergoing surges. However, measuring seasonal velocity is challenging, as short-term changes in velocity are often within the accuracy limits of currently available satellite products, and such measurements are only available for a few accessible glaciers in the High Mountain Asia (HMA) region with in situ surveys. In this study, we present a novel approach using near-daily, high-resolution PlanetScope Dove Classic imagery to derive monthly velocities with a precision of 0.02 to 0.03 m/day. We developed new corrections for geolocation issues associated with PlanetScope Dove Classic imagery and aggregate observations from overlapping time periods to improve precision . We document the initiation of the 2018 Gando Glacier surge in great detail and highlight seasonality in flow during the surge period. We also document spatially-varying extents of seasonal velocity variations over the slow-moving, heavily debris-covered Ngozumpa and Khumbu glaciers, as well as the topographically complex and faster moving Khumbu Icefall. Our observations indicate that peak velocities occur during the summer and monsoon months, with a summer speedup of approximately 67% observed over the western tributary of Ngozumpa Glacier. The outlined methods can be applied to PlanetScope Dove Classic image time series acquired over glaciers across HMA and other regions in the world, providing the opportunity to understand seasonal glacier dynamics on a regional scale.

4.2 Introduction

The majority of High Mountain Asia (HMA) glaciers are losing mass (e.g., Brun et al., 2017; Hugonnet et al., 2021; Shean et al., 2020) and slowing down (e.g., Dehecq et al., 2019), but the region-wide rates and spatial patterns of these changes are highly heterogeneous. These variations result from the complex interplay between surface processes, internal ice dynamics, and glacier response to varying climatology. Glacier velocity is a key observable – it tells us about the dynamics of glaciers and how they respond to long-term climate forcing and short term meteorological forcing. Changes in basal sliding conditions and the subglacial hydrologic drainage system at the glacier bed drive glacier velocity changes at short timespans (e.g., Armstrong et al., 2016; Davison et al., 2020). An increase in water availability due to surface melting and/or rainfall after the onset of spring promotes basal sliding and results in glacier speed up (e.g., Cuffey and Paterson, 2010; Nienow et al., 2005). The increased velocity is generally sustained until the late summer periods when the basal drainage channels evolve and become more efficient, resulting in reduced water available to promote basal sliding, accompanied by a reduction in surface velocity (e.g., Armstrong, 2017; Davison et al., 2020). Understanding how glacier speedups evolve is important to accurately represent glacier dynamics in glacier evolution models (e.g., Shea et al., 2015) and improve projections of glacier mass balance and associated runoffs (e.g., Maussion et al., 2019; Rounce et al., 2020).

Despite the importance of seasonal glacier velocity variations for understanding basal sliding, these processes have only been observed for a few, more accessible glaciers in HMA (e.g., Kraaijenbrink et al., 2016a; Kumar and Dobhal, 1997). Satellite remote sensing allows for obtaining surface velocity measurements at large spatial scales (e.g., Dehecq et al., 2019; Millan et al., 2022). Specifically, feature tracking techniques have been applied to optical and SAR imagery to produce velocity maps at a global scale (e.g., Fahnestock et al., 2016; Millan et al., 2022; Ted Scambos, 2016). In this procedure, features on the glacier surface are identified in two orthorectified images acquired at different times, providing measurements of surface displacement (e.g., Dehecq et al., 2015; Lei et al., 2021; Leprince et al., 2007; Mouginot et al., 2023; Scambos et al., 1992; Van Wyk de Vries and Wickert, 2020). While the currently available, state-of-the-art satellite remote sensing products provide insights into long-term changes in the flow velocity of mountain glaciers (e.g., Dehecq et al., 2019; King et al., 2018), the magnitude of seasonal velocity variability is often close to or smaller than the measurement accuracy using medium-resolution imagery (e.g., LandSat-7/8/9 30m or Sentinel-2 10m products). Additionally, the records are biased towards seasons with low cloud- and snow-cover due to limited temporal repeat (5 to 16 days).

These challenges can be overcome with high-cadence, high-resolution imagery. The high-resolution (3m), near-daily optical imagery acquired by the PlanetScope constellations provides an exciting opportunity to obtain seasonal velocity measurements for glaciers, including smaller, slow-moving glaciers. While previous studies have successfully derived glacier velocity using PlanetScope Dove imagery for a limited number of observation periods (e.g., Aati et al., 2022; Pelto and Menounos, 2021; Watson and King, 2018), to our knowledge, there is no study which has attempted to study seasonal glacier evolution using the entire Planet Dove archive for a given glacier. This can be mostly attributed to the issues associated with the dataset quality (e.g., Aati et al., 2022) and computational challenges associated with the data volume.

This study presents workflows to obtain temporally dense glacier velocity products from the PlanetScope Dove Classic image archive. We discuss the geometric and radiometric issues that must be considered when using PlanetScope Dove Classic imagery. We then describe a spatiotemporal stacking and filtering strategy that uses data redundancy to obtain high-precision, monthly velocity time series. We finally present case studies for a surging glacier, the topographically complex, fast flowing Khumbu Icefall, and two slow-flowing debris-covered glaciers and discuss the seasonal flow variations in the context of climatic factors (e.g., seasonal temperature and precipitation variability).

4.3 PlanetScope Constellation: Uniqueness and Challenges

Planet operates a cubesat constellation consisting of three distinct instrument designs, Dove Classic (PS2), Dove-R (PS2-SD) and SuperDove (PSB-SD) (Team, 2023). The satellites have historically been deployed in three main orbits. The earliest satellites were deployed on the mid-inclination ISS orbits (orbital inclination: 51°, Right Ascension of Ascending Node: 235°). Since the launch of the lock 2p and flock 3p generations, satellites have been deployed in sun-synchronous, polar (orbital inclination: 96 to 98°) ascending (Right Ascension of Ascending Node: 68°) and descending orbits (Right Ascension of Ascending Node: 195° or 267°). We only considered imagery acquired from Dove Classic sensors in the study, based on known band-to-band registration issues caused by uncorrected parallax over steep surfaces and the smaller along-track dimension of individual bands in Dove-R and SuperDove sensors equipped with "butcher block" filters (e.g., Aati et al., 2022). Furthermore, we found the high terrain shadow present in the images acquired by Dove Classic sensors in mid-inclination orbit prevented meaningful feature tracking, so we only consider images acquired by the PlanetScope Dove Classic sensors deployed in polar orbits. Through the rest of the manuscript, we refer to the sensor and the product used as Dove Classic and Dove Classic image/imagery, respectively.

The Dove Classic polar, Sun Synchronous Orbit (SSO) constellation (150 Dove Classics)

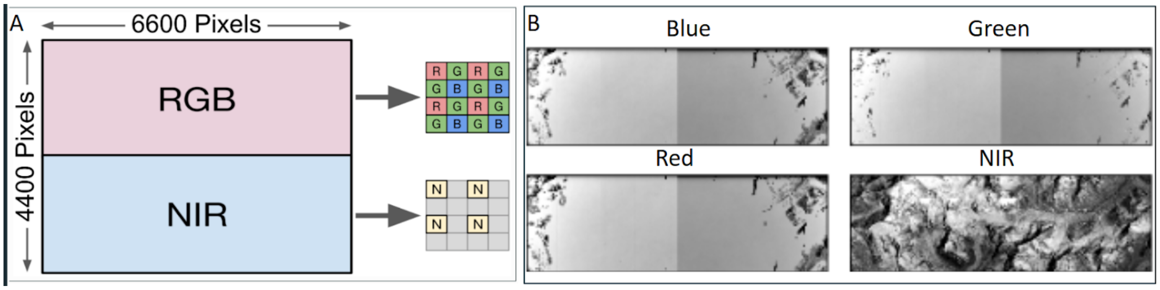

Figure 4.1: A) Dove Classic sensor layout from (Team, 2023). The detector is divided into two halves with a 2-stripe filter. The top half uses a Bayer pattern with red, green, and blue (RGB) filters while the bottom half uses a near-infrared filter. B) A sample Dove Classic image (SCENE ID: 20190330_042611_1005) over a snow-covered landscape in Nepal. The visible RGB bands are saturated, but the NIR band has excellent contrast.

began operations in mid 2016, and continued to acquire near daily high-resolution (3 m), 4-band (RGB, NIR) optical imagery for every point on the Earth's landmass until decommissioning began in April 2022 (Team, 2022). The polar SSO Dove Classic constellation served as the primary satellite in Planet's medium resolution imaging fleet and was gradually replaced by SuperDove sensors starting 2020. Images from a given sun-synchronous orbit (SSO) are acquired at approximately the same local time at each revisit (Roy et al., 2021a) with a near nadir viewing geometry (off-nadir angle between 0 to 5 degrees).

The Dove Classic detector is fitted with a Bayer pattern mask which splits the wavelength of incoming light into Red, Green and Blue (Team, 2023). A 2-stripe filter is placed on top of the Bayer pattern mask, the top half allows light from the RGB wavelengths to pass through, while the bottom half allows light only from the NIR wavelength to pass through (Figure 4.1A, Planet Team, 2023). The initial geolocation accuracy of the imagery is in the order of kilometers, which is improved by an internal multi-step alignment to an accurate basemap by Planet. After these procedures, the geolocation accuracy is improved to around 10 m (Team, 2022). During the acquisition, the NIR portion on ground coincides spatially with the RGB band from the previous snapshot acquired by the same satellite (Figure 4.1). Therefore, when these images are processed internally at Planet, the NIR band is stacked with RGB images from the previous acquisition to deliver a spatially consistent 4 band RGB-NIR product. This procedure requires several projections of the NIR image between the sensor plane geometry and the surface using elevation models. These registration procedures work mostly well in flat terrain cases (e.g., Cooley et al., 2017; Kääb et al., 2019), but chances of failure in optimization are higher in steep terrain cases. This results in spatially variable relative shifts of several pixels in the NIR bands, which are too subtle to be seen from the native eye. There is currently no systematic way to identify the affected images, with even products designated in the "standard" quality category suffering from these issues. Offsets introduced during registration and rectification are too subtle to be seen from native eye, and there is currently no systematic way to identify affected images. Furthermore, the registration and rectification procedure used by Planet to prepare the PlanetScope products changes over time, without systematic reprocessing of the archive, resulting in temporally variable systematic artifacts and errors.

4.3.1 Differences in optical feature tracking using Dove Classic vs Landsat/Sentinel-2 products

We now briefly discuss the fundamental differences in large scale feature tracking with Dove Classic imagery vs. image products acquired by medium resolution sensors like Landsat-8/9 and Sentinel-2. The first point of difference is the much shorter revisit time for PlanetScope constellations in comparison to medium resolution data. The theoretical near-daily revisit time of PlanetScope constellations (e.g., Roy et al., 2021a) allows more opportunities to acquire cloud-free imagery even during periods of extensive cloud cover (Figure 4.2). This is important for glaciers which are located in areas experiencing monsoon and are cloud-covered when the ice flow and melt is expected to vary the most (e.g., Kneib et al., 2022b).

The second point of difference is the image resolution, and our improved ability to measure surface displacement with finer image resolution. Assuming perfect geolocation accuracy and a 0.2 pixel feature tracking precision, the theoretical displacement accuracy for L-8/9, S-2 and Dove Classic image pairs is 3 m, 2 m and 0.6 m, respectively. In this case, to obtain velocity maps with 0.1 m/day accuracy, a minimum temporal baseline of 30 days and 20 days respectively would be required for L8 and S2 image pairs, while only a 6 day interval would be required for Dove Classic image pairs. In reality, geolocation accuracy is never absolutely perfect, and reduced accuracy is specially expected for areas with steep topography. Even in these circumstances, a higher number of unique Dove Classic imagery from the same period would allow the formation of more image pairs, which theoretically reduces measurement uncertainty when stacking operations are performed.

Finally, there are important differences in the size and location of on-ground footprint of Dove Classic products. The imagery acquired by Dove Classic satellites does not follow a standard path and row system as used by Landsat-8/9 or Sentinel-2. A single Dove Classic "scene" product covers approximately 24 x 8 km^2 on the ground (Team, 2022), while a typical Landsat-8/9 image covers ∼182 x 185 km^2 and a typical Sentinel-2 image tile covers ∼100 x 100 km^2. Therefore, to compute glacier velocity over a glacier such as Ngozumpa (∼61 km^2), we must use multiple overlapping pairs from 3-4 consecutive along-track image Dove

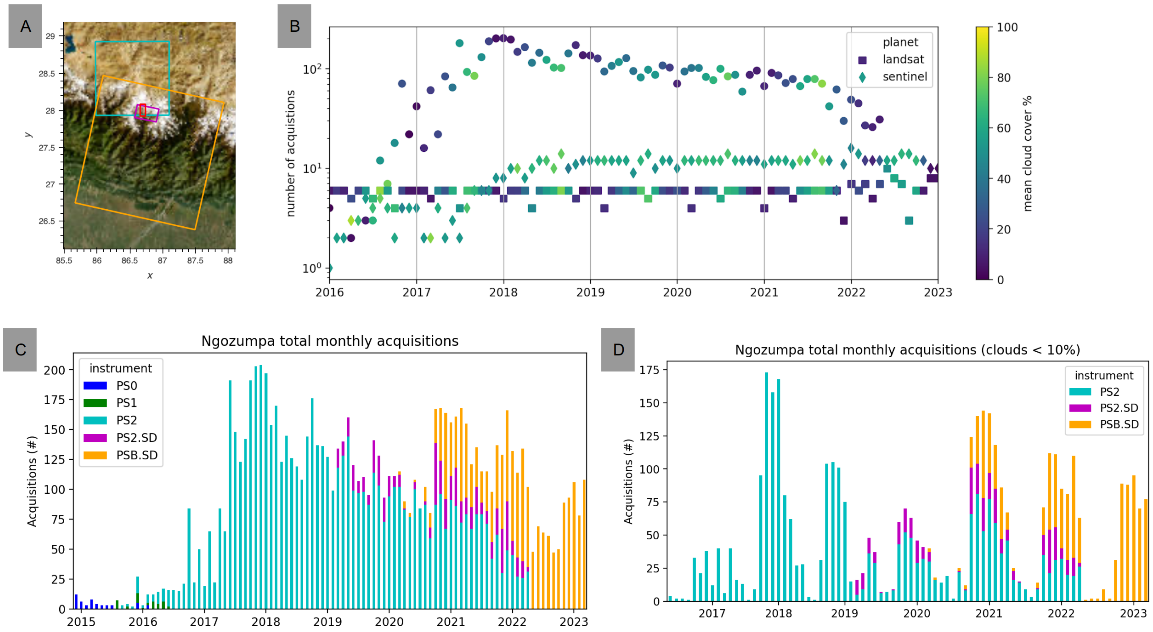

Figure 4.2: A) Basemap over Ngozumpa Glacier with footprints of a single PlanetScope, Landsat-8 and Sentinel-2 image for context. B) Number of images acquired by PlanetScope, LandSat-8/9 and Sentinel-2 constellations over Ngozumpa Glacier. C) Distribution of imagery among the different generations of PlanetScope sensors over Ngozumpa Glacier. D) Same as C, but with cloud cover ¡10%. Note the markedly small footprint of PlanetScope image in-comparison to LandSat-8 and Sentinel-2 (A), but higher number of acquisitions (B), with usable imagery even during the monsoons (D).

Classic scenes acquired on the two different dates. The same glacier covers only 0.2% (0.6%) of a Landsat (Sentinel-2) pair, with an always consistent footprint over time. As a result, we need to form a higher number of pairs for all possible intersections between the smaller Dove Classic images and perform additional post-processing to prepare stacked velocity data cubes with a common extent over a given area. These steps require a different approach than conventional processing strategies developed for products from Landsat-8/9 or Sentinel-2 with self-consistent coverage (e.g., those employed in ITS_LIVE, Gardner et al., 2022). The high-resolution Dove Classic images also require increased computational resources, which are scalable, such as those in supercomputing clusters and commercial clouds.

4.4 Study Sites

We examine the quality of Planet data for glacier velocity extraction on three glaciers, which are spread across the High Mountain Asia, with different flow regime, orientation, climatic regime and surrounding topography (Figure 4.3). Ngozumpa and Khumbu Glaciers are located in Sagarmatha National Park in Nepal, with extreme topographic relief in the area (Figure 4.3A). The region's climatology is heavily influenced by Indian Summer Monsoons (ISM), which account for the majority of precipitation during the months of June to September. The lower parts of these glaciers are stagnant and covered by thick debris, with mobility limited to upper regions only.

Gando Glacier is located in the Pamir mountain range, with comparatively lower relief around the glacier surface (Figure 4.3B). The glacier has been reported to surge from 2018 onward (Wang et al., 2023). The region's climatology is dominated by Westerlies, and has no influence of ISM. This results in a higher number of cloud free images during summer months.

4.5 Data

We worked with the Planet engineering team on the issues we discovered in our initial evaluation, and they reprocessed the entire archive data over our study site using a consistent rectification and registration procedure. After this reprocessing, we were able to use the Level-3B orthorectified 4-band products . We used the porder toolbox (Roy et al., 2021b) and Planet API v1.0 to identify and download all archived Dove Classic imagery (20160101 and 202201231) with less than 40% cloud cover. We then extracted the NIR band (band 4, Figure 1B) from the original products for subsequent processing.

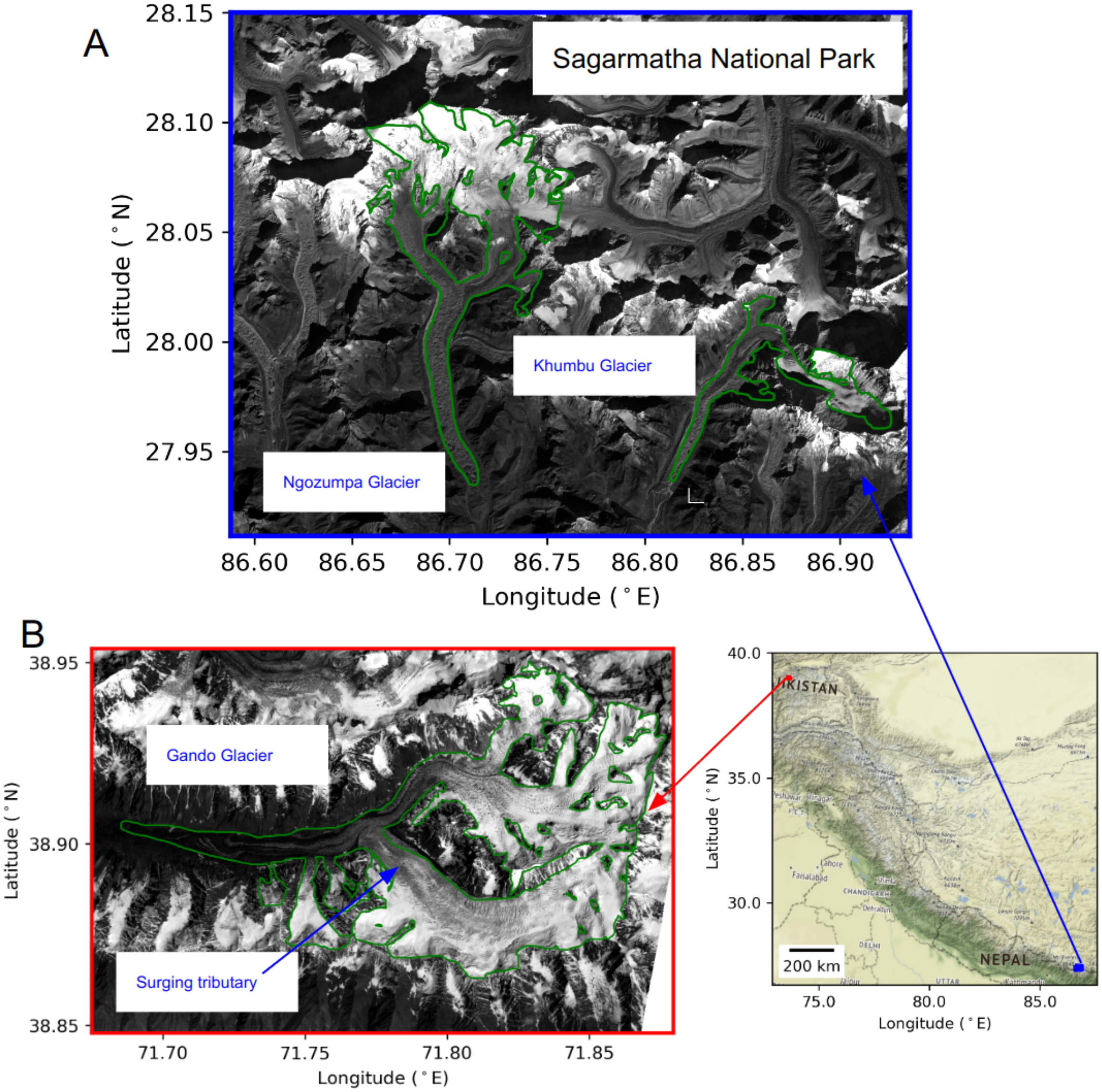

Figure 4.3: The two study sites are located in A) Sagarmatha National Park in Nepal and B) in the Pamir range in Tajikistan. Dove Classic near-infrared (NIR) orthoimage mosaics collected on 20181123 and 20190729 by satellite ids (104a, 103b, 1018) and 1013 for the Sagarmatha (A) and Pamir (B) sites, respectively. We focus on the debris-covered Ngozumpa and Khumbu Glaciers in Sagarmatha National Park, and on the Gando Glacier in Pamir. Green outlines show corresponding glacier outlines from the Randolph Glacier Inventory (RGI) v6.0 (Pfeffer et al., 2014; RGI Consortium, 2017b).

4.6 Methods

4.6.1 Image pair identification

The first step in our workflow is to select candidate scene pairs for feature tracking. Following Aati et al. (2022), we limit pairing to images obtained from Dove Classic sensors in the same orbit (e.g. SSO with ascending node, or SSO with descending node) to minimize orthorectification error related to perspective differences. We classify images to have been collected from ascending SSO orbits if the ground footprint of the scene has an positive azimuth angle between 0° to 30° from North. If the azimuth angle for the image is between 330° to 355°, the scenes are classified as having been collected in descending orbit. We then compute the intersection between the same orbit images, and all pairs with an intersection area greater than 30 km2 (15% of a Dove Classic scene) are selected. Finally, we apply a temporal filter, and only preserve image pairs with a temporal baseline between 15 to 120 days. For Gando Glacier, we also included pairs with temporal baselines between 5 to 15 days, as the magnitude of flow velocity is expected to be higher than the signal to noise ratio of 5 day pairs during the surge cycle. Details of the scene pairing algorithm can be accessed in the code (**dove_vmap_jobs.py**).

4.6.2 Feature tracking

We used NASA JPL's autoRIFT feature tracking software (Gardner et al., 2018; Lei et al., 2021) to prepare pixel displacement maps for the input PlanetScope images. The feature tracking workflow begins by resampling the 16-bit images to common extent and applying a 15 x 15 pixel preprocessing Laplacian filter on each image to bring out edges and enhance high frequency details. The filtered images are then rescaled to 8-bit integers to improve computational efficiency during image correlation (Lei et al., 2021). Pixel wise disparity measurements are obtained using the Normalised Cross Correlation (NCC) algorithm implemented in autoRIFT. Table 4.1 lists the specific correlation parameters used in this study, including the modified disparity filtering parameters used in the Normalised Coherence Displacement (NDC) function (Lei et al., 2021) for the higher resolution of PlanetScope images (3 m) . This filter removes pixels with disparity values that deviate a lot (low coherence) randomly from their neighbors, which is typically encountered in cases when one or both of the images in the pair contain scattered clouds (Figure C.1).

We performed all data processing using the NASA Pleiades supercomputer. Jobs for each site were submitted with a multi-node request for either the Broadwell or Haswell node depending on node availability at a given time. Each Broadwell (Haswell) node is tasked to run 28 (24) **autoRIFT_vmap.py** jobs with 2 threads available to each job. The

Table 4.1: AutoRIFT correlation parameters

Correlation kernel size (px)	Khumbu/Ngozumpa: 32 to 256, Gando: 64 to 256
Skip rate (px)	8
prefilter kernel width (px)	15
NDC filter width (px)	15
NDC filter fracValid	110/225
NDC filter fracSearch	0.2

Table 4.2: Quantitative description of input image volume which is used for feature tracking at each site and the output volume of the velocity products.

Site	Number of images	Input image volume	Number of pairs	Output data volume
Gando	3807	295 GB	81080	4.7 TB
Ngozumpa	5457	365 GB	135383	1.6 TB
Khumbu	3961	265 GB	96475	458 GB

total walltime for the entire processing depends on availability of nodes. To put things in perspective, over Ngozumpa Glacier, we identified 5000 scenes with less than 40% cloud cover, totalling to 365 GB of NIR band data. From these, we identified 124950 and 34270 pairs acquired in the ascending and descending orbit, respectively. These pairs were processed using 50 Hashwell nodes in about 14 hours, resulting in 1.6 TB of output files written to disk (Table 4.2).

Disparity measurements in pixel units are converted to surface velocity measurements using the resampled image resolution (3 m) and temporal baseline of the pair. Finally, assuming non-glacierized surfaces to have remained static during the period of observation, we compute the median east-west and north-south displacement values over all such static surfaces in each pair to estimate relative geolocation bias, and then remove these values from the corresponding displacement products. Details of the workflow can be found in the script **autoRIFT_vmap.py**.

We performed all data processing using the NASA Pleiades supercomputer. Jobs for each site were submitted with a multi-node request for either the Broadwell or Haswell node depending on node availability at a given time. Each Broadwell (Haswell) node is tasked to run 28 (24) autoRIFT_vmap.py jobs with 2 threads available to each job. The total walltime for the entire processing depends on availability of nodes. To put things in perspective, over Ngozumpa Glacier, we identified 5457 scenes with less than 40% cloud cover, totalling to 365 GB of NIR band data. From these, we identified 124950 and 34270 pairs acquired in the ascending and descending orbit, respectively. These pairs were processed using 50 Hashwell nodes in about 14 hours, resulting in 1.6 TB of output files written to disk (Table 4.2).

4.6.3 Residual relative geolocation accuracy assessment

We use residual observed displacement values (m) over static surfaces to assess the relative geolocation accuracy for each image pair. Specifically, we use two techniques. Statistics of all displacement values (mean, median) over static areas are used to determine the relative location offset for a given image pair. For assessing geometric accuracy, we limit our analysis to pairs with a temporal baseline less than 40 days, to minimize the effects of changing illumination (e.g., shadow) and surface conditions (e.g., snow cover). We assess this by computing the robust offset metric, which we define as the root sum of squares of the Normalised Median Absolute Difference (NMAD) (Höhle and Höhle, 2009) and median displacement distribution over static surfaces in the entire image pair intersection area.

Image pairs exhibiting considerable residual relative geolocation offsets are subjected to visual analysis to comprehend the error distribution. Notably, pairs displaying characteristic error patterns are identified to document systematic error patterns that prospective users may encounter in surface displacement measurements derived from Dove Classic image products.

4.6.4 Velocity time series stack preparation

Individual pairwise velocity maps have different extents, temporal baselines (5 to 120 days), and suffer from both random and systematic errors , reducing signal to noise. To overcome this, we employ a series of additional filters, stacking and aggregation techniques. Velocity maps for a given time period obtained from the same satellite pair are mosaicked into a virtual raster over a common rectangular extent covering the entire area of the study glacier. A centerline is defined along the glacier using the Open Global Glacier Model (Maussion et al., 2019) centerline algorithm (Kienholz et al., 2013). The centerline is split into 600 m segments and buffered by 200 m on each side. The 600 by 400 m boxes are used to extract pixels from the individual glacier velocity maps and median velocity (hereby referred to as box median) is computed for both x and y direction components. The median value over a large area (600 x 400 m) is by design more robust to random errors expected at pixel scale. Next, we compute the mean and standard deviation of the box median x and y velocity components for the entire time series. We then remove all box median observations which are outside the mean ± 1*standard deviation limits obtained from the entire time series. Finally, monthly median values are obtained from the filtered values, by considering all observations which coincided with a particular month. This includes short baseline observations which fall

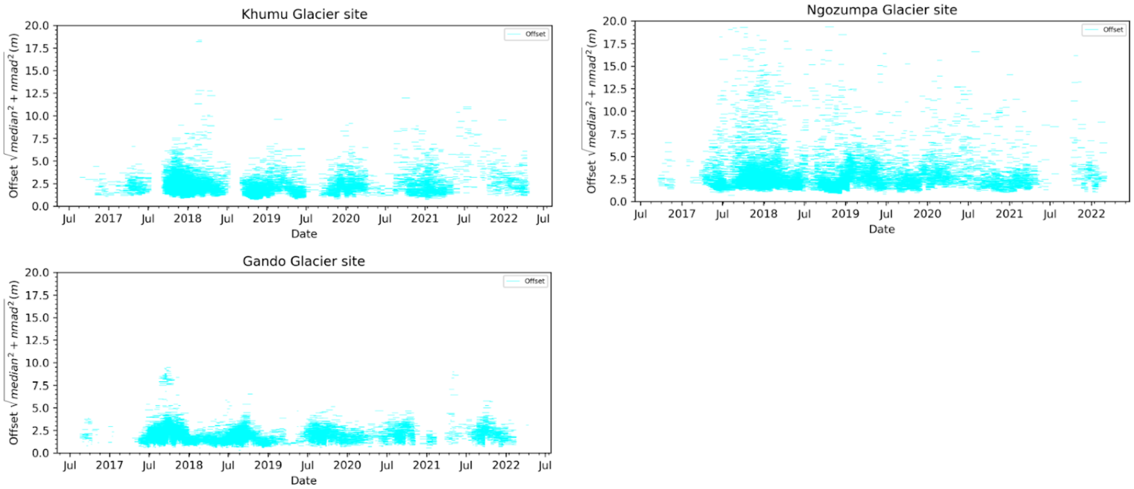

Figure 4.4: Residual relative geolocation offset between candidate pairs with temporal baseline less than 40 days. Length of the lines span from the first to second date of observation.

within the considered month, long baseline observations which cover the entire month and a period larger than the month, and all short/long baseline pairs which cover the considered month only partially. Our filtering approach does not apply over the surging Gando Glacier example, where the surge velocities can be an order of magnitude higher than the quiescent phase velocity (Bhambri et al., 2017; Guillet et al., 2022). A step by step example of the workflow is outlined in the notebook (**Khumbu_small_kernel.ipynb**).

We also prepare distributed maps of median monthly velocities, by following the temporal stacking procedure described above, but without the outlier filtering scheme.

4.7 Results

4.7.1 Accuracy Assessment: Relative geolocation error

Our results reveal the average residual relative geolocation accuracy, as measured by our robust RMSE metric (Section 4.6.3), is within the product accuracy statistics of 10 m as specified by Planet. Specifically, for all three sites, at least 50% of the short baseline pairs achieved relative subpixel accuracy (< 3 m). For Khumbu Glacier and Gando Glacier sites, 84% and 95% of pairs had subpixel accuracy. Scenes over Ngozumpa Glacier displayed higher errors, with very high spread observed over pairs acquired between 2017 to end of 2018 (Figure 4.4).

4.7.2 Accuracy Assessment: Spatial characterization of systematic errors

The sub-pixel block offsets observed in the original NIR band imagery (Figure 4.5) were one of the most critical issues we encountered, which seriously precluded estimation of meaningful glacier velocity time series. These errors were mostly mitigated in the reprocessed data provided by Planet, but a few limited artifacts still persisted. We found many displacement pairs to have a topographically correlated error, where high displacement values were observed over areas of extremely high elevation and slope (headwalls) and at low elevation and gentle topography (valleys) (Figure 4.6). These types of artifacts were not found in all the displacement pairs, and sometimes only occurred on some measurements acquired by a given satellite pair, but absent on the preceding measurements acquired in the same pass (Figure C.1). Finally, we observed that some displacement maps prepared using autoRIFT's default 5 pixel Walis image preprocessing filter contained hatched artifacts with offsets as high as 4 m, which were mitigated by use of Laplacian filter with kernel size of 15 pixel, without any appreciable reduction in data coverage (Figure C.2). This issue was observed more in images acquired in 2017 and 2018, and less in the later images. The hatch pattern errors (Figure C.2) might be an artifact due to the image resampling kernels during the rectification process at Planet, as also noted in Aati et al. (2022).

4.7.3 Glacier velocity: Gando Glacier surge initiation and evolution

Our velocity time series for Gando Glacier captures the 2018 surge initiation and propagation with unprecedented detail (Figure 4.7B,C). We observe pre-surge build up in the southern tributary as early as in July/August 2017, with sustained velocities of 0.6 to 0.8 m/day observed over the sampled record extracted from the orange box (Figure 4.7A,B). The surge appears to start around June 2018 and reaches the yellow box (6.5 km downstream of the orange box) by July 2021, 3 years later. Peak velocities of ¿4 m/day (1460 m/yr) were recorded above the point of confluence of the Southern tributary with the main trunk around November 2018. We also observe seasonality in flow speed after surge initiation, with high velocities sustained during summer to fall, sustained decline till next February/March and a gradual increase in velocity post that. The surge appears to slow down around the fall of 2021, with a more homogeneous distribution of velocity in the southern tributary and the main trunk after that (Figure 4.7B,C). Finally, we also observed rapid short term fluctuations in pairwise velocity values during summer months when the surge was active.

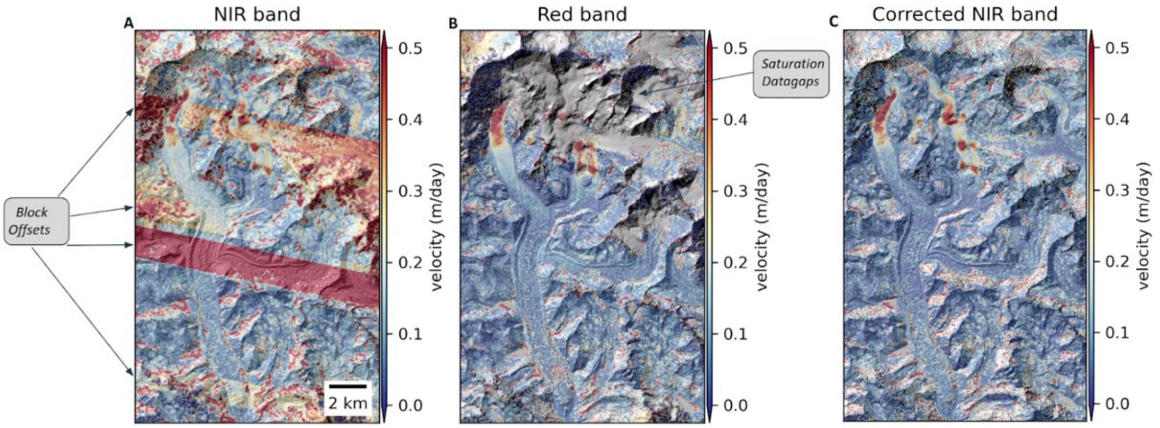

Figure 4.5: Sample velocity products and corresponding artifacts for Ngozumpa Glacier, generated using PlanetScope Dove Classic images from January 2, 2019 and January 18, 2019. A) NIR and B) Red band images. Background image is hillshade mosaic derived from co-registered 8 m HiMAT DEMs (Shean, 2017). All processing parameters were kept the same for both the tests. The velocity maps obtained from the NIR bands suffer from systematic artifacts due to "block offsets" which preclude interpretation of underlying glacier motion. The glacier velocity map from the red band imagery is free from the block offset artifacts, but suffers from data losses over higher accumulation areas of the glacier caused by saturation of visible bands. We communicated these unique errors to engineers at Planet, and they reprocessed NIR bands over our test site with the enhanced e2e registration. C) Velocity maps obtained from the Planet-reprocessed NIR bands for the given date are devoid of block offsets (A), and offer near complete coverage over the glacier overcoming saturation effects in visible bands (B).

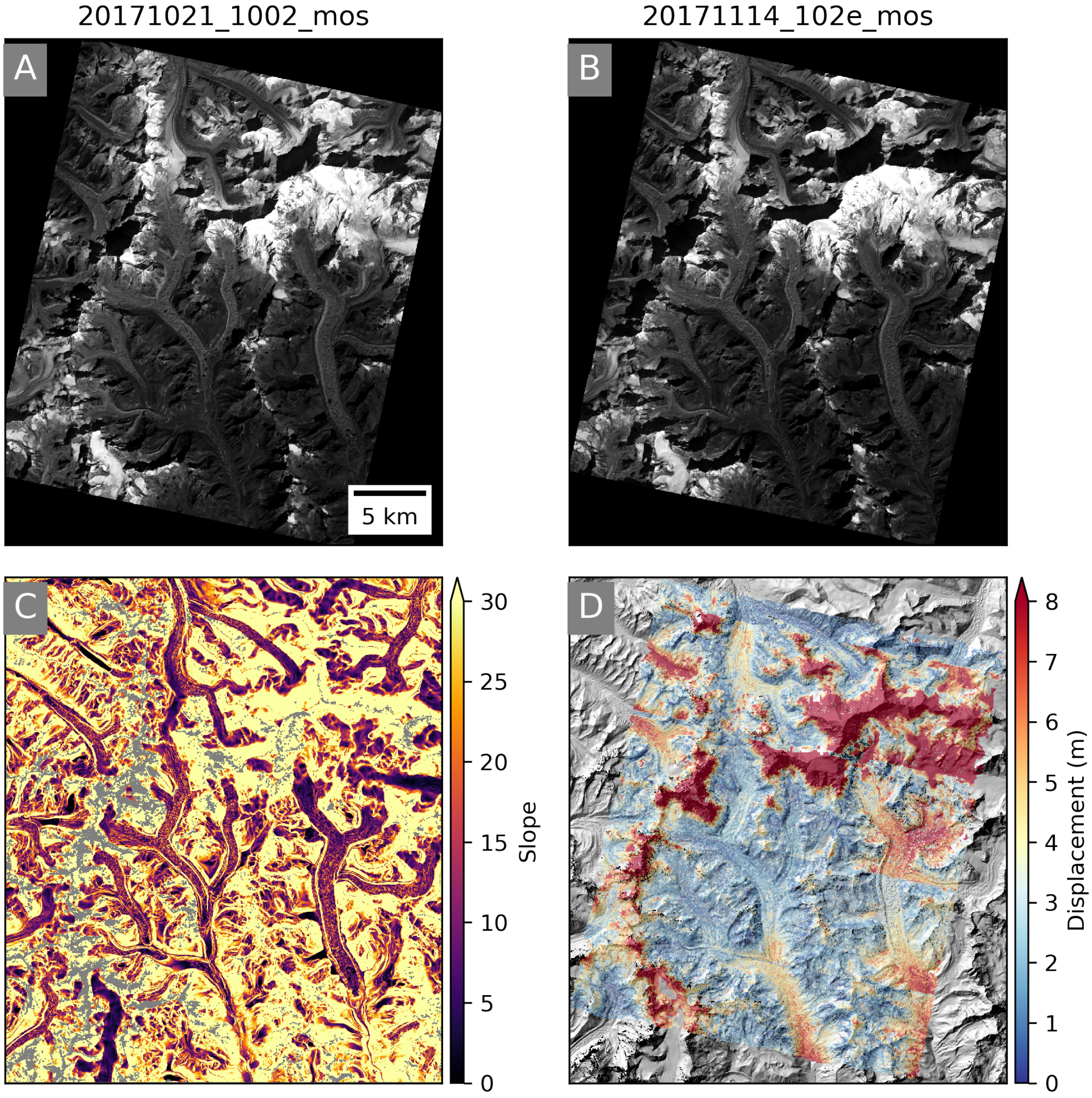

Figure 4.6: Intra-scene relative geolocation artifacts correlated with topography. Orthoimage mosaics prepared from NIR images collected on A) 20171021 and B) 20171114 by satellites 1002 and 102e respectively. C) Per-pixel slope map derived from HiMAT-1 DEM mosaic (Shean, 2017). D) Displacement map obtained from correlation of orthoimage mosaics shown in A and B and overlaid on hillshade generated from HiMAT-1 DEM mosaic (Shean, 2017). Note high relative displacement values along relatively gently sloped glacier valleys and along crest of mountain tops.

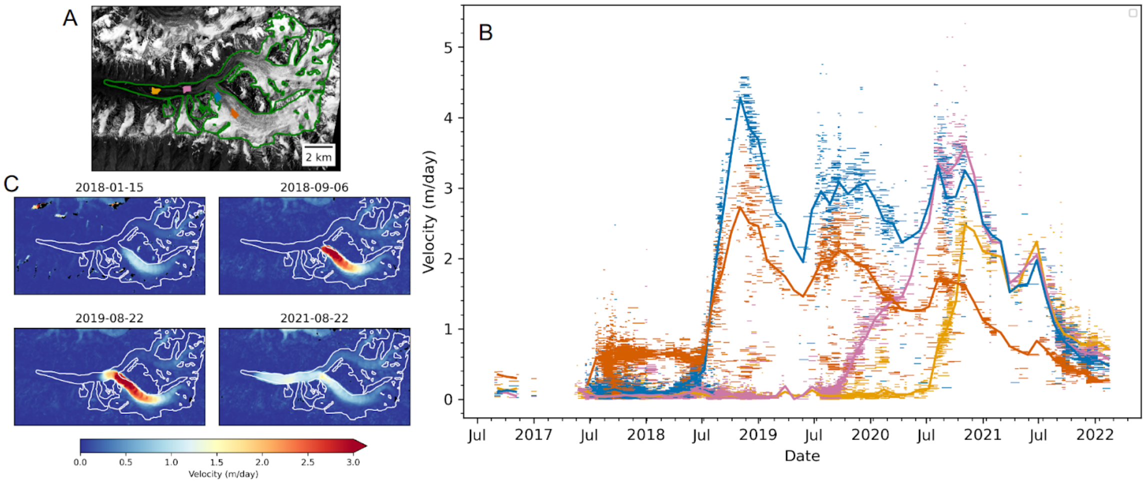

Figure 4.7: Surface velocity product over the A) Gando Glacier. B) Time series of velocity from short baseline pairs (¡40 days) sampled over 600 * 400 m boxes labeled in A). Width of the horizontal line denotes the time period of pairwise observations. Solid line is monthly median velocity. C) Distributed monthly median velocity maps through different phases of the surge, map titles represent center date of monthly median values. Note the propagation of surge from the southern tributary to the main trunk in the three year period C), and observed seasonality in flow imprinted on the surge cycle in (B) for the boxes orange, blue and pink.

4.7.4 Glacier velocity: Debris-covered glacier seasonal flow dynamics

Our spatio-temporally dense results over the heavily debris-covered Ngozumpa and Khumbu Glacier reveal dynamic flow patterns, with different extents and timings of speedups observed over the two glaciers. Over Ngozumpa Glacier, we observe clear seasonality over most of the western trunk, with peak velocities recorded in June and July (Figure 4.8E). Difference maps between peak (June) and minimum (November) flow velocities show the spatial extent of this speedup (Figure 4.8C,D). Along the main trunk, we observe isolated patches of speedup (Figure 4.8C,D), which on close inspection appear to be close to the locations of ice cliffs and supraglacial ponds. The change in velocity during June to November is approximately 66% of the November winter velocities. We also observe a difference in timing of speedup onset timing, mostly varying between February and April between 2018 to 2021, where we have sufficient data to obtain median velocities with high confidence (Figure 4.8E). We also observe post monsoon, fall speedup in the year of 2018 and 2019 for the pink box Figure 4.8A,E) and in the fall of 2019 over the blue box (Figure 4.8A,E). The time series over the orange box sampled near the terminus shows limited variability.

The patterns of seasonal speedup are more variable over Khumbu Glacier (Figure 4.9). We find that a large part of the main trunk exhibits seasonality (NMAD of monthly median values ¿0.04 m/day), until approximately 5 km away from the terminus (Figure 4.9B). The highest variability is exhibited over the famous Khumbu Glacier icefall (¿0.1 m/day), with lower magnitudes above and below it (Figure 4.9B). We first present results over areas below the icefall, and then discuss the dynamics around the icefall in the next section. We find that, in general, the peak velocity is achieved during the monsoon season, but with year to year variability in timing of velocity speedup onset (Figure 4.9C). The first three boxes are sampled over an area of exposed, clean ice, with ample crevasses. The next boxes are located over the debris cover region below the clean ice to debris transition zone. For the brown and orange boxes, we observe the onset of velocity increase either in the winter (December) or spring months (March/April). The time series over the red box shows some deviation from the general cycle in the years 2017, 2019 and 2020, where we observe speedup onset in the fall, straight after the expected end of the monsoon season. We do note the higher spread of individual pairwise values in the years of 2017 and 2020, which might explain the anomalous behavior. The velocity time series sampled from the boxes over the debris-covered areas show lower seasonal variability, but follow a similar pattern of maximum velocity being observed during the summer, monsoon months (Figure 4.9C).

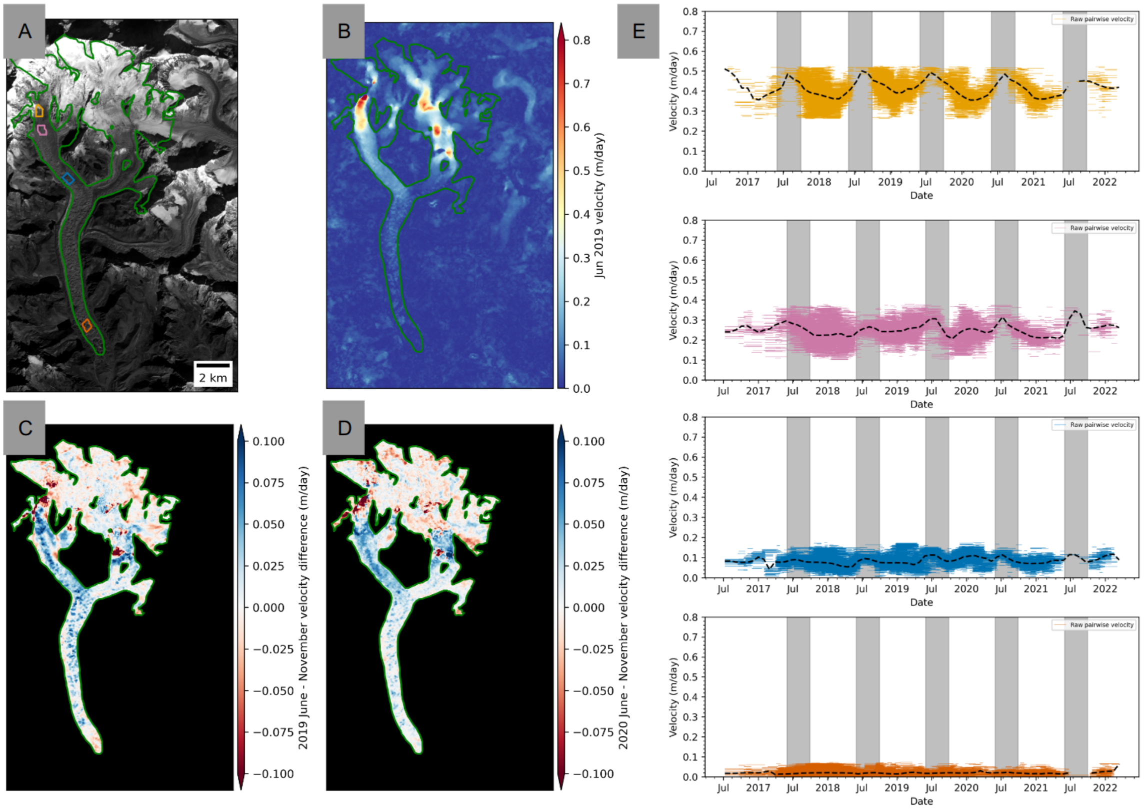

Figure 4.8: Surface velocity time series over Ngozumpa Glacier. A) Orthoimage prepared from Dove Classic NIR imagery acquired on 20181123 by Dove Classic satellites (104a, 103b, 1018), with locations of four boxes over which velocity measurements were sampled in (E). B) June 2019 median monthly velocity. Difference between June and November surface velocities during C) 2019 and D) 2020, with coherent patches blue denoting regions of speedup. E) Surface velocity time series sampled over boxes plotted in A). Horizontal lines represent individual pairwise velocity measurements obtained over the period denoted by the length of the horizontal colored lines. Black dotted line denotes the monthly median velocities. Gray boundary denotes the typical Monsoon period (June 1st to September 30). Note the seasonality in surface velocity, with maximum velocities observed during summer months of June/July/August for boxes on the western main trunk, with limited variability over the orange box sampled near the terminus.

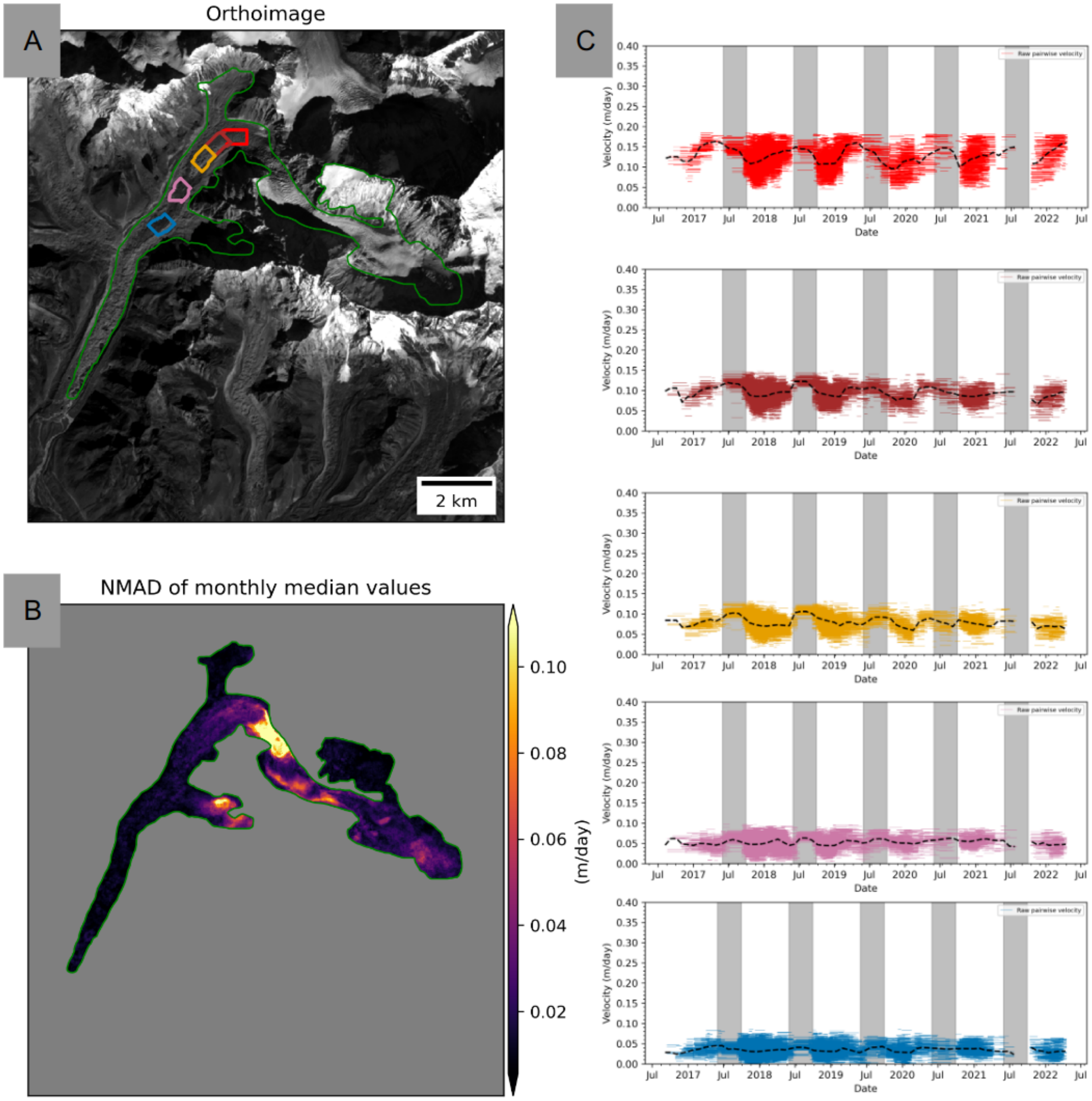

Figure 4.9: Khumbu Icefall dynamics. A) Orthoimage prepared from PlanetScope NIR imagery acquired on 20191010 by Dove Classic satellite 101b, with locations of colored boxes representing where velocity measurements are sampled in (C). B) Per-pixel NMAD map from the stack of monthly median values for the entire time series, which provides the robust variability metric. C) Velocity time series sampled over boxes shown in (A). We only used short baseline pairs (¡40 days) over icefall. Horizontal lines represent individual pairwise velocity measurements obtained over the period denoted by the length of the line. Black dotted line denotes the monthly median velocities. Gray boundary denotes typical Monsoon period (June 1st to September 30). Note highest velocities are obtained generally during monsoon period.

4.7.5 Glacier velocity: Khumbu Icefall dynamics

Icefalls are characterized by steep slopes where fast flowing ice stretches and thins, producing rapidly changing, highly crevassed surfaces. Icefalls in glaciers are analogous to the waterfalls in rivers, and it is very difficult to measure meaningful velocity over these glaciers using medium resolution, long temporal baseline image pairs. We now examine the performance of Dove Classic derived velocity products over the notoriously famous Khumbu Icefall (e.g., Altena and Kääb, 2020). We define the area covered by red and green boxes (Figure 4.10A,B) as the main icefall area, where the glacier narrows, is steep (¿20°, Figure 4.10B), sports a series of crevasses (Figure 4.10A,B) and has low ice thickness (¡100 m, Figure 4.10C). Above the icefall, we observe maximum surface velocity in June and July. Over the highly crevassed area above the main icefall, we see enhanced velocity seasonality, with maximum velocity achieved in June to August and sustained through the beginning of the winter period (October). Over the main icefall, we focus on only short baseline pairs (¡40 days), as long baseline pairs produce lower quality results due to feature decorrelation between the longer observation intervals. We find a maximum speedup of 33% during the 2017/18 and 2018/19 winters over the main icefall, with high velocities sustained through the end of the Julian year. There were very limited observations during the monsoon season of 2017 and 2018, but the data from following years hint that maximum velocity is achieved in July/August, which is sustained through the end of the Julian year. We observe a sharp decline in velocity in the box immediately downstream of the icefall, and less clear signs of seasonal variability from the available data, but do observe a velocity speedup during the spring season (March onward) (Figure 4.10D).

4.8 Discussion

4.8.1 Geometric quality of PlanetScope data, usability for glacier velocity measurement

The near daily, high resolution Dove Classic data provides huge potential for geodetic applications such as surface displacement mapping due to glacier flow or seismic events (earthquakes), but they have seen limited use due to product quality issues. As previously noted in several earlier studies, we also observed radiometric and geolocation artifacts, which need to be carefully considered when performing feature tracking. We find that after geolocation debiasing over static surfaces, the robust offset metric had near pixel accuracy for most cases. The extremely variable topography coupled with the smaller dimensions of a single Dove Classic image results in additional spatially variable geolocation artifacts for some image pairs. For instance, a single Dove Classic image covering the actively flowing western trunk and the snow-covered accumulation area of the Ngozumpa Glacier (Figure

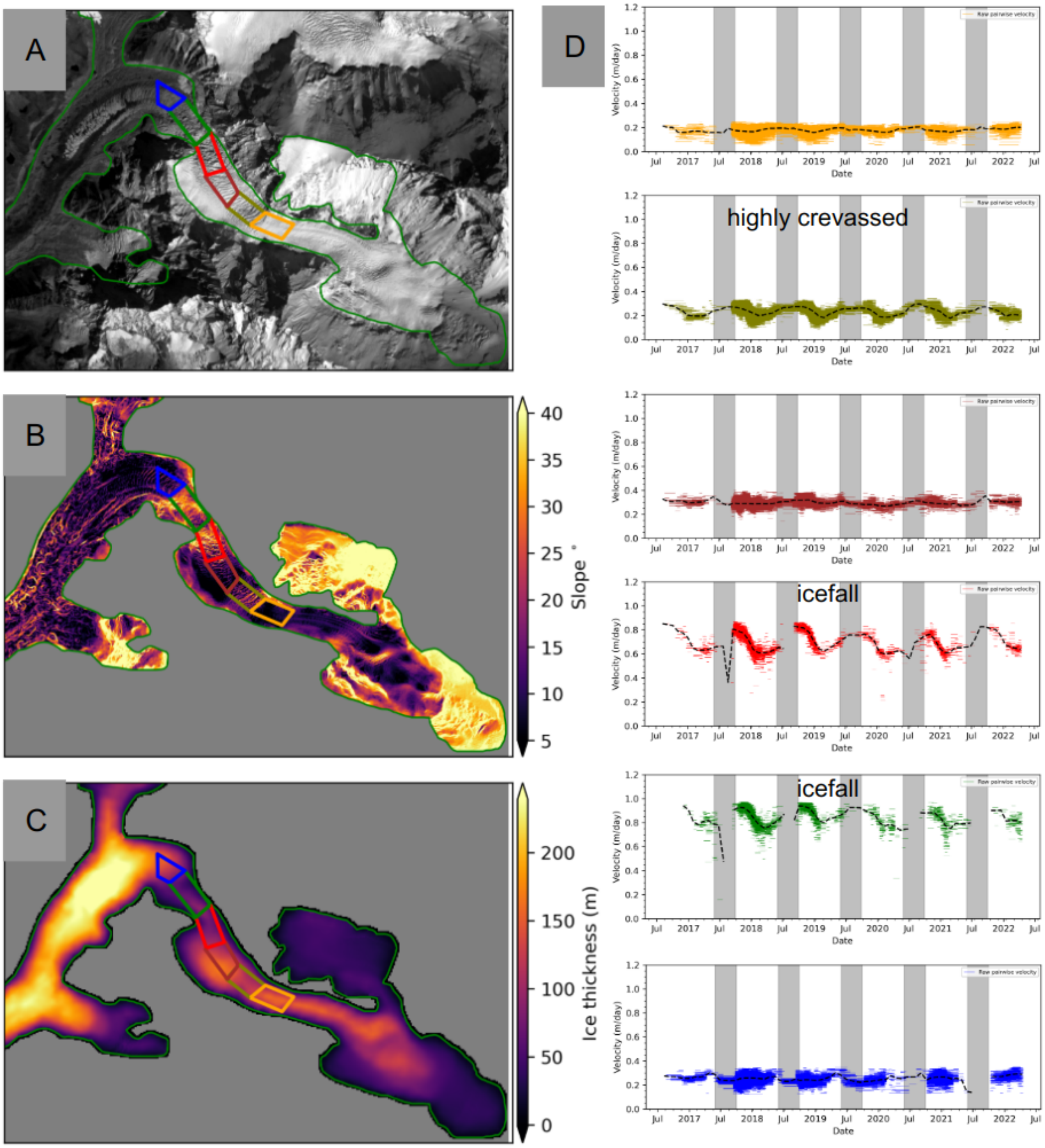

Figure 4.10: Khumbu Icefall dynamics. A) Orthoimage prepared from Dove Classic NIR imagery acquired on 20191010 by Dove Classic satellite 101b, with locations of boxes over which velocity measurements are sampled above, on and below the icefall. B) Slope map derived from HiMAT-v1 composite DEM (Shean, 2017) and C) Ice thickness map from Farinotti et al. (2019a). D) Velocity time series sampled over boxes shown in A,B and C. We only used short baseline pairs (<40 days) over icefall. Horizontal lines represent individual pairwise velocity measurements obtained over the period denoted by the length of the line. Black dotted line denotes the monthly median velocities. Gray boxes denote the typical Monsoon period (June 1st to September 30). Note enhanced seasonality in highly crevassed areas above the icefall (olive box) and over the icefall (red and green boxes), with sustained high velocities sustained in the fall period till October.

4.8A) vertical relief of 2 km, within the horizontal along-track image footprint of 8 km. We observed geolocation artifacts correlated with topography for several pairwise displacement observations. In these cases, the geolocation artifacts were preferentially isolated towards topographic highs (mountain crests) and lows (valleys). We investigated several potential sensor specific causes for these artifacts, such as unaccounted lens distortion and optical decentring issues, with consultation with engineers at Planet, but could not isolate sensors with known optical issues to always cause these errors. The example depicted in Figure C.1, where we found topographically correlated geolocation artifacts over one displacement map, but not in the next map collected in the same ascending pass by the same satellite pair, suggests that these errors are possibly caused during internal rectification procedures employed at Planet. This makes these errors difficult to predict, as they are also not discernible in visible imagery, without performing full scale feature tracking.

The use of consistent rectification procedures resulted in fewer NIR derived displacement pairs with topographically related geolocation artifacts, and the procedure greatly reduced the subpixel block offset artifact. Our spatiotemporal median aggregation algorithm reduced the geolocation artifacts further, and the monthly median velocity maps show lower effect of geolocation errors, with robust offset metric over stable terrain being less than 0.02 m/day in most cases.

4.8.2 Potential causes for observed velocity variability

Short term fluctuations in glacier flow are driven by changes in surface and basal hydrologic conditions and are greatly influenced by climatic factors (e.g., surface melt, precipitation), but observations of the same over mountain glaciers around the world are still limited. Using the near daily Dove Classic imagery, we are able to decipher interesting patterns in seasonal surface velocity for glaciers moving at widely different speeds. For the surging Gando Glacier, our velocity record captured the initial surge episode at 2018 in great detail, and shows evidence of flow seasonality superimposed on the surge-enhanced velocity during the period of investigation. The increase in flow velocity during the spring season is expected, and can most likely be explained by increased availability of water at the glacier base due to the onset of melt at the surface, resulting in enhanced basal sliding (e.g., Iken and Bindschadler, 1986; Moon et al., 2014). The flow velocity decreases gradually through the season, as the basal channel becomes developed to hold more water, resulting in a reduction in basal sliding (e.g., Cuffey and Paterson, 2010) . We also observe some variability at very short time spans during the summer period after the surge onset, which might be caused due to increased water fluctuations at the base due to short term forcings (e.g., due to increased rainfall, Kehrl et al., 2015). Underpinning the exact phenomenon causing these short term fluctuations is beyond the scope of our current study, but our preliminary record and workflow is a good place to start. Similar seasonal variation in velocity has been observed for surging (e.g., Beaud et al., 2022; Dunse et al., 2015; Round et al., 2017) and non-surging glaciers (e.g., Nanni et al., 2022; Vijay et al., 2019) around the world. While we used a standard one month median approach, given the high magnitude of the signal we could also extract the signals at shorter intervals, which will provide the opportunity to model these events in great detail, as shown in Beaud et al. (2022).

The seasonal flow fluctuations over the Ngozumpa and Khumbu Glaciers confirm that flow seasonality exists over the debris-covered glaciers, with increases in velocity always occurring during the start of spring and summer. Velocities are highest during the monsoon period. The results indicate that the combination of summer surface melt and monsoonal rainfall provide enough water to propagate to the base of the glacier, resulting in flow enhancement. Parts of the glacier in higher accumulation areas also depict fall speedup during certain years, a phenomenon which was also observed in a recent study over Pamir Himalaya by Nanni et al. (2022). In our case, the fall speedup did not propagate over longer lengths downstream, and appear to be localized. Nanni et al. (2022) hypothesized that the fall speedup might be explained by drainage events of supraglacial ponds or the gradual closure of the hydrological system. These processes could be explored in detail in future work. While the observations from our study of enhanced flow during summers are expected and have been observed for glaciers elsewhere, our spatio-temporal measurements provide the unique potential to study the time at which the velocity speed up begins, how long it continues, and the magnitude of velocity change. These measurements also provide the opportunity to study these variations in the context of the availability of surface water by melting or rainfall. Continued research along this direction will help in improving the flow modeling components of glacier evolution models, and understand how these parameters will evolve with changes in climate and surface debris evolution.

Finally, our study is the first to show flow fluctuations over an icefall, which are generally difficult to observe using coarse resolution imagery. While Altena and Kääb (2020) used short temporal baseline measurements to derive a composite Khumbu Icefall velocity product, they did not use the product to reveal the seasonal fluctuations. The flow fluctuations over Khumbu Icefall are contrary to the existing literature over glaciers in Alaska (Armstrong et al., 2017) and Mt. Rainier (Allstadt et al., 2015), where flow velocities over icefalls were found to be the same during summer and winter periods. We now provide some reasons which could explain our contrasting observations. Firstly, the Khumbu Icefall is longer, and has higher ice thickness than those observed in the Alaskan glaciers or Nisqually Glacier on Mt. Rainier. Modeled ice thickness estimates (Farinotti et al., 2019a) also indicate thicker ice (50 m) when compared to that over the Nisqually Glacier icefall (0 m). This might result in a smaller hydraulic potential gradient over the Khumbu Glacier icefall, which could still allow changes in subglacial hydrology to develop (Armstrong et al., 2017), resulting in flow fluctuations. The second reason might be the different observation time periods in the Armstrong et al. (2017) and Allstadt et al. (2015) studies, and the time period over which velocity variation was observed over the Khumbu Icefall. In our case, the velocity decline generally starts at the start of the new Julian year, and appears to be similar during monsoon to December. Allstadt et al. (2015)'s study period only spanned June to November, over a period where variability was also limited over Khumbu (Figure 4.10E). Similarly Armstrong et al. (2017) only compared changes between summer and winter averaged from measurements acquired over several years, which might have missed the time period during which an icefall would show variability. The reason why velocity is sustained through summer and fall over the Khumbu Icefall is difficult to assign and should be evaluated in future work.

4.9 Summary and conclusions

Glacier surface velocity controls the mass redistribution over a glacier and allows for adjustment of the glacier to the input climate forcing. Short term changes in surface velocity are driven by changes in basal sliding and subglacial hydrology systems, and are controlled by ambient meteorological conditions (e.g., temperature, precipitation). Observations of seasonal flow fluctuations over glaciers in High Mountain Asia are currently very limited, mostly owing to the detection limits of currently available ice velocity products (e.g., ITS_LIVE) over slow flowing glaciers. Archives of near daily, high-resolution Planet imagery provide an exciting opportunity to approach seasonal flow estimation research, but have seen limited use by the community due to variable data quality and high computational demand. In this work, we explore the potential of using PlaneScope Dove Classic imagery to derive systematic flow velocity evolution over glaciers in HMA. During our research, we discovered geolocation and radiometric artifacts, which were communicated with engineers at Planet who provided us with data reprocessed using a standard processing scheme, with greatly improved geometric quality. We used the improved dataset and distributed, scalable computing resources to process a large sample of ice velocity maps over seasonal intervals. We then used spatio-temporal median stacking strategies to derive continuous monthly velocity measurements with precision on the order of 0.01 to 0.03 m/day.

The results are used to study short term seasonal flow variations over three glaciers in two regions with different climatic regimes and undergoing different flow regimes. Over the surging Gando Glacier, our record captures the surge propagation in great detail and shows evidence of flow seasonality imprinted upon the surge signal. Our results also capture short term changes during summer, which might be explained by rapid changes in subglacial water availability. Over the heavily debris-covered Ngozumpa and Khumbu Glaciers, we observe enhanced flow velocities during the spring and summer monsoon period, which could be explained by the increased water availability at the glacier base jointly driven by summer surface melt and monsoon rainfall. We also observed the otherwise unlikely event of fall speedup localized over the upper ablation areas in certain years. Seasonal speedup was not evident over the heavily debris-covered terminus of Ngozumpa and Khumbu Glaciers. These regions registered limited velocity variability, apart from isolated signals due to geomorphological evolution along ice cliffs and supraglacial ponds. The magnitude of speedup over the western trunk of Ngozumpa Glacier was approximately 67% of the base winter flow. Our results also capture velocity variations over the Khumbu Icefall, where high flow velocities are sustained throughout the summer and fall months. Khumbu Icefall flow declines from December to early spring, with an average decrease of 33%. Changes in flow over an icefall have not been documented in previous research.

Our workflow to estimate seasonal flow velocity from Planet data shows promise in deriving short term velocity measurements with high precision. Future work should explore the relationships between flow fluctuations and meteorological conditions at the surface (temperature, precipitation, melt onset timings) to better understand how the flow patterns respond to changes in forcing. Improved understanding of these interactions will help in better parameterization of glacier flow in glacier evolution models, and ultimately predict how the glacier flow patterns will evolve in a future warming world.

Acknowldgements

Shashank Bhushan was supported by the NASA FINESST fellowship (80NSSC19K1338) and the NASA HiMAT-2 award (80NSSC20K1595). David Shean was supported by the NASA HiMAT-2 award (80NSSC20K1595). We acknowledge discussions with the GLAFT team, velocity sub-group of the NASA HiMAT-2 team and the Planet-Caltech-UW stereo processing group, which greatly improved the methods and motivations of the study. Resources supporting this work were provided by the NASA High-End Computing (HEC) Program through the NASA Advanced Supercomputing (NAS) Division at Ames Research Center. Access to Planet data was provided by the NASA Commercial SmallSat Data Acquisition Program (`https://www.earthdata.nasa.gov/esds/csda`). We thank the Ph.D. thesis committee members (Dr. Jessica Lundquist and Dr. David Rounce) for reading and providing feedback on the drafts. We acknowledge support provided by Seth Vanderwilt and Shahzaib Khan in deciphering Sentinel-2 product footprint.

Author Contributions

SB and DS conceived the project. SB and DS participated in funding acquisition. SB performed literature survey, led method and code development, produced and analyzed results, produced the figures and wrote the first draft of the manuscript. DS supervised the entire research and provided essential feedback during methods development and analysis. SH provided feedback on the data processing strategy, conducted the cloud cover analysis and provided additional mentorship. SP provided inputs on the satellite images, and produced the systematically reprocessed products which were used in the final analysis.

Chapter 5

PHOTOGRAMMETRY APPLICATIONS BEYOND HIGH-RESOLUTION GLACIER SURFACE MASS BALANCE AND DYNAMICS: CONTRIBUTIONS TO COLLABORATIVE EFFORTS

This chapter briefly discusses some of the co-authored collaborative projects I participated in during the Ph.D. program. Specifically, I discuss the links between the three main chapters in the dissertation and the co-authored works.

5.1 HMA glacier mass balance study by Shean et al. (2020)

This study estimated the glacier-wide mass balance of 99% of glaciers in High Mountain Asia using time series of ASTER and Maxar GeoEye and WorldView-1/2/3 DEMs. We estimated a total mass loss of 19.0 ± 2.5 Gt/yr (0.19 ± 0.03 m w.e./yr) over the entire region. We found that excess glacier meltwater runoff due to negative glacier mass balance in each basin constitutes 12 to 53% of the total basin-specific glacier meltwater runoff.

This collaborative work allowed me to do a thorough literature review of existing work and helped me realize the key processes that still required improved observations. This was very helpful as I composed my NASA FINESST proposal. Additionally, I assisted in computing basin-wide uncertainty estimates by properly accounting for error correlation length scales. I performed a geostatistical semi-variogram analysis by considering elevation change uncertainty for all 95000 individual glaciers and determined to what distances these values were correlated (Figure 5.1). Based on this assessment, we divided the entire region into tessellated hexagons. We assumed the glacier mass balance uncertainties for all glaciers within the hexagon to be correlated and summed them to estimate the mass balance uncertainty of each hexagonal bin. We then aggregated these hexagon uncertainties over different basins and the entire HMA domain in quadrature, assuming they were independent and uncorrelated.

5.2 Chamoli disaster response effort by Shugar et al. (2021)

On February 7th, 2021, a massive flood in the RishiGanga/Dhauliganga rivers in the Chamoli district of Uttarakhand, India, caused massive infrastructure damage at two NTPC Hydropower stations and left more than 200 people missing or dead. There were various

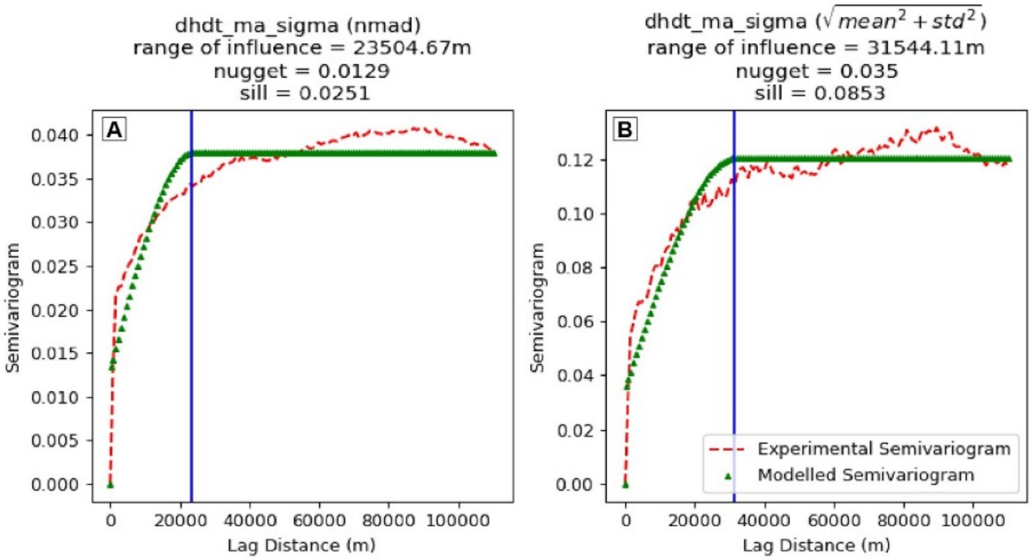

Figure 5.1: Spherical variogram fits used to assess spatial autocorrelation of glacier mass balance uncertainty values between glacier polygon centroids. Two different glacier mass balance uncertainty metrics were considered, using statistics for observed dh/dt values over static surfaces around each polygon: A) NMAD and B) RMSE ($mean^2 + std^2$). Semi-variograms were fit for elevation change uncertainty. The red curve is the experimental semi-variogram, the green curve is the corresponding modeled spherical semi-variogram, and the blue line is the lag distance (range of influence) at which the model attains the sill value.

initial hypotheses as to what might have been the geophysical causes behind the events, and the risk of cascading hazard events loomed large. We collaborated with an international group of scientists to coordinate a rapid remote-sensing investigation. We collaborated with colleagues from CNES/CNRS, France, to produce high-resolution DEMs and orthoimage time series from 2014 to 2021. Specifically, the UW team coordinated satellite tasking (Maxar/DigitalGlobe and Planet) to acquire post-event imagery and queried/acquired archive pre-event imagery from Maxar/DigitalGlobe and ISRO/NRSC. We rapidly processed these images and released the derived DEMs (e.g., Figure 5.2) using open-data Creative Commons licenses. We used the DEM-derived elevation change maps to pinpoint the source of the landslide triggering the event, study the evolution of antecedent conditions before the landslide, and provide inputs on the geomorphic change post the event (mass movement from the landslide source area, sediment deposition, and erosion along the valleys). The larger group also used the products to perform numerical simulations of the flood path and explore the potential of future cascading hazards. The combined findings from this international group were communicated to response teams in India in near real time.

It was during this effort that I rapidly tested different stereo-processing parameters to come up with a workflow that provided the highest resolution DEM with minimum possible processing noise, which was crucial for a lot of geomorphological and modeling efforts. Additionally, just before the effort, I was learning the ropes of autoRIFT through collaborations with the feature tracking group. During this effort, I wrote the custom, end-to-end autoRIFT wrapper script to produce a velocity map from Planet image pairs.

5.3 Analysis of the pre-collapse motion of Chamoli rock-ice avalanche by Van Wyk de Vries et al. (2022a)

We conducted a follow-up study to explore the pre-collapse motion of the failed block using datasets from multiple satellite observations. This study was led by fellow graduate student Maximillian Van Wyk de Vries. We found that the failed block was in motion several years before the collapse, and a crack opening had developed in ∼2016. The crack was subsequently filled with snow and debris in the later years. This loading of extra material, coupled with the degradation of the crack might have reduced the block stability, resulting in its eventual failure. We concluded that while all the observations indicated the block was becoming increasingly unstable, we could not have predicted the collapse time with the currently available satellite observations alone. This study has important implications for future hazard preparedness activities and highlights the advantages and limitations of satellite observations for observing such events in the future.

I processed additional CartoSat-1 DEMs to derive elevation change and surface velocity measurements when the crack in the headwall had started developing. During this study, I first used Planet image time series to derive velocity maps from multiple pairs acquired in 2020. Max and I then began exploring combining multiple pairwise velocity observations into fewer aggregated observations using the weighted average (Van Wyk de Vries and Wickert, 2020) and least-squares SBAS flavor inversion technique (Yunjun et al., 2019). We found that the systematic outliers in the Planet velocity time series resulted in noise in the reduced velocity maps. I realized these issues need to be addressed for deriving short-term velocity measurements. Nevertheless, velocity maps from CartoSat-1 and average annual velocity maps from Planet imagery were used to validate the Sentinel-2 derived results (Figure 5.3).

5.4 GLAcier Feature Tracking testkit (GLAFT): A statistically- and physically-based framework for evaluating glacier velocity products derived from satellite image feature tracking by Zheng et al. (2023)

As described in Chapters 3 and 4, feature tracking is a versatile technique to observe surface displacement, including glacier velocity. The choice of processing software and processing parameters results in different levels of details and associated measurement noise, even from using the same image products. The processing choices are dictated by the level of detail a particular project requires, and often, researchers test a series of non-standardized processing parameters to determine what works best for their case. In this study led by Whyzay Zheng, we proposed two metrics that depend on a) identifying correct matches and associated uncertainty over surrounding non-glacierized, static areas, and b) evaluating the spatial coherence of output glacier velocity and its relationship with glacier strain rates, which can be used to evaluate glacier velocity products from different softwares/parameters. The metrics were evaluated by comparing results from different feature tracking packages to in situ GNSS record at the Kaskawulsh Glacier, Yukon, Canada, and to synthetically shifted images (Figure 5.4). Whyzay led the development of the open-source GLAFT package, which sets up a benchmark for future large-scale glacier velocity intercomparison exercises.

While working in this group, I invested a lot of time exploring the different pre-processing parameters, which was very helpful for Chapter 4. As a group, we discussed common nuisances in feature tracking, which are described in Zheng et al. (2023). While working with this group, I was introduced to autoRIFT. I provided results from the vmap and autoRIFT software and the initial code for conducting tests with synthetically shifted images.

5.5 Stereo geoemetry experiments by Hu et al. in prep

The output DEM accuracy from satellite stereogrammetry is a function of the input image resolution, view geometry (e.g., Jeong et al., 2015), and the stereo processing parameters [e.g., correlation algorithm, point cloud gridding strategy (e.g., Dehecq et al., 2020)] used to produce the DEMs. In an effort led by J. Michelle Hu, we systematically evaluated these parameters to determine the best strategies to derive DEMs for our science applications involving glacier change in High-Mountain Asia and quantifying seasonal snow depth over sites in the Western U.S.

Our experiments used two same-day overlapping WorldView-3 stereo pairs over Grand Mesa, Colorado. This allowed us to form six pairs (2 along-track, 4 cross-track) at varying stereo geometries (9 to 50° convergence angles). All the input images were resampled at varying resolutions (0.36 to 4 m) and processed with different settings in the NASA Ames Stereo Pipeline. We evaluated the derived DEM accuracy by assessing the topography structure resolved in the output DEM and by comparing the DEMs to contemporaneous (8 days apart) airborne LiDAR point clouds (ASO). We find that large convergence angle stereo pairs produce more accurate point clouds and DEMs at the expense of increased data gaps over steep and isolated pointed surfaces (e.g., trees, Figure 5.5) for both independent experiments. Additionally, the output DEM quality over snow surfaces decreased with coarser resolution input imagery due to correlation issues. The DEM production workflow and settings from this experiment were used to produce DEMs for chapters presented in Michelle's and my dissertation (Chapter 3).

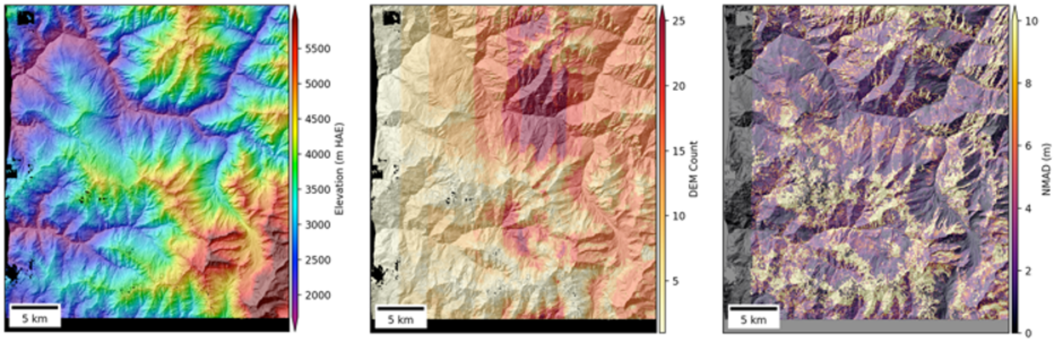

Figure 5.2: Pre-event DEM products derived using 38 stereo pairs formed by 11 snow-free Maxar WV-1/2 stereo pairs from fall 2015 (Bhushan and Shean, 2021). Left) Wt.average composite, middle) per-pixel count map, and right) per-pixel elevation NMAD describing the product's relative accuracy.

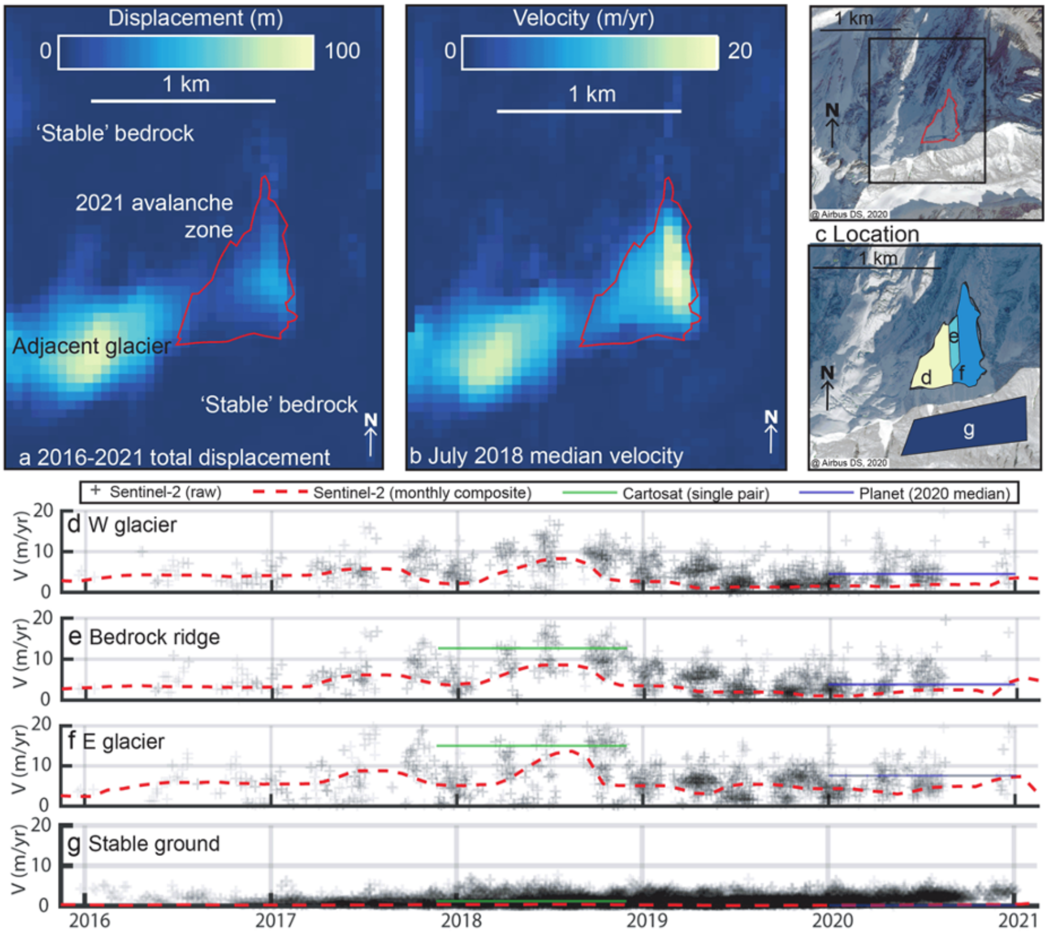

Figure 5.3: From Van Wyk de Vries et al. (2022a), this figure describes the horizontal movement of the collapse block since 2016. a) Total displacement map from 2016 to 2021 derived using images from Sentinel-2. b) median velocity from July 2018, when the block's velocity was the highest, c) Location map for context. The bottom panels depict velocity time series for d) West Glacier, e) bedrock ridge, f) East Glacier, and g) stable ground, with locations marked in (c). Measurements from Cartosat-1 image pairs and Planet image time series were used to corroborate the Sentinel-2 velocity measurements for 2018 and 2020 periods, respectively.

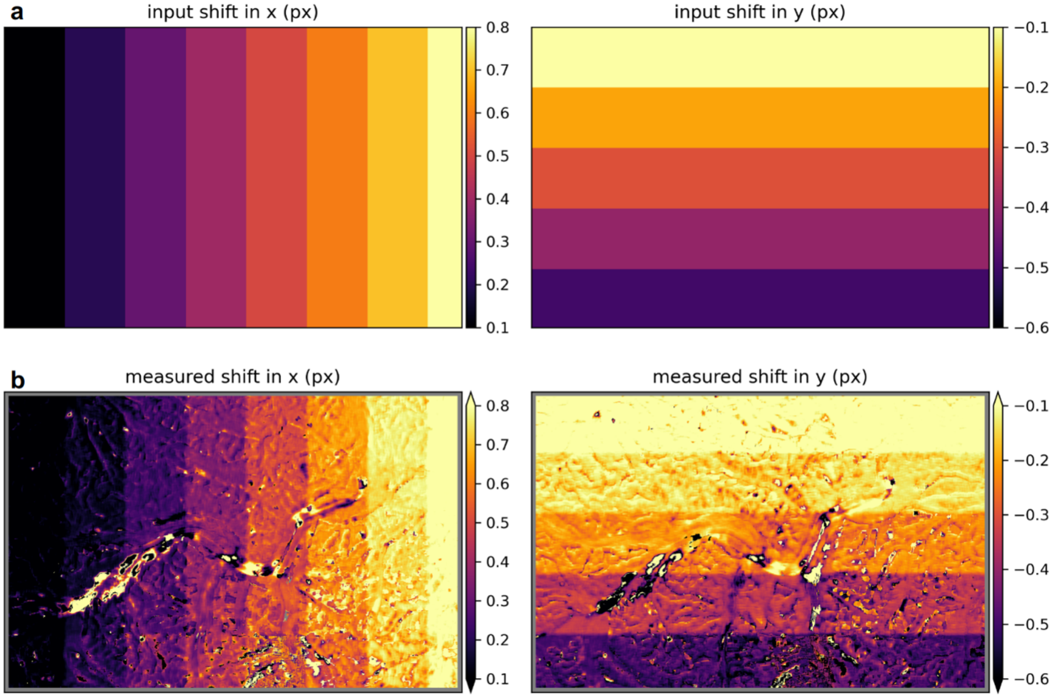

Figure 5.4: From Zheng et al. (2023), this figure demonstrates feature tracking performance by measuring known, synthetic offsets in an image. A) The x and y components of the synthetic offset field applied to a single Landsat 8 image acquired on 20180304 and B) Feature tracking results (vmap, kernel size = 35px, parabolic subpixel refinement). The output velocity map shows a larger deviation on the glacier flow area than the static region.

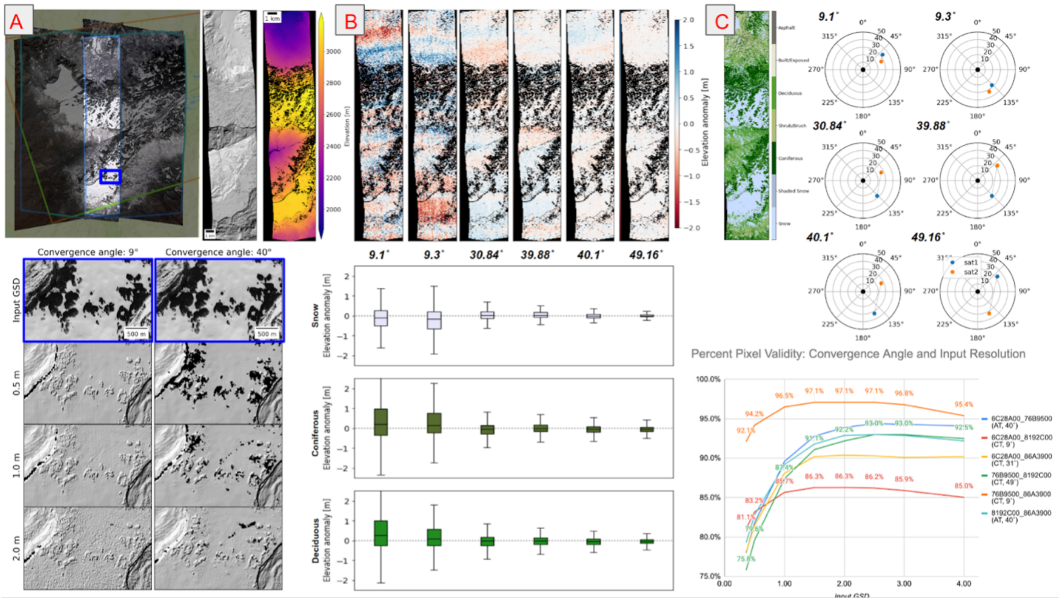

Figure 5.5: Results from on-orbit stereo parameter tests using single-pass, 4-image multi-view WV-3 stereo collection over Grand Mesa, CO, on 2/1/17. The lower left shows orthoimages, and stereo DSM shaded relief maps for resampled input GSD and small (9°) and large (40°) stereo convergence angles. Note variable noise and gaps (occlusions, failed correlation) over vegetation and flat surfaces. The upper center shows DEM "anomaly" maps for all possible stereo pairs relative to a per-pixel median DSM composite. The bottom center shows bias and spread for priority STV landcover types (snow, coniferous, deciduous) defined by ML classification (C) output using 8-band MS images (Hu and Shean, 2022). Larger convergence angles result in reduced "jitter" artifacts and noise. The upper right shows stereo geometry for each pair. The bottom right shows the percentage of DSM that is gap-free vs. input image GSD.

BIBLIOGRAPHY

Aati, S., Avouac, J.-P., Rupnik, E., and Deseilligny, M.-P. (2022). Potential and Limitation of PlanetScope Images for 2-D and 3-D Earth Surface Monitoring With Example of Applications to Glaciers and Earthquakes. *IEEE Transactions on Geoscience and Remote Sensing* 60, 1–19. doi:10.1109/TGRS.2022.3215821

Ageta, Y. and Higuchi, K. (1984). Estimation of Mass Balance Components of a Summer-Accumulation Type Glacier in the Nepal Himalaya. *Geografiska Annaler. Series A, Physical Geography* 66, 249. doi:10.2307/520698

Albino, F., Smets, B., d'Oreye, N., and Kervyn, F. (2015). High-resolution TanDEM-X DEM: An accurate method to estimate lava flow volumes at Nyamulagira Volcano (D. R. Congo): TANDEM-X DEM TO DERIVE LAVA FLOW VOLUMES. *Journal of Geophysical Research: Solid Earth* 120, 4189–4207. doi:10.1002/2015JB011988

[Dataset] Alexandrov, O. (2017). IceBridge DMS L3 Ames Stereo Pipeline Photogrammetric DEM, Version 1. doi:10.5067/HYV1T0G7LVHE. Type: dataset

Alley, K. E., SCAMBOS, T. A., ANDERSON, R. S., RAJARAM, H., POPE, A., and HARAN, T. M. (2018). Continent-wide estimates of antarctic strain rates from landsat 8-derived velocity grids. *Journal of Glaciology* 64, 321–332. doi:10.1017/jog.2018.23

Allstadt, K. E., Shean, D. E., Campbell, A., Fahnestock, M., and Malone, S. D. (2015). Observations of seasonal and diurnal glacier velocities at Mount Rainier, Washington, using terrestrial radar interferometry. *The Cryosphere* 9, 2219–2235. doi:10.5194/tc-9-2219-2015

Altena, B. and Kääb, A. (2020). Ensemble matching of repeat satellite images applied to measure fast-changing ice flow, verified with mountain climber trajectories on khumbu icefall, mount everest. *Journal of Glaciology* 66, 905–915. doi:10.1017/jog.2020.66

Amer, F. (2006). DIGITAL BLOCK ADJUSTMENT. *The Photogrammetric Record* 4, 34–49. doi:10.1111/j.1477-9730.1962.tb00324.x

Anderson, L. S., Armstrong, W. H., Anderson, R. S., and Buri, P. (2021). Debris cover and the thinning of Kennicott Glacier, Alaska: in situ measurements, automated ice cliff delineation and distributed melt estimates. *The Cryosphere* 15, 265–282. doi:10.5194/tc-15-265-2021

Armstrong, R. L., Rittger, K., Brodzik, M. J., Racoviteanu, A., Barrett, A. P., Khalsa, S.-J. S., et al. (2019). Runoff from glacier ice and seasonal snow in High Asia: separating melt water sources in river flow. *Regional Environmental Change* 19, 1249–1261. doi: 10.1007/s10113-018-1429-0

Armstrong, W. H. (2017). Glacier Sliding from Space: Multi-Scale Remote Sensing, Geodesy, and Numerical Modeling to Understand Glacier Mechanics , 130

Armstrong, W. H., Anderson, R. S., Allen, J., and Rajaram, H. (2016). Modeling the WorldView-derived seasonal velocity evolution of Kennicott Glacier, Alaska. *Journal of Glaciology* 62, 763–777. doi:10.1017/jog.2016.66

Armstrong, W. H., Anderson, R. S., and Fahnestock, M. A. (2017). Spatial Patterns of Summer Speedup on South Central Alaska Glaciers: Patterns of Glacier Summer Speedup. *Geophysical Research Letters* 44, 9379–9388. doi:10.1002/2017GL074370

Armstrong, W. H., Polashenski, D., Truffer, M., Horne, G., Hanson, J. B., Hawley, R. L., et al. (2022). Declining Basal Motion Dominates the Long-Term Slowing of Athabasca Glacier, Canada. *Journal of Geophysical Research: Earth Surface* 127. doi:10.1029/2021JF006439

Ballesteros-Cánovas, J. A., Trappmann, D., Madrigal-González, J., Eckert, N., and Stoffel, M. (2018). Climate warming enhances snow avalanche risk in the Western Himalayas. *Proceedings of the National Academy of Sciences* 115, 3410–3415. doi:10.1073/pnas.1716913115

Beaud, F., Aati, S., Delaney, I., Adhikari, S., and Avouac, J.-P. (2022). Surge dynamics of Shisper Glacier revealed by time-series correlation of optical satellite images and their utility to substantiate a generalized sliding law. *The Cryosphere* 16, 3123–3148. doi:10.5194/tc-16-3123-2022

Belart, J. M. C., Berthier, E., Magnússon, E., Anderson, L. S., Pálsson, F., Thorsteinsson, T., et al. (2017). Winter mass balance of Drangajökull ice cap (NW Iceland) derived from satellite sub-meter stereo images. *The Cryosphere* 11, 1501–1517. doi:10.5194/tc-11-1501-2017

Benn, D., Bolch, T., Hands, K., Gulley, J., Luckman, A., Nicholson, L., et al. (2012). Response of debris-covered glaciers in the Mount Everest region to recent warming, and implications for outburst flood hazards. *Earth-Science Reviews* 114, 156–174. doi: 10.1016/j.earscirev.2012.03.008

Benn, D. I., Thompson, S., Gulley, J., Mertes, J., Luckman, A., and Nicholson, L. (2017). Structure and evolution of the drainage system of a Himalayan debris-covered glacier, and its relationship with patterns of mass loss. *The Cryosphere* 11, 2247–2264. doi: 10.5194/tc-11-2247-2017

Berthier, E., Floriciou, D., Gardner, A. S., Gourmelen, N., Jakob, L., Paul, F., et al. (2023). Measuring glacier mass changes from space—a review. *Reports on Progress in Physics* 86, 036801. doi:10.1088/1361-6633/acaf8e

Berthier, E. and Vincent, C. (2012). Relative contribution of surface mass-balance and ice-flux changes to the accelerated thinning of mer de glace, french alps, over1979-2008. *Journal of Glaciology* 58, 501–512. doi:10.3189/2012JoG11J083

Berthier, E., Vincent, C., Magnússon, E., Gunnlaugsson, , Pitte, P., Le Meur, E., et al. (2014). Glacier topography and elevation changes derived from Pléiades sub-meter stereo images. *The Cryosphere* 8, 2275–2291. doi:10.5194/tc-8-2275-2014

[Dataset] Beyer, R., Alexandrov, O., ScottMcMichael, Broxton, M., Lundy, M., Husmann, K., et al. (2020). Neogeographytoolkit/stereopipeline 2.7.0. doi:10.5281/zenodo.3963341

Beyer, R. A., Alexandrov, O., and McMichael, S. (2018). The Ames Stereo Pipeline: NASA's Open Source Software for Deriving and Processing Terrain Data. *Earth and Space Science* 5, 537–548. doi:10.1029/2018EA000409

Bhambri, R., Hewitt, K., Kawishwar, P., and Pratap, B. (2017). Surge-type and surge-modified glaciers in the Karakoram. *Scientific Reports* 7. doi:10.1038/s41598-017-15473-8

[Dataset] Bhushan, S. and Shean, D. (2021). Chamoli Disaster Pre-event 2-m DEM Composite: September 2015. doi:10.5281/zenodo.4554647

[Dataset] Bhushan, S., Shean, D., Alexandrov, O., and Henderson, S. (2020). uw-cryo/skysat_stereo: Zenodo doi release. doi:10.5281/zenodo.3940086

Bhushan, S., Shean, D., Alexandrov, O., and Henderson, S. (2021). Automated digital elevation model (DEM) generation from very-high-resolution Planet SkySat triplet stereo and video imagery. *ISPRS J. Photogramm. Remote Sens* doi:https://doi.org/10.1016/j.isprsjprs.2020.12.012

Bisset, R. R., Dehecq, A., Goldberg, D. N., Huss, M., Bingham, R. G., and Gourmelen, N. (2020). Reversed Surface-Mass-Balance Gradients on Himalayan Debris-Covered Glaciers Inferred from Remote Sensing. *Remote Sensing* 12, 1563. doi:10.3390/rs12101563

Bolch, T., Kulkarni, A., Kääb, A., Huggel, C., Paul, F., Cogley, J. G., et al. (2012). The State and Fate of Himalayan Glaciers. *Science* 336, 310–314. doi:10.1126/science.1215828

Brook, M., Hagg, W., and Winkler, S. (2013). Debris cover and surface melt at a temperate maritime alpine glacier: Franz Josef Glacier, New Zealand. *New Zealand Journal of Geology and Geophysics* 56, 27–38. doi:10.1080/00288306.2012.736391

Brun, F., Berthier, E., Wagnon, P., Kääb, A., and Treichler, D. (2017). A spatially resolved estimate of High Mountain Asia glacier mass balances from 2000 to 2016. *Nature Geoscience* 10, 668–673. doi:10.1038/ngeo2999

Brun, F., Wagnon, P., Berthier, E., Shea, J. M., Immerzeel, W. W., Kraaijenbrink, P. D. A., et al. (2018). Ice cliff contribution to the tongue-wide ablation of Changri Nup Glacier, Nepal, central Himalaya. *The Cryosphere* 12, 3439–3457. doi:10.5194/tc-12-3439-2018

Buri, P., Miles, E. S., Steiner, J. F., Ragettli, S., and Pellicciotti, F. (2021). Supraglacial Ice Cliffs Can Substantially Increase the Mass Loss of Debris-Covered Glaciers. *Geophysical Research Letters* 48. doi:10.1029/2020GL092150

Buri, P. and Pellicciotti, F. (2018). Aspect controls the survival of ice cliffs on debris-covered glaciers. *Proceedings of the National Academy of Sciences* 115, 4369–4374. doi:10.1073/pnas.1713892115

Buri, P., Pellicciotti, F., Steiner, J. F., Miles, E. S., and Immerzeel, W. W. (2016). A grid-based model of backwasting of supraglacial ice cliffs on debris-covered glaciers. *Annals of Glaciology* 57, 199–211. doi:10.3189/2016AoG71A059

Büyüksalih, G. and Jacobsen, K. (2006). Generation and validation of Digital Elevation Models based on satellite images , 6

Christopherson, J., Ramaseri Chandra, S., and Quanbeck, J. (2019). *2019 Joint Agency Commercial Imagery Evaluation—Land remote sensing satellite compendium: U.S. Geological Survey Circular 1455*. Tech. rep. doi:doi.org/10.3133/cir1455

Coe, J. A., Bessette-Kirton, E. K., and Geertsema, M. (2018). Increasing rock-avalanche size and mobility in Glacier Bay National Park and Preserve, Alaska detected from 1984 to 2016 Landsat imagery. *Landslides* 15, 393–407. doi:10.1007/s10346-017-0879-7

Cooley, S., Smith, L., Stepan, L., and Mascaro, J. (2017). Tracking Dynamic Northern Surface Water Changes with High-Frequency Planet CubeSat Imagery. *Remote Sensing* 9, 1306. doi:10.3390/rs9121306

Cuffey, K. and Paterson, W. S. B. (2010). *The physics of glaciers* (Burlington, MA: Butterworth-Heinemann/Elsevier), 4th ed edn. OCLC: ocn488732494

Dai, C., Durand, M., Howat, I. M., Altenau, E. H., and Pavelsky, T. M. (2018). Estimating River Surface Elevation From ArcticDEM. *Geophysical Research Letters* 45, 3107–3114. doi:10.1002/2018GL077379

Dai, C. and Howat, I. M. (2018). Detection of Saturation in High-Resolution Pushbroom Satellite Imagery. *IEEE Journal of Selected Topics in Applied Earth Observations and Remote Sensing* 11, 1684–1693. doi:10.1109/JSTARS.2018.2814543

d'Angelo, P. and Kuschk, G. (2012). Dense multi-view stereo from satellite imagery. In *2012 IEEE International Geoscience and Remote Sensing Symposium* (Munich, Germany: IEEE), 6944–6947. doi:10.1109/IGARSS.2012.6352565

d'Angelo, P. and Reinartz, P. (2012). Dsm based orientation of large stereo satellite image blocks. *ISPRS - International Archives of the Photogrammetry, Remote Sensing and Spatial Information Sciences* XXXIX-B1, 209–214. doi:10.5194/isprsarchives-XXXIX-B1-209-2012

Das, I., Hock, R., Berthier, E., and Lingle, C. S. (2014). 21st-century increase in glacier mass loss in the wrangell mountains, alaska, usa, from airborne laser altimetry and satellite stereo imagery. *Journal of Glaciology* 60, 283–293. doi:10.3189/2014JoG13J119

Davison, B. J., Sole, A. J., Cowton, T. R., Lea, J. M., Slater, D. A., Fahrner, D., et al. (2020). Subglacial Drainage Evolution Modulates Seasonal Ice Flow Variability of Three

Tidewater Glaciers in Southwest Greenland. *Journal of Geophysical Research: Earth Surface* 125. doi:10.1029/2019JF005492

de Franchis, C., Meinhardt-Llopis, E., Michel, J., Morel, J.-M., and Facciolo, G. (2014). An automatic and modular stereo pipeline for pushbroom images. *ISPRS Annals of Photogrammetry, Remote Sensing and Spatial Information Sciences* II-3, 49–56. doi:10.5194/isprsannals-II-3-49-2014

Dehecq, A., Gardner, A. S., Alexander, O., McMichael, S., Hugonnet, R., Shean, D., et al. (2020). Automated processing of declassified KH-9 Hexagon satellite images for global elevation change analysis since the 1970s

Dehecq, A., Gourmelen, N., Gardner, A. S., Brun, F., Goldberg, D., Nienow, P. W., et al. (2019). Twenty-first century glacier slowdown driven by mass loss in High Mountain Asia. *Nature Geoscience* 12, 22–27. doi:10.1038/s41561-018-0271-9

Dehecq, A., Gourmelen, N., and Trouve, E. (2015). Deriving large-scale glacier velocities from a complete satellite archive: Application to the Pamir–Karakoram–Himalaya. *Remote Sensing of Environment* 162, 55–66. doi:10.1016/j.rse.2015.01.031

Deilami, K. and Hashim, M. (2011). Very High Resolution Optical Satellites for DEM Generation: A Review. *European Journal of Scientific Research* 49, 14

Delon, J. and Rougé, B. (2007). Small Baseline Stereovision. *Journal of Mathematical Imaging and Vision* 28, 209–223. doi:10.1007/s10851-007-0001-1

Deschamps-Berger, C., Gascoin, S., Berthier, E., Deems, J., Gutmann, E., Dehecq, A., et al. (2020). *Snow depth mapping from stereo satellite imagery in mountainous terrain: evaluation using airborne lidar data.* preprint, Snow/Remote Sensing. doi:10.5194/tc-2020-15

[Dataset] Dewitz, J. (2019). National Land Cover Dataset (NLCD) 2016 Products. doi:10.5066/P96HHBIE. Type: dataset

[Dataset] DigitalGlobe (2016). Accuracy of worldview products. Last accessed 30 May 2020

Dunse, T., Schellenberger, T., Hagen, J. O., Kääb, A., Schuler, T. V., and Reijmer, C. H. (2015). Glacier-surge mechanisms promoted by a hydro-thermodynamic feedback to summer melt. *The Cryosphere* 9, 197–215. doi:10.5194/tc-9-197-2015

Dussaillant, I., Berthier, E., Brun, F., Masiokas, M., Hugonnet, R., Favier, V., et al. (2019). Two decades of glacier mass loss along the Andes. *Nature Geoscience* 12, 802–808. doi:10.1038/s41561-019-0432-5

d'Angelo, P., Máttyus, G., and Reinartz, P. (2016). Skybox image and video product evaluation. *International Journal of Image and Data Fusion* 7, 3–18. doi:10.1080/19479832.2015.1109565

Edwards, L. and Broxton, M. (2006). Automated 3D Surface Reconstruction from Orbital Imagery. In *Space 2006* (San Jose, California: American Institute of Aeronautics and Astronautics). doi:10.2514/6.2006-7435

Edwards, L., Sims, M., Kunz, C., Lees, D., and Bowman, J. (2005). Photo-realistic Terrain Modeling and Visualization for Mars Exploration Rover Science Operations. In *2005 IEEE International Conference on Systems, Man and Cybernetics* (Waikoloa, HI, USA: IEEE), vol. 2, 1389–1395. doi:10.1109/ICSMC.2005.1571341

Facciolo, G., Franchis, C. d., and Meinhardt, E. (2015). MGM: A Significantly More Global Matching for Stereovision. In *Procedings of the British Machine Vision Conference 2015* (Swansea: British Machine Vision Association), 90.1–90.12. doi:10.5244/C.29.90

Fahnestock, M., Scambos, T., Moon, T., Gardner, A., Haran, T., and Klinger, M. (2016). Rapid large-area mapping of ice flow using Landsat 8. *Remote Sensing of Environment* 185, 84–94. doi:10.1016/j.rse.2015.11.023

Farinotti, D., Huss, M., Fürst, J. J., Landmann, J., Machguth, H., Maussion, F., et al. (2019a). A consensus estimate for the ice thickness distribution of all glaciers on Earth. *Nature Geoscience* 12, 168–173. doi:10.1038/s41561-019-0300-3

Farinotti, D., Round, V., Huss, M., Compagno, L., and Zekollari, H. (2019b). Large hydropower and water-storage potential in future glacier-free basins. *Nature* 575, 341–344. doi:10.1038/s41586-019-1740-z

Farr, T. G., Rosen, P. A., Caro, E., Crippen, R., Duren, R., Hensley, S., et al. (2007). The Shuttle Radar Topography Mission. *Reviews of Geophysics* 45, RG2004. doi:10.1029/2005RG000183

Fischer, L., Kääb, A., Huggel, C., and Noetzli, J. (2006). Geology, glacier retreat and permafrost degradation as controlling factors of slope instabilities in a high-mountain rock wall: the Monte Rosa east face. *Natural Hazards and Earth System Sciences* 6, 761–772. doi:10.5194/nhess-6-761-2006

Florentine, C., O'Neel, S., Sass, L., McNeil, C., and Baker, E. (2019). Analyzing the Geodetic Mass Balance Uncertainty Budget on North American Benchmark Glaciers. In *AGU Fall Meeting Abstracts*. vol. 2019, C22A–02

Frans, C., Istanbulluoglu, E., Lettenmaier, D. P., Fountain, A. G., and Riedel, J. (2018). Glacier Recession and the Response of Summer Streamflow in the Pacific Northwest United States, 1960-2099. *Water Resources Research* 54, 6202–6225. doi:10.1029/2017WR021764

Frey, H., Machguth, H., Huss, M., Huggel, C., Bajracharya, S., Bolch, T., et al. (2014). Estimating the volume of glaciers in the Himalayan–Karakoram region using different methods. *The Cryosphere* 8, 2313–2333. doi:10.5194/tc-8-2313-2014

Fürst, J. J., Gillet-Chaulet, F., Benham, T. J., Dowdeswell, J. A., Grabiec, M., Navarro, F., et al. (2017). Application of a two-step approach for mapping ice thickness to various glacier types on Svalbard. *The Cryosphere* 11, 2003–2032. doi:10.5194/tc-11-2003-2017

[Dataset] Gardner, A., Fahnestock, M., and Scambos, T. (2022). MEASURES ITS_live Regional Glacier and Ice Sheet Surface Velocities, Version 1. doi:10.5067/6II6VW8LLWJ7. Type: dataset

Gardner, A. S., Moholdt, G., Cogley, J. G., Wouters, B., Arendt, A. A., Wahr, J., et al. (2013). A Reconciled Estimate of Glacier Contributions to Sea Level Rise: 2003 to 2009. *Science* 340, 852–857. doi:10.1126/science.1234532

Gardner, A. S., Moholdt, G., Scambos, T., Fahnstock, M., Ligtenberg, S., van den Broeke, M., et al. (2018). Increased West Antarctic and unchanged East Antarctic ice discharge over the last 7 years. *The Cryosphere* 12, 521–547. doi:10.5194/tc-12-521-2018

Ghuffar, S. (2018). DEM Generation from Multi Satellite PlanetScope Imagery. *Remote Sensing* 10, 1462. doi:10.3390/rs10091462

Guillet, G., King, O., Lv, M., Ghuffar, S., Benn, D., Quincey, D., et al. (2022). A regionally resolved inventory of High Mountain Asia surge-type glaciers, derived from a multi-factor remote sensing approach. *The Cryosphere* 16, 603–623. doi:10.5194/tc-16-603-2022

Hansen, J., Sato, M., Ruedy, R., Lo, K., Lea, D. W., and Medina-Elizade, M. (2006). Global temperature change. *Proceedings of the National Academy of Sciences* 103, 14288–14293. doi:10.1073/pnas.0606291103

Harrison, S., Kargel, J. S., Huggel, C., Reynolds, J., Shugar, D. H., Betts, R. A., et al. (2018). Climate change and the global pattern of moraine-dammed glacial lake outburst floods. *The Cryosphere* 12, 1195–1209. doi:10.5194/tc-12-1195-2018

Herreid, S. and Pellicciotti, F. (2018). Automated detection of ice cliffs within supraglacial debris cover. *The Cryosphere* 12, 1811–1829. doi:10.5194/tc-12-1811-2018

Herreid, S. and Pellicciotti, F. (2020). The state of rock debris covering Earth's glaciers. *Nature Geoscience* 13, 621–627. doi:10.1038/s41561-020-0615-0

Holm, K., Bovis, M., and Jakob, M. (2004). The landslide response of alpine basins to post-Little Ice Age glacial thinning and retreat in southwestern British Columbia. *Geomorphology* 57, 201–216. doi:10.1016/S0169-555X(03)00103-X

Hotaling, S., Hood, E., and Hamilton, T. L. (2017). Microbial ecology of mountain glacier ecosystems: biodiversity, ecological connections and implications of a warming climate. *Environmental Microbiology* 19, 2935–2948. doi:10.1111/1462-2920.13766

Howat, I. M., Porter, C., Smith, B. E., Noh, M.-J., and Morin, P. (2019). The Reference Elevation Model of Antarctica. *The Cryosphere* 13, 665–674. doi:10.5194/tc-13-665-2019

Hu, J. M. and Shean, D. (2022). Improving Mountain Snow and Land Cover Mapping Using Very-High-Resolution (VHR) Optical Satellite Images and Random Forest Machine Learning Models. *Remote Sensing* 14, 4227. doi:10.3390/rs14174227

Hu, M. and Shean, D. (2020). *Machine Learning Classification and Derived Snow Metrics from Very-high-resolution Multispectral Satellite Imagery in Complex Terrain*. other, Hydrology. doi:10.1002/essoar.10501632.1

Hubbard, A., Willis, I., Sharp, M., Mair, D., Nienow, P., Hubbard, B., et al. (2000). Glacier mass-balance determination by remote sensing and high-resolution modelling. *Journal of Glaciology* 46, 491–498. doi:10.3189/172756500781833016

Hugonnet, R., McNabb, R., Berthier, E., Menounos, B., Nuth, C., Girod, L., et al. (2021). Accelerated global glacier mass loss in the early twenty-first century. *Nature* 592, 726–731. doi:10.1038/s41586-021-03436-z

Huintjes, E., Neckel, N., Hochschild, V., and Schneider, C. (2015). Surface energy and mass balance at Purogangri ice cap, central Tibetan Plateau, 2001–2011. *Journal of Glaciology* 61, 1048–1060. doi:10.3189/2015JoG15J056

Huss, M. (2013). Density assumptions for converting geodetic glacier volume change to mass change. *The Cryosphere* 7, 877–887. doi:10.5194/tc-7-877-2013

Huss, M. and Farinotti, D. (2012). Distributed ice thickness and volume of all glaciers around the globe: GLOBAL GLACIER ICE THICKNESS AND VOLUME. *Journal of Geophysical Research: Earth Surface* 117, n/a–n/a. doi:10.1029/2012JF002523

Huss, M. and Hock, R. (2015). A new model for global glacier change and sea-level rise. *Frontiers in Earth Science* 3. doi:10.3389/feart.2015.00054

Huss, M. and Hock, R. (2018). Global-scale hydrological response to future glacier mass loss. *Nature Climate Change* 8, 135–140. doi:10.1038/s41558-017-0049-x

Höhle, J. and Höhle, M. (2009). Accuracy assessment of digital elevation models by means of robust statistical methods. *ISPRS Journal of Photogrammetry and Remote Sensing* 64, 398–406. doi:10.1016/j.isprsjprs.2009.02.003

Iken, A. and Bindschadler, R. A. (1986). Combined measurements of Subglacial Water Pressure and Surface Velocity of Findelengletscher, Switzerland: Conclusions about Drainage System and Sliding Mechanism. *Journal of Glaciology* 32, 101–119. doi: 10.3189/S0022143000006936

Immerzeel, W. W., Lutz, A. F., Andrade, M., Bahl, A., Biemans, H., Bolch, T., et al. (2020). Importance and vulnerability of the world's water towers. *Nature* 577, 364–369. doi:10.1038/s41586-019-1822-y

Kamb, B. and Echelmeyer, K. A. (1986). Stress-gradient Coupling in Glacier Flow: IV. Effects of the " *T* " Term. *Journal of Glaciology* 32, 342–349. doi:10.3189/S0022143000012016

Kehrl, L. M., Horgan, H. J., Anderson, B. M., Dadic, R., and Mackintosh, A. N. (2015). Glacier velocity and water input variability in a maritime environment: Franz Josef Glacier, New Zealand. *Journal of Glaciology* 61, 663–674. doi:10.3189/2015JoG14J228

Kehrl, L. M., Joughin, I., Shean, D. E., Floricioiu, D., and Krieger, L. (2017). Seasonal and interannual variabilities in terminus position, glacier velocity, and surface elevation at Helheim and Kangerlussuaq Glaciers from 2008 to 2016: Helheim and Kangerlussuaq Glaciers. *Journal of Geophysical Research: Earth Surface* 122, 1635–1652. doi:10.1002/2016JF004133

Kellndorfer, J., Walker, W., Pierce, L., Dobson, C., Fites, J. A., Hunsaker, C., et al. (2004). Vegetation height estimation from Shuttle Radar Topography Mission and National Elevation Datasets. *Remote Sensing of Environment* 93, 339–358. doi:10.1016/j.rse.2004.07.017

Kennedy, L. A. and Russell, J. K. (2012). Cataclastic production of volcanic ash at Mount Saint Helens. *Physics and Chemistry of the Earth, Parts A/B/C* 45-46, 40–49. doi:10.1016/j.pce.2011.07.052

Khadka, M., Kayastha, R. B., and Kayastha, R. (2020). Future projection of cryospheric and hydrologic regimes in Koshi River basin, Central Himalaya, using coupled glacier dynamics and glacio-hydrological models. *Journal of Glaciology* 66, 831–845. doi:10.1017/jog.2020.51

Khanal, S., Lutz, A., Kraaijenbrink, P. D. A., van den Hurk, B., Yao, T., and Immerzeel, W. W. (2021). Variable 21st Century Climate Change Response for Rivers in High Mountain Asia at Seasonal to Decadal Time Scales. *Water Resources Research* 57. doi:10.1029/2020WR029266

Kienholz, C., Hock, R., and Arendt, A. A. (2013). A new semi-automatic approach for dividing glacier complexes into individual glaciers. *Journal of Glaciology* 59, 925–937. doi:10.3189/2013JoG12J138

Kim, J.-W., Lu, Z., Qu, F., and Hu, X. (2015). Pre-2014 mudslides at Oso revealed by InSAR and multi-source DEM analysis. *Geomatics, Natural Hazards and Risk* 6, 184–194. doi:10.1080/19475705.2015.1016556

King, O., Dehecq, A., Quincey, D., and Carrivick, J. (2018). Contrasting geometric and dynamic evolution of lake and land-terminating glaciers in the central Himalaya. *Global and Planetary Change* 167, 46–60. doi:10.1016/j.gloplacha.2018.05.006

King, O., Turner, A. G. D., Quincey, D. J., and Carrivick, J. L. (2020). Morphometric evolution of Everest region debris-covered glaciers. *Geomorphology* 371, 107422. doi: 10.1016/j.geomorph.2020.107422

Kirschbaum, D., Watson, C. S., Rounce, D. R., Shugar, D. H., Kargel, J. S., Haritashya, U. K., et al. (2019). The State of Remote Sensing Capabilities of Cascading Hazards Over High Mountain Asia. *Frontiers in Earth Science* 7, 197. doi:10.3389/feart.2019.00197

Kneib, M., Fyffe, C. L., Miles, E. S., Lindemann, S., Shaw, T. E., Buri, P., et al. (2022a). *Controls on Ice Cliff Formation, Distribution and Characteristics on Debris-Covered Glaciers*. preprint, Preprints. doi:10.22541/essoar.167048294.48382892/v1

Kneib, M., Miles, E., Jola, S., Buri, P., Herreid, S., Bhattacharya, A., et al. (2021). Mapping ice cliffs on debris-covered glaciers using multispectral satellite images. *Remote Sensing of Environment* 253, 112201. doi:10.1016/j.rse.2020.112201

Kneib, M., Miles, E. S., Buri, P., Fugger, S., McCarthy, M., Shaw, T. E., et al. (2022b). Sub-seasonal variability of supraglacial ice cliff melt rates and associated processes from time-lapse photogrammetry. *The Cryosphere* 16, 4701–4725. doi:10.5194/tc-16-4701-2022

Knuth, F., Shean, D., Alexandrov, O., and Bhushan, S. (2020). *Automated production of high-resolution DEMs from historical imagery for quantitative analysis of glacier and geomorphological change*. other, Hydrology. doi:10.1002/essoar.10501805.1

Kraaijenbrink, P., Meijer, S. W., Shea, J. M., Pellicciotti, F., De Jong, S. M., and Immerzeel, W. W. (2016a). Seasonal surface velocities of a Himalayan glacier derived by automated correlation of unmanned aerial vehicle imagery. *Annals of Glaciology* 57, 103–113. doi: 10.3189/2016AoG71A072

Kraaijenbrink, P., Shea, J., Pellicciotti, F., Jong, S. d., and Immerzeel, W. (2016b). Object-based analysis of unmanned aerial vehicle imagery to map and characterise surface features on a debris-covered glacier. *Remote Sensing of Environment* 186, 581–595. doi:10.1016/j.rse.2016.09.013

Kraaijenbrink, P. D. A., Bierkens, M. F. P., Lutz, A. F., and Immerzeel, W. W. (2017). Impact of a global temperature rise of 1.5 degrees Celsius on Asia's glaciers. *Nature* 549, 257–260. doi:10.1038/nature23878

Kronenberg, M., van Pelt, W., Machguth, H., Fiddes, J., Hoelzle, M., and Pertziger, F. (2022). Long-term firn and mass balance modelling for abramov glacier in the data-scarce pamir alay. *The Cryosphere* 16, 5001–5022. doi:10.5194/tc-16-5001-2022

Kumar, S. and Dobhal, D. (1997). Climatic effects and bedrock control on rapid fluctuations of Chhota Shigri glacier, northwest Himalaya, India. *Journal of Glaciology* 43, 467–472. doi:10.3189/S0022143000035061

Kääb, A., Altena, B., and Mascaro, J. (2019). River-ice and water velocities using the Planet optical cubesat constellation. *Hydrology and Earth System Sciences* 23, 4233–4247. doi:10.5194/hess-23-4233-2019

Kääb, A., Berthier, E., Nuth, C., Gardelle, J., and Arnaud, Y. (2012). Contrasting patterns of early twenty-first-century glacier mass change in the Himalayas. *Nature* 488, 495–498. doi:10.1038/nature11324

Kääb, A., Jacquemart, M., Gilbert, A., Leinss, S., Girod, L., Huggel, C., et al. (2021). Sudden large-volume detachments of low-angle mountain glaciers – more frequent than thought? *The Cryosphere* 15, 1751–1785. doi:10.5194/tc-15-1751-2021

Lague, D., Brodu, N., and Leroux, J. (2013). Accurate 3d comparison of complex topography with terrestrial laser scanner: Application to the rangitikei canyon (n-z). *ISPRS Journal of Photogrammetry and Remote Sensing* 82, 10–26. doi:https://doi.org/10.1016/j.isprsjprs.2013.04.009

Lalande, M., Ménégoz, M., Krinner, G., Naegeli, K., and Wunderle, S. (2021). Climate change in the high mountain asia in cmip6. *Earth System Dynamics* 12, 1061–1098. doi:10.5194/esd-12-1061-2021

Langhammer, L., Grab, M., Bauder, A., and Maurer, H. (2019). Glacier thickness estimations of alpine glaciers using data and modeling constraints. *The Cryosphere* 13, 2189–2202. doi:10.5194/tc-13-2189-2019

Lavé, J. and Avouac, J. P. (2001). Fluvial incision and tectonic uplift across the Himalayas of central Nepal. *Journal of Geophysical Research: Solid Earth* 106, 26561–26591. doi:10.1029/2001JB000359

Lei, Y., Gardner, A., and Agram, P. (2021). Autonomous Repeat Image Feature Tracking (autoRIFT) and Its Application for Tracking Ice Displacement. *Remote Sensing* 13, 749. doi:10.3390/rs13040749

Leotta, M. J., Long, C., Jacquet, B., Zins, M., Lipsa, D., Shan, J., et al. (2019). Urban Semantic 3D Reconstruction From Multiview Satellite Imagery. In *2019 IEEE/CVF Conference on Computer Vision and Pattern Recognition Workshops (CVPRW)* (Long Beach, CA, USA: IEEE), 1451–1460. doi:10.1109/CVPRW.2019.00186

Leprince, S., Ayoub, F., Klinger, Y., and Avouac, J.-P. (2007). Co-Registration of Optically Sensed Images and Correlation (COSI-Corr): an operational methodology for ground deformation measurements. In *2007 IEEE International Geoscience and Remote Sensing Symposium* (Barcelona, Spain: IEEE), 1943–1946. doi:10.1109/IGARSS.2007.4423207

Litt, M., Shea, J., Wagnon, P., Steiner, J., Koch, I., Stigter, E., et al. (2019). Glacier ablation and temperature indexed melt models in the Nepalese Himalaya. *Scientific Reports* 9, 5264. doi:10.1038/s41598-019-41657-5

Losapio, G., Cerabolini, B. E. L., Maffioletti, C., Tampucci, D., Gobbi, M., and Caccianiga, M. (2021). The Consequences of Glacier Retreat Are Uneven Between Plant Species. *Frontiers in Ecology and Evolution* 8, 616562. doi:10.3389/fevo.2020.616562

Mandal, A., Angchuk, T., Azam, M. F., Ramanathan, A., Wagnon, P., Soheb, M., et al. (2022). An 11-year record of wintertime snow-surface energy balance and sublimation at 4863 m a.s.l. on the chhota shigri glacier moraine (western himalaya, india). *The Cryosphere* 16, 3775–3799. doi:10.5194/tc-16-3775-2022

Marc, O., Behling, R., Andermann, C., Turowski, J. M., Illien, L., Roessner, S., et al. (2019). Long-term erosion of the Nepal Himalayas by bedrock landsliding: the role of monsoons, earthquakes and giant landslides. *Earth Surface Dynamics* 7, 107–128. doi:10.5194/esurf-7-107-2019

Mark, B. G., Bury, J., McKenzie, J. M., French, A., and Baraer, M. (2010). Climate Change and Tropical Andean Glacier Recession: Evaluating Hydrologic Changes and Livelihood Vulnerability in the Cordillera Blanca, Peru. *Annals of the Association of American Geographers* 100, 794–805. doi:10.1080/00045608.2010.497369

Marta, S. (2018). PLANET IMAGERY PRODUCT SPECIFICATIONS , 91

Maurer, J. M., Schaefer, J. M., Rupper, S., and Corley, A. (2019). Acceleration of ice loss across the Himalayas over the past 40 years. *Science Advances* 5, eaav7266. doi: 10.1126/sciadv.aav7266

Maussion, F., Butenko, A., Champollion, N., Dusch, M., Eis, J., Fourteau, K., et al. (2019). The Open Global Glacier Model (OGGM) v1.1. *Geoscientific Model Development* 12, 909–931. doi:10.5194/gmd-12-909-2019

Menounos, B., Hugonnet, R., Shean, D., Gardner, A., Howat, I., Berthier, E., et al. (2019). Heterogeneous Changes in Western North American Glaciers Linked to Decadal Variability in Zonal Wind Strength. *Geophysical Research Letters* 46, 200–209. doi: 10.1029/2018GL080942

Meyer, J. and Skiles, S. M. (2019). Assessing the Ability of Structure From Motion to Map High-Resolution Snow Surface Elevations in Complex Terrain: A Case Study From Senator Beck Basin, CO. *Water Resources Research* 55, 6596–6605. doi:10.1029/2018WR024518

Mihalcea, C., Mayer, C., Diolaiuti, G., Lambrecht, A., Smiraglia, C., and Tartari, G. (2006). Ice ablation and meteorological conditions on the debris-covered area of Baltoro glacier, Karakoram, Pakistan. *Annals of Glaciology* 43, 292–300. doi:10.3189/172756406781812104

Mikhail, E. M., Bethel, J. S., and McGlone, J. C. (2001). *Introduction to modern photogrammetry* (New York : Chichester: Wiley). OCLC: ocm45735791

Miles, E., McCarthy, M., Dehecq, A., Kneib, M., Fugger, S., and Pellicciotti, F. (2021). Health and sustainability of glaciers in High Mountain Asia. *Nature Communications* 12, 2868. doi:10.1038/s41467-021-23073-4

Miles, E. S., Willis, I., Buri, P., Steiner, J. F., Arnold, N. S., and Pellicciotti, F. (2018a). Surface Pond Energy Absorption Across Four Himalayan Glaciers Accounts for 1/8 of Total Catchment Ice Loss. *Geophysical Research Letters* 45, 10,464–10,473. doi: 10.1029/2018GL079678

Miles, K. E., Hubbard, B., Quincey, D. J., Miles, E. S., Sherpa, T. C., Rowan, A. V., et al. (2018b). Polythermal structure of a Himalayan debris-covered glacier revealed by borehole thermometry. *Scientific Reports* 8. doi:10.1038/s41598-018-34327-5

Millan, R., Mouginot, J., Rabatel, A., Jeong, S., Cusicanqui, D., Derkacheva, A., et al. (2019a). Mapping Surface Flow Velocity of Glaciers at Regional Scale Using a Multiple Sensors Approach. *Remote Sensing* 11, 2498. doi:10.3390/rs11212498

Millan, R., Mouginot, J., Rabatel, A., and Morlighem, M. (2022). Ice velocity and thickness of the world's glaciers. *Nature Geoscience* 15, 124–129. doi:10.1038/s41561-021-00885-z

Millan, R. M., von Steiger, R., Ariel, M., Bartalev, S., Borgeaud, M., Campagnola, S., et al. (2019b). Small satellites for space science. *Advances in Space Research* 64, 1466–1517. doi:10.1016/j.asr.2019.07.035

Mishra, N. B., Miles, E. S., Chaudhuri, G., Mainali, K. P., Mal, S., Singh, P. B., et al. (2022). Quantifying heterogeneous monsoonal melt on a debris-covered glacier in Nepal Himalaya using repeat uncrewed aerial system (UAS) photogrammetry. *Journal of Glaciology* 68, 288–304. doi:10.1017/jog.2021.96

Montesano, P. M., Neigh, C., Sun, G., Duncanson, L., Van Den Hoek, J., and Ranson, K. J. (2017). The use of sun elevation angle for stereogrammetric boreal forest height in open canopies. *Remote Sensing of Environment* 196, 76–88. doi:10.1016/j.rse.2017.04.024

Montesano, P. M., Neigh, C. S., Wagner, W., Wooten, M., and Cook, B. D. (2019). Boreal canopy surfaces from spaceborne stereogrammetry. *Remote Sensing of Environment* 225, 148–159. doi:10.1016/j.rse.2019.02.012

Moon, T., Joughin, I., Smith, B., van den Broeke, M. R., van de Berg, W. J., Noël, B., et al. (2014). Distinct patterns of seasonal Greenland glacier velocity. *Geophysical Research Letters* 41, 7209–7216. doi:10.1002/2014GL061836

Morrison, R. A., Turner, J. T., Barwick, M., and Hardaway, G. M. (2005). Urban reconnaissance with an airborne laser radar (Invited Paper) (Orlando, Florida, USA), 1. doi:10.1117/12.609675

Mouginot, J., Rabatel, A., Ducasse, E., and Millan, R. (2023). Optimization of Cross Correlation Algorithm for Annual Mapping of Alpine Glacier Flow Velocities; Application to Sentinel-2. *IEEE Transactions on Geoscience and Remote Sensing* 61, 1–12. doi:10.1109/TGRS.2022.3223259

Müller, J., Gärtner-Roer, I., Thee, P., and Ginzler, C. (2014). Accuracy assessment of airborne photogrammetrically derived high-resolution digital elevation models in a high mountain environment. *ISPRS Journal of Photogrammetry and Remote Sensing* 98, 58–69. doi:10.1016/j.isprsjprs.2014.09.015

Naito, N. (2011). Summer Accumulation Type Glaciers. In *Encyclopedia of Snow, Ice and Glaciers*, eds. V. P. Singh, P. Singh, and U. K. Haritashya (Dordrecht: Springer Netherlands). 1107–1108. doi:10.1007/978-90-481-2642-2_552

Nakata, T. (1989). Active faults of the Himalaya of India and Nepal. In *Geological Society of America Special Papers* (Geological Society of America), vol. 232. 243–264. doi:10.1130/SPE232-p243

Nanni, U., Scherler, D., Ayoub, F., Millan, R., Herman, F., and Avouac, J.-P. (2022). Climatic control on seasonal variations of glacier surface velocity. *EGUsphere* , 1–39doi: 10.5194/egusphere-2022-1035

NASA Earth Science Division (2020). *Commercial SmallSat Data Acquisition Program Pilot Evaluation Report*. Tech. rep., NASA Earth Science Division. Last accessed 30 October 2020

[Dataset] NASA Shuttle Radar Topography Mission (SRTM) (2013). Shuttle Radar Topography Mission (SRTM) Global. doi:10.5069/G9445JDF. Distributed by OpenTopography. Last accessed 5 November 2020

[Dataset] Nefian, A. V., Husmann, K., Broxton, M., To, V., Lundy, M., and Hancher, M. D. (2009). A bayesian formulation for sub-pixel refinement in stereo orbital imagery

Nicholson, L. and Benn, D. I. (2006). Calculating ice melt beneath a debris layer using meteorological data. *Journal of Glaciology* 52, 463–470. doi:10.3189/172756506781828584

Nicholson, L., Wirbel, A., Mayer, C., and Lambrecht, A. (2021). The Challenge of Non-Stationary Feedbacks in Modeling the Response of Debris-Covered Glaciers to Climate Forcing. *Frontiers in Earth Science* 9, 662695. doi:10.3389/feart.2021.662695

Nienow, P. W., Hubbard, A. L., Hubbard, B. P., Chandler, D. M., Mair, D. W. F., Sharp, M. J., et al. (2005). Hydrological controls on diurnal ice flow variability in valley glaciers: ICE FLOW VARIABILITY IN VALLEY GLACIERS. *Journal of Geophysical Research: Earth Surface* 110, n/a–n/a. doi:10.1029/2003JF000112

Noh, M.-J. and Howat, I. M. (2015). Automated stereo-photogrammetric DEM generation at high latitudes: Surface Extraction with TIN-based Search-space Minimization (SETSM) validation and demonstration over glaciated regions. *GIScience & Remote Sensing* 52, 198–217. doi:10.1080/15481603.2015.1008621

Nuimura, T., Fujita, K., Fukui, K., Asahi, K., Aryal, R., and Ageta, Y. (2011). Temporal Changes in Elevation of the Debris-Covered Ablation Area of Khumbu Glacier in the Nepal Himalaya since 1978. *Arctic, Antarctic, and Alpine Research* 43, 246–255. doi:10.1657/1938-4246-43.2.246

Nuth, C. and Kääb, A. (2011). Co-registration and bias corrections of satellite elevation data sets for quantifying glacier thickness change. *The Cryosphere* 5, 271–290. doi:10.5194/tc-5-271-2011

Ozcanli, O. C., Dong, Y., Mundy, J. L., Webb, H., Hammoud, R., and Tom, V. (2016). Automatic Geolocation Correction of Satellite Imagery. *International Journal of Computer Vision* 116, 263–277. doi:10.1007/s11263-015-0852-7

Pelto, B. M., Maussion, F., Menounos, B., Radić, V., and Zeuner, M. (2020). Bias-corrected estimates of glacier thickness in the Columbia River Basin, Canada. *Journal of Glaciology* 66, 1051–1063. doi:10.1017/jog.2020.75

Pelto, B. M. and Menounos, B. (2021). Surface Mass-Balance Gradients From Elevation and Ice Flux Data in the Columbia Basin, Canada. *Frontiers in Earth Science* 9, 675681. doi:10.3389/feart.2021.675681

Pelto, B. M., Menounos, B., and Marshall, S. J. (2019). Multi-year evaluation of airborne geodetic surveys to estimate seasonal mass balance, Columbia and Rocky Mountains, Canada. *The Cryosphere* 13, 1709–1727. doi:10.5194/tc-13-1709-2019

Pelto, M., Panday, P., Matthews, T., Maurer, J., and Perry, L. B. (2021). Observations of Winter Ablation on Glaciers in the Mount Everest Region in 2020–2021. *Remote Sensing* 13, 2692. doi:10.3390/rs13142692

Perry, L. B., Matthews, T., Guy, H., Koch, I., Khadka, A., Elmore, A. C., et al. (2020). Precipitation Characteristics and Moisture Source Regions on Mt. Everest in the Khumbu, Nepal. *One Earth* 3, 594–607. doi:10.1016/j.oneear.2020.10.011

Pfeffer, W. T., Arendt, A. A., Bliss, A., Bolch, T., Cogley, J. G., Gardner, A. S., et al. (2014). The Randolph Glacier Inventory: a globally complete inventory of glaciers. *Journal of Glaciology* 60, 537–552. doi:10.3189/2014JoG13J176

Piermattei, L., Marty, M., Karel, W., Ressl, C., Hollaus, M., Ginzler, C., et al. (2018). Impact of the Acquisition Geometry of Very High-Resolution Pléiades Imagery on the Accuracy of Canopy Height Models over Forested Alpine Regions. *Remote Sensing* 10, 1542. doi:10.3390/rs10101542

Pomerleau, F., Colas, F., Siegwart, R., and Magnenat, S. (2013). Comparing ICP variants on real-world data sets: Open-source library and experimental protocol. *Autonomous Robots* 34, 133–148. doi:10.1007/s10514-013-9327-2

[Dataset] Porter, C., Morin, P., Howat, I., Noh, M.-J., Bates, B., Peterman, K., et al. (2018). ArcticDEM. doi:10.7910/DVN/OHHUKH. Type: dataset

Pritchard, H. D., King, E. C., Goodger, D. J., McCarthy, M., Mayer, C., and Kayastha, R. (2020). Towards Bedmap Himalayas: development of an airborne ice-sounding radar for glacier thickness surveys in High-Mountain Asia. *Annals of Glaciology* 61, 35–45. doi:10.1017/aog.2020.29

Qiu, J. (2015). Dirty glaciers melt just as fast as clean ones. *Science* doi:10.1126/science.aaa6411

Racoviteanu, A., Nicholson, L., Glasser, N., Miles, E., Harrison, S., and Reynolds, J. (2022). Debris-covered glacier systems and associated glacial lake outburst flood hazards: challenges and prospects. *Journal of the Geological Society* 179, jgs2021–084. doi:10.1144/jgs2021-084

Ramsankaran, R., Pandit, A., and Azam, M. F. (2018). Spatially distributed ice-thickness modelling for Chhota Shigri Glacier in western Himalayas, India. *International Journal of Remote Sensing* 39, 3320–3343. doi:10.1080/01431161.2018.1441563

Rasul, G. (2014). Food, water, and energy security in South Asia: A nexus perspective from the Hindu Kush Himalayan region. *Environmental Science & Policy* 39, 35–48. doi:https://doi.org/10.1016/j.envsci.2014.01.010

RGI Consortium (2017a). *Randolph Glacier Inventory – A Dataset of Global Glacier Outlines: Version 6.0: Technical Report*. Tech. rep., Global Land Ice Measurements from Space, Colorado, USA. Digital Media. doi:10.7265/N5-RGI-60

RGI Consortium (2017b). *Randolph Glacier Inventory – A Dataset of Global Glacier Outlines: Version 6.0: Technical Report*. Tech. rep., Global Land Ice Measurements from Space, Colorado, USA. Digital Media. doi:10.7265/N5-RGI-60

[Dataset] Robinson, S. T., J.E. and Swinney, D. (2010). Digital topographic map showing the extents of glacial ice and perennial snowfields at mount rainier, washington, based on the lidar survey of september 2007 to october 2008

Rounce, D. R., Hock, R., Maussion, F., Hugonnet, R., Kochtitzky, W., Huss, M., et al. (2023). Global glacier change in the 21st century: Every increase in temperature matters. *Science* 379, 78–83. doi:10.1126/science.abo1324

Rounce, D. R., Hock, R., McNabb, R. W., Millan, R., Sommer, C., Braun, M. H., et al. (2021). Distributed Global Debris Thickness Estimates Reveal Debris Significantly Impacts Glacier Mass Balance. *Geophysical Research Letters* 48. doi:10.1029/2020GL091311

Rounce, D. R., Hock, R., and Shean, D. E. (2020). Glacier Mass Change in High Mountain Asia Through 2100 Using the Open-Source Python Glacier Evolution Model (PyGEM). *Frontiers in Earth Science* 7, 331. doi:10.3389/feart.2019.00331

Rounce, D. R., King, O., McCarthy, M., Shean, D. E., and Salerno, F. (2018). Quantifying Debris Thickness of Debris-Covered Glaciers in the Everest Region of Nepal Through Inversion of a Subdebris Melt Model. *Journal of Geophysical Research: Earth Surface* 123, 1094–1115. doi:10.1029/2017JF004395

Rounce, D. R. and McKinney, D. C. (2014). Debris thickness of glaciers in the Everest area (Nepal Himalaya) derived from satellite imagery using a nonlinear energy balance model. *The Cryosphere* 8, 1317–1329. doi:10.5194/tc-8-1317-2014

Round, V., Leinss, S., Huss, M., Haemmig, C., and Hajnsek, I. (2017). Surge dynamics and lake outbursts of Kyagar Glacier, Karakoram. *The Cryosphere* 11, 723–739. doi:10.5194/tc-11-723-2017

Roy, D. P., Huang, H., Houborg, R., and Martins, V. S. (2021a). A global analysis of the temporal availability of PlanetScope high spatial resolution multi-spectral imagery. *Remote Sensing of Environment* 264, 112586. doi:10.1016/j.rse.2021.112586

[Dataset] Roy, S., Swetnam, T. L., Hinks, I. I., Avery, R., Shean, D., Lukach, A., et al. (2021b). tyson-swetnam/porder: porder: Simple CLI for Planet ordersV2 API. doi: 10.5281/ZENODO.5079783

Ruiz, L., Berthier, E., Masiokas, M., Pitte, P., and Villalba, R. (2015). First surface velocity maps for glaciers of Monte Tronador, North Patagonian Andes, derived from sequential Pléiades satellite images. *Journal of Glaciology* 61, 908–922. doi:10.3189/2015JoG14J134

Rupper, S. and Roe, G. (2008). Glacier Changes and Regional Climate: A Mass and Energy Balance Approach*. *Journal of Climate* 21, 5384–5401. doi:10.1175/2008JCLI2219.1

Sakai, A., Nakawo, M., and Fujita, K. (2002). Distribution Characteristics and Energy Balance of Ice Cliffs on Debris-covered Glaciers, Nepal Himalaya. *Arctic, Antarctic, and Alpine Research* 34, 12–19. doi:10.1080/15230430.2002.12003463

Sakai, A., Takeuchi, N., Fujita, K., and Nakawo, M. (2016). Role of supraglacial ponds in the ablation process of a debris-covered glacier in the Nepal Himalayas , 12

Saunier, S., Karakas, G., Yalcin, I., Done, F., Mannan, R., Albinet, C., et al. (2022). SkySat Data Quality Assessment within the EDAP Framework. *Remote Sensing* 14, 1646. doi:10.3390/rs14071646

Scambos, T. A., Dutkiewicz, M. J., Wilson, J. C., and Bindschadler, R. A. (1992). Application of image cross-correlation to the measurement of glacier velocity using satellite image data. *Remote Sensing of Environment* 42, 177–186. doi:10.1016/0034-4257(92)90101-O

Scherler, D., Wulf, H., and Gorelick, N. (2018). Global Assessment of Supraglacial Debris-Cover Extents. *Geophysical Research Letters* 45, 11,798–11,805. doi:10.1029/2018GL080158

Schilling, S. P., Carrara, P. E., Thompson, R. A., and Iwatsubo, E. Y. (2004). Posteruption glacier development within the crater of Mount St. Helens, Washington, USA. *Quaternary Research* 61, 325–329. doi:10.1016/j.yqres.2003.11.002

Schönberger, J. L. and Frahm, J.-M. (2016). Structure-from-Motion Revisited. In *Conference on Computer Vision and Pattern Recognition (CVPR)*

Schönberger, J. L., Zheng, E., Pollefeys, M., and Frahm, J.-M. (2016). Pixelwise View Selection for Unstructured Multi-View Stereo. In *European Conference on Computer Vision (ECCV)*

Shea, J. M., Immerzeel, W. W., Wagnon, P., Vincent, C., and Bajracharya, S. (2015). Modelling glacier change in the Everest region, Nepal Himalaya. *The Cryosphere* 9, 1105–1128. doi:10.5194/tc-9-1105-2015

[Dataset] Shean, D. (2017). High Mountain Asia 8-meter DEMs Derived from Cross-track Optical Imagery, Version 1. doi:10.5067/0MCWJJH5ABYO. Type: dataset

[Dataset] Shean, D. and Bhushan, S. (2021). Chamoli Disaster Pre-event DEM (2015-05-07 WorldView-1 Stereo). doi:10.5281/ZENODO.4533679. Type: dataset

[Dataset] Shean, D., Bhushan, S., Berthier, E., Deschamps-Berger, C., Gascoin, S., and Knuth, F. (2021). Chamoli Disaster Post-event 2-m DEM Composite (February 10-11, 2021) and Difference Map. doi:10.5281/zenodo.4558692

[Dataset] Shean, D., Bhushan, S., Lilien, D., and Meyer, J. (2019a). dshean/demcoreg: Zenodo doi release. doi:10.5281/zenodo.3243481

Shean, D., Bhushan, S., Montesano, P., Rounce, D. R., Arendt, A., and Osmanoglu, B. (2020). A Systematic, Regional Assessment of High Mountain Asia Glacier Mass Balance. *Frontiers in Earth Science* 7, 363. doi:10.3389/feart.2019.00363

Shean, D. E., Alexandrov, O., Moratto, Z. M., Smith, B. E., Joughin, I. R., Porter, C., et al. (2016). An automated, open-source pipeline for mass production of digital elevation models (DEMs) from very-high-resolution commercial stereo satellite imagery. *ISPRS Journal of Photogrammetry and Remote Sensing* 116, 101–117. doi:10.1016/j.isprsjprs.2016.03.012

Shean, D. E., Joughin, I. R., Dutrieux, P., Smith, B. E., and Berthier, E. (2019b). Ice shelf basal melt rates from a high-resolution digital elevation model (DEM) record for Pine Island Glacier, Antarctica. *The Cryosphere* 13, 2633–2656. doi:10.5194/tc-13-2633-2019

Shugar, D. H. (2020). Rapid worldwide growth of glacial lakes since 1990. *Nature Climate Change* 10, 21

Shugar, D. H., Jacquemart, M., Shean, D., Bhushan, S., Upadhyay, K., Sattar, A., et al. (2021). A massive rock and ice avalanche caused the 2021 disaster at Chamoli, Indian Himalaya. *Science* doi:10.1126/science.abh4455

Sisson, T., Robinson, J., and Swinney, D. (2011). Whole-edifice ice volume change A.D. 1970 to 2007/2008 at Mount Rainier, Washington, based on LiDAR surveying. *Geology* 39, 639–642. doi:10.1130/G31902.1

[Dataset] Slabaugh, G., Schafer, R., and Livingston, M. (2001). Optimal ray intersection for computing 3d points from n-view correspondences. `http://gregslabaugh.net/publications/opray.pdf`

Sold, L., Huss, M., Hoelzle, M., Andereggen, H., Joerg, P. C., and Zemp, M. (2013). Methodological approaches to infer end-of-winter snow distribution on alpine glaciers. *Journal of Glaciology* 59, 1047–1059. doi:10.3189/2013JoG13J015

Somers, L. D., McKenzie, J. M., Zipper, S. C., Mark, B. G., Lagos, P., and Baraer, M. (2018). Does hillslope trenching enhance groundwater recharge and baseflow in the Peruvian Andes ? *Hydrological Processes* 32, 318–331. doi:10.1002/hyp.11423

Srivastava, S. and Azam, M. F. (2022). Mass- and Energy-Balance Modeling and Sublimation Losses on Dokriani Bamak and Chhota Shigri Glaciers in Himalaya Since 1979. *Frontiers in Water* 4, 874240. doi:10.3389/frwa.2022.874240

St-Onge, B. and Grandin, S. (2019). Estimating the Height and Basal Area at Individual Tree and Plot Levels in Canadian Subarctic Lichen Woodlands Using Stereo WorldView-3 Images. *Remote Sensing* 11, 248. doi:10.3390/rs11030248

Steiner, J. F., BURI, P., MILES, E. S., RAGETTLI, S., and PELLICCIOTTI, F. (2019). Supraglacial ice cliffs and ponds on debris-covered glaciers: spatio-temporal distribution and characteristics. *Journal of Glaciology* 65, 617–632. doi:10.1017/jog.2019.40

Steiner, J. F., Kraaijenbrink, P. D. A., and Immerzeel, W. W. (2021). Distributed Melt on a Debris-Covered Glacier: Field Observations and Melt Modeling on the Lirung Glacier in the Himalaya. *Frontiers in Earth Science* 9, 678375. doi:10.3389/feart.2021.678375

Stumm, D., Joshi, S. P., Gurung, T. R., and Silwal, G. (2021). Mass balances of Yala and Rikha Samba glaciers, Nepal, from 2000 to 2017. *Earth System Science Data* 13, 3791–3818. doi:10.5194/essd-13-3791-2021

[Dataset] Team, P. (2022). PLANET IMAGERY PRODUCT SPECIFICATIONS

[Dataset] Team, P. (2023). Understanding PlanetScope Instruments

[Dataset] Ted Scambos, M. F. (2016). Global Land Ice Velocity Extraction from Landsat 8 (GoLIVE). doi:10.7265/N5ZP442B. Type: dataset

Thompson, S., Benn, D. I., Mertes, J., and Luckman, A. (2016). Stagnation and mass loss on a Himalayan debris-covered glacier: processes, patterns and rates. *Journal of Glaciology* 62, 467–485. doi:10.1017/jog.2016.37

Tian, J., Reinartz, P., and D'angelo, P. (2012). Change detection analysis of forest areas using satellite stereo data. In *Informationstechnologie für eine nachhaltige Landbewirtschaftung – Fokus: Forstwirtschaft*, eds. M. Clasen, G. Fröhlich, H. Bernhardt, K. Hildebrand, and B. Theuvsen (Bonn: Gesellschaft für Informatik e.V.), 311–314

Triggs, B., McLauchlan, P. F., Hartley, R. I., and Fitzgibbon, A. W. (2000). Bundle Adjustment — A Modern Synthesis. In *Vision Algorithms: Theory and Practice*, eds. G. Goos, J. Hartmanis, J. van Leeuwen, B. Triggs, A. Zisserman, and R. Szeliski (Berlin, Heidelberg: Springer Berlin Heidelberg), vol. 1883. 298–372. doi:10.1007/3-540-44480-7_21

Van Tricht, L., Huybrechts, P., Van Breedam, J., Fürst, J. J., Rybak, O., Satylkanov, R., et al. (2021a). Measuring and inferring the ice thickness distribution of four glaciers in the Tien Shan, Kyrgyzstan. *Journal of Glaciology* 67, 269–286. doi:10.1017/jog.2020.104

Van Tricht, L., Huybrechts, P., Van Breedam, J., Vanhulle, A., Van Oost, K., and Zekollari, H. (2021b). Estimating surface mass balance patterns from unoccupied aerial vehicle measurements in the ablation area of the Morteratsch–Pers glacier complex (Switzerland). *The Cryosphere* 15, 4445–4464. doi:10.5194/tc-15-4445-2021

Van Wyk de Vries, M., Bhushan, S., Jacquemart, M., Deschamps-Berger, C., Berthier, E., Gascoin, S., et al. (2022a). Pre-collapse motion of the february 2021 chamoli rock–ice avalanche, indian himalaya. *Natural Hazards and Earth System Sciences* 22, 3309–3327. doi:10.5194/nhess-22-3309-2022

Van Wyk de Vries, M., Carchipulla-Morales, D., Wickert, A. D., and Minaya, V. G. (2022b). Glacier thickness and ice volume of the Northern Andes. *Scientific Data* 9, 342. doi: 10.1038/s41597-022-01446-8

Van Wyk de Vries, M. and Wickert, A. D. (2020). *Glacier Image Velocimetry: an open-source toolbox for easy andrapid calculation of high-resolution glacier-velocity fields*. preprint, Glaciers/Remote Sensing. doi:10.5194/tc-2020-204

Vijay, S., Khan, S. A., Kusk, A., Solgaard, A. M., Moon, T., and Bjørk, A. A. (2019). Resolving Seasonal Ice Velocity of 45 Greenlandic Glaciers With Very High Temporal Details. *Geophysical Research Letters* 46, 1485–1495. doi:10.1029/2018GL081503

Vincent, C., Cusicanqui, D., Jourdain, B., Laarman, O., Six, D., Gilbert, A., et al. (2021). Geodetic point surface mass balances: a new approach to determine point surface mass balances on glaciers from remote sensing measurements. *The Cryosphere* 15, 1259–1276. doi:10.5194/tc-15-1259-2021

Vincent, C., Wagnon, P., Shea, J. M., Immerzeel, W. W., Kraaijenbrink, P., Shrestha, D., et al. (2016). Reduced melt on debris-covered glaciers: investigations from Changri Nup Glacier, Nepal. *The Cryosphere* 10, 1845–1858. doi:10.5194/tc-10-1845-2016

Wagnon, P., Vincent, C., Arnaud, Y., Berthier, E., Vuillermoz, E., Gruber, S., et al. (2013). Seasonal and annual mass balances of Mera and Pokalde glaciers (Nepal Himalaya) since 2007. *The Cryosphere* 7, 1769–1786. doi:10.5194/tc-7-1769-2013

Wan, X., Liu, J., Yan, H., Morgan, G. L., and Sun, T. (2016). 3D super resolution scene depth reconstruction based on SkySat video image sequences. In *2016 IEEE International Geoscience and Remote Sensing Symposium (IGARSS)* (Beijing, China: IEEE), 6653–6656. doi:10.1109/IGARSS.2016.7730737

Wang, B. and LinHo (2002). Rainy Season of the Asian–Pacific Summer Monsoon*. *Journal of Climate* 15, 386–398. doi:10.1175/1520-0442(2002)015⟨0386:RSOTAP⟩2.0.CO;2

Wang, Z., Jiang, Z., Wu, K., Liu, S., Zhang, Y., Wang, X., et al. (2023). Characteristics of Glaciers Surging in the Western Pamirs. *Remote Sensing* 15, 1319. doi:10.3390/rs15051319

Watson, C. S. and King, O. (2018). Everest's thinning glaciers: implications for tourism and mountaineering. *Geology Today* 34, 18–25. doi:10.1111/gto.12215

WATSON, C. S., QUINCEY, D. J., SMITH, M. W., CARRIVICK, J. L., ROWAN, A. V., and JAMES, M. R. (2017). Quantifying ice cliff evolution with multi-temporal point clouds on the debris-covered khumbu glacier, nepal. *Journal of Glaciology* 63, 823–837. doi:10.1017/jog.2017.47

Webster, P. J., Magaña, V. O., Palmer, T. N., Shukla, J., Tomas, R. A., Yanai, M., et al. (1998). Monsoons: Processes, predictability, and the prospects for prediction. *Journal of Geophysical Research: Oceans* 103, 14451–14510. doi:10.1029/97JC02719

Westoby, M. J., Rounce, D. R., Shaw, T. E., Fyffe, C. L., Moore, P. L., Stewart, R. L., et al. (2020). Geomorphological evolution of a debris-covered glacier surface. *Earth Surface Processes and Landforms* 45, 3431–3448. doi:10.1002/esp.4973

Willis, M. J., Herried, B. G., Bevis, M. G., and Bell, R. E. (2015). Recharge of a subglacial lake by surface meltwater in northeast Greenland. *Nature* 518, 223–227. doi:10.1038/nature14116

Wulf, H., Bookhagen, B., and Scherler, D. (2016). Differentiating between rain, snow, and glacier contributions to river discharge in the western Himalaya using remote-sensing data and distributed hydrological modeling. *Advances in Water Resources* 88, 152–169. doi:10.1016/j.advwatres.2015.12.004

Yunjun, Z., Fattahi, H., and Amelung, F. (2019). Small baseline InSAR time series analysis: Unwrapping error correction and noise reduction. *Computers & Geosciences* 133, 104331. doi:10.1016/j.cageo.2019.104331

Zekollari, H. and Huybrechts, P. (2018). Statistical modelling of the surface mass-balance variability of the morteratsch glacier, switzerland: strong control of early melting season meteorological conditions. *Journal of Glaciology* 64, 275–288. doi:10.1017/jog.2018.18

Zekollari, H., Huybrechts, P., Fürst, J., Rybak, O., and Eisen, O. (2013). Calibration of a higher-order 3-D ice-flow model of the Morteratsch glacier complex, Engadin, Switzerland. *Annals of Glaciology* 54, 343–351. doi:10.3189/2013AoG63A434

Zeller, L., McGrath, D., Sass, L., O'Neel, S., McNeil, C., and Baker, E. (2022). Beyond glacier-wide mass balances: parsing seasonal elevation change into spatially resolved patterns of accumulation and ablation at Wolverine Glacier, Alaska. *Journal of Glaciology* , 1–16doi:10.1017/jog.2022.46

Zhai, C., Dyer, J., Lu, E., and Buie, M. (2018). Technical Note: Asteroid Detection Demonstration from SkySat-3* B612 Data using Synthetic Tracking , 17

Zhang, K., Sun, J., and Snavely, N. (2019). Leveraging Vision Reconstruction Pipelines for Satellite Imagery. In *ICCV Workshop on 3D Reconstruction in the Wild (3DRW)*

Zheng, W., Bhushan, S., Van Wyk De Vries, M., Kochtitzky, W., Shean, D., Copland, L., et al. (2023). *GLAcier Feature Tracking testkit (GLAFT): A statistically- and physically-based framework for evaluating glacier velocity products derived from satellite image feature tracking*. preprint, Glaciers/Remote Sensing. doi:10.5194/tc-2023-38

östrem, G. (1959). Ice Melting under a Thin Layer of Moraine, and the Existence of Ice Cores in Moraine Ridges. *Geografiska Annaler* 41, 228–230. doi:10.1080/20014422.1959.11907953

Appendix A

SUPPLEMENTARY MATERIAL FOR CHAPTER 2: AUTOMATED DIGITAL ELEVATION MODEL (DEM) GENERATION FROM VERY-HIGH-RESOLUTION PLANET SKYSAT TRIPLET STEREO AND VIDEO IMAGERY

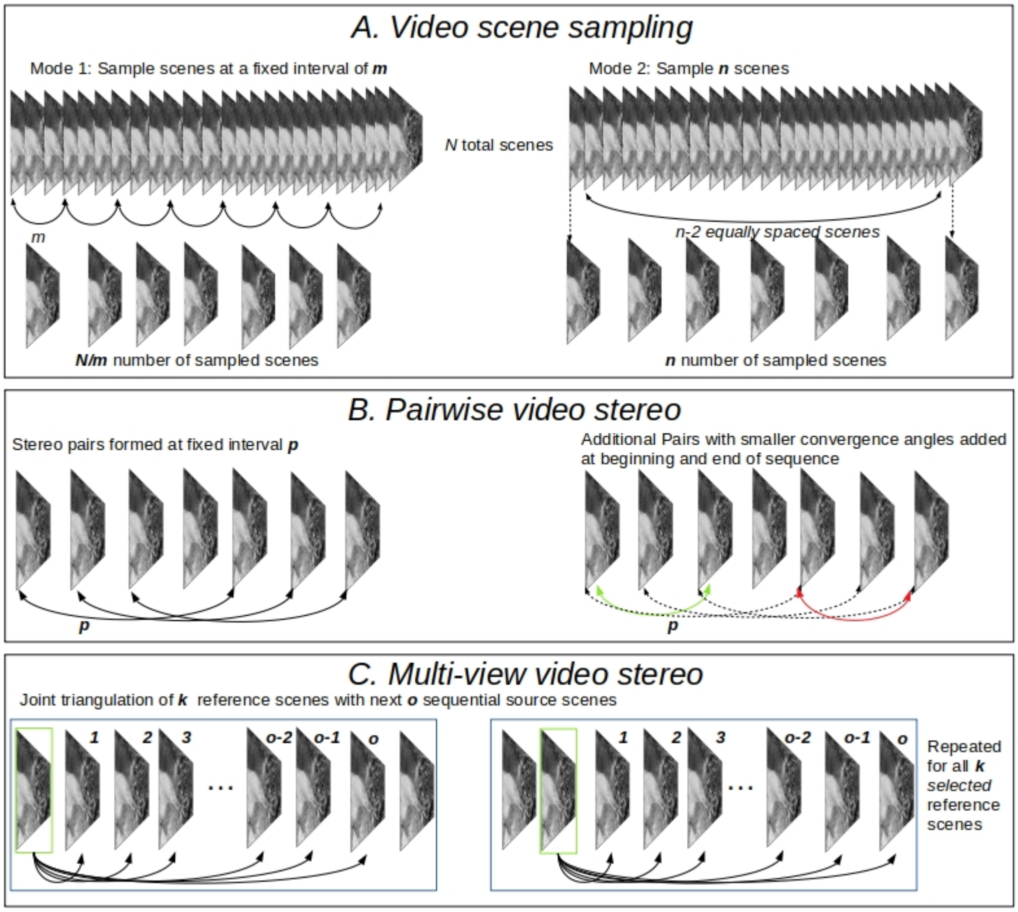

Figure A.1: Schematic representation of A) SkySat video scene sampling and subsequent pairing strategies for B) pairwise and C) multi-view stereo reconstruction.

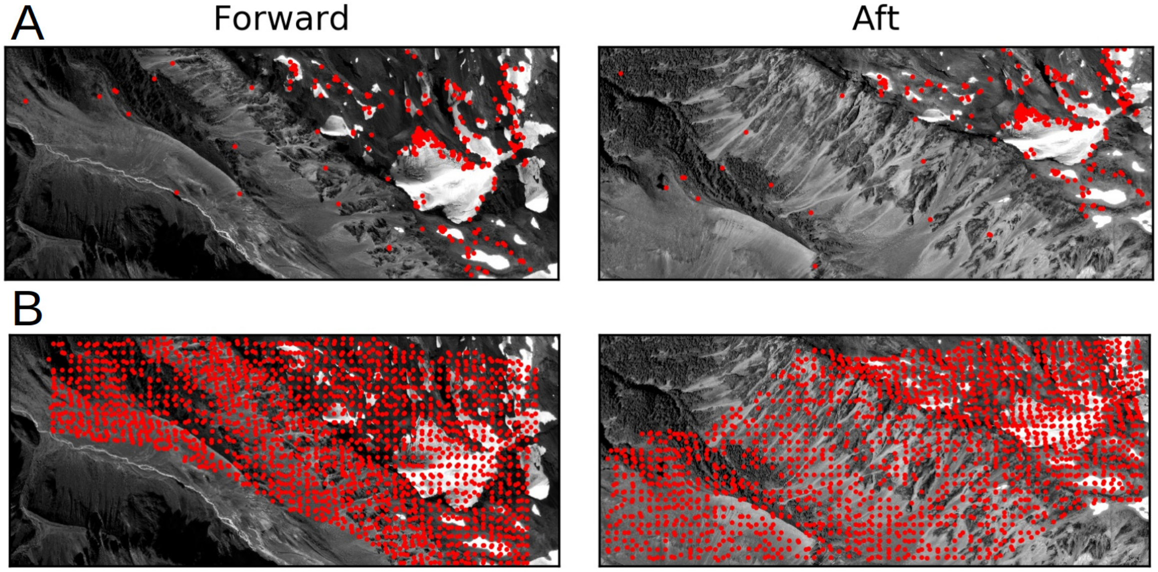

Figure A.2: Example of feature match points between two overlapping SkySat scenes with a large convergence angle (∼55°) using: A) SIFT, and B) the approach outlined by Dehecq et al. (2020) involving dense matches obtained from ASP's sub-pixel image correlator for orthorectified scenes. L1B imagery is ©Planet, 2019.

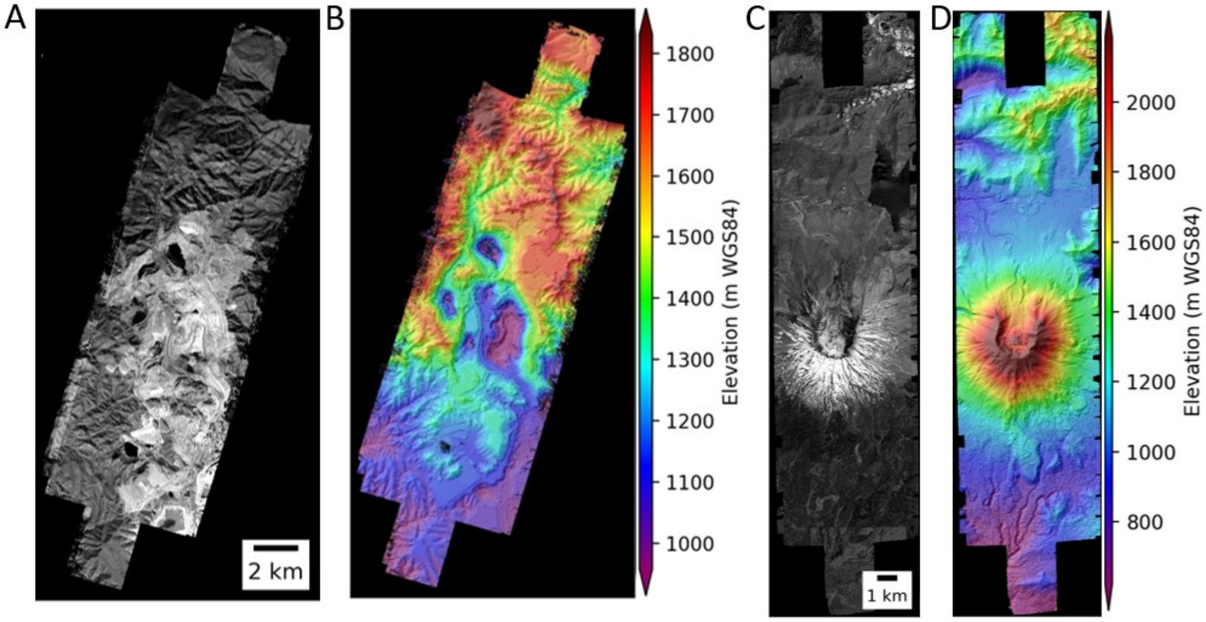

Figure A.3: Additional SkySat triplet stereo orthomosaic and DEM composite products for A,B) Morenci mine site, Arizona derived from two stereo triplets acquired on January 28, 2019 (identifiers: 20190128_174855_ssc3, 20190128_174929_ssc3, 20190128_175004_ssc3 and 20190128_204710_ssc6, 20190128_204744_ssc6, 20190128_204819_ssc6), and C,D) Mt. St. Helen's, Washington state, derived from one stereo triplet acquired on June 13, 2019 (identifiers: 20190613_190047_ssc4, 20190613_190121_ssc4, 20190613_190157_ssc4)). The orthoimage mosaics were derived from L1B imagery that is ©Planet, 2019.

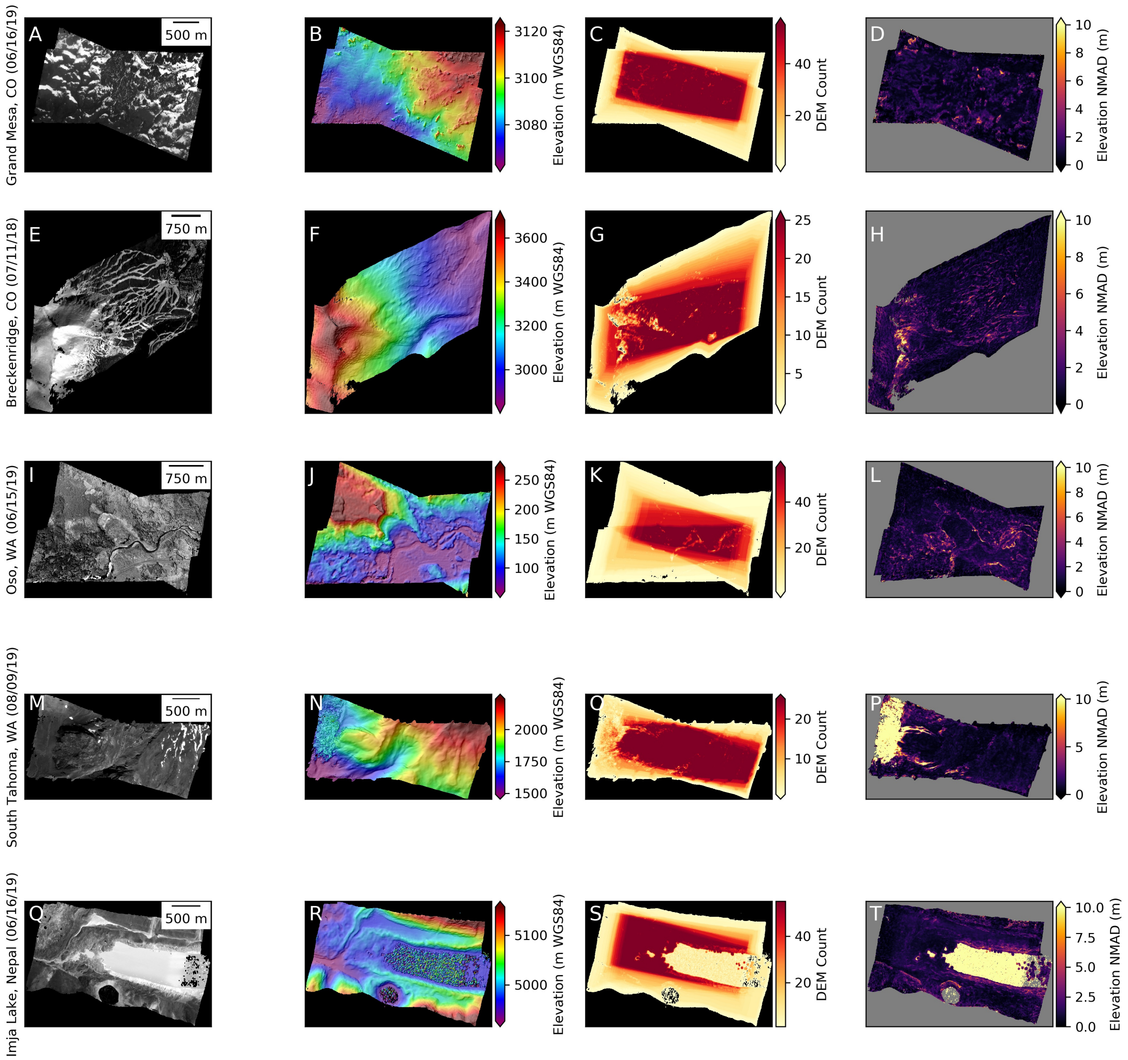

Figure A.4: Additional SkySat video products over A-D) Grand Mesa, CO; E-H) Breckenridge, CO; I-L) Oso landslide site, WA; M-P) South Tahoma Glacier outburst flood site, Mt. Rainier, WA; and Q-T) Imja Lake, Nepal. Refer to Figure 2.7 caption for details. Higher NMAD values are present over portions of the South Tahoma Glacier (P) and Imja Lake (T) sites due to moving clouds and water, respectively. The orthoimage mosaics were derived from L1A imagery that is ©Planet, 2019.

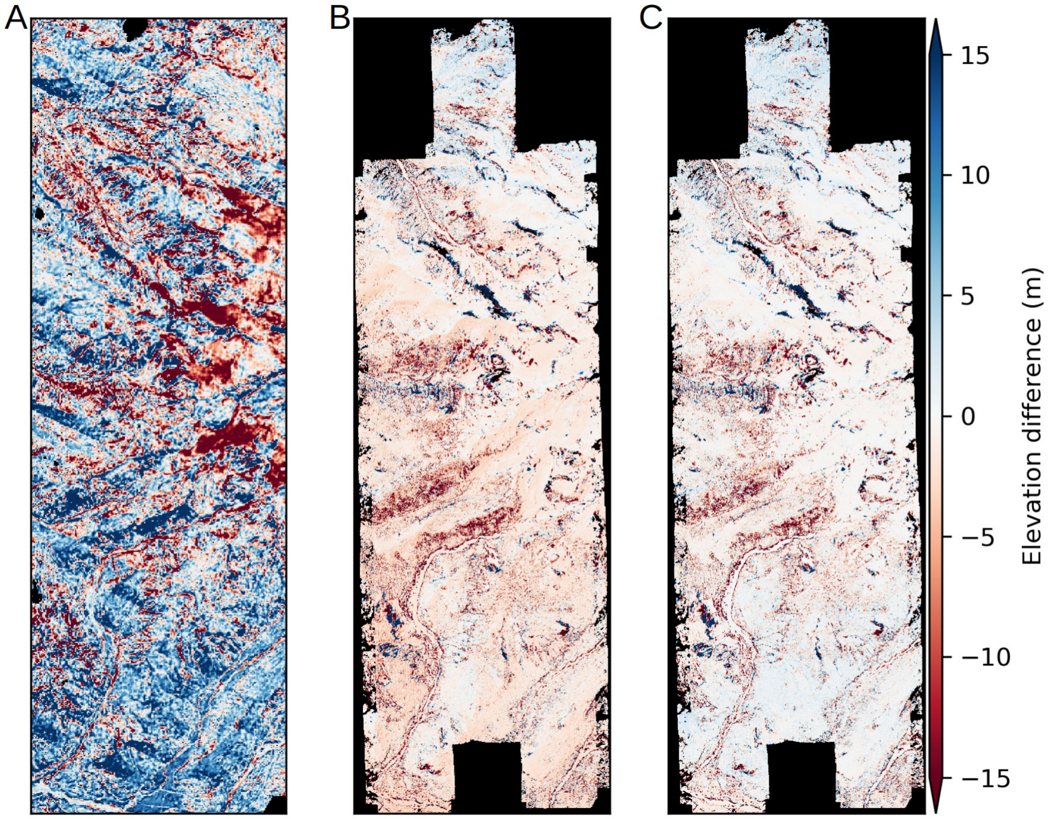

Figure A.5: Reference DEM evaluation for Mt. Rainier SkySat triplet stereo case study. A) Elevation difference map between the 2007/2008 LiDAR DSM and 2000 SRTM-GL1 reference DEM. Negative values (red) show thinning over glaciers between 2000 and 2007/2008. Note the residual positive (blue) values over forested areas, likely introduced by penetration of the SRTM C-band radar. B) Elevation difference between the two SkySat DEMs derived using the SRTM-GL1 and LiDAR reference DEMs. C) Same as in (B) but after additional relative co-registration of the output SkySat DEMs.

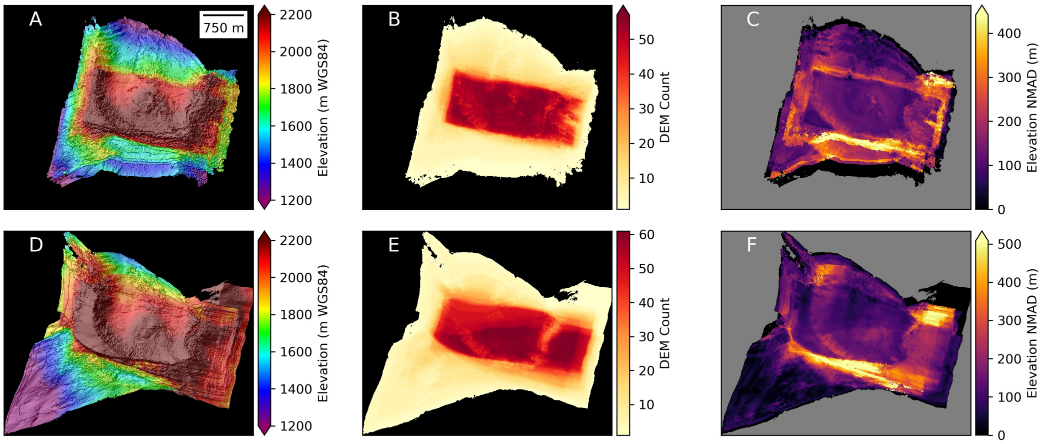

Figure A.6: SkySat video products for Mt. St. Helen's test cases derived using the original RPC camera models provided by Planet: A-C) Snow-on, and D-F) Snow-off. See Figure 2.7 caption for more details. Note large relative geolocation and vertical elevation error compared to corresponding products generated using our refined camera models (Figure 2.7).

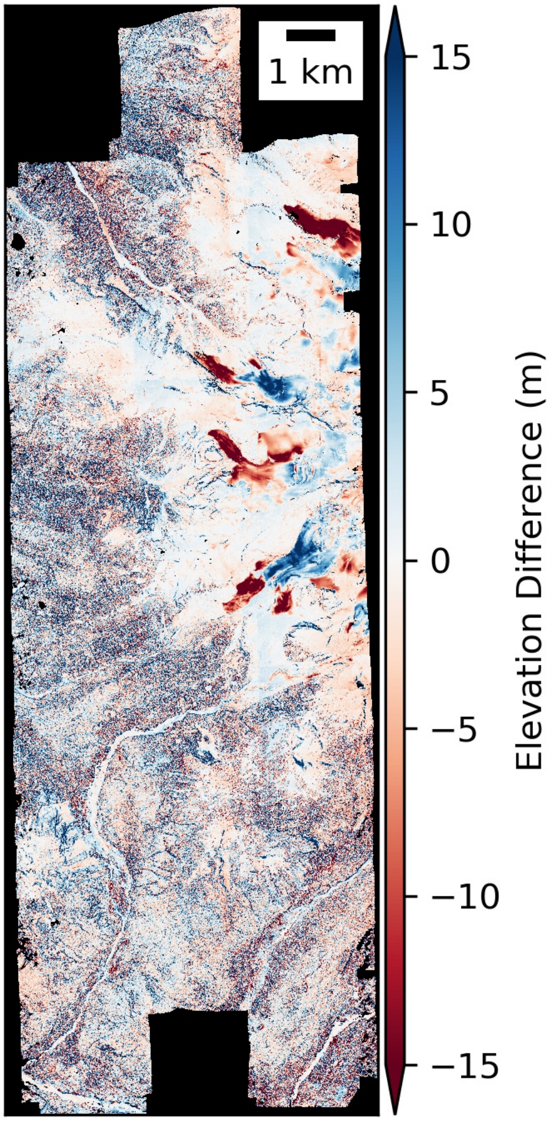

Figure A.7: Elevation difference map for the Mt. Rainier SkySat triplet stereo DEM composite created after individually co-registering pairwise DEMs to the LiDAR reference DEM, instead of first creating a DEM composite and then co-registering the composite to the reference DEM (as in Figure 2.5D,E). Note reduced errors, especially for scenes around the margins of the composite. This pairwise DEM co-registration approach works well for sites with sufficient local topographic roughness and static surface distribution, but will fail for more planar surfaces.

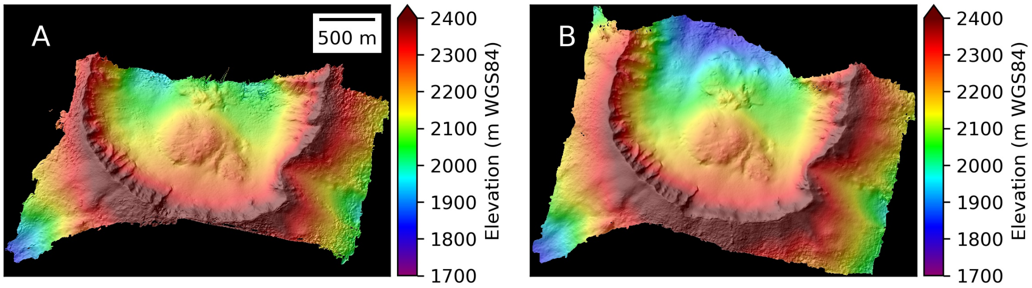

Figure A.8: Composite DEMs for the SkySat snow-on video collection on April 4, 2019, prepared using A) ASP multi-view stereo (MVS) workflow (Section 2.4.2) with 14 multi-view DEMs, following d'Angelo et al. (2016), and B) our preferred pairwise stereo workflow (as in Figure 2.7) involving 62 pairwise DEMs. Note the reduced footprint and presence of additional artifacts compared to the products in Figure 2.7

Appendix B

SUPPLEMENTARY MATERIAL FOR CHAPTER 3: SEASONAL AND ANNUAL SURFACE MASS BALANCE FOR DEBRIS-COVERED GLACIERS IN HIGH-MOUNTAIN ASIA FROM FLOW-CORRECTED SATELLITE STEREO DEM TIME SERIES

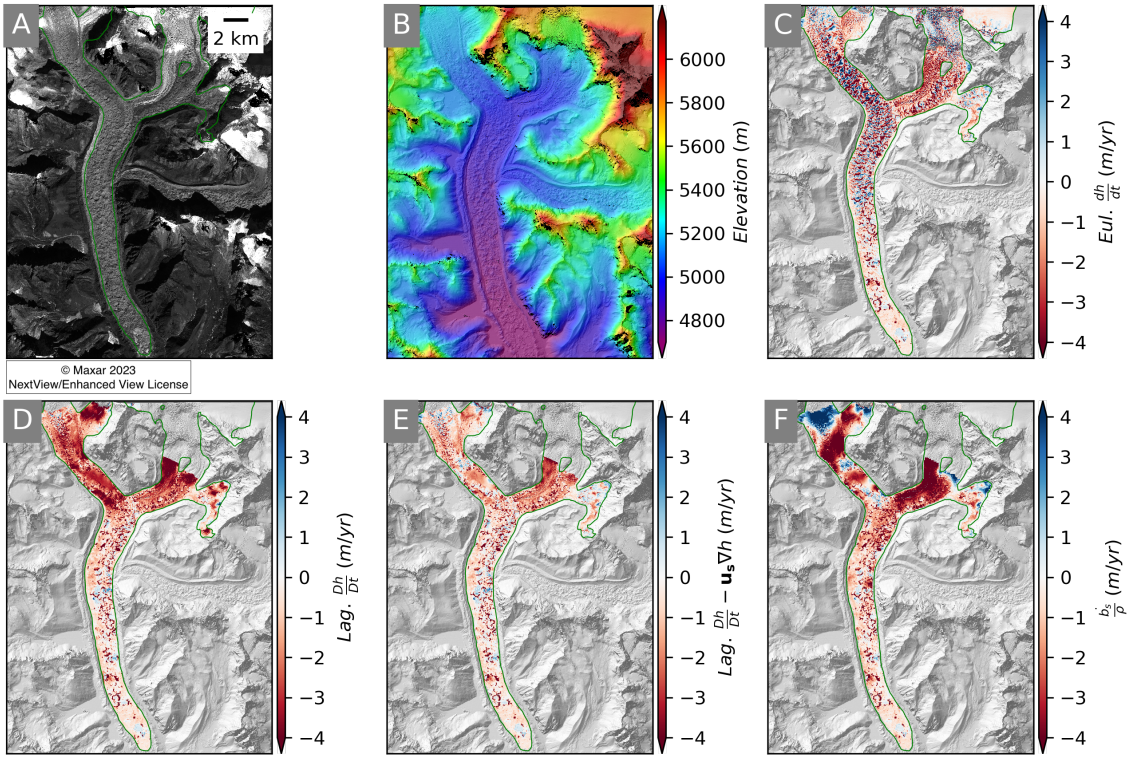

© Maxar 2023
NextView/Enhanced View License

Figure B.1: Surface elevation change products over Ngozumpa Glacier for the period December 23, 2012 to January 15, 2015: A) Panchromatic GE01 orthoimage from December 23, 2012, B) Color shaded relief map, C) Eulerian elevation change rate ($\frac{dh}{dt}$), D) Lagrangian elevation change rate ($\frac{Dh}{Dt}$), E) slope-corrected Lagrangian elevation change rate ($\frac{Dh}{Dt} - \mathbf{u_s}\nabla h$) and F) Lagrangian SMB ($\frac{\dot{b}_s}{\rho}$) obtained by adding flux divergence to (E). Note the reduction in signal aliasing for products in Lagrangian frame of reference (D, E, F) and enhancement of SMB signal where flux divergence is high (F).

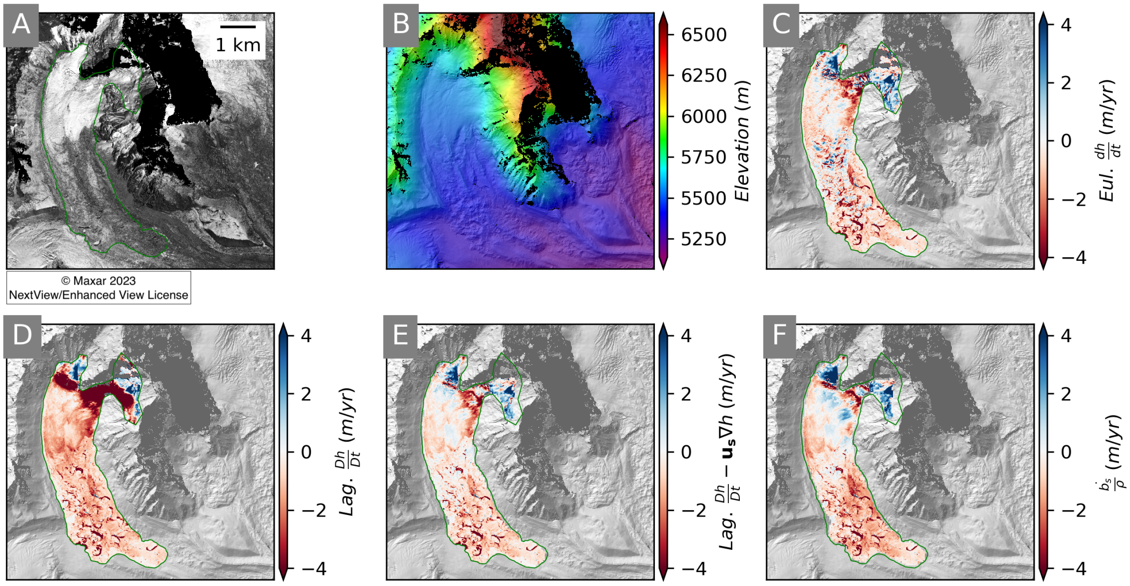

Figure B.2: Surface elevation change products over Black Changri Nup Glacier for the period November 02, 2015 to October 25, 2016: A) Panchromatic WV03 orthoimage from November 02, 2015, B) Color shaded relief map, C) Eulerian elevation change rate ($\frac{dh}{dt}$), D) Lagrangian elevation change rate ($\frac{Dh}{Dt}$), E) slope-corrected Lagrangian elevation change rate ($\frac{Dh}{Dt} - \mathbf{u_s}\nabla h$) and F) Lagrangian SMB ($\frac{\dot{b_s}}{\rho}$) obtained by adding flux divergence to (E). Note the reduction in signal aliasing for products in Lagrangian frame of reference (D, E, F) and enhancement of SMB signal where flux divergence is high (F).

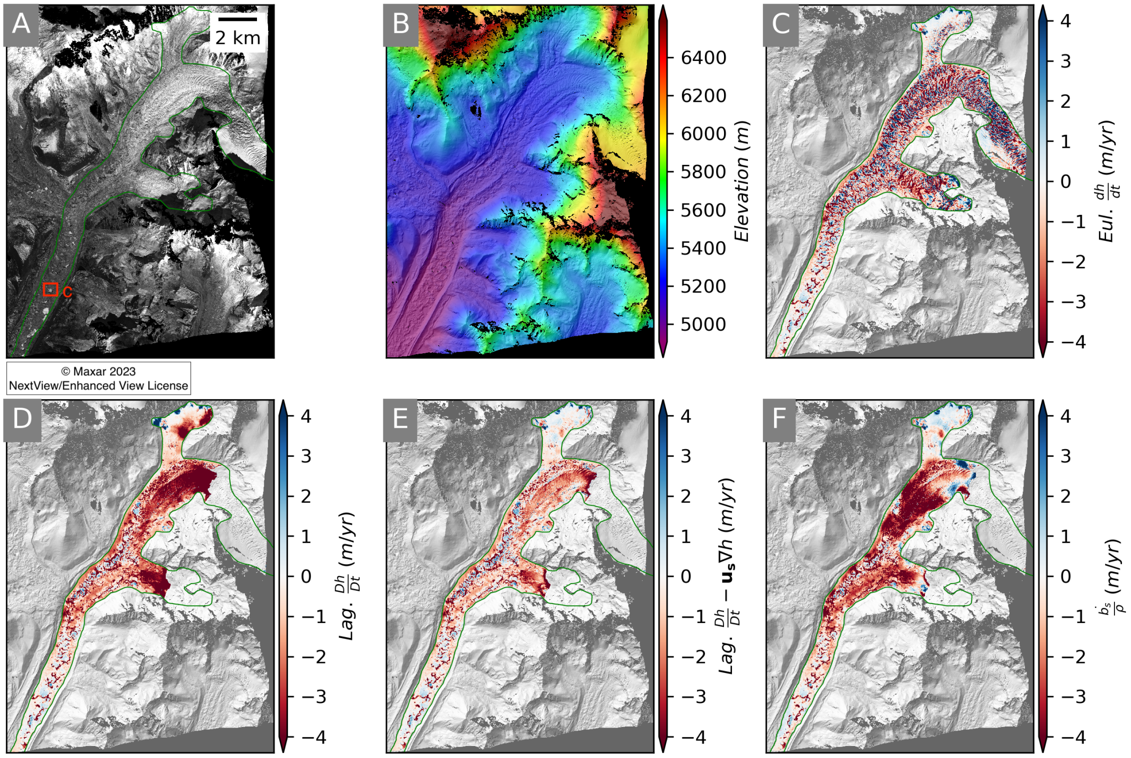

Figure B.3: Surface elevation change products over Khumbu Glacier for the period November 02, 2015 to October 25, 2016: A) Panchromatic WV03 orthoimage from November 02, 2015, B) Color shaded relief map, C) Eulerian elevation change rate ($\frac{dh}{dt}$), D) Lagrangian elevation change rate ($\frac{Dh}{Dt}$), E) slope-corrected Lagrangian elevation change rate ($\frac{Dh}{Dt} - \mathbf{u_s}\nabla h$) and F) Lagrangian SMB rate ($\frac{\dot{b_s}}{\rho}$) obtained by adding flux divergence to (E). Lagrangian SMB rates over red panel (c) in the orthoimage (A) are shown in detail in (Figure 10 C). Note the reduction in signal aliasing for products in Lagrangian frame of reference (D, E, F) and enhancement of SMB signal where flux divergence is high (F).

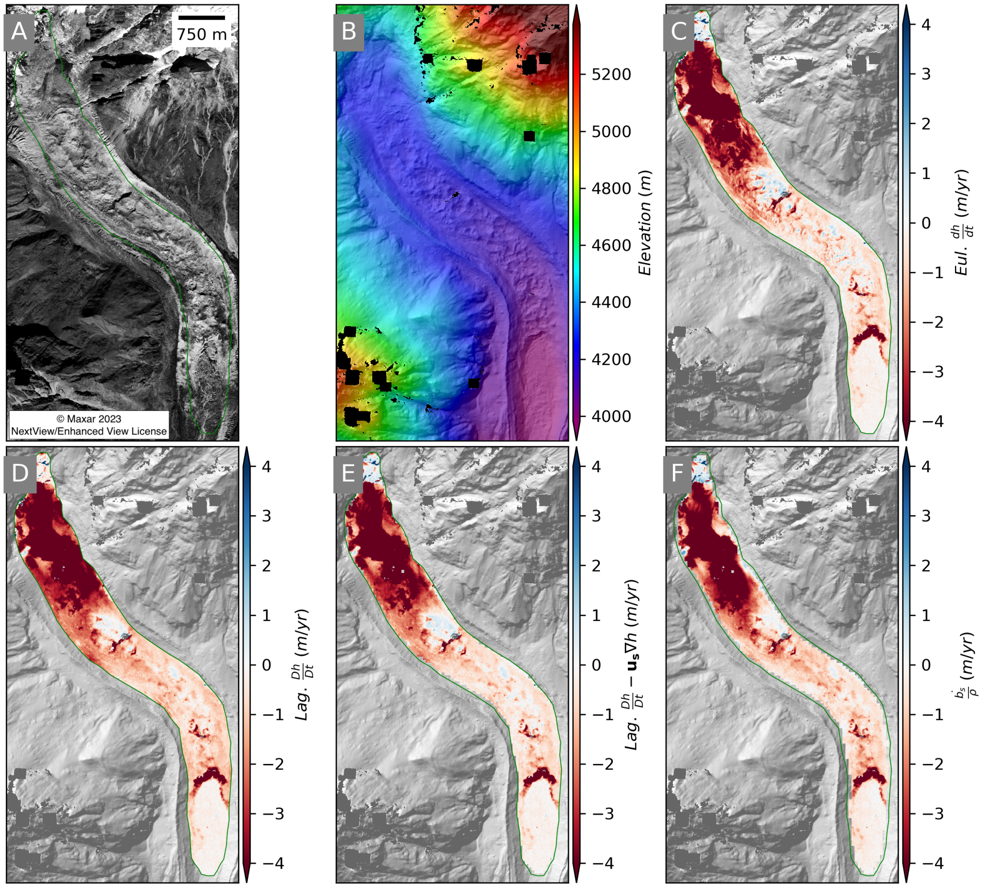

Figure B.4: Surface elevation change products over Lirung Glacier for the period November 06, 2016 to December 22, 2017: A) Panchromatic WV02 orthoimage from November 06, 2016, B) Color shaded relief map, C) Eulerian elevation change rate ($\frac{dh}{dt}$), D) Lagrangian elevation change rate ($\frac{Dh}{Dt}$), E) slope-corrected Lagrangian elevation change rate ($\frac{Dh}{Dt} - \mathbf{u_s}\nabla h$) and F) Lagrangian SMB rate ($\frac{\dot{b}_s}{\rho}$) obtained by adding flux divergence to (E). Note the reduction in signal aliasing for products in Lagrangian frame of reference (D, E, F) and enhancement of SMB signal where flux divergence is high (F).

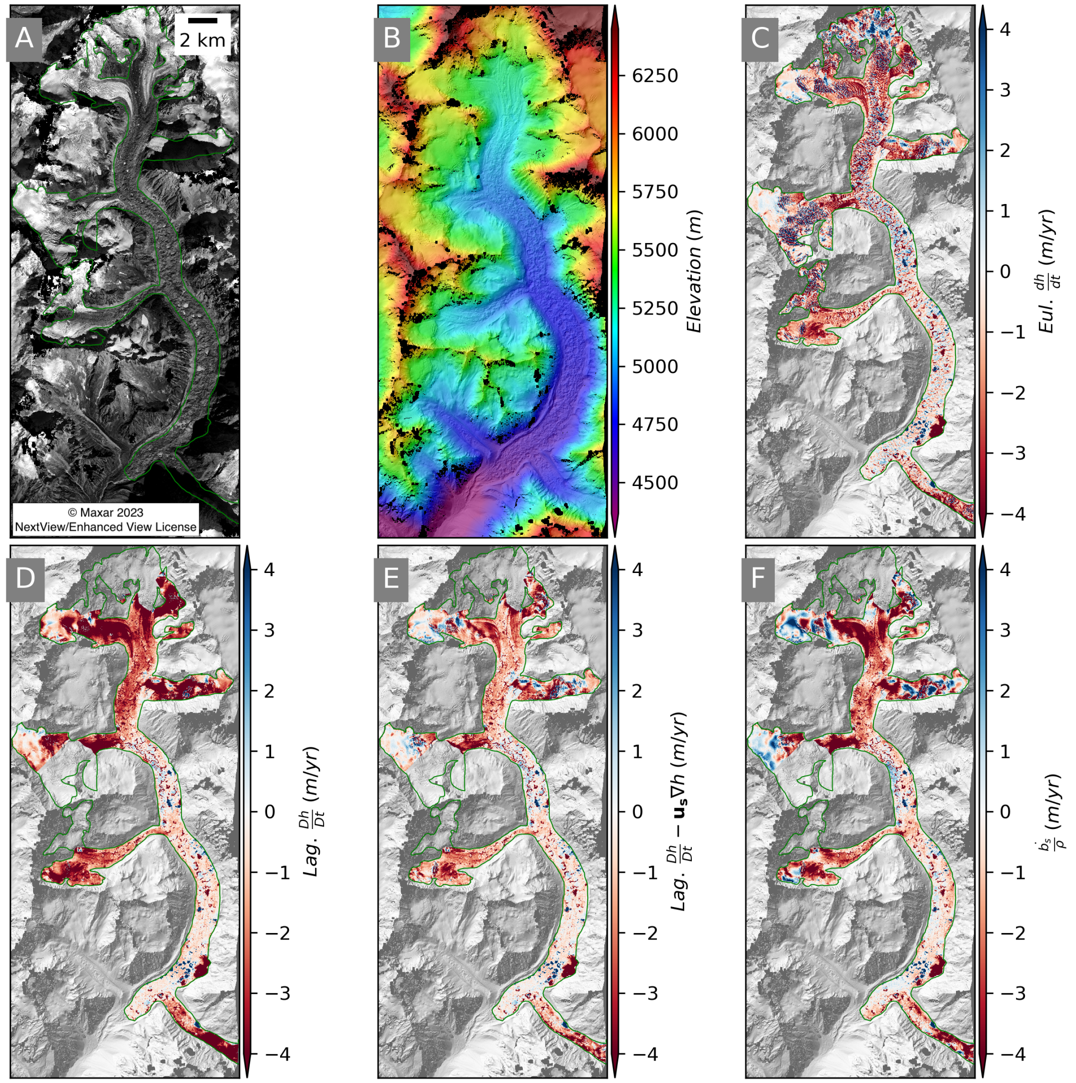

Figure B.5: Surface elevation change products over Langtang Glacier for the period February 22, 2015 to January 07, 2016: A) Panchromatic WV02 orthoimage from January 07, 2016, B) Color shaded relief map, C) Eulerian elevation change rate ($\frac{dh}{dt}$), D) Lagrangian elevation change rate ($\frac{Dh}{Dt}$), E) slope-corrected Lagrangian elevation change rate ($\frac{Dh}{Dt} - \mathbf{u_s}\nabla h$) and F) Lagrangian SMB rate ($\frac{\dot{b_s}}{\rho}$) obtained by adding flux divergence to (E). Note the reduction in signal aliasing for products in Lagrangian frame of reference (D, E, F) and enhancement of SMB signal where flux divergence is high (F).

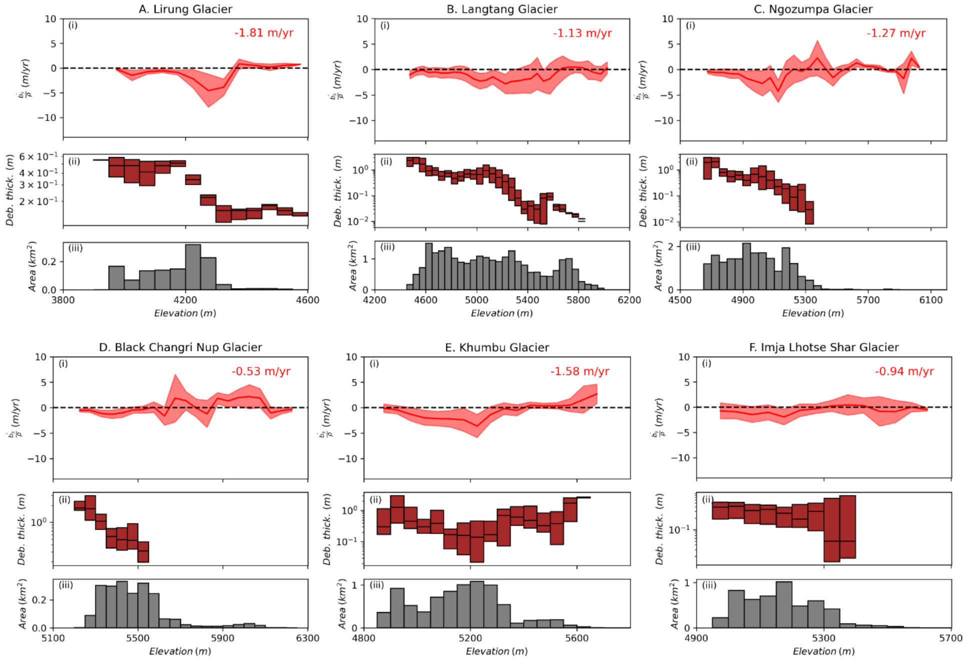

Figure B.6: Lagrangian SMB and hypsometry profiles for A) Lirung, B) Langtang, C) Ngozumpa, D) Black Changri Nup, E) Khumbu, and F) Imja Lhotse Shar Glacier: i) Lagrangian SMB, ii) debris thickness, and iii) glacier area aggregated over 50 m elevation bins. Shaded area around SMB curve represents NMAD range for that elevation bin, while limits of box plot for debris thickness represents bin's interquartile debris thickness range, which is plotted in Logarithmic scale. Text on upper right corner in subplots denotes the area weighted average of SMB rates. Note most negative SMB occurs at higher elevations and not at the glacier terminus for all glaciers. Also, refer to spatial coverage of SMB maps in (Figure 3.5, B.1, B.2,B.3, B.4 and B.5) when interpreting area weighted SMB averages.

Appendix C

SUPPLEMENTARY MATERIAL FOR CHAPTER 4: SEASONAL TO MONTHLY GLACIER VELOCITY ESTIMATION USING NEAR-DAILY, PLANETSCOPE DOVE CLASSIC IMAGERY

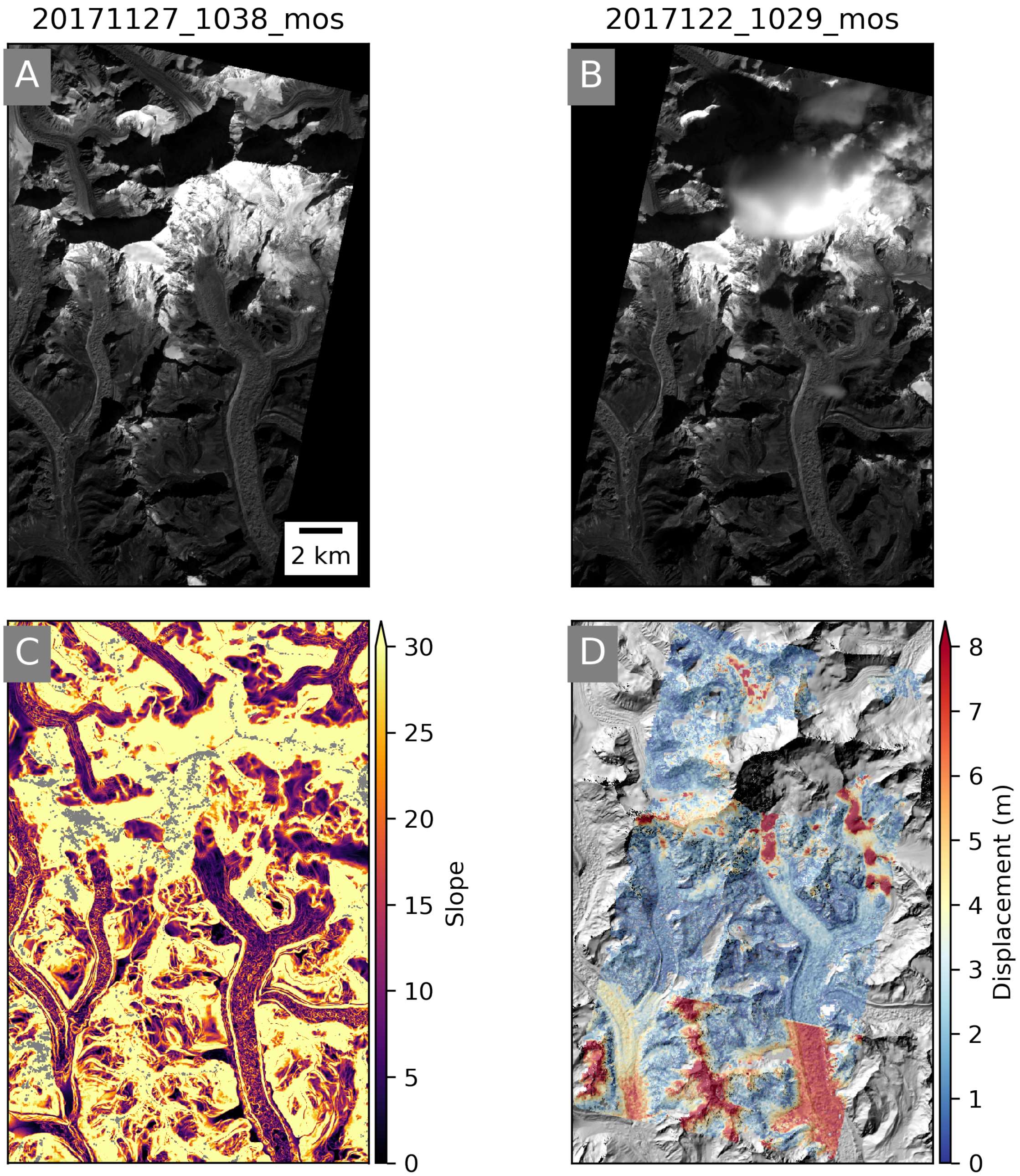

Figure C.1: Intra-image relative displacement artifacts correlated with topography. Orthoimage mosaics prepared from NIR images collected on A) 20171127 and B) 20171222 by satellites 1038 and 1029 respectively. C) Per-pixel slope map derived from HiMAT-1 DEM mosaic (Shean 2017). D) Displacement map obtained from correlation of orthoimage mosaics shown in A and B and overlaid on hillshade generated from HiMAT-1 DEM mosaic (Shean 2017). Note high relative displacement values along slow sloped glacier valleys and along crest of mountain tops in the southern pair but limited such artifact in the displacement pairs north to it.

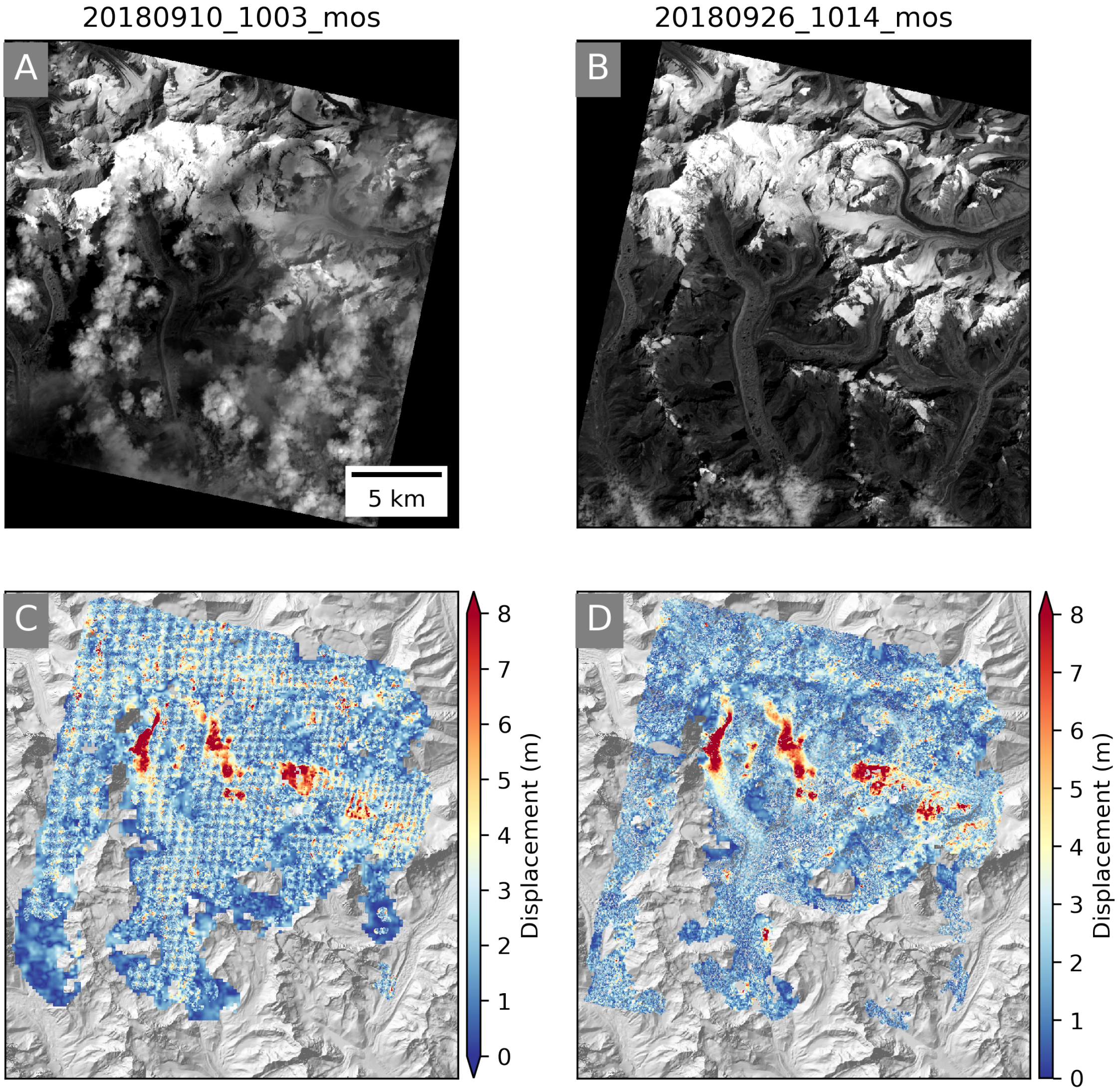

Figure C.2: Intra-image relative displacement artifacts induced by pre-processing contrast enhancement step. Orthoimage mosaics prepared from NIR images collected on A) 20171021 and B) 20171114 by satellites 1002 and 102e respectively. Displacement map obtained from correlation of orthoimage mosaics shown in A and B using C) autoRIFT default Wallis Filter with kernel width = 5 pixel and D) Laplacian filter with kernel width = 15 pixel. The displacement maps are overlaid on hillshade generated from HiMAT-1 DEM mosaic (Shean 2017). Note the removal of hatched displacement artifacts in yellow (∼4 m) using a Wallis filter with small kernels, which are mitigated when using Laplacian edge enhancement technique with a larger kernel, without considerable loss in coverage. All other autoRIFT_vmap.py parameters were the same in both the runs.

VITA

Shashank Bhushan was born and raised in Patna, India, a city located on the floodplains of River Ganges. The fact that the Ganges River receives a part of its summer flow from snow and ice melt in the mountains was Shashank's only connection to the mountains, before perusing cryospheric research as an undergrad :) Shashank obtained a Integrated MSc. (Tech.) degree in Applied Geology from IIT (ISM) Dhanbad in 2018. While at IIT (ISM), he got an opportunity to work at the Applied Physics Lab, University of Washington as a student intern, where actually for the first time Shashank saw glacier(s), mountain(s), and volcano in one go (Mt. Rainier). He returned to the UW as a graduate student in 2018. Shashank has also worked at Planet Labs as a Photogrammetry Intern in 2020, just when the pandemic started :) Going forward, Shashank is interested in expanding his knowledge on satellite remote sensing, and hopes to pursue Earth Science research ideas which benefit people in the currently warming world!

Most of the time when not staring a screen, Shashank can be found cracking terrible jokes, maybe sometimes biking, or mostly cooking food and feeding his friends and family :)